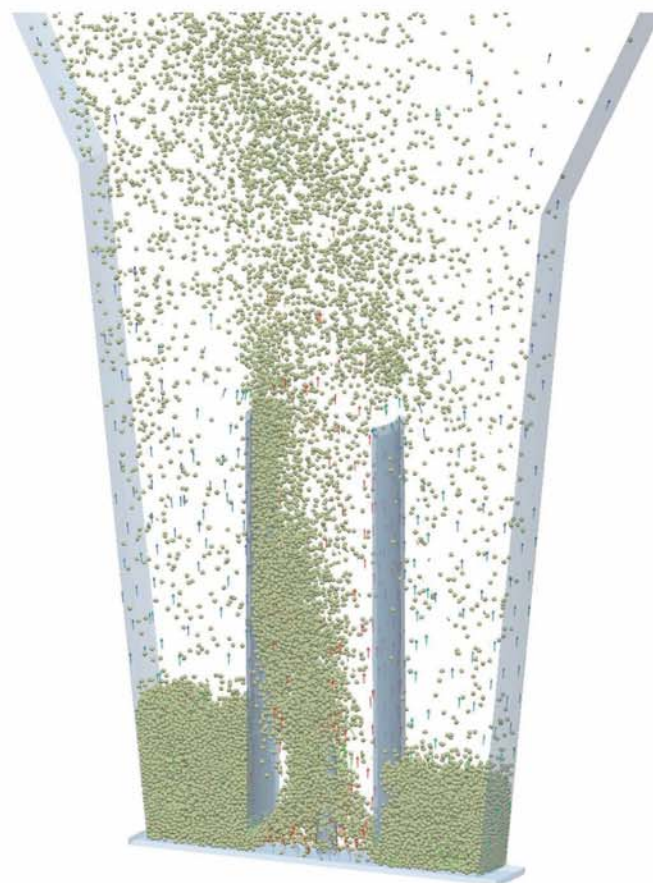


Lennart Fries

Discrete particle modeling of a fluidized bed granulator



Cuvillier Verlag Göttingen
Internationaler wissenschaftlicher Fachverlag



Discrete particle modeling of a fluidized bed granulator





Discrete particle modeling of a fluidized bed granulator

**Vom Promotionsausschuss der
Technischen Universität Hamburg-Harburg
zur Erlangung des akademischen Grades eines**

Doktor-Ingenieur (Dr.-Ing.)

genehmigte Dissertation

von Dipl.-Ing. Lennart Fries

aus Hamburg.

2012



Bibliografische Information der Deutschen Nationalbibliothek

Die Deutsche Nationalbibliothek verzeichnet diese Publikation in der Deutschen Nationalbibliografie; detaillierte bibliografische Daten sind im Internet über <http://dnb.d-nb.de> abrufbar.

1. Aufl. - Göttingen : Cuvillier, 2012

Zugl.: (TU) Hamburg-Harburg, Univ., Diss., 2012

978-3-95404-245-6

Gutachter

1. Prof. Dr.-Ing. habil. Stefan Heinrich, Technische Universität Hamburg-Harburg
2. Prof. Dr.-Ing. habil. Stefan Palzer, Nestlé Product Technology Centre York
3. Prof. Dr. ir. J.A.M. Kuipers, Eindhoven University of Technology

Tag der mündlichen Prüfung

16.08.2012

© CUVILLIER VERLAG, Göttingen 2012

Nonnenstieg 8, 37075 Göttingen

Telefon: 0551-54724-0

Telefax: 0551-54724-21

www.cuvillier.de

Alle Rechte vorbehalten. Ohne ausdrückliche Genehmigung des Verlages ist es nicht gestattet, das Buch oder Teile daraus auf fotomechanischem Weg (Fotokopie, Mikrokopie) zu vervielfältigen.

1. Auflage, 2012

Gedruckt auf säurefreiem Papier

978-3-95404-245-6



The world belongs to those who set out to conquer it
armed with self confidence and good humour.

Charles Dickens





Vorwort

Die vorliegende Arbeit entstand während meiner Tätigkeit als wissenschaftlicher Mitarbeiter am Institut für Feststoffverfahrenstechnik und Partikeltechnologie an der Technischen Universität Hamburg-Harburg.

Bei meinem Doktorvater, Herrn Prof. Dr.-Ing. habil. Stefan Heinrich, Leiter des Instituts für Feststoffverfahrenstechnik und Partikeltechnologie, möchte ich mich an dieser Stelle ganz besonders für die Unterstützung und aktive Förderung sowie für das entgegengebrachte Vertrauen bedanken. Sein Enthusiasmus und sein unermüdliches Engagement waren ein besonderer Ansporn für mich. Sowohl die fachliche Expertise als auch der kollegiale Umgang innerhalb der von ihm geführten Arbeitsgruppe waren Voraussetzung für den Erfolg dieser Arbeit.

Mein besonderer Dank gilt Herrn Dr.-Ing. Sergiy Antonyuk sowie Herrn Dr.-Ing Daniel Dopfer für die fachliche Betreuung und die zahlreichen Diskussionen, die wesentlich zum Gelingen der Dissertation beigetragen haben.

Ebenso danke ich Herrn Prof. Dr.-Ing. habil. Stefan Palzer, Leiter des Nestlé Product Technology Centre for Confectionary in York, Großbritannien, für seine zahlreichen Anregungen, die der Fokussierung der Praxisrelevanz dieser Arbeit dienten. Meinen Dank aussprechen möchte ich ihm ebenfalls für die Einladung zu einem Forschungsaufenthalt am Nestlé Research Center Lausanne und für die Übernahme des ersten externen Gutachtens.

Für die fachliche Begleitung dieser Arbeit und für die Übernahme des zweiten Gutachtens danke ich Herrn Prof. Dr. ir. J.A.M. Kuipers, Leiter der Multiphase Reactors Forschungsgruppe an der Technischen Universität Eindhoven, Niederlande.

Ein besonderer Dank gebührt allen meinen Kollegen am Institut für Partikeltechnologie, die mich durch stetige Diskussionen unterstützt haben. Eine zentrale Hilfe für mich waren auch die Studenten Irina Valcheva, Xiuhan Yu, Violeta Popova und Annika Rosseburg, die durch die



Anfertigung ihrer Bachelor-, Master- bzw. Studien- und Diplomarbeiten maßgeblich Anteil am Gelingen der experimentellen Arbeit haben.

Großen Dank schulde ich auch den technischen Mitarbeitern des Instituts, Heiko Rohde, Frank Rimoschat und Bernhard Schult für ihr außergewöhnliches Engagement beim Auf- und Umbau der Versuchsanlage.

Den Kollegen in der Gruppe Solid Products am Nestlé Research Center in Lausanne, Herrn Laurent Forny, Cédric Dubois, Alessandro Gianfrancesco und Gerhard Niederreiter danke ich für die exzellente Zusammenarbeit schon während meiner Promotionszeit sowie für die Durchführung von Strukturanalysen am Röntgentomographen.

Bei der Firma Nestlé bedanke ich mich für die großzügige Finanzierung meines Projektes.

Widmen möchte ich diese Arbeit meinen Eltern Monika und Sören Fries. Mit ihrer unaufgeregten Art haben sie mich entscheidend geprägt, mich während der gesamten Ausbildungszeit unterstützt und meinen Lebensweg in Nah und Fern aufmerksam begleitet. Dafür danke ich ihnen.

Lausanne, 20.08.2012

Lennart Fries



Abstract

Size-enlargement and structuration processes in fluidized beds such as granulation and agglomeration play an important role in the pharmaceutical and fine chemical industries as well as in food technology to improve the flowability and the instant properties of solid products. Dust-free and free-flowing particles can be produced in a process with favourable heat- and mass transfer conditions. Furthermore, this technology allows the formulation of particles with novel functionalities by applying coating layers or via the encapsulation of active ingredients. Several interdependent micro mechanisms including particle collisions, wetting, drying and phase transitions govern the process dynamics and complicate predictions on the effect of variable operating conditions on product properties such as structure, strength and re-dissolution behaviour. Profound knowledge on these mechanisms is needed to understand the influence of individual process parameters on the final product properties.

A suitable approach to model the particle interactions in fluidized beds is the Discrete Element Method (DEM) coupled with Computational Fluid Dynamics (CFD). Information on gas and particle velocities, particle rotation and collision dynamics, which are very complicated to measure in fluidized beds, can be studied in detail with this technique.

This thesis presents DEM-CFD simulation results for three different granulator configurations (top-spray, Wurster-coater, spouted bed) in comparison to experimental results, regarding the agglomeration of amorphous maltodextrin (DE 21). In simulation and experiment the identical geometry of the equipment was used. Mechanical material properties, such as the coefficient of restitution and the Young's modulus, which are required for the DEM model and which are frequently used as fitting parameters, were measured via static and dynamic deformation tests using maltodextrin agglomerates, beads and bars. The strength of the experimentally produced agglomerates was characterized with a compression tester. Their flow behaviour was assessed with the help of a shear cell.

Very promising results were obtained showing that the homogeneity of particle wetting can well be approximated with the residence time distribution of the particles inside the spray zone.

Homogeneous wetting allows achieving a narrow product size distribution (Fries et al., 2011a). Furthermore, the growth rate of the agglomerates can well be correlated with the simulated wetting intensity, the collision frequency and the collision velocity distribution inside the spray zone. The agglomerate strength shows a strong correlation with the particle-wall collision frequency and velocity distribution found in the simulations. Good agreement was found between the simulation results for the maximum particle deformation and for the energy dissipation during collisions and the measured deformation at the breakage point and the breakage energy.

Due to the high numerical effort, DEM is only suitable for small scale applications. However, the obtained information on the kinetics of particle-particle interactions can be applied as input for macroscopic process models in the framework of a multi scale modeling scheme (Fries et al., 2011b; Werther et al., 2011).

It can be concluded that DEM is a powerful tool for the detailed characterization of fluidized bed granulators. Highly relevant practical answers can be obtained from the model such as the choice of the optimal equipment geometry depending on material properties and product requirements. The model can point out where to position the spray nozzles in order to achieve homogeneous particle wetting and if a draft tube is helpful to maintain stable particle circulation. Based on such findings the model shows potential to increase the throughput of a fluidized bed granulator, while avoiding a bed collapse.



Table of contents

Vorwort	V
Abstract	VII
1 Introduction	1
1.1 General process description.....	1
1.2 Types of fluidized bed agglomeration equipment.....	3
1.2.1 Top-spray granulator.....	4
1.2.2 Bottom-spray granulator.....	4
1.2.3 Wurster-coater.....	5
1.2.4 Rotor granulator.....	5
1.2.5 Spouted bed.....	6
1.2.6 Development of optimized equipment geometries.....	6
1.3 Overview of previous research.....	7
1.3.1 Micro mechanisms in fluidized bed agglomeration.....	7
1.3.2 Modeling approaches for fluid bed granulation and agglomeration.....	17
1.3.3 Applications of the Discrete Element Method.....	20
1.4 Objective and strategy.....	22
1.5 Outline of the thesis.....	24
2 Experimental techniques	26
2.1 Introduction.....	26
2.2 Agglomeration experiments.....	26
2.2.1 Granulator configurations.....	30
2.2.2 Sampling procedure.....	31
2.3 Analysis of the product agglomerates.....	32
2.3.1 Particle size analysis.....	32
2.3.2 Compression tests.....	34
2.4 Mechanical material characterization.....	36
2.4.1 Free-fall test setup for determination of the restitution coefficient.....	36
2.4.2 Three-point bending test for determination of the elastic modulus.....	37
2.4.3 Shear test for determination of the friction coefficient.....	39
3 Discrete Particle Model	43

3.1	Introduction	43
3.2	Fundamental model equations	44
3.3	Resolution of the gas flow field	46
3.4	Coupling between the gas and particle phases	47
3.4.1	Drag correlation for monodisperse systems	47
3.4.2	Calculation of the cell porosity	48
3.4.3	General algorithm	48
3.5	Model describing particle contacts	49
3.6	Definition of a collision	53
3.7	Wet particle interactions	56
3.8	Multi scale modeling framework	57
3.8.1	The micro scale	58
3.8.2	The meso scale	59
3.8.3	The macro scale	60
4	Material characterization for model parameters	62
4.1	Glass transition of amorphous maltodextrin	62
4.2	Coefficient of restitution	64
4.2.1	Free-fall tests with agglomerates	64
4.2.2	Free-fall tests with spherical beads	66
4.2.3	Viscous energy dissipation in a liquid film	67
4.3	Modulus of elasticity	68
4.4	Friction coefficient	69
5	Characterization of a Wurster-coater	72
5.1	Introduction	72
5.2	Simulation conditions	73
5.3	Numerical study on the influence of material properties on the particle and collision dynamics	75
5.3.1	Influence of the elastic modulus	76
5.3.2	Influence of the restitution coefficient	84
5.3.3	Influence of the bed mass	88
5.3.4	Conclusion	93
5.4	Experimental and computational study of the influence of process parameters on particle dynamics and product design	94
5.4.1	Influence of the fluidization air flow rate	96



5.4.2	Influence of the process temperature.....	96
5.4.3	Influence of the liquid injection rate.....	100
5.4.4	Influence of the atomizer gas flow rate.....	101
5.4.5	Influence of the gap distance between Wurster tube and bottom plate.....	106
5.4.6	Conclusion.....	109
5.5	Numerical study on the influence of viscous energy dissipation.....	111
5.5.1	Simulation conditions.....	111
5.5.2	Influence of viscous forces on the particle dynamics.....	112
5.5.3	Influence of viscous forces on the collision dynamics.....	119
5.5.4	Conclusion.....	123
6	Comparison of different granulator geometries	124
6.1	Numerical study on the influence of the equipment geometry.....	124
6.1.1	Simulation conditions.....	125
6.1.2	Particle dynamics.....	127
6.1.3	Collision dynamics.....	134
6.1.4	Particle interactions inside the spray zone.....	142
6.1.5	Residence time distribution in the spray zone.....	146
6.2	Experimental verification of the Discrete Particle Model.....	149
6.2.1	Comparison of the agglomeration rate in different granulator configurations.....	150
6.2.2	Comparison of structure and strength of agglomerates from different granulator configurations.....	153
6.3	Conclusion.....	164
7	Conclusions	165
	Appendix	168
A	Fundamentals in particle technology.....	168
A1	Cumulative size distribution.....	168
A2	Size density distribution.....	169
A3	Sauter mean diameter.....	169
A4	Droplet deposition on a single particle.....	170
B	Specifications of used equipment.....	170
B1	Components of the fluidized bed agglomeration plant.....	170
B2	Particle size analysis.....	173
C	Statistical evaluation of experimental results.....	173
C1	Standard deviation.....	173
C2	Confidence interval.....	173



D Three-dimensional structure thickness.....	174
References	175
List of publications	188
Peer-reviewed journal publications	188
Conference proceedings	188
Curriculum vitae	191



List of figures

Figure 1-1: Principle of fluid bed granulation (a), photograph of urea granules produced by melt injection (b).....	2
Figure 1-2: Principle of fluid bed agglomeration (a), photograph of an aerogel agglomerate (b).....	2
Figure 1-3: Schemes of different fluidized bed spray granulator configurations.	3
Figure 1-4: Particle-level description of fluid bed agglomeration according to Iveson et al. (2001).....	8
Figure 1-5: Particle-level description of fluid bed coating according to (Hede, 2008).....	8
Figure 1-6: Micro mechanisms in fluidized bed agglomeration.	9
Figure 1-7: Droplet deposition on a particle according to Löffler (1988).	10
Figure 1-8: Interfaces at the contact of a liquid droplet with a solid plane (based on Teipel & Mikonsaari, 2004).....	11
Figure 1-9: Schematic of two colliding particles covered by a liquid film (based on Ennis et al., 1991).....	13
Figure 1-10: Schematic representation of the level of detail in different modeling approaches for dense gas-solid flows (based on van der Hoef et al., 2004).	19
Figure 2-1: Glatt lab system used for fluidized bed agglomeration experiments.....	28
Figure 2-2: GF3 top-spray insert (a), GF3 Wurster-coater (b) and ProCell® 5 spouted bed (c).	28
Figure 2-3: Flowsheet of the Glatt ProCell® 5 fluidized bed agglomeration plant.....	29
Figure 2-4: Photograph (a) and schematic drawing (b) of the used Schlick Series 970 spray nozzle.....	30
Figure 2-5: Cross cut through the used granulator configurations: a) top-spray, b) Wurster-coater, c) spouted bed. ...	30
Figure 2-6: Segmented distributor plate used in the Wurster-coater.	31
Figure 2-7: Principle of a focused beam reflectance sensor (Mettler-Toledo).	33
Figure 2-8: Determination of a chord length distribution with the FMBR® sensor (Mettler-Toledo).	33
Figure 2-9: Photograph of the used Texture Analyser (a) and schematic view of the compression test (b).....	34
Figure 2-10: Typical force-displacement curve for maltodextrin agglomerates at 0.01 mm/s test speed.	35
Figure 2-11: Free-fall test setup to measure the normal restitution coefficient e_n	37
Figure 2-12: Deflection of a thin beam under centered load and its cross-sectional area.	38
Figure 2-13: Schematic representation of the strain applied to the sample as a function of time (a) as well as the resulting modulus of elasticity (b).	38
Figure 2-14: Shear cell of a Jenike shear tester for the analysis of the flowability of powders (Stieß, 1992).	39
Figure 2-15: Typical force-displacement curves for pre-consolidation and shear to failure of a consolidated powder sample.	40



Figure 2-16: Typical individual yield locus plot	41
Figure 3-1: Principle motion scheme of an individual particle according to the DPM.	44
Figure 3-2: Principle scheme of gas and particle interactions in a DPM for a fluidized bed.	45
Figure 3-3: Tetrahedral mesh of a top spray granulator for the calculation of the gas flow profile (a). Two-dimensional slice cut out of the mesh vertically at the center of the granulator (b).....	46
Figure 3-4: Steps in coupling the motion of discrete and continuous phase.....	49
Figure 3-5: Mechanical analogue in normal and tangential direction for a particle-particle contact in a soft-sphere DPM (Antonyuk, 2006).....	50
Figure 3-6: Coordinate system used in the description of the collision model (based on Deen et al., 2007).	51
Figure 3-7: Force-displacement curve obtained using the contact model proposed by Tsuji et al. (1992). Simulation parameters: $e = 0.8$, $v_0 = 0.78$ m/s, $E^* = 2.1 \cdot 10^{10}$ Pa, $R^* = 5 \cdot 10^{-4}$ m, $d_p = 1$ mm, $\rho_p = 1500$ kg/m ³	53
Figure 3-8: Schematic course of a collision.....	54
Figure 3-9: Representation of a dispersed solid phase according to KTFG.	55
Figure 3-10: Normal and tangential component of the viscous force according to Eq. 3-30 and 3-31, with $R^* = 0.1$ mm, $v_{rel} = 1$ m/s, as a function of the liquid viscosity (a) at $D = 0.1$ mm. Viscous force as a function of the separation distance (b) at $\eta_{liq} = 0.05$ Pa s.	57
Figure 3-11: Structure of a multi scale model for fluidized bed agglomeration (based on Werther et al., 2011).	58
Figure 4-1: Glass transition temperature of maltodextrin (DE 21 and DE 47) as a function of the moisture content (Haider, 2010).	63
Figure 4-2: High-speed photographs of the impact of a maltodextrin agglomerate onto a steel plate (v : impact velocity, v_R : rebound velocity, ω_R : angular rebound velocity).....	64
Figure 4-3: Restitution coefficient of maltodextrin agglomerates impacting on a steel plate.	65
Figure 4-4: SEM picture of a maltodextrin DE21 primary particle at 1000x magnification (a) and dense spherical maltodextrin beads (b).....	66
Figure 4-5: Restitution coefficient of glassy maltodextrin beads as a function of their moisture content for two different impact velocities (5 cm and 30 cm falling height). Impact on a steel plate and impact on a maltodextrin plate of equal moisture content.....	67
Figure 4-6: Restitution coefficient of glassy maltodextrin beads for dry and wet impact on a steel plate at 2.3 m/s impact velocity.	68
Figure 4-7: Short-time modulus of elasticity E_0 of maltodextrin DE 21 and DE 47 as a function of the moisture content, expressed as difference between the test temperature T and the glass transition temperature T_g of the sample (Haider, 2010).	69



Figure 4-8: Yield locus for internal particle friction, measured with a Jenike shear cell for maltodextrin DE 21 agglomerates (moisture content: 4 % (wet based), mean particle diameter: 0.6 mm).....	70
Figure 5-1: Cross-sectional view of the modeled Wurster-coater: (a) Glatt GF3 geometry, (b) simplified geometry for DPM simulations, (c) mesh for CFD simulation.....	73
Figure 5-2: Segmented distributor plate of the Wurster-coater: representation with 3 homogeneous zones used in the simulations.....	74
Figure 5-3: Instantaneous particle positions and velocity distribution at simulation time $t=2.0$ s for different values of the elastic modulus: a) 0.25 GPa, b) 0.5 GPa, c) 1.0 GPa.....	77
Figure 5-4: Time-averaged radial distribution of the particles in the Wurster-coater in the dense bottom zone ($z = 20$ mm) as a function of the elastic modulus of the particles.	78
Figure 5-5: Time-averaged radial distribution of the particles in the Wurster-coater at the top of the draft tube ($z = 220$ mm) as a function of the elastic modulus of the particles.....	78
Figure 5-6: Influence of a variation of the elastic modulus on (a) the time-averaged number density distribution of the particle-particle collision velocity and (b) on the particle-wall collision velocity distribution in a Wurster-coater.	80
Figure 5-7: Influence of the elastic modulus on the collision velocity and the collision frequency in a Wurster-coater.	81
Figure 5-8: Influence the elastic modulus on the vertical profile of (a) the time-averaged particle-particle collision frequency and (b) the solids volume fraction in a Wurster-coater.....	83
Figure 5-9: Influence of the elastic modulus on the radial distribution of the time-averaged particle-particle collision frequency in a Wurster-coater at different bed heights: a) $z = 20$ mm, b) $z = 220$ mm.....	84
Figure 5-10: Influence of the restitution coefficient on the particle dynamics in a Wurster-coater.....	85
Figure 5-11: Influence of a variation of the restitution coefficient on (a) the time-averaged number density distribution of the particle-particle collision velocity and (b) on the particle-particle collision velocity distribution inside the draft tube of a Wurster-coater.....	86
Figure 5-12: Influence of the restitution coefficient on the collision dynamics in a Wurster-coater.....	86
Figure 5-13: Influence of the restitution coefficient on the collision frequency in a Wurster-coater.....	87
Figure 5-14: Influence of a variation of the restitution coefficient on the profile of (a) the time-averaged particle-particle collision frequency and (b) the solids volume fraction over the bed height in a Wurster-coater..	88
Figure 5-15: Instantaneous particle positions and velocity distributions at simulation time $t = 2.0$ s for different values of the bed mass: a) 0.251 kg (100 000 particles), b) 0.377 kg (150 000 particles), c) 0.503 kg (200 000 particles).....	89
Figure 5-16: Influence of the bed mass on the particle dynamics in a Wurster-coater.....	90



Figure 5-17: Influence of a variation of the bed mass on (a) the time-averaged number density distribution of the particle-particle collision velocity and (b) on the particle-wall collision velocity distribution in a Wurster-coater.....	91
Figure 5-18: Influence of the bed mass on the collision dynamics in a Wurster-coater.....	92
Figure 5-19: Influence of the bed mass on the collision frequency in a Wurster-coater.....	92
Figure 5-20: Influence of a variation of the bed mass on the profile of (a) the time-averaged particle-particle collision frequency and (b) the solids volume fraction over the bed height in a Wurster-coater.....	93
Figure 5-21: Measured effect of process temperature on the Sauter mean diameter of the agglomerates.....	97
Figure 5-22: Measured average breakage force (a) and contact stiffness (b) as a function of the process temperature at an injection time of 15 min.....	99
Figure 5-23: Measured average displacement increment (a) and breakage energy (b) as a function of the process temperature at an injection time of 15 min.....	100
Figure 5-24: Measured Sauter mean diameter (d_{32}) of water droplets as a function of the atomizer pressure and the tip height h_D using a Schlick Series 970 two-fluid nozzle.....	102
Figure 5-25: Influence of the atomizer flow rate on instantaneous particle positions and particle velocity distributions in the Wurster-coater: a) $0.9 \text{ m}^3/\text{h}$ (case 1), b) $4.5 \text{ m}^3/\text{h}$ (case 2), c) $7.2 \text{ m}^3/\text{h}$ (case 3).....	103
Figure 5-26: Measured mean agglomerate diameter as a function of the injection time for different atomizer gas flow rates in the Wurster-coater. Wurster gap distance: 30 mm, atomizer capillary tip height h_D : 0.29 mm. ...	105
Figure 5-27: Instantaneous particle positions and particle velocity distributions in the Wurster-coater for different gap distances: a) 10 mm (case 3), b) 20 mm (case 4), c) 30 mm (case 5).....	107
Figure 5-28: Measured evolution of the Sauter diameter (d_{32}) of the agglomerates (DE 21 maltodextrin) as a function of the injection time for different gap distances.....	109
Figure 5-29: Instantaneous particle positions and velocity distributions in the Wurster-coater at simulation time $t = 2.2 \text{ s}$ for different scenarios involving viscous forces: a) case 1 (dry reference), b) case 2 ($\Phi = 10 \%$, $\eta_{liq} = 0.1 \text{ Pa s}$), c) case 3 ($\Phi = 10 \%$, $\eta_{liq} = 0.01 \text{ Pa s}$), d) case 4 ($\Phi = 5 \%$, $\eta_{liq} = 0.1 \text{ Pa s}$).....	113
Figure 5-30: Influence of viscous forces on the particle velocity distribution in a Wurster-coater.....	114
Figure 5-31: Influence of the viscosity of the liquid film on the vertical profile of the particle concentration (a) and of the particle velocity (b) in a Wurster-coater. Wetted surface fraction $\Phi = 10 \%$	116
Figure 5-32: Influence of viscous forces on the radial particle distribution (a) and the particle velocity profile (b) in the dense bed of a Wurster coater (height $z = 20 \text{ mm}$, as indicated in Fig. 5-4).....	117
Figure 5-33: Influence of viscous forces on the radial particle distribution (a) and the particle velocity profile (b) at the upper end of the Wurster tube (height $z = 220 \text{ mm}$, as indicated in Fig. 5-5).....	118
Figure 5-34: Influence of viscous forces on the collision velocity distribution in the dense bed of a Wurster-coater.....	120

Figure 5-35: Influence of viscous forces on the collision frequency in a Wurster-coater. Vertical profile (a) and radial profile at height $z = 20$ mm (b).....	122
Figure 6-1: Cross section of the used fluidized bed granulator geometries: (a) & (d) Top-spray granulator (Glatt GF3), (b) & (e) Wurster-coater (Glatt GF3), (c) & (f) Spouted bed (Glatt ProCell 5).....	125
Figure 6-2: Air inlet slots of the spouted bed in the DPM.....	126
Figure 6-3: Geometry of the spray zone.....	127
Figure 6-4: Instantaneous particle positions and particle velocity distribution at identical process conditions for the top-spray granulator (a), the Wurster-coater (b) and the spouted bed (c). Colours indicate the particle velocity.....	128
Figure 6-5: Time-averaged gas velocity and solids volume fraction in three slices (positioned at $x=0$, $x=50$ and $x=100$ mm).....	130
Figure 6-6: Transient profile of the average particle velocity in the top-spray granulator, the spouted bed and the Wurster-coater, (b) density distribution of the time-averaged particle velocity.....	131
Figure 6-7: Time-averaged velocity profile (a) and solids volume fraction (b) along the height of the granulator.....	133
Figure 6-8: Transient profile of the average particle-particle collision velocity in the top-spray granulator, the spouted bed and the Wurster-coater, (b) average particle-wall collision velocity as a function of the simulation time.....	135
Figure 6-9: (a) Density distribution of the relative collision velocity of all particle-particle collisions in the reference time interval ($t = 5-6$ s simulation time) for three different granulator configurations, (b) density distribution of the particle-wall collision velocity.....	136
Figure 6-10: Comparison of time-averaged maxima of the collision energy (a), the energy dissipation (b) and the particle deformation (c) in the Wurster-coater, the spouted bed and the top-spray granulator.....	138
Figure 6-11: Collision frequency (collisions per particle pair per second) as a function of the simulation time for (a) particle-particle collisions, (b) particle-wall collisions.....	139
Figure 6-12: Time-averaged particle-particle collision frequency (collisions per particle pair per second) along the height of the granulator.....	140
Figure 6-13: Time-averaged particle-particle collision frequency (collisions per particle pair per second) as a function of the average solids volume fraction, in comparison to the kinetic theory based models by Martin (1980) and Gidaspow (1994).....	141
Figure 6-14: (a) Average angular velocity of particles positioned inside the spray zone in the top-spray granulator, the spouted bed and the Wurster-coater as a function of the simulation time, (b) density distribution of the time-averaged angular velocity of particles in the spray zone.....	143
Figure 6-15: Time-averaged density distribution of the particle-particle collision velocity of particles positioned inside the spray zone.....	145



Figure 6-16: a) Density distribution of the residence time of the particles inside the spray zone for Wurster-coater, spouted bed and top-spray granulator after 7 s of simulation time, b) cumulative distribution of the residence time inside the spray zone for the Wurster-coater as a function of time.	147
Figure 6-17: Cumulative mass-based size distribution of the agglomerates as a function of the process time.	150
Figure 6-18: Evolution of the Sauter mean diameter of the agglomerates with time.....	152
Figure 6-19: Evolution of the growth rate of the agglomerates with time.	153
Figure 6-20: SEM images of maltodextrin agglomerates produced in the Wurster-coater at 70°C.....	154
Figure 6-21: SEM images of maltodextrin agglomerates produced in the spouted bed and Wurster-coater: Evolution of the agglomerate structure with process time.	156
Figure 6-22: X-ray tomographic images of the 3D structure of maltodextrin agglomerates produced in the Wurster-coater. a) 5 min. liquid injection time, b) 30 min. liquid injection time.....	157
Figure 6-23: Volume-based density distribution of the 3D structure thickness as a function of the injection time. .	158
Figure 6-24: a) Contact stiffness and b) breakage force as a function of time for agglomerates produced in the Wurster-coater and in the spouted bed (30°C process temperature, size fraction $1.4 \text{ mm} < d_p < 2.0 \text{ mm}$).	159
Figure 6-25: a) displacement increment and b) breakage energy as a function of time for agglomerates produced in the Wurster-coater and in the spouted bed (30°C process temperature, size fraction $1.4 \text{ mm} < d_p < 2.0 \text{ mm}$).	160
Figure 6-26: Comparison of numerical and experimental results relating the collisional energy dissipation and the agglomerate strength in three different granulator configurations.	162
Figure 6-27: Comparison of numerical and experimental results relating the contact force during collisions and the agglomerate strength in three different granulator configurations.	163
Figure 6-28: Comparison of numerical and experimental results relating the deformation during collisions and the agglomerate strength in three different granulator configurations.	163
Figure A-1: Continuous representation of the cumulative particle size distribution $Q(x)$	168
Figure A-2: Continuous representation of the size density distribution $q(x)$	169
Figure A-3: Characteristic of the used air ventilator.	171



List of tables

Table 1-1: Overview of viscous force models in the literature.....	15
Table 4-1: Flow behaviour of maltodextrin DE21 agglomerates as a function of the process conditions measured via shear tests.	70
Table 5-1: Simulation conditions of the case study regarding the sensitivity of particle properties (bold number indicate settings of base case).	75
Table 5-2: Influence of the elastic modulus, the restitution coefficient and the bed mass on the particle dynamics in a Wurster-coater.	79
Table 5-3: Influence of the elastic modulus, the restitution coefficient and the bed mass on the collision dynamics in a Wurster-coater.	82
Table 5-4: Influence of the elastic modulus, the restitution coefficient and the bed mass on the collision frequency in a Wurster-coater.	83
Table 5-5: Experimental conditions.....	94
Table 5-6: Simulation conditions.....	95
Table 5-7: Influence of the fluidization air flow rate on growth rate and process stability.....	96
Table 5-8: Water content of the tested maltodextrin agglomerates as a function of the operating temperature. The corresponding glass transition temperature was calculated according to the model by (Gordon & Taylor, 1952) (Eq. 4-1).	98
Table 5-9: Parameters characterizing the particle motion inside the Wurster tube for simulation cases 1 to 3.....	104
Table 5-10: Parameters characterizing the particle motion in the Wurster tube for simulation cases 3 to 5.....	108
Table 5-11: Optimal process conditions for the agglomeration of DE 21 maltodextrin in a Glatt GF3 Wurster-coater	110
Table 5-12: Simulation conditions for the case study including viscous energy dissipation.	112
Table 5-13: Influence of viscous forces on the particle dynamics in a Wurster-coater.	114
Table 5-14: Influence of viscous forces on the collision dynamics in a Wurster-coater.....	119
Table 5-15: Influence of viscous forces on the collision frequency in a Wurster-coater.....	121
Table 6-1: Overview on simulation parameters.....	127
Table 6-2: Time-averaged particle and collision velocity and collision frequency (collisions per particle pair per second) in the Wurster-coater, the spouted bed and the top-spray granulator.....	137
Table 6-3: Parameters for Martin's and Gidaspow's models.....	142



Table 6-4: Time-averaged particle and collision velocity and collision frequency inside the spray zone (collisions per particle pair per second) in the Wurster-coater, the spouted bed and the top-spray granulator.	144
Table 6-5: Average and maximum residence time of the particles in the spray zone (percentage of the simulation time) for the Wurster-coater, the spouted bed and the top-spray granulator after 7 s of simulation time.	148
Table 6-6: Average strength of agglomerates produced in different granulator geometries ($t = 15$ min, $T = 70^{\circ}\text{C}$, size fraction: $1.4 \text{ mm} < d_p < 2.0 \text{ mm}$).....	161



Nomenclature

Latin symbols

A	Area	m^2
B_{agg}	Birth term in population balance	-
c	Mean particle velocity fluctuation	m s^{-1}
c_D	Drag coefficient	-
d	Diameter	m
D	Separation distance	m
D_{agg}	Death term in population balance	-
e_n	Normal coefficient of restitution	-
E	Modulus of elasticity	Pa
E_B	Breakage energy	J
E_{kin}	Kinetic energy	J
f_c	Collision frequency	s^{-1}
ff_c	Flow function	-
\mathbf{F}	Force	N
\mathbf{g}	Gravitational acceleration	m s^{-2}
g_0	Radial distribution function	-
G	Shear modulus	Pa
h	Height	m
h_A	Adhesion probability	-
I	Moment of inertia	$\text{kg}\cdot\text{m}^2$
k	Contact stiffness (linear spring)	N m^{-1}
k_d	Displacement-related contact stiffness	$\text{N m}^{-1.5}$
m	Mass	kg
\dot{m}	Mass flow	kg s^{-1}
\mathbf{n}_{ab}	Normal unit vector on the contact plane	-



n	Number of particles	-
n_p	Number of molecules per unit volume	m^{-3}
N	Number, specified by subscript	-
p	Pressure	Pa
P	Drying potential	kg s^{-1}
q_3	Mass-based density distribution of the particle size	m^{-1}
Q_3	Cumulative mass-based particle size distribution	-
R	Radius	m
s	Displacement	m
S_p	Sink term for fluid-particle drag force	N m^{-3}
t	Time	s
T	Torque	N m
T	Temperature	$^{\circ}\text{C}$
T_g	Glass transition temperature	$^{\circ}\text{C}$
u	Gas velocity	m s^{-1}
v	Particle velocity	m s^{-1}
v_{ab}	Relative velocity at the contact point	m s^{-1}
V	Volume	m^3
\dot{V}	Volume flow	$\text{m}^3 \text{s}^{-1}$
w	Water content (wet-based)	$\text{kg}_{\text{water}}/\text{kg}$
W_A	Specific work of adhesion	J m^{-2}
Y	Air humidity	$\text{kg}_{\text{water}}/\text{kg}_{\text{dry air}}$

Greek letters

α	Energy dissipation factor	-
β	Aggregation kernel	-
β_{g-p}	Interphase momentum transfer coefficient	$\text{kg m}^{-3} \text{s}^{-1}$
δ	Displacement	m
ε	Strain	-



ε	Porosity	-
γ	Interfacial energy	J m^{-2}
η	Drying potential	-
η_g	Dynamic viscosity of the gas phase	$\text{kg m}^{-1} \text{s}^{-1}$
η_n	Damping factor (normal direction)	N s m^{-1}
η_p	Impingement efficiency	-
λ	Mean free path of the particles	m
λ_g	Solid phase bulk viscosity	$\text{kg m}^{-1} \text{s}^{-1}$
λ_b	Spreading coefficient (liquid on solid)	J m^{-2}
μ	Coefficient of sliding friction	-
μ_R	Coefficient of rolling friction	-
ν	Poisson ratio	-
θ	Contact angle	degrees
θ	Granular temperature	$\text{m}^2 \text{s}^{-2}$
ρ	Density	kg m^{-3}
σ	Shear stress	Pa
σ_c	Compression strength	Pa
τ	Normal stress	Pa
τ_c	Cohesion	Pa
τ_g	Gas phase stress tensor	Pa
τ_s	Spreading time	s
τ_p	Penetration time	s
φ	Spraying angle	degrees
φ_A	Deposition efficiency	-
φ_t	Internal friction angle	degrees
Φ	Wetted surface fraction	-
Ψ_A	Dimensionless Stokes number	-
ω	Angular velocity	s^{-1}

**Subscripts**

0	Initial
agg	Aggregation
asp	Asperities
b	Bridge
B	Breakage
c	Contact
cell	Computational cell
d	Droplet
eff	effective
f	Fluid
F	Fluidization
g	gas
gap	Gap between bottom plate and Wurster tube
i	Particle index
in	Inlet
l, liq	Liquid
mf	Minimum fluidization condition
n	Normal direction
p	Particle
r	Rebound
rel	relative
s	Solid
spout	Spout, injection at the nozzle
t	Tangential direction
tot	Total
v	Vapour
W	Wurster

**Abbreviations**

CFD	Computational fluid dynamics
DEM	Discrete Element Method
DPM	Discrete Particle Model
SB	Spouted bed
SPE	Solids Process Engineering
TS	Top-spray
WC	Wurster-coater





1 Introduction

1.1 General process description

Gas fluidized beds play an important role in a variety of chemical processes including combustion, pyrolysis and polymerization as well as in the manufacturing and handling of particulate solids in the pharmaceutical and food industries. Gravitational and inter-particle forces are overcome using a gas flow which passes through the bed, until at the point of minimum fluidization the equilibrium is reached with the drag force exerted by the gas. Particles can now move freely through the bed like the molecules in a fluid, which is where the term “fluidized bed” comes from. Due to this liquid-like behaviour, fluidized beds have fundamental advantages regarding the mobility of particles in continuous processes and they allow homogeneous particle mixing. Isothermal conditions can be achieved throughout the bed avoiding local hot-spots and fluidized beds offer favourable heat and mass transfer conditions due to the intense gas-solid contact.

A special application of the fluidized bed technology are spray granulation and agglomeration processes, which are both widely used in the food, fine chemicals and pharmaceutical industries to produce dust-free and free-flowing particles. They are important size-enlargement processes allowing formulation and structuration of particulate solid products in one process step. Further motives are the improvement of appearance or taste of particles or protection from oxygen, humidity, light or incompatible active agents and to control the dissolution time (Knight, 2001; Hemati et al., 2003; Jacob et al., 2004; Turchiuli et al., 2005; Szulc & Lenart, 2010; Jacob, 2010; Dhanalakshmi et al., 2011).

Liquid suspension or a solution or melt is injected into a fluidized bed of particles in such way that fine droplets of coating material are gradually deposited on the particle surface. This results in encapsulation of the particle core, which is called coating or in particle growth by layering, which is called granulation. The principle of fluid bed granulation is visualized in Fig. 1-1 a). The



injected liquid may also work as binder, forming a liquid bridge in case that two wetted particles collide. Depending on the fluidization conditions this coalescence may either be temporary or permanent. If the liquid bridge is strong enough to resist further particle collisions, the subsequent drying by the hot fluidization air will lead to the formation of a stable solid bridge (Iveson et al., 2001). In that case an agglomerate is formed which may grow further due to repeated wetting and adhesion of other particles in the course of the process. The principle of fluid bed agglomeration is illustrated in Fig. 1-2 a).

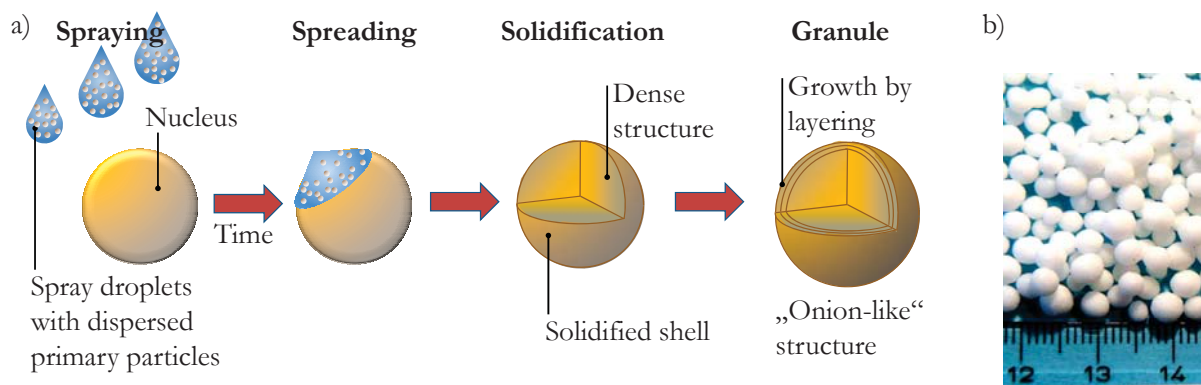


Figure 1-1: Principle of fluid bed granulation (a), photograph of urea granules produced by melt injection (b).

Agglomeration may be desired, as for the size-enlargement of food powders, or undesired, as in pharmaceutical coating processes or in fertilizer granulation processes, where spherical and dense particles are to be produced. Typical examples for products granulated or agglomerated in fluidized beds are shown in Fig. 1-1 b) and 1-2 b).

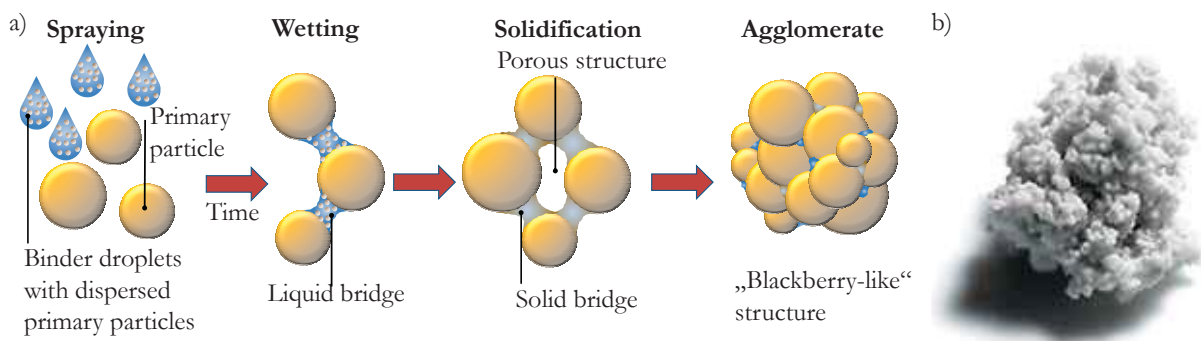


Figure 1-2: Principle of fluid bed agglomeration (a), photograph of an aerogel agglomerate (b).

This work will focus on fluid bed agglomeration of amorphous water-soluble food powders. For instant food products quick redispersability is a key requirement that defines a main consumer

benefit compared to fine food powders. Agglomerate structures with open pores are therefore desired, which allow a quick penetration of water into the particle matrix.

Before different micro mechanisms in fluid bed agglomeration are discussed, a brief introduction will be given to fluid bed agglomeration equipment.

1.2 Types of fluidized bed agglomeration equipment

Fluid beds for agglomeration are classified according to the nozzle position (top spray, bottom spray or tangential injection) and to the operating conditions (batch or continuous) (Uhlemann & Mörl, 2000). According to the equipment geometry, fluidized bed granulators or agglomerators can be categorized by five different configurations, which are schematically shown in Fig. 1-3:

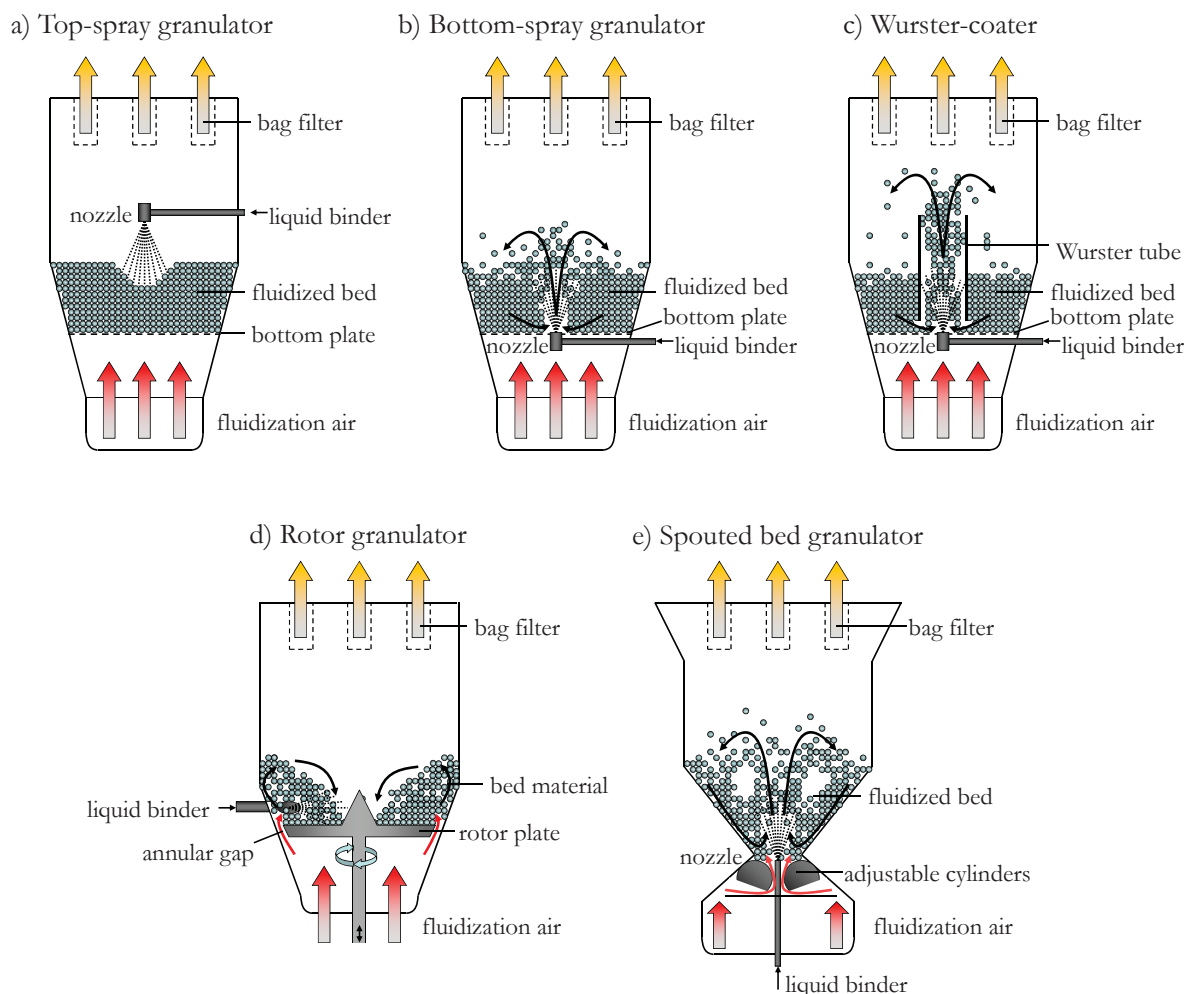


Figure 1-3: Schemes of different fluidized bed spray granulator configurations.



Except for the rotor granulator and the Wurster-coater, all devices are built with both a circular cross section, as shown in Fig. 1-3 or with a rectangular cross section of the process chamber (Jacob, 2010). For continuous operation, conical fluidized bed granulators are equipped with an outlet tube, where classification air is used to reject fines. Devices with rectangular cross-section are usually equipped with an outlet weir at the end opposite to the inlet.

1.2.1 Top-spray granulator

The most conventional equipment configuration is the top-spray granulator (Fig. 1-3 a). A bubbling fluidized bed is established using a homogeneous distributor plate and the nozzle is positioned above the moving powder bed spraying downwards. Usually no inserts are applied. Top spray granulators are used by the food industry for size enlargement of culinary powders, seasonings, beverage powders and food ingredients (Bouffard et al., 2005; Jinapong et al., 2008; Werner et al., 2007b). Apart from having the simplest equipment geometry, the large product surface available for the deposition of droplets is the main advantage of this configuration (Uhlemann and Mörl, 2000). However, due to the random particle motion and the fluctuating bed height, it is difficult to control the distance and flight time of the droplets before they impact on a particle. This may increase the loss of liquid binder due to premature evaporation of the droplets (Link & Schlünder, 1997; Ronsse et al., 2008). The amount of liquid deposited on individual particles may be inhomogeneous and hard to control. Regarding the hydrodynamics of the bed the top-spray granulator is characterized by the periodic formation of bubbles at the distributor plate. The bubbles travel upwards in the bed and grow on their way to the bed surface, where they collapse. Rising bubbles continuously agitate and mix the particle bed in a stochastic manner.

1.2.2 Bottom-spray granulator

Bottom spray installations are preferably applied for agglomeration of dairy powders (Fig. 1-3 b). Here, the spray is introduced from a nozzle located at the center and bottom of the bed, inside the powder bulk. Overspray is minimized due to the low distance and short flight time between the injection of droplets and their impact on a particle. Very small droplets can therefore be applied, that would otherwise dry out in the spray. However, wetting is inhomogeneous in a simple bottom spray installation due to the stochastic particle motion. Local overwetting in the spray zone and lump formation may be the result.



1.2.3 Wurster-coater

Advanced bottom spray granulators like the Wurster-coater (Fig. 1-3 c) are equipped with a draft tube to separate the wetting and drying zones. The name goes back to Prof. Dale Wurster of the University of Wisconsin, who invented the cylindrical draft tube inserted to the fluid bed in 1949 (Wurster, 1949). The Wurster-coater is a common device in the pharmaceutical industry used to coat tablets and smaller particles in the range of 20-1000 μm ; (Tang et al., 2008; Karlsson et al., 2009). Another important field of application is the encapsulation of flavours (Uhlemann & Reiß, 2010). The Wurster-coater is described by Teunou & Poncelet (2002) as the most efficient batch fluid bed coating equipment. A cylindrical draft tube is inserted vertically into the granulator. The segmented distributor plate has larger orifices below the Wurster tube and therefore the fluidization gas enters at higher velocity at the center than in the annulus. Due to the central gas/liquid injection which is concurrent to the particle motion, a circulating movement of the particles is induced and the geometry can be divided into a wetting and a drying zone. In the central part inside the Wurster tube the particles are transported upwards in a spout and collide with droplets from the atomizer. The wetted particles decelerate in the expansion chamber above the tube and fall down to the dense region of particles in the annulus outside the tube, while they are dried by the heated fluidization air current. From the dense region, the particles are sucked into the Wurster tube, where they enter the next motion cycle. The height of the draft tube inside the apparatus is adjustable, so that the gap distance between the Wurster tube and the bottom plate can be varied. This gap distance is an important process parameter controlling the number of particles transported towards the center into the spout and the particle concentration inside the wetting zone.

1.2.4 Rotor granulator

A fourth type of fluid bed is known as the rotor system (Fig. 1-3 d). A rotor plate placed at the bottom of the bed is turning and air is fed through an annular gap between the rotor plate and the wall. Liquid is sprayed onto the roping solids flow from a tangential injection nozzle. In pharmaceutical, food and chemical industries the application of the fluid-bed rotor processor for production of dense granules with a high strength and sphericity is widely distributed. The rotor granulator represents a combination of a spheronization device and a fluidized bed. The additional horizontal rotating disk provides a homogeneous and well defined spiral particle motion in the process chamber and allows an uniform mechanical stress of the product (Jäger &



Bauer, 1982; Kristensen et al., 2000; Dixit & Puthli, 2009). The particles are dried by the fluidized air stream, which passes through the gap between the rotor and stationary chamber wall. Several processing operations, e.g. powder layering, film coating or spheronization can be performed with fluid-bed rotor processors (Yang et al., 1992).

1.2.5 Spouted bed

In food, pharmaceutical and chemical industry, also fine and polydisperse solids as well as cohesive powders and needle shaped particles are manufactured and handled. Usually a homogeneous fluidization regime cannot be established for such materials due to inter-particle forces. The spouted bed (Fig. 1-3 e) offers a promising alternative here (Epstein & Grace, 2011; Jacob, 2009; Gryczka et al., 2008). Different types of spouted beds have been reported in the literature such as conical spouted beds (Rovero et al., 1983; Altzibar et al., 2009), spout fluidized beds (Link et al., 2008) and prismatic spouted beds (Mörl et al., 2000; Gryczka et al., 2009). In this work only the latter type of spouted bed is considered. Unlike fluid bed processes, in a spouted bed the air does not enter the process chamber through a sieve bottom but through longitudinal slots. The speed of the process air entering the process chamber can be adjusted by varying the size of the gap. High gas velocity ensures that even large, irregular-shaped or adhesive and wet particles are fluidized. Particles are entrained in a spout at the center of the apparatus and fall back downwards along the side walls, so that a circulating motion of the material is created. Liquid is injected from a bottom spray-nozzle positioned at the center above the inlet slots. Spouted bed technology can be applied for coating (Kfuri & Freitas, 2005; Jono, 2000), spray granulation (Mann, 1983; Borini et al., 2009) and agglomeration (Jacob, 2009; Gryczka et al., 2009).

1.2.6 Development of optimized equipment geometries

Since so far operating conditions and the equipment geometry have been developed empirically, the fundamental physical mechanisms governing the process on the micro scale are not well understood (Werner et al., 2007a; Turton, 2008). Experimental results are mostly specific to material and equipment selection. Furthermore, the effectiveness of improvements on the vessel shape or inserts like the Wurster tube is hard to assess, as it is difficult to measure the flow field and particle motion inside the bed.



A lot of research work has been done recently to overcome these limitations and to achieve a fundamental understanding of the granulation process on the “micro scale”, i.e. the scale of individual particle interactions (Iveson et al., 2001; Litster, 2003; Tan et al., 2006; Peglow et al., 2007; Rajniak et al., 2009). However, due to its complexity, a comprehensive physically based process model of fluidized bed granulation is still not available. The choice of an agglomerator/granulator type still remains rather a question of philosophy than a decision based on facts.

1.3 Overview of previous research

In this chapter the state of the art regarding the process dynamics of fluidized bed spray granulation and the existing modeling approaches will be introduced. The chapter is an outline of the current modeling principles and their boundaries. More extensive reviews on this topic may be found in Iveson et al. (2001), Cameron et al. (2005) and Salman et al. (2007). A special focus will be set on the micro scale description using the Discrete Element Method (DEM).

1.3.1 Micro mechanisms in fluidized bed agglomeration

The build-up of granules or agglomerates is in continuous competition with disruptive mechanisms such as attrition and breakage, which complicates a comprehensive process description. Hapgood et al. (2007) give an extensive overview of the particle-scale mechanisms which govern the agglomeration process dynamics. They distinguish between 3 groups of phenomena, as illustrated in Fig. 1-4:

1. Wetting and nucleation,
2. Growth and consolidation,
3. Breakage and attrition.

The addition and distribution of the binder liquid is the first step of the process, which leads to the formation of granule nuclei. Liquid droplets added via a spray nozzle impinge on primary particles and wet the particle surface. Depending on the surface properties, the liquid may spread, penetrate into pores or even dissolve. If the droplet size is large compared to the particle size, loosely packed lumps are formed which will consolidate through collisions with other particles and the equipment walls. According to Hapgood et al. (2007) the size distribution of the nuclei



has a large influence on the final product size distribution, while the intensity of agitation in the bed controls the final porosity of the agglomerates.

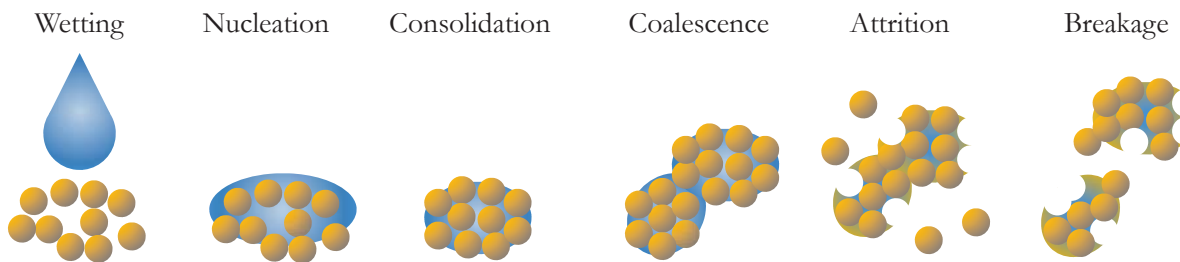


Figure 1-4: Particle-level description of fluid bed agglomeration according to Iveson et al. (2001).

Usually in fluid bed spray processes the droplet size is small compared to the diameter of the primary particles (Waldie, 1991), which is different than the scenario described in Hapgood et al. (2007). Therefore, Hede (2008) proposed to organize the relevant micro mechanisms in the following three groups according to the scheme shown in Fig. 1-5:

1. Wetting and possible droplet penetration into core particles,
2. Coating and possible agglomeration,
3. Attrition and breakage.

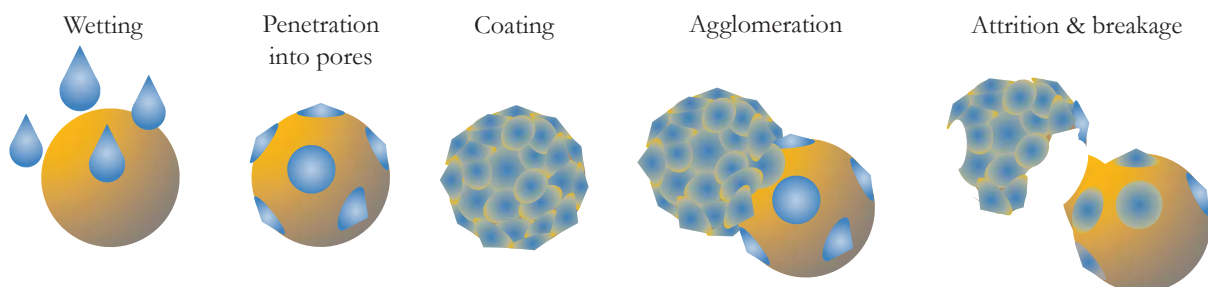


Figure 1-5: Particle-level description of fluid bed coating according to (Hede, 2008).

Werner et al. (2007a) proposed a list of 10 micro-level processes relevant for coating of food powders. Four processes were identified as key for the developer of new products and processes with respect to the coating objectives and process inefficiencies. These are:

1. Drying,
2. Droplet impact and spreading,
3. Droplet impact and adherence,
4. Inter-particle agglomeration.



However, stickiness dominates the latter two micro-level processes because surface viscosity changes by many orders of magnitude during drying. An own overview on the system of micro-mechanisms is given schematically in Fig. 1-6.

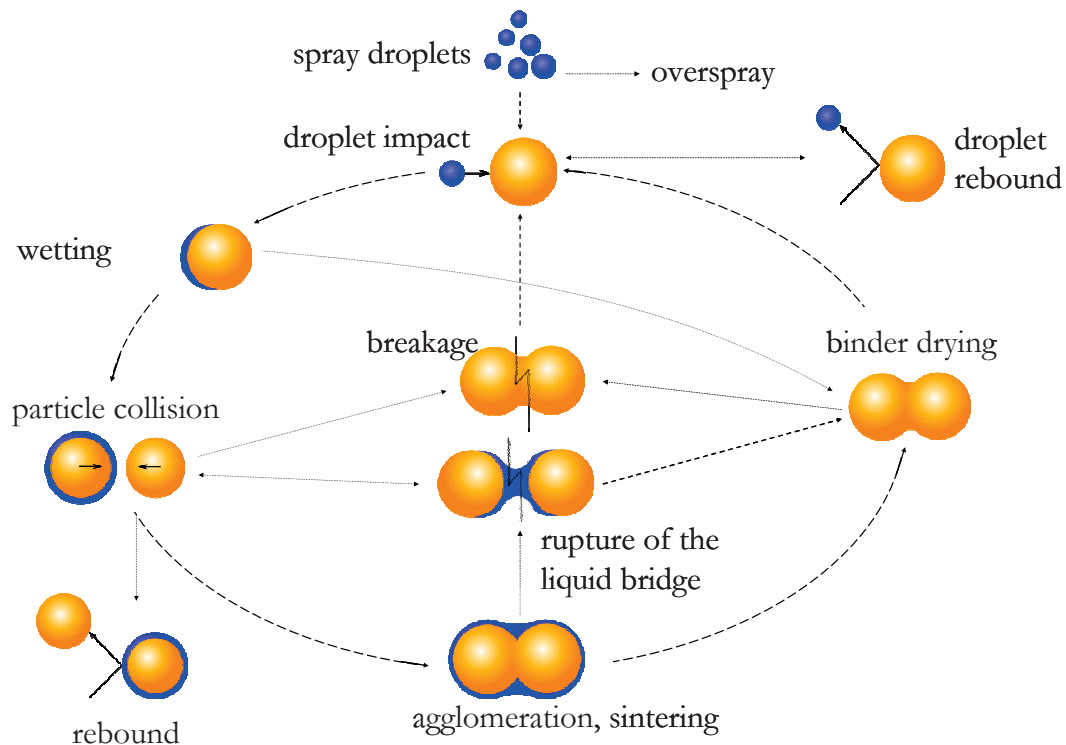


Figure 1-6: Micro mechanisms in fluidized bed agglomeration.

All shown mechanisms may occur simultaneously in a fluidized bed agglomeration process. Arrows indicate possible routes connecting the different mechanisms. Once a stable solid bridge is formed connecting two primary particles, the next process cycle may begin with the adhesion of a liquid droplet. For longer process times an equilibrium will be established between the build-up of agglomerates and breakage events. Comparable schemes were proposed by Tan et al. (2006) and Terrazas-Velarde (2010). Time scales of different micro mechanisms are analyzed in Chua et al. (2011a, 2011b, 2011c).

1.3.1.1 Droplet deposition

The initial step of the process is to bring small liquid droplets, which are formed at the spray nozzle, into contact with primary particles. The collision frequency can be approximated using the Kinetic Theory of Granular Flow (KTGF) (Martin, 1980; Gidaspow, 1994; Anh Ho & Sommerfeld, 2002), which will be discussed in section 3.6. The deposition of droplets on a particle is frequently modeled based on an approach by Löffler (1988). In this model the



deposition efficiency φ_A is defined as the product of the impingement efficiency η_p and the adhesion probability h_A :

$$\varphi_A = \eta_p h_A \quad (1-1)$$

$$\eta_p = \left(\frac{d_{eff}}{d_p} \right)^2 = \left(\frac{\psi_A}{\psi_A + a} \right)^b \quad (1-2)$$

$$\psi_A = \frac{\rho_{liq} \cdot v_{rel} \cdot d_d^2}{18 \cdot \eta_{liq} \cdot d_p} \quad (1-3)$$

where the parameters a and b are dependent of the Reynolds number. They can be found in appendix A4 and in Li et al. (2011). The dimensionless Stokes number Ψ_A is a function of density ρ_{liq} and viscosity of the liquid η_{liq} as well as of the particle diameter d_p and the droplet diameter d_d . The impact scenario is schematically represented in Fig. 1-7.

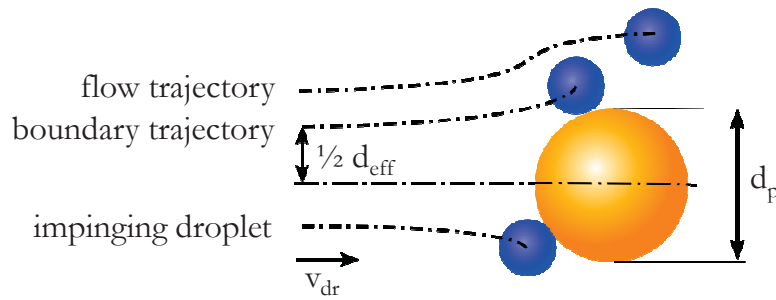


Figure 1-7: Droplet deposition on a particle according to Löffler (1988).

A different droplet deposition model was proposed by Dubrovsky et al. (1992) for droplet-droplet and particle-droplet collisions in a spray drying process. They define the adhesion probability h_A as a function of the dimensionless Reynolds and Laplace numbers:

$$h_A = \begin{cases} 1 - 0.044 \cdot B & \text{for } B \leq 22.7 \\ 0 & \text{for } B > 22.7 \end{cases} \quad (1-4)$$

$$B = \text{Re}^{0.85} \cdot \text{Lp}_d^{-0.32} \cdot \left(\frac{d_p}{d_d} \right)^{-0.34} \cdot \theta^{0.32} \quad (1-5)$$

$$\text{Lp}_d = \frac{d_d \rho_{liq} \sigma_{liq}}{\eta_{liq}^2} \quad (1-6)$$



The Laplace number of a droplet Lp_d is defined as the ratio of surface energy to viscous energy of a droplet. An implementation of this model can be found in Blei (2005) for spray dryers.

1.3.1.2 Wetting

After impact, the droplets spread on the particle surface and penetrate into pores of the core particle. The wetting behaviour is determined by the contact angle θ between the solid particle and the liquid phase and by the spreading coefficient of the liquid phase over the solid phase (Iveson et al., 2001). Three interfaces are present when a droplet is added to a particle, each of them described by the interfacial energy γ : the solid/liquid (γ_{sl}), solid/vapour (γ_{sv}) and liquid/vapour (γ_{lv}) interface. The situation is depicted in Fig. 1-8. In order to minimize the total surface energy, an equilibrium is established between the horizontal components of the interfacial tensions (Goodwin, 2009). This is described by the Young equation (Young, 1805):

$$\gamma_{sv} - \gamma_{sl} = \gamma_{lv} \cdot \cos \theta \quad (1-7)$$

The contact angle θ is a function of the physical properties of both the liquid and the solid material and of the roughness and porosity of the wetted surface.

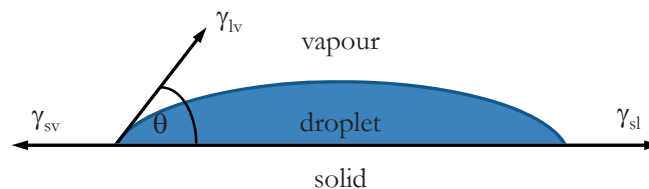


Figure 1-8: Interfaces at the contact of a liquid droplet with a solid plane (based on Teipel & Mikonsaari, 2004)

The work of adhesion W_A , which is required to separate an interface into two separate surfaces, is given by the Young-Dupré equation (Goodwin, 2009).

$$W_A = \gamma_{lv} + \gamma_{sv} - \gamma_{sl} = \gamma_{lv}(1 + \cos \theta) \quad (1-8)$$

This equation relates the work of adhesion to the contact angle. However, in practice the thermodynamic equilibrium of the interphases might not be established due to insufficient time and simultaneous drying processes on the particle surface. Whether or not a liquid will form a film on the particle surface is determined by the spreading coefficient λ_s . It is defined as the difference between the work of adhesion W_A and the work of cohesion W_C , which can be expressed as $W_C = 2\gamma_{lv}$ for a liquid component according to Iveson et al. (2001).



$$\lambda_{ls} = W_A - W_C = \gamma_{lv}(1 + \cos \theta) - 2\gamma_{lv} \quad (1-9)$$

Looking at rate constants for the different micro processes in granulation Chua et al. (2011a) found an approximate spreading time τ_s of $10^{-5} - 10^{-3}$ seconds for commonly used binders in fluid bed granulation, based on Volume-of-Fluid simulations.

A competing mechanism with droplet spreading is the penetration into pores, which is driven by the surface tension, the contact angle and the pore radius. Relations for the penetration time were published by Denesuk (1994), Palzer (2000) and Hapgood (2002). According to Denesuk (1994) and Schaafsma et al. (1998) the spreading time τ_s is often far smaller than the droplet penetration time τ_p . Palzer et al. (2003) showed that even non-wetting liquids can penetrate into pores, if the droplets are small enough.

1.3.1.3 Growth

For granule growth, two mechanisms can be distinguished: Layer wise growth or granulation is achieved, if the solid content of the binder remains on a particle surface while the solvent evaporates. On the other hand, wet particles may collide and stick together, which is called growth by coalescence or agglomeration. In this case the kinetic energy of the collision must be dissipated by viscous and capillary forces as well as plastic deformation so that the particles do not rebound. Furthermore, a strong bond must be formed at the contact between the colliding particles. Agglomeration is very sensitive to the presence of liquid at the particle surface. Therefore, the coalescence rate and the liquid content are closely related.

Some theoretical models are available in the literature for predicting whether or not a collision of wetted particles will result in rebound or coalescence. The most commonly applied approach in the literature is the model proposed by Ennis et al. (1991). It considers the impact of two non-deformable spheres of equal diameter which are covered by a thin liquid film of thickness h_{liq} , as shown in Fig. 1-9. Agglomeration is assumed, if the kinetic energy of the impact is fully dissipated by viscous forces in the liquid film, while capillary forces in the liquid bridge are neglected. Ennis et al. (1991) defined the viscous Stokes number St_v (Eq. 1-10) as the ratio of the kinetic energy before the impact to the viscous energy dissipation in the liquid film

$$St_v = \frac{2E_{kin}^*}{F_{vis} \cdot D} = \frac{m^* (v_{rel})^2}{6 \frac{\pi \eta_{liq} R^{*2} v_{rel}}{D} \cdot D} = \frac{m^* v_{rel}}{6\pi \eta_{liq} R^{*2}} \quad (1-10)$$



Here, D is the separation distance, $v_{rel} = 2 v_0$ is the relative velocity of the particles at the impact, and η_{liq} is the viscosity of the liquid film.

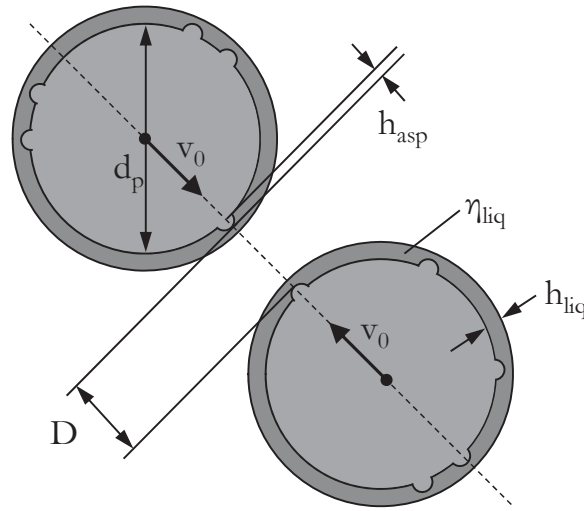


Figure 1-9: Schematic of two colliding particles covered by a liquid film (based on Ennis et al., 1991).

An important limitation of this model is the assumption that both particles move at equal velocity v_0 before the impact. The reduced mass m^* and radius R^* of two particles a and b are defined as:

$$m^* = \left(\frac{1}{m_a} + \frac{1}{m_b} \right)^{-1}, \quad (1-11)$$

$$R^* = \left(\frac{1}{R_a} + \frac{1}{R_b} \right)^{-1}. \quad (1-12)$$

Note that in case two particles of equal mass m and radius R collide, m^* is $\frac{1}{2} m$ and R^* is $\frac{1}{2} R$.

Agglomeration takes place if the relative velocity of the particles reaches zero at the end of the collision. Here, three contributions for the loss of kinetic energy are considered by Ennis et al. (1991): Viscous dissipation in the liquid film during the approach, energy dissipation through the contact of the core particles and viscous dissipation during the rebound phase. The coalescence criterion is fulfilled, if the viscous Stokes number St_v before the impact is smaller than the critical Stokes number St^* :

$$St^* = \left(1 + \frac{1}{e} \right) \ln \left(\frac{h_{liq}}{h_{asp}} \right) \quad (1-13)$$



Here, e is the constant coefficient of restitution of the core particles and h_{asp} denotes the typical height of surface asperities of the colliding particles. Implementations of this model can for example be found for example in Litster & Sarwono (1996), Talu et al. (2000), Blei (2005) and Braumann et al. (2007). Ennis' model brought significant progress to the modeling of fluid bed agglomeration on the scale of individual particles as it was the first to consider dynamic effects such as viscous dissipation in a liquid layer. However, the model is limited by its assumptions, e.g. the existence of a uniform particle collision velocity, the neglect of particle rotation and the simplification to consider the volume of the liquid bridge as infinite.

Other expressions for the viscous force on the basis of Reynold's lubrication theory (Reynolds, 1886) were published for example by Matthewson (1988) for the impact of a sphere on a flat surface. Pitois et al. (2001) extended the expression by Ennis et al. (1991) by a factor taking into account the limited volume of the liquid bridge. An overview on the different viscous force models is given in Table 1-1.

Some authors such as Seville (2000) and Darabi et al. (2009) argue that static capillary forces also contribute to the adhesion of particles. For the dynamics situation of particle collisions, however, they are of minor relevance, as was shown by Antonyuk et al. (2009) both theoretically and experimentally.

Liu et al. (2000) extended the model by Ennis et al. (1991) to account also for deformable core particles. They distinguish between 4 impact scenarios:

1. Coalescence without contact of the core particles. The kinetic energy is entirely dissipated by viscous forces during the approach of the particles. This will be the case for very small particles (St_v is large), highly viscous binder liquids and low impact velocities.
2. Coalescence after an elastic impact of the core particles. The kinetic energy of the collision is high enough to cause a contact of the core particles, but the relative velocity goes down to zero during the rebound phase due to viscous forces in the liquid film.
3. Coalescence after plastic deformation of the core particles. Viscous forces in the liquid film and plastic dissipation during the contact combine to dissipate the kinetic impact energy.
4. Rebound. For very high impact velocities no agglomeration will occur.

Implementations of this model can for example be found in Gantt & Gatzke (2005) and Rajniak et al. (2009). This model is particularly relevant for processes with high impact velocities, such as



high shear mixers. It does, however, not bring any improvement regarding the viscous Stokes theory itself.

Table 1-1: Overview of viscous force models in the literature.

Reference	Model equations	Comments
Cameron (1981); Adams & Edmondson (1987); Barnocky & Davis (1988); Ennis et al. (1991); Lian et al. (2001); Antonyuk et al. (2009)	$F_{vis} = 6 \frac{\pi \eta_{liq} R^{*2}}{D} v_{rel}$	For particle-particle impact, D = separation distance η = liquid viscosity R^* = reduced radius according to Eq. 1-12.
Pitois et al. (2001)	$F_{vis} = 6 \frac{\pi \eta_{liq} R^{*2}}{D} v_{rel} \cdot \zeta_v^2$ with $\zeta_v = 1 - \left(1 + \frac{4V_{liq}}{\pi d_p D^2}\right)^{-0.5}$	V_{liq} = liquid bridge volume
Matthewson (1988)	$F_{vis} = 6 \frac{\pi \eta_{liq} R^2}{D} v_{rel} \cdot \zeta_v^2$ with $\zeta_v = 1 - \frac{D}{D + \frac{r_b^2}{2R}}$	For particle-wall impact, R = particle radius, r_b = radius of liquid bridge
Adams & Perchard (1985)	$F_{vis} = \frac{\pi}{n+3} \left(\frac{2n+1}{2n}\right)^n \frac{kb^{n+3} v_{rel}^n}{D^{2n+1}}$	For a non-Newtonian fluid with power law index n. b = radius of contact area k = consistency constant
Goldman et al. (1967); Lian et al. (1998)	$F_{vis,t} = \left(\frac{8}{15} \ln \frac{R}{D} + 0.9588\right) v_{rel,t} \cdot 6\pi\eta R$	Motion of a sphere of radius R parallel to a flat surface with tangential relative velocity $v_{rel,t}$.
Popov (2010)	$F_{vis,t} = 2\pi\eta R \cdot v_{rel,t} \cdot \ln\left(1 + \frac{R}{2D}\right)$	



1.3.1.4 Breakage

Breakage of agglomerates occurs due to collisions with other particles and with the walls of the equipment and limits the final product size. Also the agglomerate strength is influenced by breakage processes in the process, since only agglomerates that can withstand the applied intensity of agitation in the bed survive. Extensive descriptions of breakage mechanisms are given in Reynolds et al. (2005), Antonyuk (2006) and Salman et al. (2007).

Consolidation and breakage of wet granules was described by Tardos et al. (1997) with the help of a dimensionless Stokes deformation number St_{def} , which is defined as the ratio of the externally applied kinetic energy to the energy required for deformation:

$$St_{def} = \frac{m_p v_{rel}^2}{2V_p \tau(\dot{\gamma})} \quad (1-14)$$

In Eq. 1-14 m_p is the particle mass, V_p the particle volume and τ is a characteristic stress in the granule, which can be approximated by the yield strength τ_y for concentrated wet granules. (Tardos et al., 1997) measured granule deformation and break up under shear in a novel constant shear fluidized bed granulator. Granules first elongated under shear and then broke at a Stokes deformation number of approximately 0.2.

Attrition and breakage of dry granules or agglomerates is a very complex process due to the inhomogeneous structure of the particles. Iveson et al. (2001) suggest that dry granules fail in brittle or semi-brittle fashion, i.e. they fail in tension by the propagation of pre-existing cracks, which concentrate stress. Thus, the fracture stress may be much less than the inherent tensile strength of bonds between particles in the granule. Due to the unknown micro structure of the particles regarding the distribution and length of cracks, which is different in each individual particle, a general model for breakage of granules or agglomerates is not available today.

Antonyuk (2006) investigated the deformation and breakage behaviour of different types of granules and suggests that the Discrete Element Method is a suitable tool to describe the mechanical properties of agglomerates. Multi-body systems can be represented as spheres connected via a network of solid bridge bonds. However, the model requires measured values of the mechanical properties such as the contact stiffness and the tensile strength of both the primary particles and the solid bridge bonds as input parameters.



1.3.2 Modeling approaches for fluid bed granulation and agglomeration

In the literature, many attempts have been made to model granulation and agglomeration processes in a fluidized bed in terms of population balances (Hounslow et al., 1988; Litster et al., 1995; Heinrich et al., 2003; Kumar et al., 2006). In a one-dimensional scheme using the particle size as internal coordinate the evolution of the particle size distribution with time can be described according to different mechanisms for size enlargement (continuous growth, discrete aggregation) and size reduction (continuous attrition, discrete breakage). A complex set of partial integro-differential equations is obtained, which can be solved numerically applying a discretization scheme. The kinetics of each mechanism are unknown, a-priori, and must be obtained with the help of experimental data. Rate constants needed as input parameters by the population balance equations are the growth rate, the aggregation rate, the aggregation kernel, the attrition rate, the breakage rate and the breakage function. Usually, these parameters are specific to the applied process conditions and to properties of the used material, which is the main limitation regarding the application of such a model. The model can reproduce the process behaviour in the condition that it was calibrated to, but it often fails to predict other process states and it is impossible to extrapolate data from one material system to another. Population balance models are an elegant way to describe the dynamics of a fluidized bed agglomeration process, but they cannot represent the underlying physics. More detailed models have therefore been developed, which try to include as many as possible of the micro mechanisms described in section 1.3.1.

Terrazas-Velarde et al. (2009) presented a stochastic model for fluidized bed granulation where the micro process kinetics of binder addition, particle collision, particle wetting, agglomeration/rebound, drying of deposited droplets and breakage are considered individually. The simulation box used in their work contained 2000 particles, but fluid dynamics were not represented by the model. The results indicate that the mechanism of droplet-capture is the rate-determining step during agglomeration. In the development of stochastic and population balance models, the assumption of a spatially homogeneous (well-mixed) system is usually employed. However, since powder characteristics and essential hydrodynamic and kinetic parameters regarding liquid-solid contact and granule agglomeration, particle mixing and segregation are lumped into the kinetic rate constants, population balance models assuming homogeneity cannot be applied for a priori design and scale-up of the fluid bed granulation process (Goldschmidt, 2001).



In a fluidized bed granulator, the wetting and drying rates are highly dependent on the flow field of gas and particles. Local temperatures in the equipment volume are important for the moisture equilibrium and influence the drying rate (Hede et al., 2009). But not only are the drying kinetics a function of moisture, relative velocity and temperature, also the agglomeration kinetics which strongly depend on the mechanical material properties are governed by the local process conditions and the humidity distribution. Especially for amorphous food powders, the mechanical particle properties are highly dependent on the moisture content (Palzer, 2009). While exceeding the glass transition temperature T_g by 10-30 °C, the viscosity decreases from 10^{10} - 10^{12} Pa·s to approximately 10^8 - 10^9 Pa·s (Ferry, 1980). At such viscosity, particles get adhesive. To predict agglomeration events, a model of a fluidized bed should include a fine resolution of the local temperature and humidity fields.

Following the concept of the Kinetic Theory of Granular Flow (KTGF), multiphase Computational Fluid Dynamic (CFD) models have been established to describe the fluid dynamics of spout fluidized bed systems (Gryczka et al., 2009). According to this approach, both the solid and the liquid phase are considered as continua (Euler-Euler). The method allows simulating a lab-scale fluidized bed within a reasonable period of time. Karlsson et al. (2009) developed a 3D multiphase CFD model of the particle and gas motion in the Wurster process including heat and mass transfer between the particles and the gas phase and the continuous injection of liquid through a central spray nozzle. However, all Eulerian multiphase models developed so far fundamentally lack a description of the particle-particle friction and inter-particle cohesive forces (Patil et al., 2005). Energy dissipation through non ideal elastic collisions can only be incorporated into the model by using a damping or restitution coefficient to describe the material properties and their temperature and moisture dependency.

The Discrete Element Method (DEM) can overcome this limitation for the price of a higher numerical effort. As each particle is tracked individually, the method allows a complete representation of the particle-particle and particle-wall interactions and their influence on the process dynamics. The principle of this modeling technique will be presented in detail in Chapter 3. If DEM is combined with a flow solver based on CFD, a Discrete Particle Model (DPM) can be set up (Euler-Lagrange approach). The geometry of the system is discretized in mesh cells for the calculation of the gas flow profile, which is achieved using volume-averaged Navier-Stokes equations. As the mesh is coarse compared to the particle size, the flow field is not fully resolved. Therefore, a drag correlation is required as closure model to calculate the drag force the fluid exerts on the particles.



The highest level of detail is obtained via Direct Numerical Simulation (DNS) of the gas flow field around the particles. Here, the computational grid is smaller than the particle size, which allows the calculation of the gas-particle-interaction force without closure models. Due to the extremely high numerical effort, until now DNS has only been applied to fixed arrays of very few spherical particles (Deen et al., 2009; Washino et al., 2011). DNS is the most accurate simulation tool, but full detail of the flow in all parts of the process is usually not required. Therefore, it is an elegant approach to combine DNS on the small scale with coarser models such as DPM or multiphase CFD models in a multi scale model, as presented in Fig. 1-10.

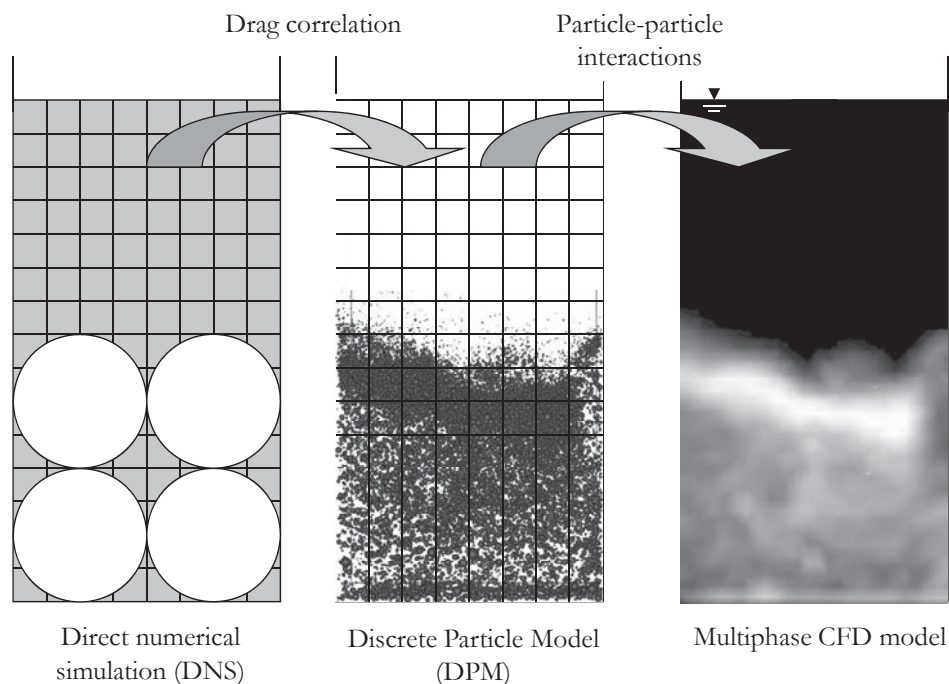


Figure 1-10: Schematic representation of the level of detail in different modeling approaches for dense gas-solid flows (based on van der Hoef et al., 2004).

DNS can be used to extract a drag force correlation, which is then used in a DPM model (Hill et al., 2001; van der Hoef et al., 2005; Sarkar et al., 2009). DPM simulations can yield information on the inter-particle friction (van der Hoef et al., 2004). This multi-scale modeling concept can be further extended to the macroscopic process description using population balances. To achieve a physically based process description, while still keeping the advantage of relatively low computational effort, some authors have tried to extract information on the aggregation kernel from DPM or multiphase CFD simulations (Gantt et al., 2006; Rajniak et al., 2009). Liu & Litster (2002) proposed an aggregation kernel based on the coalescence model proposed by Ennis et al. (1991) and Liu et al. (2000) (see section 1.3.1.3 in this work).



1.3.3 Applications of the Discrete Element Method

Initially introduced by Cundall & Strack (1979), the Discrete Element Method has found a wide range of applications in particle technology in recent years. Diverse problems such as rock mechanics (Potyondy & Cundall, 2004), landslides and rock fall (Bourrier et al., 2008), bulk particle characterization via sandpiles (Li et al., 2005), compaction of particles (Martin, 2003), discharge from a hopper (Zhu & Yu, 2004), flow in mixers (Radl et al., 2010) and flow in rotating drums and mills (Mishra, 2003) have been modeled with the help of DEM.

To be able to model a fluidized bed, several authors have coupled DEM and CFD to set up a Discrete Particle Model (DPM). Recently, large progress was published in the field of DPM simulations of fluidized beds. For an overview, the reader is referred to the review papers by Deen et al. (2007) and Zhu et al. (2008). Based on pioneering work of Tsuji et al. (1993) and Hoomans et al. (1996) in 2D, simulation results were reported focusing on fluid and particle dynamics (Kafui et al., 2002; Link et al., 2009; Fries et al., 2011a), mixing behaviour (Feng et al., 2004; Zhu et al., 2011; Deen et al., 2010), moisture distribution (Fries et al., 2011b) and particle coating (Czok et al., 2005; Ketterhagen, 2011). For the dry state of the process, detailed flow regime maps were established for fluidized beds and spout fluidized beds (Xu & Yu, 1997; Li & Kuipers, 2002; Link et al., 2005; van Buijtenen et al., 2009). Yet, due to the high numerical effort it is still not possible today to track more than about a million particles within reasonable simulation times, even though recent advances in GPU computation seem very promising (Radeke et al., 2010). Due to limited knowledge about the drag force exerted on the particles by the fluid, DPM simulations until now represent the particles as monodisperse array of spheres.

Some attempts have also been made to model the fluidized bed spray granulation process using DEM. Goldschmidt (2003) modeled in 2D the agglomeration of glass beads in a top spray fluidized bed, where an aqueous solution of polyethylene glycol (PEG) binder is injected. In their concept, 3 particle species are tracked: dry particles, wet particles and droplets. While the collision of dry particles is described using a traditional hard-sphere contact model, collisions at a wet spot on the particle surface always lead to agglomeration (which is in practice not always the case). Upon collision with a droplet, the particle surface is wetted partially with a film of constant thickness. The wetted area is shrinking at a constant rate to account for drying of the binder. In reality, the liquid penetrates into the solid matrix or dissolves. Drying of the binder is characterized by a continuously increasing surface viscosity. Link et al. (2007) extended this model to represent a spout fluidized bed. They found for a two phase injection nozzle using a



discrete element simulation that 95 % of the droplets were deposited on a particle within a limited spray zone. The geometry of this spray zone can be approximated by a biconical shape. Gantt & Gatzke (2005) modeled the agglomeration of glass beads in a high shear granulator. They developed a comprehensive implementation of the coalescence model by Liu et al. (2000) including compaction and breakage mechanisms. Unfortunately, due to the high numerical effort required, the investigated system included only 192 particles. Kafui & Thornton (2008) presented a 3D model of a fluidized bed spray granulator, where the contact model for wet particles is based on the concept of surface energy (JKR Model, Johnson et al., 1971). Particles are wetted, i.e. they pick up surface energy according to their position and residence time inside a conical spray zone.

In most cases flat pseudo-2D beds were simulated, in order to allow experimental validation of the gas and particle dynamics via optical methods such as particle image velocimetry (PIV) and digital image analysis (DIA) (Deen, 2006; Laverman et al., 2008). Müller et al. (2008) used magnetic resonance tomography (MRT) to validate the particle dynamics in a flat fluidized bed with rectangular basis and found good agreement. Stronger than in fully-3D equipment the particle motion in these flat fluidized beds is influenced by wall effects, due to the large internal surface to volume ratio. Still, using a two-fluid model, Kobayashi et al. (2000) showed that the circulation of solids in a rectangular bed is similar to the circulation in a cylindrical bed. Villa-Briongos et al. (2005) found that for Geldart B and D type particles, the hydrodynamics of 2D and 3D systems are qualitatively comparable.

On the other hand, Geldart (1970) has found experimentally that due to out-of-line coalescence, bubbles in a 3D bed typically grow larger than in a 2D bed under comparable conditions. Smaller bubble size and lower rise velocity were observed with 2D beds (van Wachem et al., 1998). Peirano et al. (2001) compared numerical and experimental results of the power spectra of pressure fluctuations, the bed height and the solids volume fraction for a rectangular based bubbling fluidized bed. Using an Euler-Euler model they observed significant differences between 2D and 3D simulations and only the 3D model could predict the correct bed height and pressure spectra. Xie et al. (2008) compared the gas and particle dynamics in flat 2D fluidized beds to cylindrical and rectangular 3D-configurations using an Eulerian two-fluid-model. Their results show that a 2D Cartesian system can be used to successfully simulate and predict a bubbling fluidized bed. However, caution must be exercised when using a pseudo-2D simulation to describe other regimes such as slugging or turbulent fluidization. It can be concluded that the flow regimes reported in the literature are in most cases specific to the simulated flat geometry



and therefore limited in their application. Regarding fluid bed granulation, turbulent conditions dominate in many equipment configurations such as spouted beds, Wurster-coaters or bubbling beds with jet injections, which therefore demand a 3D hydrodynamic model.

Gas- and particle dynamics in 3D beds with rectangular base (Kafui & Thornton, 2008; Tsuji et al., 2008; Link et al., 2009) or cylindrical base (Takeuchi et al., 2004; Fries et al., 2011b) as well as cone-shaped geometries (Takeuchi et al., 2008; Zhu et al., 2011) were recently simulated. Here, experimental validation can be achieved using fiber-optical probes (Link et al., 2009) or particle monitoring techniques such as positron emission particle tracking (PEPT) (Hoomans et al., 2001; Link et al., 2008), electrical capacitance tomography (ECT) (Makkawi & Wright, 2002) or magnetic monitoring (Mohs et al., 2009). To allow a comparison between DEM simulations on a rectangular geometry and experimental data obtained in a cylindrical pilot plant, Link et al. (2009) propose a scaling law keeping the dimensionless Reynolds and Archimedes numbers as well as the minimum fluidization velocity u_{mf} constant. Still, to the authors' knowledge all simulation studies reported in the literature so far have used simplified geometries of the fluidized bed apparatus compared to common commercially available lab-scale experimental devices such as the Glatt ProCell[®] 5 or GF3 inserts (Glatt GmbH). In sensitivity studies parameters like the inclination of the wall or size and position of a draft tube were varied (Takeuchi et al., 2008), but the chosen values do not correspond to those of existing experimental devices, which were mostly designed empirically based on practical process experience.

Compared to particle dynamics, the collision dynamics in fluidized beds have found much less attention in the literature so far. Freireich et al. (2009) studied the sensitivity of mechanical material parameters on the collision dynamics in a rotating drum granulator and found a strong influence of the contact stiffness and the restitution coefficient of the particles on the collision frequency and the average collision velocity. An extensive study of the collision dynamics in a fluidized bed granulator will be presented in the chapters 5 and 6 of this work.

1.4 Objective and strategy

In fluidized bed agglomeration the main objective is to produce the maximum amount of particles within a certain size range. Oversize agglomerates need to be milled and recycled together with fines in the product, which increases the energy consumption and reduces the overall capacity. Other specifications such as density, pore size or strength of the product



particles usually apply as well. The performance of the granulator is influenced by both the operation conditions and by the geometry of the granulator.

The aim of this study is to improve the control over the particle size distribution and the strength of product particles resulting from fluid bed agglomeration by gaining insight into the underlying fundamental processes. Due to the complex micro-scale interactions, simultaneous information on all components present within the system is required to allow a fundamental study of the behaviour of the system itself. Experimental techniques allow the detailed observation of single tracer particles or a description of the overall result of the agglomeration process, but it is impossible today to monitor all relevant parameters within the system. A detailed numerical model is therefore a suitable tool to study the system on the scale of individual particles.

In this work, DEM and CFD are coupled in a Discrete Particle Model (DPM) to consider the interactions between the fluid phase fluid and the particles using the Euler-Lagrange approach. The description of the overall flow behaviour is considered to be of critical importance for any model describing a fluid bed granulator. Extensive studies on the influence of material and process parameters on the fluid and particle dynamics are therefore performed. Regarding the agglomerate structure and strength, a special focus is set on the dynamics of particle collisions. Their frequency and kinetic energy is used as an indicator for breakage and compaction in the process. On the basis of a profound description of dry particle interactions, the DPM is combined with a simple model of particle wetting. The effect of the geometry of the apparatus on the homogeneity of wetting is analyzed in order to understand the performance and specificity of different granulator configurations.

Parallel to the simulations, batch agglomeration experiments are performed on the same granulator configurations to validate the implications drawn from the simulation results.

In the framework of a multi scale modeling scheme, which is briefly introduced in this thesis, it is theoretically and practically attractive to employ DEM for the derivation of physically based expressions for aggregation and breakage kernels of a population balance model representing the granulation process on a macroscopic scale.



1.5 Outline of the thesis

Experimental validation is essential to be able to rely on the results obtained by the DPM simulations. Therefore in chapter 2 the experimental techniques used in this work to characterize the product agglomerates are presented. Fluidized bed granulator configurations used to produce the agglomerates and the applied process conditions are introduced. Since the material properties are required as input parameters by the DPM, adequate measurement techniques are presented.

Chapter 3 is dedicated to the Discrete Particle Model. Details of the coupling between gas and particle phase are discussed along with a presentation of the used closure model for the fluid drag. The applied particle-particle contact model is presented in detail as well as the used definition of a collision. For wet particle interactions, formulations of viscous forces acting within the liquid film are introduced. At the end of this chapter principles of a multi scale modeling approach for the fluidized bed agglomeration process are given.

Mechanical material properties are sensitive input parameters for the Discrete Particle Model, since a realistic representation of the particle-particle interactions depends on these values. In chapter 4 an introduction is given to the mechanical material properties of the used particles. Amorphous maltodextrin is a model substance to mimic the behaviour of various food powders. Experimental results for the coefficient of restitution, the modulus of elasticity and the friction coefficient for the material system chosen in this work are presented.

After the definition of the required input parameters, in chapter 5 the Discrete Particle Model is applied to study the particle and collision dynamics in a fluidized bed granulator for the example of a Wurster-coater. A sensitivity analysis of the influence of mechanical material parameters as well as viscous forces on the particle and collision dynamics is presented. In a combined experimental and computational study, the influence of process parameters on the agglomeration behaviour is analyzed in order to define the optimal operational setpoint.

In chapter 6, a top-spray granulator, a Wurster-coater and a spouted bed granulator are compared numerically with a special focus on the internal particle circulation and its implications on the homogeneity of particle wetting. The moisture distribution among the particles is predicted regarding the residence time distribution of the particles in the spray zone. Particle and collision dynamics are studied to characterize the fluidization regime of the three different types of equipment. Parallel to that the results of agglomeration experiments are presented. Size, structure,



strength and moisture content of the agglomerates produced in the three different granulator configurations are evaluated in comparison to the prediction by the DPM.

Finally, chapter 7 concludes on the results of this thesis and gives an outlook on further research work.



2 Experimental techniques

2.1 Introduction

To study the influence of material and process parameters on the agglomeration behaviour of amorphous maltodextrin, batch agglomeration experiments were performed. The devices used for the agglomeration trials as well as the applied methods for characterization of the agglomerate properties are presented in this chapter. For the Discrete Particle Model it is of key importance to find the correct material parameters which characterize the mechanical behaviour of the material. Adequate measurement techniques for this purpose are introduced in chapter 2.4.

2.2 Agglomeration experiments

A modular lab-scale fluidized bed spray granulation system of the company Glatt GmbH is used for the experiments in this work. The typical batch size is 1 kg. In Fig. 2-1 the used plant is shown. Three different inserts were applied to vary the geometry of the process chamber. Photographs of the used configurations are presented in Fig. 2-2 a), b) and c).

The flowsheet of the granulation plant is shown in Fig. 2-3. Central part of the plant is the process chamber (1), where the particles are agglomerated. In Fig. 2-3 the insert for the spouted bed (ProCell[®]5) is shown, which can be exchanged by the GF3 insert for a bubbling fluidized bed or a Wurster-coater. The inlet air passes through an electric heater (2) and enters the process chamber from the bottom. Inside the process chamber the injection nozzle (3) can either be located in top-spray or in bottom-spray position, depending on the granulator configuration. An externally mixing two-fluid nozzle (Schlick series 970, see Fig. 2-4) is used for the dispersion of the binder liquid, which is fed to the nozzle via a peristaltic pump (4). Above the fluidized bed an expansion chamber (5) is located to reduce the gas velocity and to avoid the elutriation of fine particles. The outlet air leaves the granulator through internal bag filters (6). Behind the filters the



blower (7) is positioned, so that the whole plant is operated in suction mode. For continuous removal of product agglomerates the granulator can be equipped with a zigzag sifter (8). The plant is equipped with 4 temperature sensors. TIRC2 is positioned in the inlet air tube directly behind the heater and is used to protect the heating cartridge. TIRC1 is positioned below the bottom plate at the inlet of the process chamber. This temperature is controlled via the heating energy. The temperature inside the powder bed is measured (TIR3) as well as the temperature of the outlet air before the blower (TIR4). The pressure drop of the bottom plate is measured (DPIR1) as well as the bed pressure drop (DPIR2) and the pressure drop of the bag filters (DPIRC1). At the inlet, before the heater (MIR1) and in the outlet air before the blower (MIR2) humidity sensors are positioned. Compressed air is supplied for the atomizer, as classification air for the sifter and for the upper and lower sealing of the process chamber. The entire process is controlled using a Siemens SPS system and all relevant data is stored on a PC.

Specifications of all components of the fluidized bed agglomeration plant and the used measurement devices for temperature, pressure and humidity are given in the appendix B1.



Figure 2-1: Glatt lab system used for fluidized bed agglomeration experiments.

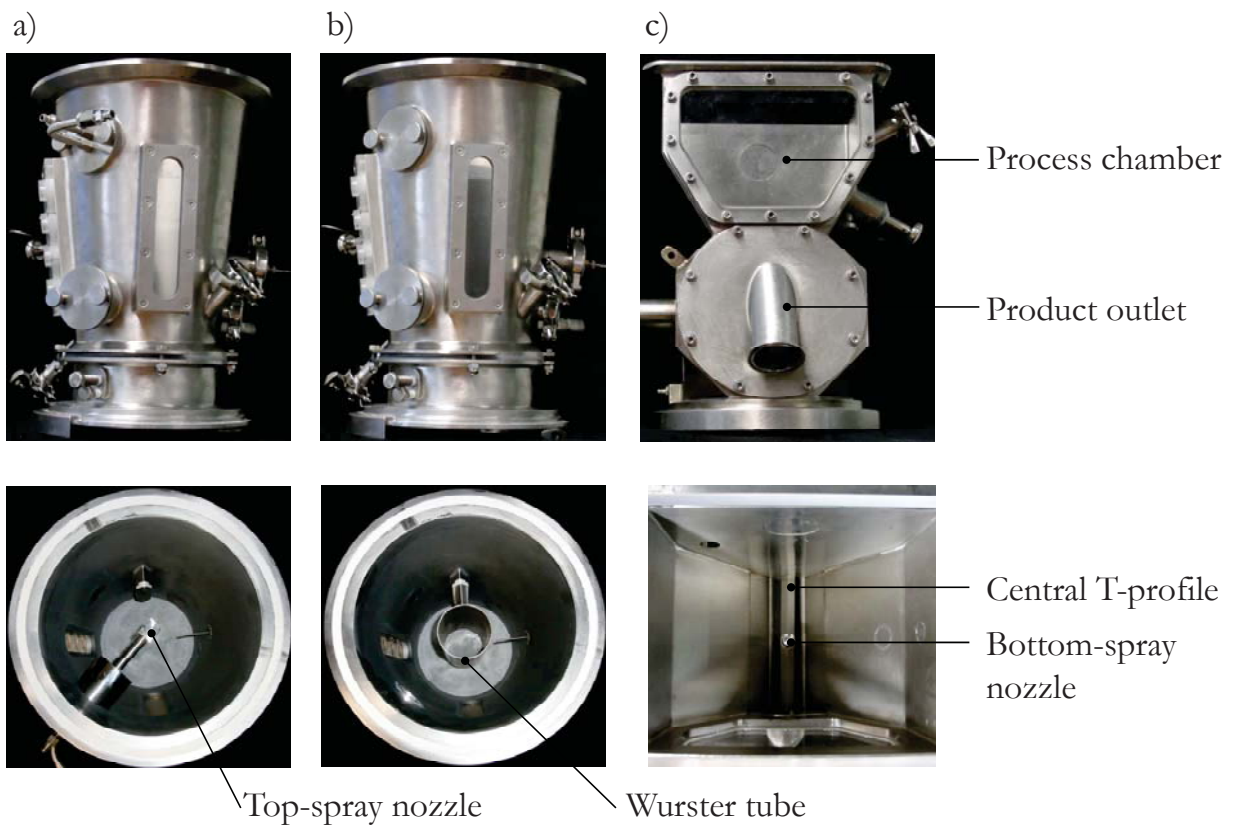


Figure 2-2: GF3 top-spray insert (a), GF3 Wurster-coater (b) and ProCell® 5 spouted bed (c).

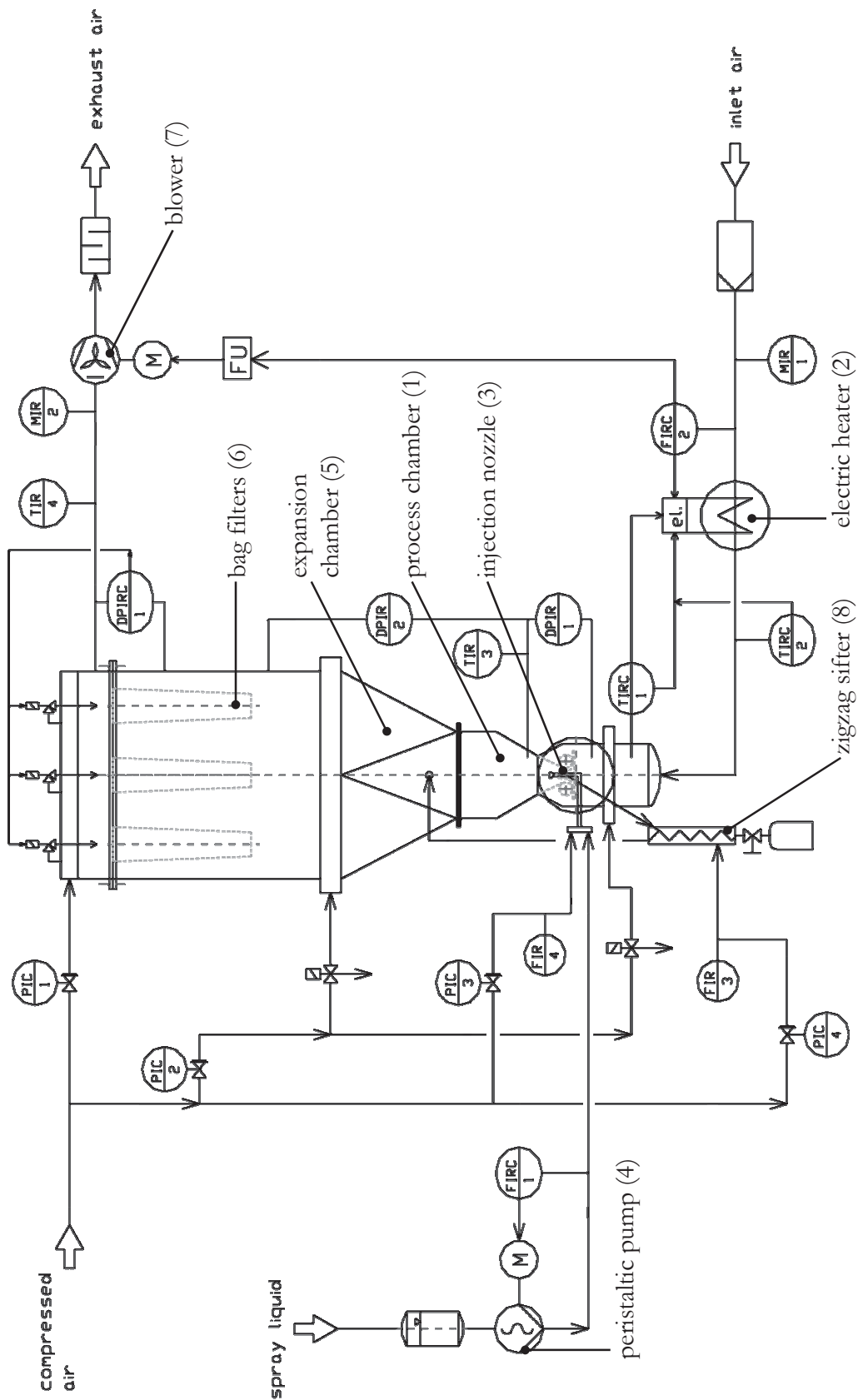


Figure 2-3: Flowsheet of the Glatt ProCell® 5 fluidized bed agglomeration plant.

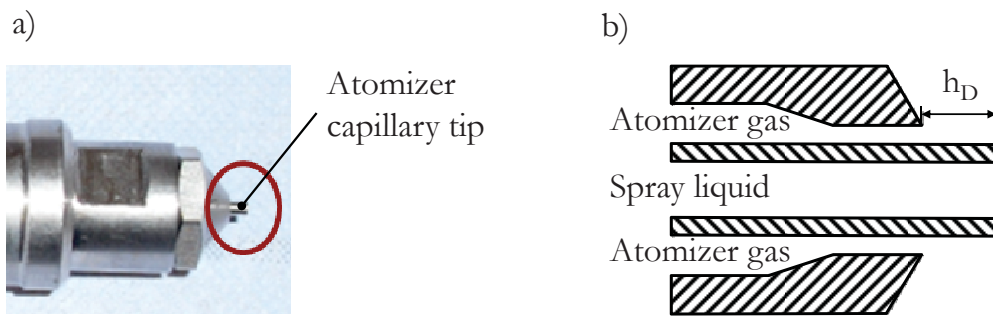


Figure 2-4: Photograph (a) and schematic drawing (b) of the used Schlick Series 970 spray nozzle.

2.2.1 Granulator configurations

Three different granulator configurations were compared in the experiments as well as in the simulations, as shown schematically in Fig. 2-5. The simplest setup is the top-spray granulator (Fig. 2-5 a). Here, the process chamber has a circular inlet cross section where a homogeneous wire mesh (mesh size: 200 μm) is used as distributor plate for the fluidization air. The side walls are inclined by 6° against the vertical axis, so that the process chamber is slightly conical. At the center, 215 mm above the bottom plate the injection nozzle is positioned, spraying in downward direction countercurrent to the fluidization gas flow. The particles move on stochastic motion paths inside a bubbling fluidized bed.

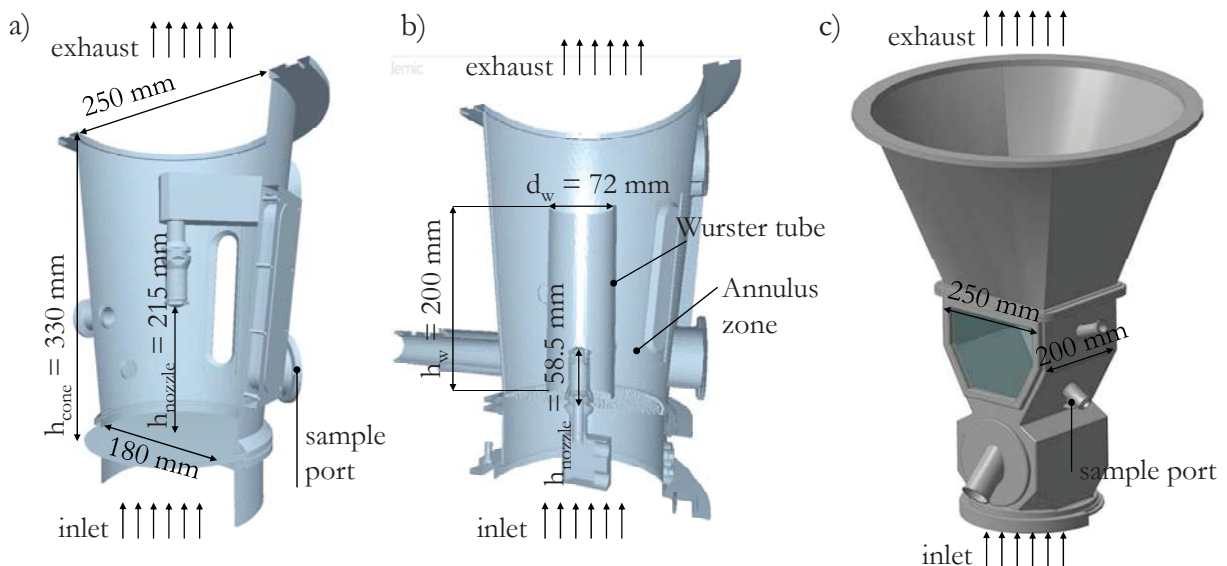


Figure 2-5: Cross cut through the used granulator configurations: a) top-spray, b) Wurster-coter, c) spouted bed.



The Wurster-coater is a bottom-spray fluidized bed granulator with a cylindrical draft tube inserted vertically above the nozzle, as presented in Fig. 2-5 b). This configuration creates a circulating particle motion and allows homogeneous wetting. It is primarily used for tablet coating in the pharmaceutical industry. Yet, for very sticky products like maltodextrin, it can also be used for agglomeration. The Wurster-coater has the same outer dimensions as the top-spray granulator. Here, a segmented perforated bottom plate is used which consists of three zones, as indicated in Fig. 2-6. Higher porosity at the center below the draft tube causes an increased gas velocity in this zone. At the center the nozzle is positioned spraying upwards at a tip height of 58.5 mm above the bottom plate. The Wurster tube is a cylindrical insert (height h : 200 mm, diameter d_i : 72 mm) which separates the wetting zone near the nozzle from the drying zone in the annulus. The gap distance between the bottom plate and the Wurster tube can be adjusted in a range of 0 – 50 mm. The particles are kept on a cyclic motion path around the Wurster tube where they are wetted inside the tube and dried in the annulus zone.

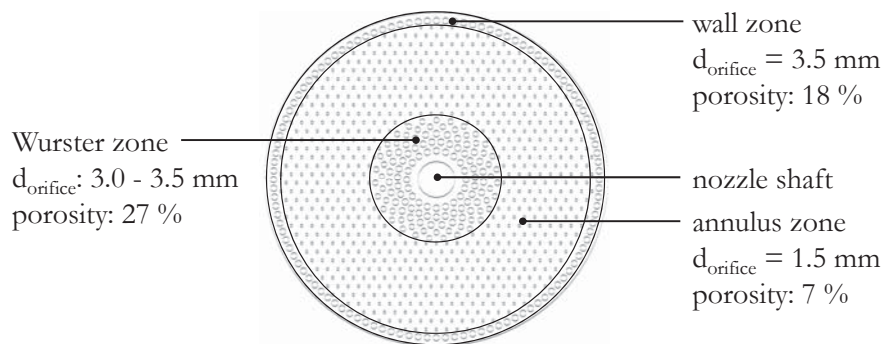


Figure 2-6: Segmented distributor plate used in the Wurster-coater.

The spouted bed (see Fig. 2-5 c) has a prismatic shaped process chamber. Air is supplied from both sides at the bottom via two adjustable inlet slots. The air is then directed upwards by a central T-profile. Different to the other two granulators, the side walls of the spouted bed are inclined by 30° against the vertical axis. In the narrow bottom zone the particles are entrained by the spout and decelerate in the expansion zone above the bed. Due to gravity they slide back downwards along the wall to close the motion cycle.

2.2.2 Sampling procedure

In all three granulator configurations samples are taken from the bed to monitor the agglomeration progress. This is done every five minutes during the injection time. In the Wurster-coater and in the spouted bed 5 % of the initial bed mass (20 g) is drawn via a sealed



port positioned 140 mm above the bottom plate. Due to the particle circulation a sufficient amount of representative particles can be captured at this position. In the top-spray granulator a port at the bottom of the bed (26 mm above the bottom plate) is used. It is crucial to sample representative lots of particles from the bed. Generally, a fluidized bed system can be regarded as well mixed, but since the particles grow significantly throughout the process, segregation may occur. To verify the representative nature of the samples, at the end of each agglomeration trial the whole bed was sieved in order to compare the size distribution of the ensemble to the size distribution of the last sample taken just before shutdown.

2.3 Analysis of the product agglomerates

To investigate the transient behaviour of the agglomeration process and to describe the effect of different granulator geometries on the product properties, size and strength of the agglomerates were analyzed.

2.3.1 Particle size analysis

Due to their irregular shape, agglomerates produced in the fluidized bed are not easy to characterize in terms of an equivalent particle diameter. Offline size analysis methods were applied. The compact and dense primary particles were characterized by laser diffraction (Sympatec Helos 12 LA, see appendix B2) and a sieve analysis was performed with the agglomerates. Sieving has the advantage that different size fractions are separately available for further analysis. A disadvantage of the sieve analysis is the risk of particle breakage due to the agitation of the sieve, which may influence the size distribution. Furthermore, a sieve analysis does not yield information on the particle shape. The agglomerate samples were sieved for 10 min at constant rate using a Fritsch Analysette sieve tower to minimize breakage and influences by the operator. The used balance has an accuracy of 0.01 g.

Inline measurement of the particle size was tested only in the Wurster-coater in comparison to a sieve analysis of samples taken from the process. For this purpose a focused beam reflectance sensor (FBRM[®] C35) was supplied by the company Mettler-Toledo, which measures pulses of backscattered light from a focused laser beam. The principle setup of the sensor is shown in Fig. 2-7. The tip of the probe is installed inside the moving powder bed, where a laser beam is emitted. To enlarge the field of view, the axis of the laser beam is rotated continuously within the



sapphire window at the tip. Particles that cross the laser beam partially reflect the light, which is recorded by the sensor.

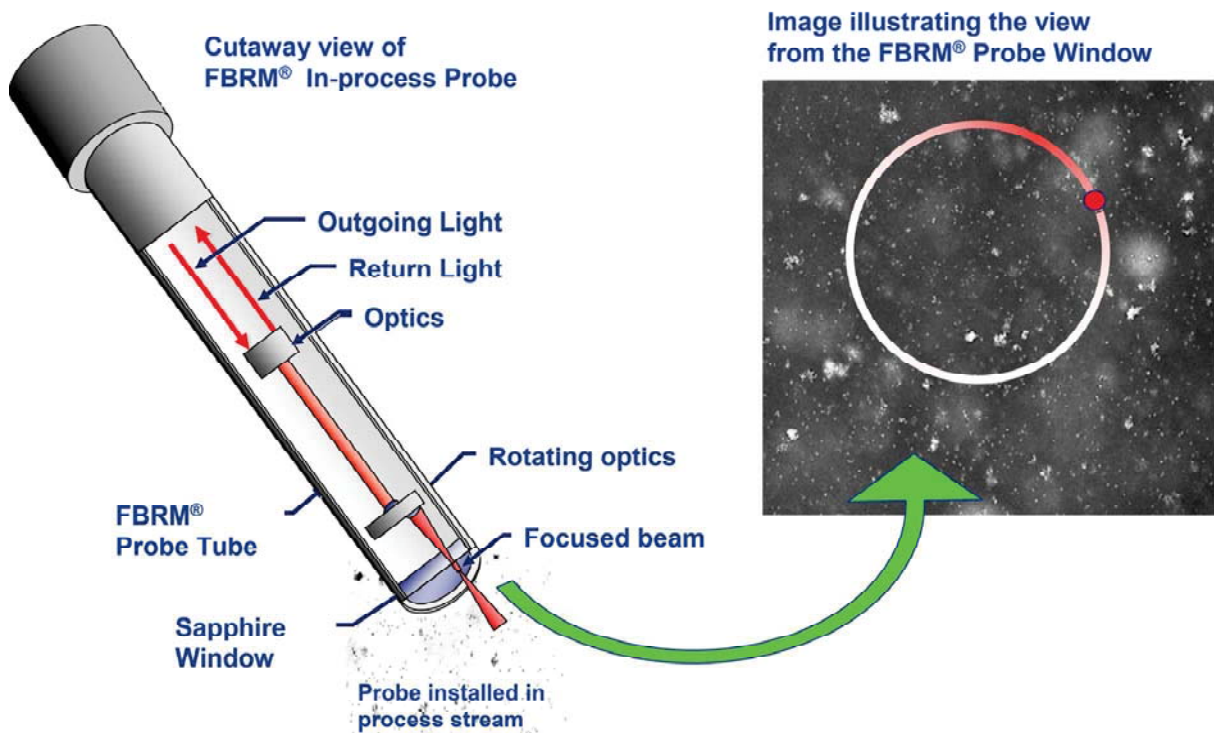


Figure 2-7: Principle of a focused beam reflectance sensor (Mettler-Toledo).

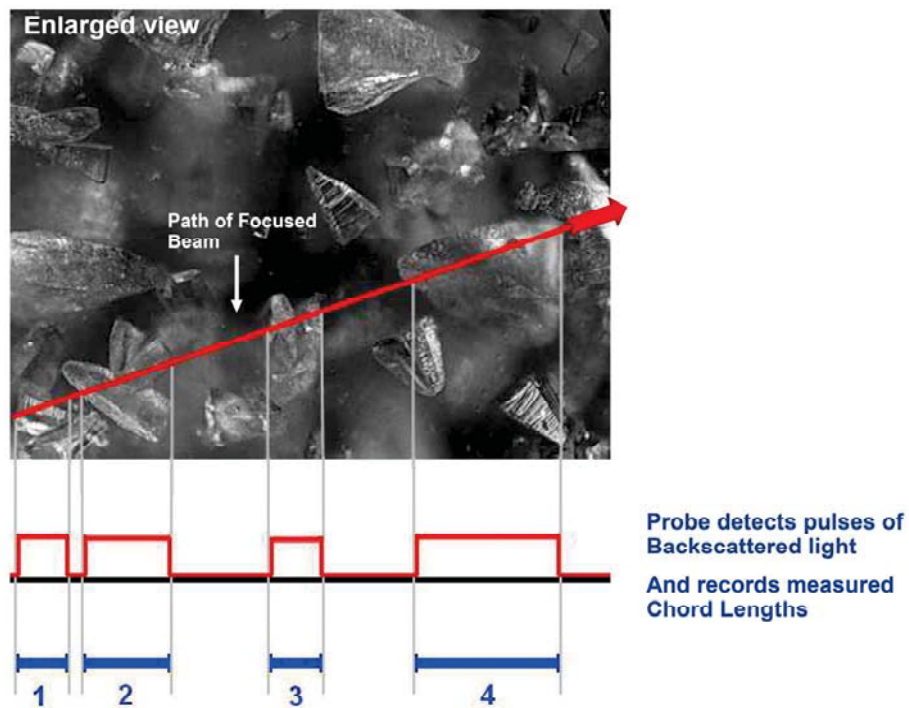


Figure 2-8: Determination of a chord length distribution with the FBRM® sensor (Mettler-Toledo).



Pulses of backscattered light are counted and interpreted as a chord length distribution as illustrated in Fig. 2-8. According to the supplier, the resolution of the optics cover particles as small as $2\ \mu\text{m}$ within a field of view of $1075 \times 825\ \mu\text{m}$. To avoid that sticky material partially blocks the sapphire window where the laser beam is emitted, an automatic wiper is installed.

Similar to the drawing of samples it is important to find a sensor position which allows to measure representative values for the ensemble of particles in the fluidized bed. For the Wurster-coater the sensor was positioned at the center of the dense bed in the annulus, 50 mm above the bottom plate and 20 mm from the wall.

2.3.2 Compression tests

To characterize the stiffness and strength of the agglomerates, a 'TA.XT plus Texture Analyzer (Stable Micro Systems Ltd., Godalming, Great Britain, see Fig. 2-9 a) is used. As shown schematically in Fig. 2-9 b), Individual agglomerates are loaded at constant test speed ($0.01\ \text{mm/s}$) with a cylindrical stainless steel tool (5 mm in diameter) up to a deformation of 0.3 mm. The step motor used for the positioning of the tool has a distance resolution of 0.001 mm. The force necessary to drive the tool at constant velocity into the sample is recorded by a load cell (capacity: 50 N, accuracy: 5 mN). Once a threshold force (0.05 N) is exceeded, data from the load cell is recorded at a frequency of 10 Hz to obtain the force-displacement curve.

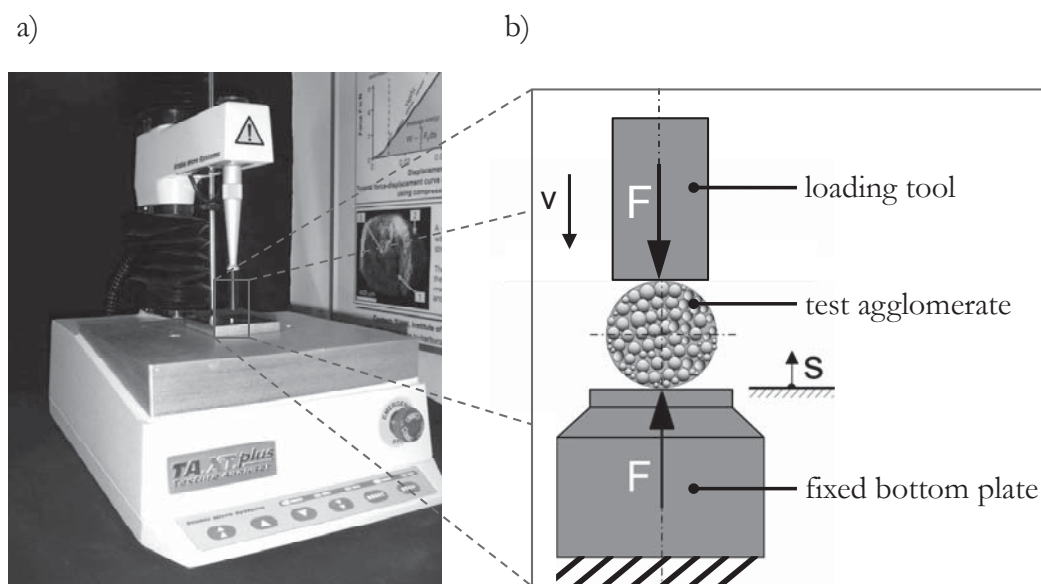


Figure 2-9: Photograph of the used Texture Analyser (a) and schematic view of the compression test (b).



A typical force-displacement curve for maltodextrin agglomerates is shown in Fig. 2-10. From the beginning of the loading up to the breakage point, a linear increase of the force-displacement curve is observed, which is typical for dominantly plastic materials. The plastic yield point is below the threshold of the instrument and can therefore not be detected. From the force-displacement curve mechanical properties of the samples can be derived. The apparent contact stiffness k is the slope of the curve from the beginning of a loading phase to the primary breakage point B:

$$k = \frac{\Delta F}{\Delta s} \quad (2-1)$$

Due to the inhomogeneous particle shape and structure the internal network of primary particles in the agglomerate is disrupted upon loading with the tool. Breakage events, which can be identified by a sudden decline of the loading force, usually occur at the weakest solid bridge in the structure, while the rest of the agglomerate remains intact. Therefore, a large variance is found for the mechanical agglomerate properties.

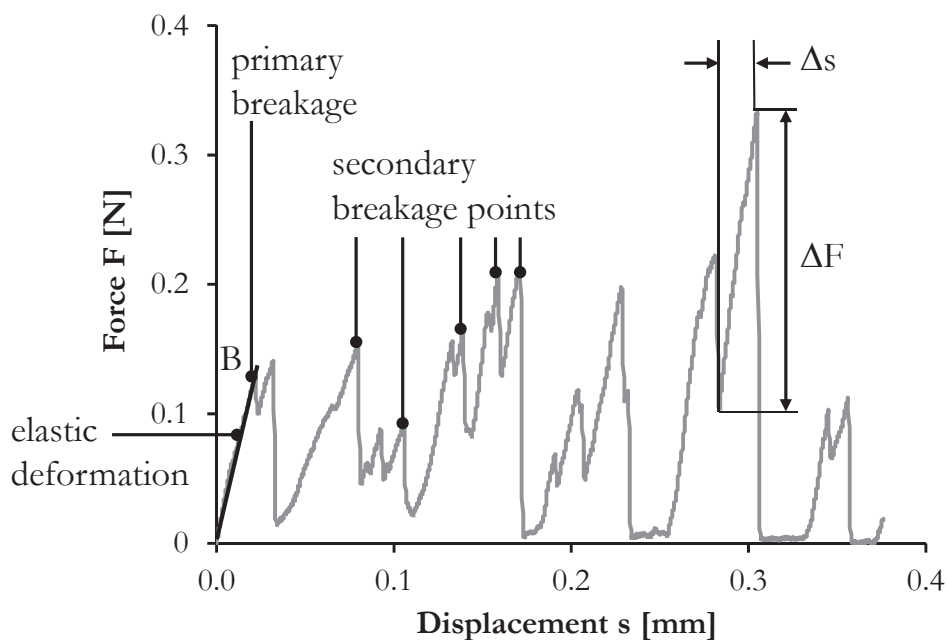


Figure 2-10: Typical force-displacement curve for maltodextrin agglomerates at 0.01 mm/s test speed.

Characteristic values for the agglomerate strength are the force increment ΔF between the beginning of a loading phase and the peak, the corresponding displacement increment Δs , the average breakage force F_B and the breakage energy E_B , which is defined by the area below the force-displacement curve for each loading phase:



$$E_B = \frac{1}{2} \Delta F \Delta s. \quad (2-2)$$

The breakage strength σ_B of the agglomerates is defined as the applied force at the breakage point divided by the loaded cross sectional area, which is the cross section of the weakest solid bridge in this case

$$\sigma_B = \frac{F_B}{A} = \frac{4F_B}{\pi d_b^2}. \quad (2-3)$$

Since the diameter of this solid bridge is unknown and may be different in each agglomerate, the absolute value of the breakage force F_B is used in this work instead of the strength σ_B .

2.4 Mechanical material characterization

A discrete particle model requires detailed information on the mechanical material properties, which are input parameters for the contact model. Regarding heterogeneously structured agglomerates it is particularly important to find a method that allows the measurement of shape-independent particle properties. Techniques for the characterization of material properties relevant for the DPM are presented in this chapter.

2.4.1 Free-fall test setup for determination of the restitution coefficient

The restitution coefficient is a very important parameter to describe the energy absorption during particle collisions in Discrete Particle Models (Mangwandi et al., 2007; Kruggel-Emden et al., 2007; Antonyuk et al., 2010). During the initial period of an impact, the contact partners are compressed and their kinetic energy is transformed into internal deformation energy, friction and adhesion. The reaction force deforms the particle, which leads to the contact displacement or overlap. The elastic contribution of the impact energy absorbed during the compression is released during the restitution phase and leads to the elastic force that separates the contact partners. The absorption of the kinetic energy during the impact can be described by a restitution coefficient. The coefficient of restitution is defined as the square root of the ratio of the elastic strain energy $E_{kin,R}$ released during the restitution to the impact energy, i.e. initial kinetic energy E_{kin} , which can be simplified to the ratio of the rebound velocity v_R to the impact velocity v :



$$e_n = \sqrt{\frac{E_{kin,r}}{E_{kin}}} = \frac{|\mathbf{v}_r|}{\mathbf{v}} \quad (2-4)$$

For the measurement of the normal coefficient of restitution a free fall tester is commonly used (Sommerfeld, 1999; Louge & Adams, 2002; Antonyuk et al., 2010), which is schematically shown in Fig. 2-11. The device consists of a stand (1) and a hardened steel target plate (2). A vacuum nozzle (4) is used to hold the particle and to drop it without initial rotation. During the test, a particle falls from a defined height h onto the horizontal target plate. The impact is filmed at 8000 frames per second with the help of a high speed camera (3) (Imaging Solutions Motion Pro Y4 S2). By image analysis (using Matlab), the impact and rebound velocity as well as the rebound angle and the rotational speed of the particle are determined.

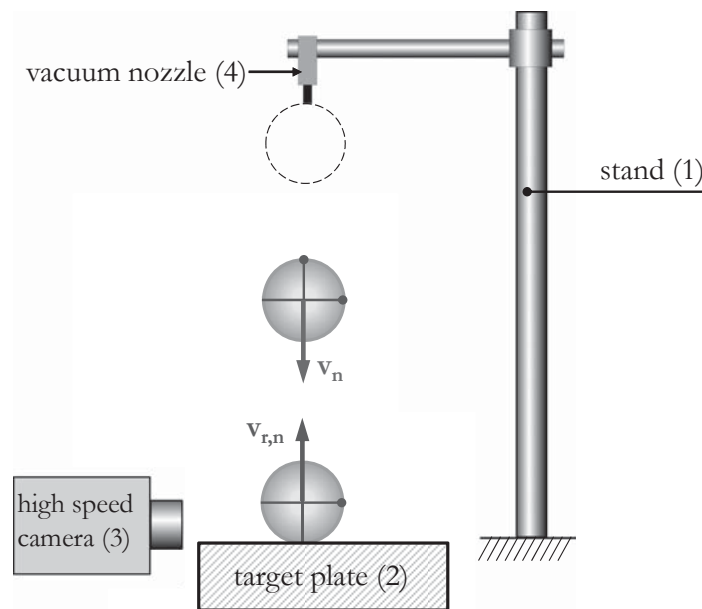


Figure 2-11: Free-fall test setup to measure the normal restitution coefficient e_n .

The restitution coefficient is an interaction parameter, i.e. its value depends on the material parameters of both contact partners.

2.4.2 Three-point bending test for determination of the elastic modulus

In response to applied stress, most starch-based food materials show visco-elastic material behaviour like polymers, which is a mixture of the elastic response of ideal solids and the viscous response of viscous liquids. The material can relax internally under load due to molecular

rearrangements. This behaviour is typically described by the time-dependent relaxation modulus $E(t)$ (Macosko, 1994):

$$E(t) = \frac{\sigma(t)}{\varepsilon_0} \quad (2-5)$$

To measure the mechanical properties of a visco-elastic material, a static relaxation test is usually applied, where for very brittle material the three-point-bending test is suitable. To apply this test, the sample must have the shape of a rectangular bar with the width b and the thickness H . The bar is loosely mounted on two bearings separated by a distance l to prevent stresses induced by fixtures. As shown in Fig. 2-12, the piston applies a predefined strain (below 0.1% to remain within the elastic range) instantaneously to the sample.

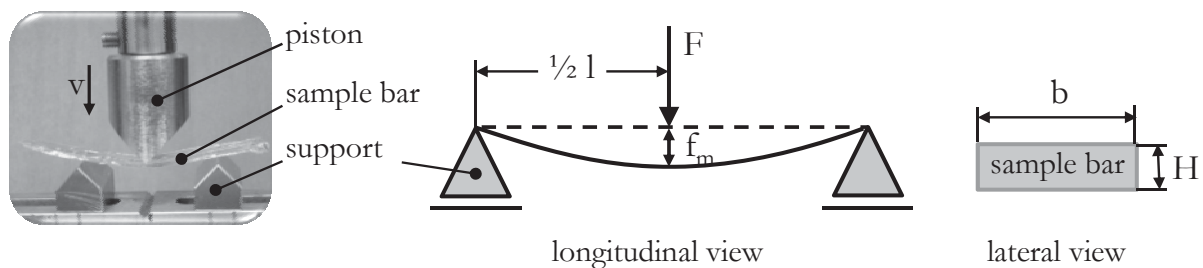


Figure 2-12: Deflection of a thin beam under centered load and its cross-sectional area.

The initial loading rate is very fast (17 mm/s), so that a stepwise increase of the strain is achieved. After that, the force necessary to hold the strain constant is monitored as a function of time. Fig. 2-13 schematically shows the applied strain versus time curve and the measured evolution of the modulus of elasticity with time.

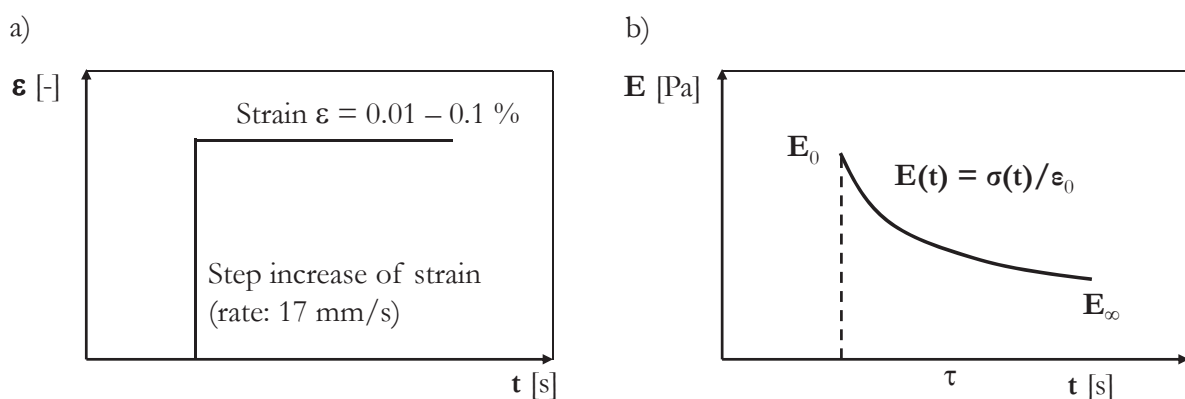


Figure 2-13: Schematic representation of the strain applied to the sample as a function of time (a) as well as the resulting modulus of elasticity (b).



From the measurements the short-time modulus of elasticity E_0 , indicating the immediate response of the material, the long-time modulus of elasticity E_∞ and the relaxation time τ can be obtained. For the scenario of particle impacts in a fluidized bed, the value of E_0 is particularly important due to the short time scale of the particle interactions.

2.4.3 Shear test for determination of the friction coefficient

The flowability of a powder bulk is commonly described with the help of a translation Jenike shear cell, which is schematically shown in Fig. 2-14. For a detailed description of the flow behaviour of cohesive powders, the reader is referred to Tomas (2004). In this section the principle of the shear test using the Jenike shear cell is briefly introduced. The space between the bottom ring and the upper ring (volume: 201.6 cm^3) is filled with the powder bulk which is to be tested. To induce shear stress, the bottom ring and the lid are shifted laterally against each other. The shear pin pushes against the frame attached to the lid to transmit a shear force F_s , which is logged by a pen recorder as a function of the shearing distance. The normal force F_n acts perpendicular to the shear force on the circular cross-sectional area A (70.88 cm^2) that separates the upper and the lower ring.

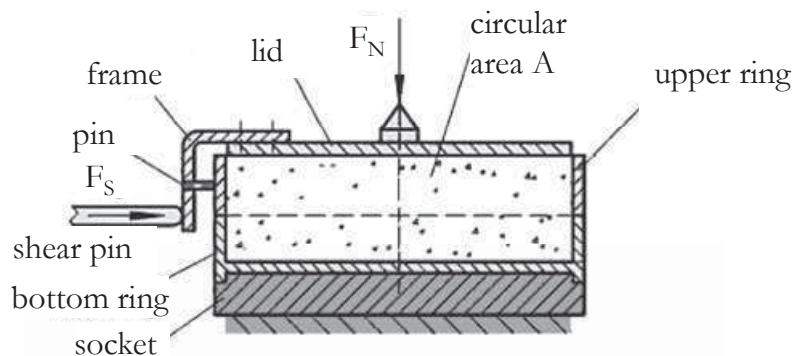


Figure 2-14: Shear cell of a Jenike shear tester for the analysis of the flowability of powders (Stieß, 1992).

To prepare the powder bulk for the shear test it is at first consolidated by the weight of the lid, the frame and by additional balance weights, which are put onto the frame. Then, further consolidation is achieved by twisting the lid under load. The shear test itself consists of two phases: pre-consolidation and shear to failure. For pre-consolidation the cell is put under defined load $F_n = F_{n,crit}$ and the sample is loaded by the shear pen, until the stationary flow regime is reached, which is characterized by a constant shear force $F_{s,crit}$ (point E in Fig. 2.15). After that the shear pin is drawn back until the shear force F_s reaches zero (point U). For the second step of



the consolidation the normal load is reduced ($F_n < F_{n,crit}$). The material is again loaded by the shear pin up to the failure of the consolidated structure, which is identified as a peak in the force-displacement curve (point G in Fig. 2-15). According to this procedure one point of the shear yield locus is obtained. To measure further points of the yield locus, the procedure is repeated under variation of the normal load F_n , while the critical normal load during preshear $F_{n,crit}$ is kept constant.

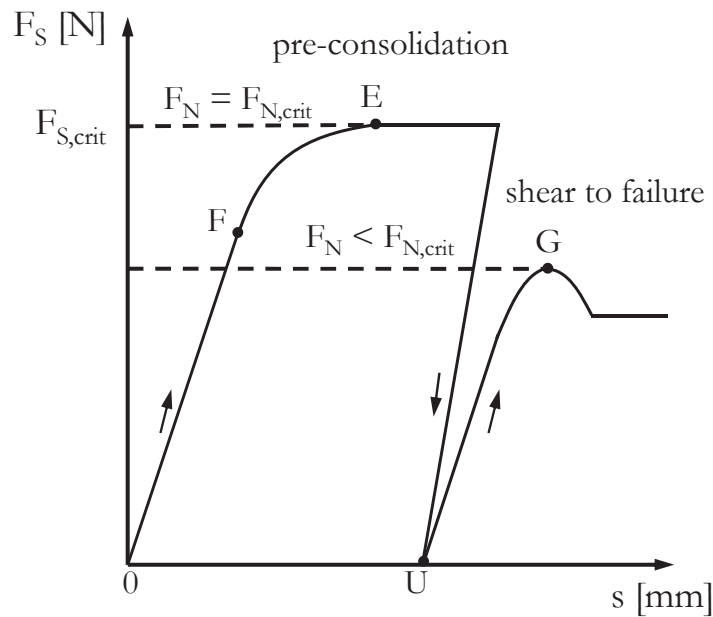


Figure 2-15: Typical force-displacement curves for pre-consolidation and shear to failure of a consolidated powder sample.

The yield locus at failure (point G) is given by the following equation:

$$\tau = \tan(\varphi_i) \cdot \sigma + \tau_c = \tan(\varphi_i) \cdot (\sigma + \sigma_Z) \quad (2-6)$$

Radius and center of the Mohr-circle are given by

$$\sigma_R = \frac{\sigma_1 - \sigma_2}{2} = \sin(\varphi_i) \cdot (\sigma_M + \sigma_Z) \quad (2-7)$$

$$\sigma_M = \frac{\sigma_1 + \sigma_2}{2} \quad (2-8)$$

The Mohr-circle for stationary flow with the main normal consolidation stresses σ_1 and σ_2 is found using the critical point K (σ_{crit} , τ_{crit}) and the tangent point E (σ_E , τ_E) of the yield locus at failure. The result is presented in a diagram plotting the shear stress τ versus the normal stress σ ,



as shown in Fig. 2-16. The yield locus at different levels of pre-consolidation is indicated by grey circles. From this figure the friction coefficient μ and the cohesion τ_c as well as the uniaxial compression strength σ_c can be obtained:

$$\mu = \tan(\varphi_i), \quad (2-9)$$

$$\tau_c = \tau(\sigma = 0). \quad (2-10)$$

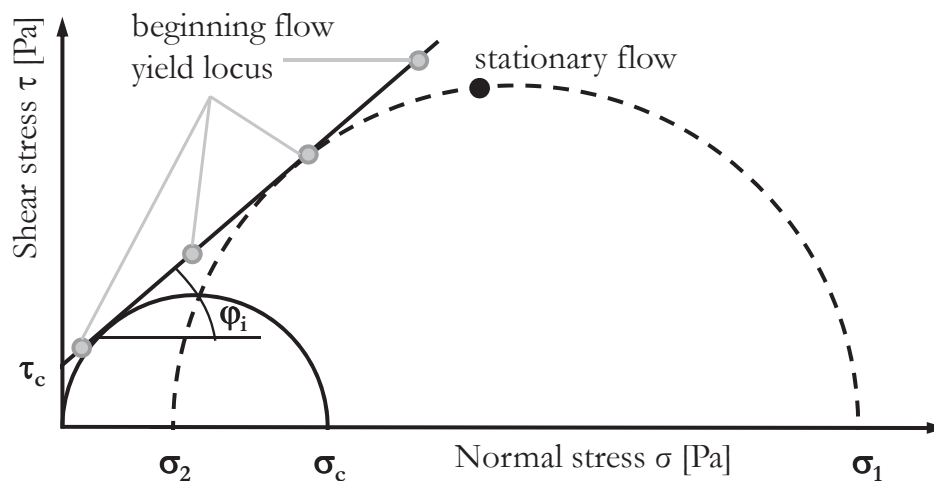


Figure 2-16: Typical individual yield locus plot.

The procedure described in this chapter allows the measurement of the internal friction coefficient μ_i which is required as input parameter by the DPM for the interaction between particles. A slight modification of the shear cell allows measuring the wall friction coefficient μ_w as well. For this purpose, a sample wall plate is positioned at the shear plane at the top of the bottom ring.

The flow function ff_c according to Jenike (1964), which describes the dependence between formation and breakage energy, is defined as the ratio between the compression stress σ_1 and the strength σ_c of the uniaxial compression. It is a commonly used indicator for the flowability of a powder. For values of $ff_c < 4$ the powder is characterized as cohesive, values in the range of $4 < ff_c < 10$ describe “easy flowing” powders and values of $ff_c > 10$ are found for free-flowing powders.

$$ff_c = \frac{\sigma_1}{\sigma_c}. \quad (2-11)$$



These stresses were measured with the help of the Texture Analyser using cylindrical pellets of maltodextrin that were compressed in a cylindrical cartridge. The flow function ff_c is not a material constant, since it depends on the stress level. For most powders the value of the flow function increases with increasing compression stress σ_1 (Schulze, 2009).



3 Discrete Particle Model

3.1 Introduction

A detailed experimental study of agglomeration in a fluidized bed is very difficult due to the complex process dynamics and due to difficulties to monitor the progress of the agglomeration experimentally. Access to the process chamber is limited and non-intrusive measurement techniques are expensive and only partially available. Therefore, computational models provide a powerful alternative for laborious experimental studies. The ultimate objective of modeling is to consider an industrial system (Werther et al., 2011), but due to the major variation in the length and time scales, continuum models constitute the only feasible option for the simulation of large scale fluid bed granulators. To increase the predictive capabilities of these models, more detailed information needs to be obtained from more sophisticated micro scale models, like the Discrete Particle Model (DPM), which is presented in this chapter.

The DPM resolves the flow profile of the gas phase and the trajectories of the individual particles in detail, while taking into account the interaction between individual particles and between particles and the gas phase. The gas phase is described by volume-averaged Navier-Stokes equations, while the movement of each individual particle is specified by Newton's laws of motion. The equations governing the dynamics of both phases are presented in section 3.2. In section 3.3 the structure and resolution of the mesh applied by the fluid flow solver is discussed. The coupling scheme between the continuous gas phase and the discrete particle phase is given in section 3.4, which also includes the drag closure model that is used to calculate the fluid-particle interaction forces, which plays a significant role in fluidized beds. Two approaches to handle particle collisions are commonly used: the soft sphere and the hard sphere approach. Both approaches are presented in section 3.5 together with the contact model proposed by Tsuji et al., (1993), which is used in this thesis. The applied definition of a collision is discussed in section 3.6.



Regarding particle flow in a fluidized bed granulator the influence of an additional liquid phase becomes important, since particles are wetted in the spray zone. A liquid film present on the particle surface induces additional adhesive contact forces, which become active in case of a collision due to the displacement of the liquid. In section 3.7 the implementation of viscous forces used in this work is introduced.

Finally, in section 3.8 the DPM simulation is set in the context of a multi-scale-modeling strategy to combine the microscopic view of particle-scale events with the macroscopic view of the entire granulation process.

3.2 Fundamental model equations

In the Discrete Particle Model the motion of each individual particle (index i) with mass m_i and volume V_i in the system is calculated using Newton's second law

$$m_i \frac{d\mathbf{v}_i}{dt} = -V_i \nabla p + \frac{V_i \beta_{g-p}}{1 - \varepsilon} (\mathbf{u}_g - \mathbf{v}_i) + m_i \mathbf{g} + \mathbf{F}_{c,i} + \mathbf{F}_{A,i}, \quad (3-1)$$

where \mathbf{v}_i is the velocity and \mathbf{r}_i the position vector of the particle i . The forces on the right hand side of Eq. (3-1) are respectively due to the pressure gradient, fluid drag, gravity, contact forces (i.e. due to collisions) and adhesive particle-particle interactions (for instance Van-der-Waals forces, viscous or capillary forces) (Deen et al., 2007).

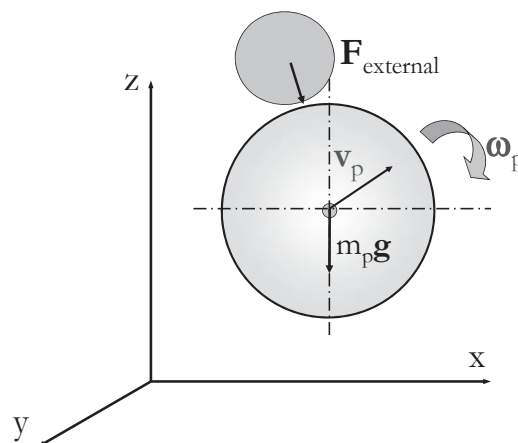


Figure 3-1: Principle motion scheme of an individual particle according to the DPM.

The tracking of the individual particle motion according to the DPM is illustrated in Fig. 3-1.



The interphase momentum transfer coefficient β_{g-p} describes the influence of the surrounding gas flow field on the particle motion. A closure model for the drag force is required at this point, which will be presented in section 3.4.

The rotational motion of the particle i is calculated with the Euler equation

$$I_i \frac{d\omega_i}{dt} = \mathbf{T}_i, \quad (3-2)$$

where \mathbf{T}_i is the torque and I_i is the moment of inertia of particle i .

For a fluidized bed the relevant external forces are fluid drag, contact forces and pressure gradients, as shown schematically in Fig. 3-2.

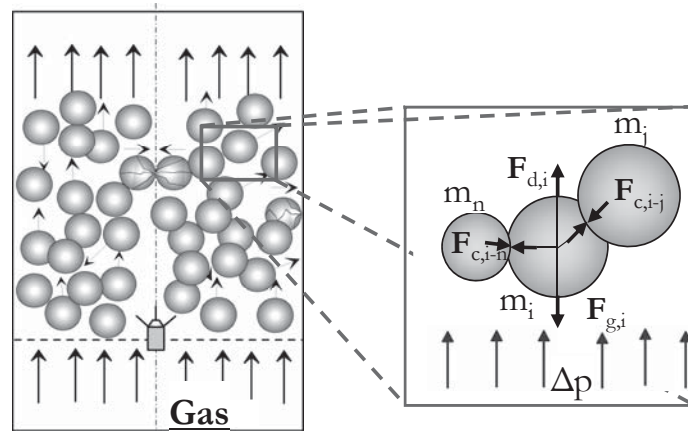


Figure 3-2: Principle scheme of gas and particle interactions in a DPM for a fluidized bed.

In the DPM the gas phase is considered as continuum. The geometry of the apparatus is discretized in mesh cells and the motion of the gas phase is calculated for each cell using the continuity and volume-averaged Navier-Stokes equations for a gas interacting with a solid phase, as originally derived by Anderson & Jackson (1967):

$$\frac{\partial}{\partial t}(\varepsilon \rho_g) + \nabla \cdot (\varepsilon \rho_g \mathbf{u}_g) = 0, \quad (3-3)$$

$$\frac{\partial}{\partial t}(\varepsilon \rho_g \mathbf{u}_g) + \nabla \cdot (\varepsilon \rho_g \mathbf{u}_g \mathbf{u}_g) = -\varepsilon \nabla p_g - \nabla \cdot (\varepsilon \boldsymbol{\tau}_g) - \mathbf{S}_p + \varepsilon \rho_g \mathbf{g}. \quad (3-4)$$

The gas-phase stress tensor $\boldsymbol{\tau}_g$ is assumed to obey the general form for a Newtonian fluid (Bird et al., 1960):



$$\boldsymbol{\tau}_g = -\left(\lambda_g - \frac{2}{3}\eta_g\right)(\nabla\mathbf{u}_g)\mathbf{I} - \eta_g\left((\nabla\mathbf{u}_g) + (\nabla\mathbf{u}_g)^T\right). \quad (3-5)$$

The bulk viscosity λ_g can be set to zero for gases. Due to the volume fraction they occupy, the particles act as obstacles and influence the velocity profile of the gas phase. This effect is accounted for by adding a sink term S_p to the momentum balance (Eq. 3-6):

$$S_p = \frac{1}{V_{cell}} \int_{V_{cell}} \sum_{i=0}^{N_p} \frac{V_i \beta_{g-p}}{1 - \varepsilon} (\mathbf{u}_g - \mathbf{v}_i) D(\mathbf{r} - \mathbf{r}_i) dV. \quad (3-6)$$

The distribution function D distributes the reaction force acting on the gas phase over the Eulerian grid. This force is the equivalent reaction to the particle drag.

3.3 Resolution of the gas flow field

As a matter of principle the flow field around the particles is not fully resolved in a DPM. Using the grid generator Gambit 2.4.6 (Ansys Inc.), the geometry of the fluidized bed granulator is divided into tetrahedral mesh cells according to the TGrid algorithm (Blake & Spragle, 1993). To avoid local extrema of the solids concentration, the gas flow field is solved on a relatively coarse grid compared to the particle size.

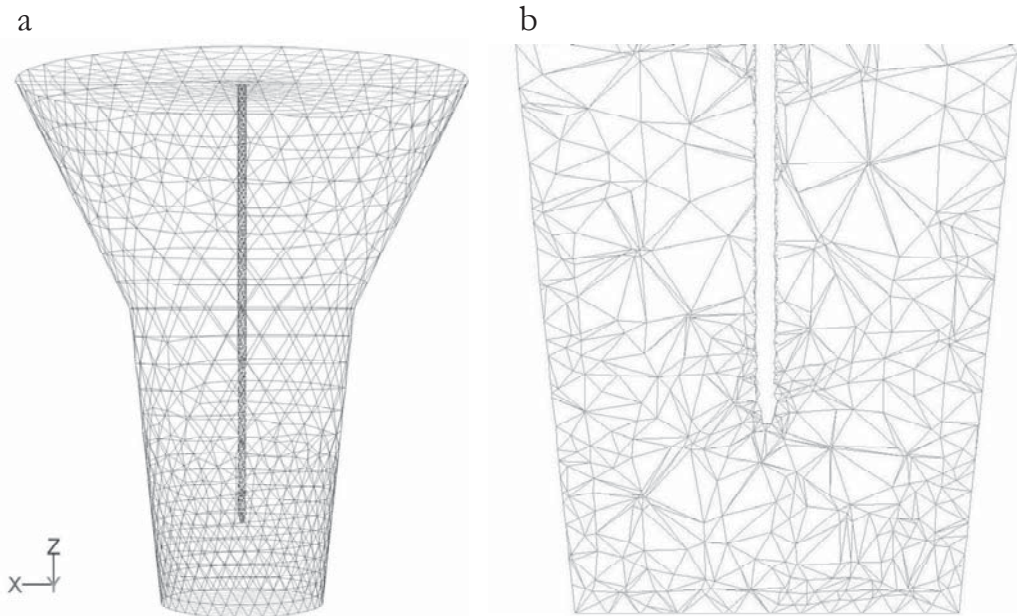


Figure 3-3: Tetrahedral mesh of a top spray granulator for the calculation of the gas flow profile (a). Two-dimensional slice cut out of the mesh vertically at the center of the granulator (b).



The side length of an average Eulerian grid element has to be large compared to the particle diameter (Deen et al., 2007). For the example of a top spray granulator the mesh used in the DPM simulations is shown in Fig. 3-3 a). In Fig. 3-3 b) a two-dimensional slice cut out vertically at the center of the mesh is shown for the region around the nozzle tip.

For each mesh cell, the average gas velocity is described by Navier Stokes equation (Eq. 3-4) and the solids volume fraction is calculated according to the scheme explained in section 3.4.3. Turbulence is included using the standard k- ϵ turbulence model. The gas injection by the nozzle is included as a free jet. The nozzle tip is a circular area (diameter 2 mm), where the gas velocity is prescribed by the boundary condition (velocity inlet). The gas volume around the nozzle tip has a refined mesh compared to the rest of the volume of the granulator (see Fig. 3-3 b). Still, this mesh is too coarse in order to achieve a precise description of the turbulent flow phenomena inside the jet (Duangkhamchan et al., 2012).

3.4 Coupling between the gas and particle phases

The continuous gas phase and the discrete particle phase interact with each other through momentum transfer and through the phase volume fractions. The integrated drag force (Eq. 3-1) acting on all particles within a fluid cell is equivalent to the sink term added to the momentum balance (Eq. 3-4). At this point the DPM requires a closure model, since the flow around each particle is not fully resolved. In this work, two different approaches are used for monodisperse and polydisperse systems.

3.4.1 Drag correlation for monodisperse systems

The interphase momentum transfer coefficient β_{g-p} , (see Eq. 3-1 and 3-6) is modeled by combining the Ergun equation (Ergun, 1952) for dense regimes ($\epsilon < 0.8$)

$$\beta_{g-p, Ergun} = \frac{\eta_g}{d_p^2} \left(150 \frac{(1-\epsilon)^2}{\epsilon} + 1.75 (1-\epsilon) \text{Re}_p \right) \quad (3-7)$$

and the correlation proposed by Wen & Yu (1966b) for dilute regimes ($\epsilon \geq 0.8$)

$$\beta_{g-p, Wen\&Yu} = \frac{3}{4} c_D \text{Re}_p \frac{(1-\epsilon)}{\epsilon^{2.65}} \cdot \frac{\eta_g}{d_p^2}, \quad (3-8)$$



$$c_D = \begin{cases} 24 \cdot \left(\frac{1 + 0.15 \text{Re}_p^{0.687}}{\text{Re}_p} \right) & \text{if } \text{Re}_p < 1000 \\ 0.44 & \text{if } \text{Re}_p \geq 1000 \end{cases}, \quad (3-9)$$

where $\text{Re}_p = \varepsilon \rho_g |\mathbf{u}_g - \mathbf{v}_i| d_p / \eta_g$ is the particle Reynolds number and ε is the gas volume fraction. This correlation is simple and efficient and has proven to give reliable results for monodisperse fluidized bed systems (Tsuji et al., 1993; Goldschmidt, 2003; Müller et al., 2008) and also for spouted beds (Takeuchi et al., 2008).

3.4.2 Calculation of the cell porosity

In order to obtain a realistic momentum transfer, it is necessary to calculate for each CFD mesh cell the volume fraction ε_s occupied by the solid. For this purpose, the volume of each particle is approximated by N cubic sample volumes. All sample cubes are checked to determine which mesh cell they lie within. The solid volume fraction ε_s of a particular mesh cell is the ratio of volume of all sample cubes that lie within that mesh cell and the total volume of the cell, as given by:

$$\varepsilon_s = 1 - \varepsilon = \frac{\sum V_{cube}}{V_{cell}} \quad (3-10)$$

Here, V_{cube} is the volume of a sample cube and V_{cell} is the volume of the fluid mesh cell. The number N is chosen in a range of 10-20 as a compromise between accuracy of the porosity calculation and numerical effort.

3.4.3 General algorithm

The general algorithm of the coupled DEM-CFD simulation is illustrated in Fig. 3-4. First, the flow field of the gas phase is resolved by the CFD solver. When a stable solution is obtained, the flow field is passed to the coupling module, where the relative velocity between each particle and the surrounding gas is calculated in order to obtain the drag force. The drag force acting on each particle is then passed to the DEM solver, which will update the particle positions in a loop, until the end of the CFD time step is reached. The new particle positions are handed back to the coupling module, which will then update the fluid cell porosities and calculate the momentum



sink term for each cell. Based on this input, the CFD solver iterates over the next time step until the flow field again converges to a stable solution.

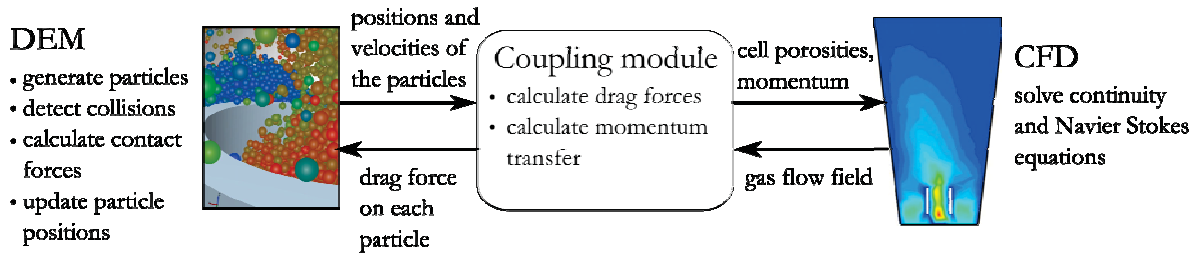


Figure 3-4: Steps in coupling the motion of discrete and continuous phase.

3.5 Model describing particle contacts

In case of a collision between particles or between a particle and the wall, the DPM requires a model to calculate the contact forces. Two approaches regarding the treatment of particle-particle interactions have been established: The hard sphere approach and the soft sphere approach.

- a) In the hard sphere approach the particles are assumed to interact through binary, quasi-instantaneous collisions with point-wise contacts. The particles are perfect, homogeneous spheres and the interaction forces are impulsive and therefore all other finite forces are negligible during the collision. Campbell & Brennen (1985) introduced collision parameters into the hard sphere approach to account for energy dissipation during the collision. The algorithm is event-driven: the simulation is updated each time a collision occurs. Therefore, the hard sphere algorithm is especially efficient for dilute systems where few collisions occur.
- b) In the soft sphere approach the particles are assumed to undergo deformation during their contact. Throughout the duration of a collision contact forces are calculated from a simple mechanical analogue involving a spring, a dash-pot and a slider, which allows for energy dissipation during the contact. An illustration of the mechanical analogue for a particle-particle contact in the contact model of a soft-sphere DPM is shown in Fig. 3-5. Forces acting between the two particles are decomposed into a normal component $\mathbf{F}_{c,n}$ and a tangential component $\mathbf{F}_{c,t}$. In a soft sphere DPM the simulation is always updated after a fixed time step (time-driven algorithm). In case a particle is in contact with several other particles the resulting contact force follows from the addition of all binary contributions.

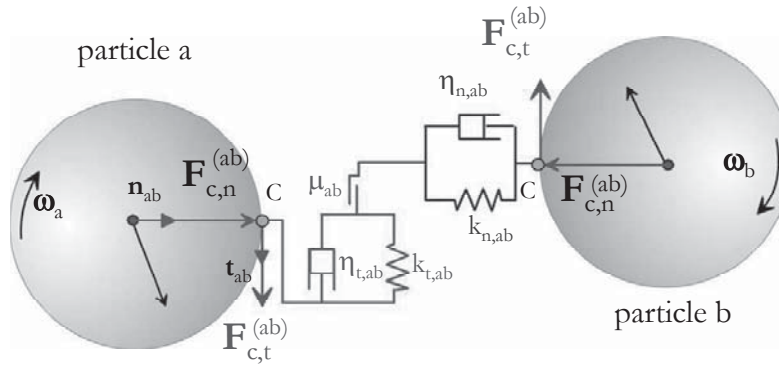


Figure 3-5: Mechanical analogue in normal and tangential direction for a particle-particle contact in a soft-sphere DPM (Antonyuk, 2006).

Both the hard sphere approach and the soft sphere approach have been applied for DPM simulations of fluidized beds by various authors. Yet, due to the resolution of a finite contact time and due to the inclusion of particle deformation, the soft sphere algorithm seems to be more appropriate for systems including non-ideal-elastic particles. For dense fluidized beds it is also numerically more efficient than the hard sphere approach. Therefore, in this work a soft sphere DPM is used. Different approaches for the contact force calculation are reported in the literature, which can be classified in four main groups according to (Kruggel-Emden et al., 2007):

- Continuous potential models (i.e. Aoki & Akiyama, 1995)
- Linear spring-dashpot models (i.e. Cundall & Strack, 1979)
- Non-linear spring-dashpot models (i.e. Tsuji et al., 1992)
- Hysteretic models (i.e. Walton & Braun, 1986)

In this work a non-linear spring-dashpot model is applied based on the theory developed by Hertz (1881) for the normal impact. A no-slip approximation of the model by Mindlin (1949) is used for the tangential component of the contact force, as proposed by Tsuji et al. (1992).

For two colliding spheres a and b with position vectors \mathbf{r}_a and \mathbf{r}_b and radii R_a and R_b (see Fig. 3-6) the relative velocity at the contact point \mathbf{v}_{ab} is defined as follows:

$$\mathbf{v}_{ab} = (\mathbf{v}_a - \mathbf{v}_b) - (R_a \boldsymbol{\omega}_a + R_b \boldsymbol{\omega}_b) \times \mathbf{n}_{ab}. \quad (3-11)$$

Here, \mathbf{n}_{ab} is the unit vector normal to the contact plane. The normal component of the relative velocity $\mathbf{v}_{ab,n}$ is given by Eq. 3-12

$$\mathbf{v}_{ab,n} = (\mathbf{v}_{ab} \cdot \mathbf{n}_{ab}) \mathbf{n}_{ab}. \quad (3-12)$$

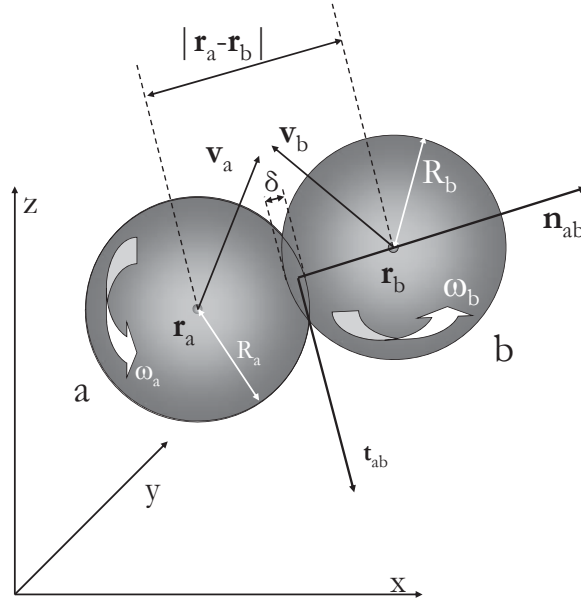


Figure 3-6: Coordinate system used in the description of the collision model (based on Deen et al., 2007).

According to the Hertzian theory, the relation between the elastic force and the displacement is nonlinear, due to the elliptical pressure distribution in the circular contact area

$$\mathbf{F}_{c,n} = -k_n \cdot \delta_n^{3/2} \cdot \mathbf{n}_{ab} - \eta_n \mathbf{v}_{ab,n}. \quad (3-13)$$

In the DEM model, the elastic part of the normal contact force $F_{c,n}$ is represented by a non-linear spring, where the force is proportional to the stiffness k_n and the displacement $\delta_n^{3/2}$ in the contact, i.e. the overlap:

$$\delta_n = R_a + R_b - |\mathbf{r}_b - \mathbf{r}_a|. \quad (3-14)$$

The displacement-related elastic contact stiffness k_n depends on the geometry and the elastic properties of the colliding bodies.

$$k_n = \frac{4}{3} E^* \sqrt{R^*}, \quad (3-15)$$

$$\frac{1}{E^*} = \frac{1-\nu_a^2}{E_a} + \frac{1-\nu_b^2}{E_b}, \quad (3-16)$$

The effective modulus of elasticity E^* of the two contact partners is given by Eq. 3-16, where ν is the Poisson ratio. The median radius R^* of the contact partners is a characteristic radius of the contact surface curvature, as defined in Eq. 1-12.



The elastic contribution of the impact energy, absorbed during the compression, is released during the restitution phase of the impact and leads to the elastic force that separates the contact partners. The absorption of kinetic energy during the impact can be described by a restitution coefficient, as introduced in section 2.4.1.

To account for visco-elastic material properties that cause energy dissipation, a damping factor η_n related to the normal coefficient of restitution e_n is included into the DEM model, as proposed by Tsuji et al. (1992):

$$\eta_n = -2\alpha\sqrt{m^* \cdot k_n} \cdot \delta_n^{1/4}, \quad (3-17)$$

$$\alpha = \begin{cases} \frac{\ln e_n}{\sqrt{\pi^2 + \ln^2 e_n}} & \text{if } 0 < e_n \leq 1 \\ 1 & \text{if } e_n = 0. \end{cases} \quad (3-18)$$

The effective mass m^* of the contact partners is given by Eq. 1-11.

For the tangential component of the contact force a Coulomb-type friction law is used

$$\mathbf{F}_{c,t} = \begin{cases} -k_t \delta_t - \eta_t \mathbf{v}_{ab,t} & \text{if } |\mathbf{F}_{c,t}| \leq \mu |\mathbf{F}_{c,n}| \\ -\mu |\mathbf{F}_{c,n}| \mathbf{t}_{ab} & \text{if } |\mathbf{F}_{c,t}| > \mu |\mathbf{F}_{c,n}| \end{cases}, \quad (3-19)$$

where k_t , δ_t , η_t and μ are the tangential spring stiffness, tangential displacement, tangential damping coefficient and friction coefficient, respectively. The tangential relative velocity $\mathbf{v}_{ab,t}$ is defined by Eq. 3-20:

$$\mathbf{v}_{ab,t} = \mathbf{v}_{ab} - \mathbf{v}_{ab,n}. \quad (3-20)$$

The tangential stiffness k_t depends on the normal displacement δ_n

$$k_t = 8G^* \sqrt{R^* \delta_n}, \quad (3-21)$$

where G^* is the equivalent shear modulus of the contact partners:

$$\frac{1}{G^*} = \frac{2 - \nu_a}{G_a} + \frac{2 - \nu_b}{G_b}. \quad (3-22)$$

The tangential damping coefficient η_t is defined according to Eq. 3-23 (Tsuji et al., 1992):

$$\eta_t = 2\alpha\sqrt{m^* \cdot k_t}. \quad (3-23)$$



As an example of the contact force calculation throughout the duration of a collision, the force-displacement curve obtained using the contact model presented in this section is presented in Fig. 3-7 for a particle-wall impact scenario.

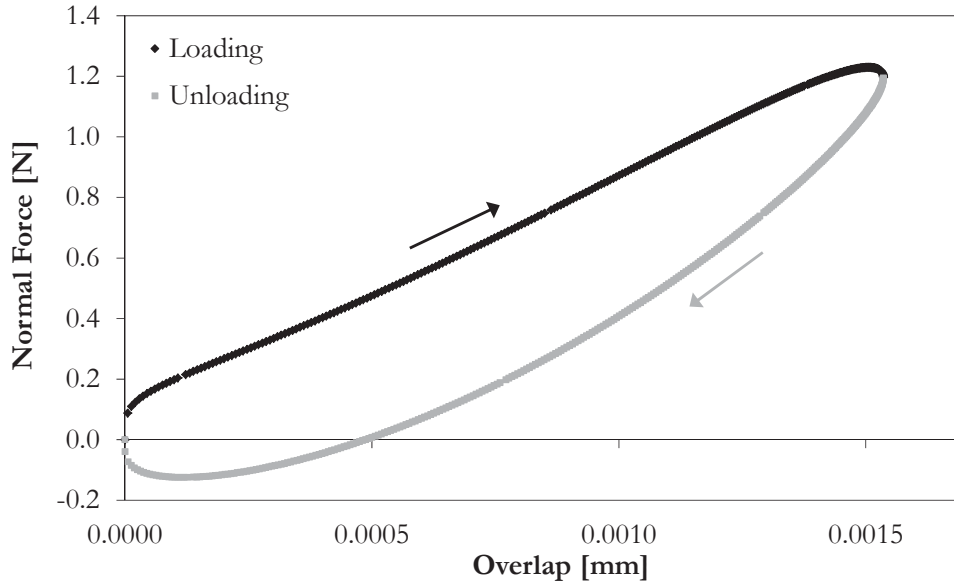


Figure 3-7: Force-displacement curve obtained using the contact model proposed by Tsuji et al. (1992). Simulation parameters: $e = 0.8$, $v_0 = 0.78$ m/s, $E^* = 2.1 \cdot 10^{10}$ Pa, $R^* = 5 \cdot 10^{-4}$ m, $d_p = 1$ mm, $\rho_p = 1500$ kg/m³.

Due to the damping factor η_n , the loading and unloading curves follow different paths. As a function of the overlap, the contact force is calculated as a combination of a repulsive elastic force and an adhesive viscous force. During the last phase of the collision (overlap < 0.0005 mm), the viscous contribution is larger than the elastic part, which results in a negative (= adhesive) contact force, even though the particles still overlap. In the current example the restitution coefficient e was set to 0.8, i.e. the rebound velocity equals 0.8 times the impact velocity. Fig. 3-7 illustrates very well how this deceleration is achieved with the help of the viscous damping part of the contact model.

3.6 Definition of a collision

According to the soft-sphere approach two colliding particles come into contact at time t_0 ; they overlap for a certain collision duration Δt_{coll} and separate again at time t_1 . The whole event is counted as one collision, regardless of how long the particles stay in contact. If more than two particles collide simultaneously, then the separation of each pair is registered as one collision. Therefore, collisions are always pairwise: Multi-body contacts are counted as multiple collisions.



Data such as the normal and tangential forces, which are acting throughout the collision duration, as defined by the contact model, the overlap and the total energy dissipation is collected. As the whole algorithm is time-driven, the resolution of the collision detection scheme is limited by the simulation time step Δt . The different steps during a collision are illustrated in Fig. 3-8.

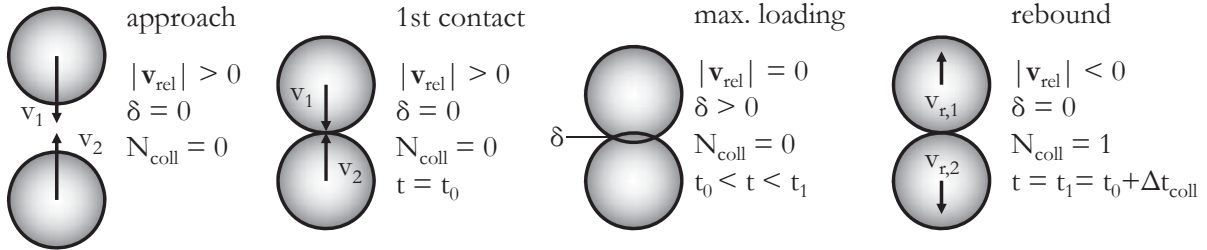


Figure 3-8: Schematic course of a collision.

In the literature some attempts can be found to measure or to model the collision frequency in fluidized beds. According to the model by Martin (1980), the collision frequency f_c depends on the mean free path λ_p and the mean fluctuation velocity c of the particles in the fluidized bed:

$$\lambda_p = \frac{1}{\sqrt{2\pi}d_p^2 n_v} = \frac{d_p}{6\sqrt{2}(1-\varepsilon_{mf})} \cdot \frac{\varepsilon - \varepsilon_{mf}}{1-\varepsilon}, \quad (3-24)$$

$$c = \sqrt{\frac{g \cdot d_p}{5(1-\varepsilon_{mf})} \cdot \frac{\varepsilon - \varepsilon_{mf}}{1-\varepsilon}}, \quad (3-25)$$

$$f_c = \frac{c}{\lambda_p}. \quad (3-26)$$

The mean particle fluctuation velocity is a function of the porosity ε of the fluidized bed and the porosity ε_{mf} in the state of minimum fluidization. According to the kinetic theory of granular flow (KTGF) a dispersed solid phase is pictured as a collection of spheres in chaotic motion, as shown in Fig. 3-9. Arrows indicate the direction of motion of the particles

According to Gidaspow (1994) the collision frequency can be described in analogy with dense gas kinetic theory, using the kinetic theory of granular flow (KTGF). For a mixture of particles of uniform size f_c can be written according to Eq. 3-27:

$$f_c = \frac{12(1-\varepsilon)g_0}{\sqrt{\pi}d_p} \cdot \sqrt{\theta}. \quad (3-27)$$



In this relation, g_0 denotes the radial distribution function

$$g_0 = \left[1 - \left(\frac{1 - \varepsilon}{1 - \varepsilon_{mf}} \right)^{1/3} \right]^{-1}, \quad (3-28)$$

and θ is referred to as the granular temperature. It is defined as one third of the mean square particle velocity fluctuation c

$$\theta = \frac{1}{3} \langle \mathbf{c}^2 \rangle. \quad (3-29)$$

A conservation equation of the granular temperature can be derived from the kinetic theory (van Wachem et al., 2001). Since in DEM simulations the instantaneous particle velocities, their locally averaged values as well as the fluctuations are known, the granular temperature can be calculated directly from the simulation data.

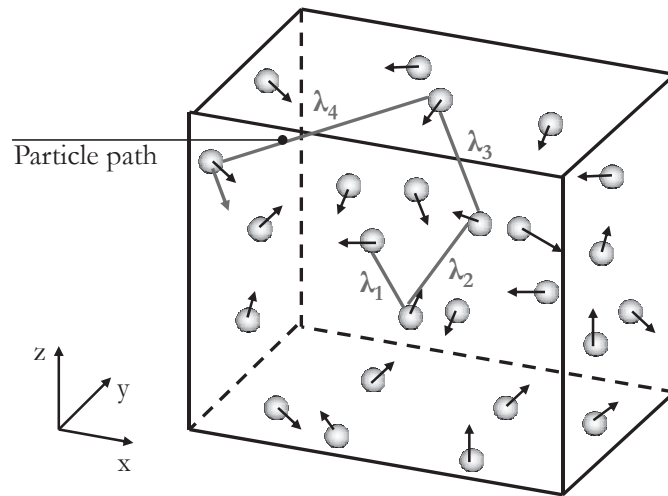


Figure 3-9: Representation of a dispersed solid phase according to KTFG.

Buffière & Moletta (2000) measured the collision frequency in an inverse three-phase fluidized bed with the help of a high-frequency-response hydrophone for different fluidization gas velocities. Unfortunately their data is related to the active surface area of the detector. Information about particle-particle collisions must be transmitted through the fluid and might only be captured in the vicinity of the transducer. Therefore, a comparison with results from a different fluidized bed setup is difficult.



3.7 Wet particle interactions

If a liquid film is present between two solid particles, viscous forces must be overcome to move the particles towards each other or away from each other. During the approach the liquid must be squeezed out as the separation distance between the particles becomes smaller. During rebound the liquid has to flow back into the gap which is opened between the particles. Therefore, the energy needed for the displacement of the liquid contributes to the dissipation of kinetic energy during collisions of surface-wet particles. In the DPM this viscous dissipation is included as an additional term in the force balance (Eq. 3-1).

An overview of different viscous force models was given in Table 1-1. For particle-particle and particle-wall impacts involving surface-wet particles the well-established correlation of Cameron (1981) is used in this work for the normal force contribution, as an improved accuracy of correlations taking into account the volume of the liquid bridge was not revealed for dynamic impact situations.

For the tangential force contribution the relation proposed by Popov (2010) is applied, which offers a simple closed formulation describing parallel particle motion in a fluid. The normal and tangential components of the viscous force \mathbf{F}_{vis} are given by:

$$\mathbf{F}_{vis,n} = -6 \frac{\pi \eta_{liq} R^{*2}}{D} \mathbf{v}_{rel,n} \quad (3-30)$$

$$\mathbf{F}_{vis,t} = -2\pi\eta R \cdot \mathbf{v}_{rel,t} \cdot \ln\left(1 + \frac{R}{2D}\right) \quad (3-31)$$

Here, η_{liq} denotes the dynamic viscosity of the liquid, R^* the reduced particle radius (see Eq. 1-12) of the impacting particles and D the initial thickness of the liquid film.

The normal and tangential components of the relative velocity are marked as $\mathbf{v}_{rel,n}$ and $\mathbf{v}_{rel,t}$, respectively. Antonyuk et al. (2009) found good agreement between experimental results for the energy dissipation during the impact of spherical particles on a liquid film and the model predictions using Eq. 3-30 and 3-31. Both the normal and the tangential viscous force are plotted in Fig. 3-10 as a function of the viscosity of the liquid η_{liq} (a) and of the separation distance D (b). The adhesive viscous force increases linearly with increasing viscosity and exponentially with reduced separation distance.

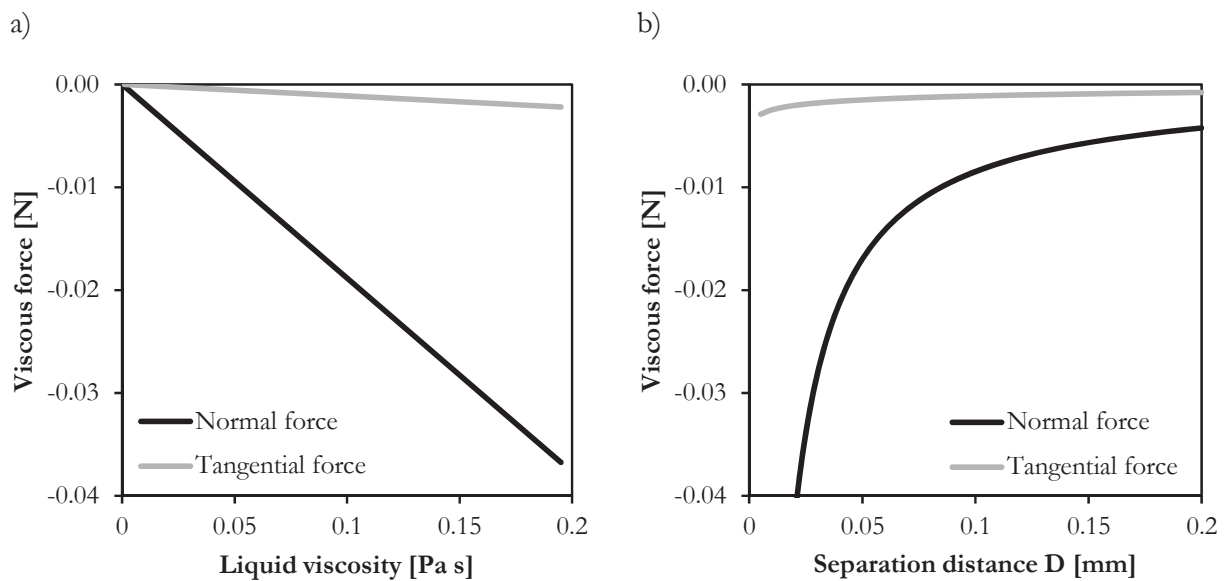


Figure 3-10: Normal and tangential component of the viscous force according to Eq. 3-30 and 3-31, with $R^* = 0.1$ mm, $v_{rel} = 1$ m/s, as a function of the liquid viscosity (a) at $D = 0.1$ mm. Viscous force as a function of the separation distance (b) at $\eta_{liq} = 0.05$ Pa s.

3.8 Multi scale modeling framework

Generally, process descriptions using a theoretical model are available on different scales with a different level of detail. In the application of a model the focus of interest is usually on the macroscopic scale, where predictions can, for example, be made on the flow rate or the concentration of the product. For solids processes like fluidized bed agglomeration such a macroscopic process description can be achieved using population balance equations. Due to the complexity of the modeled processes and due to the coarse resolution, macroscopic models are mostly of empirical or semi-empirical nature. They require input parameters, which need to be determined experimentally or may be deduced from a closure model. For the fluid bed agglomeration process, input parameters for a population balance model are for example the aggregation and breakage rates. The advantage of macroscopic models is their low computational effort and the practical relevance of the results that can describe directly the behaviour of a process on full industrial scale. On the other hand, the model is usually only descriptive near the point of operation that it was calibrated to. Predictions for other states of the process or even for other material systems are normally very difficult. In the case of variable process conditions a more detailed model is required. Micro-scale models are capable to describe the fundamental mechanisms that govern the process better and therefore they require less input parameters.

Since the relevant influences are described intrinsically by the model equations, a micro scale model can be predictive also in conditions other than a defined setpoint of the model. For solids processes, the presented DPM is an adequate tool on the micro scale. Unfortunately the numerical effort increases exponentially with the level of detail of the process description. Therefore, micro-scale models are unable to represent a production process at full scale, at least with the computing power available today.

In the framework of a multi scale modeling scheme it is theoretically and practically attractive to employ DPM for the derivation of physically based expressions for aggregation and breakage kernels of a population balance model representing the agglomeration process on a macroscopic scale. This approach is both elegant and efficient, since it avoids time-consuming computations in areas where the full level of detail is not necessary and it allows a more precise and more predictive physically-based process description. The concept of a multi scale modeling framework for fluidized bed systems was recently proposed by Van der Hoef et al. (2004), Van den Akker (2010) and Werther et al. (2011). A possible approach for a multi scale model describing the fluidized bed agglomeration process is outlined in this section. The different stages of the model and the inter-scale connections are shown in Fig. 3-10.

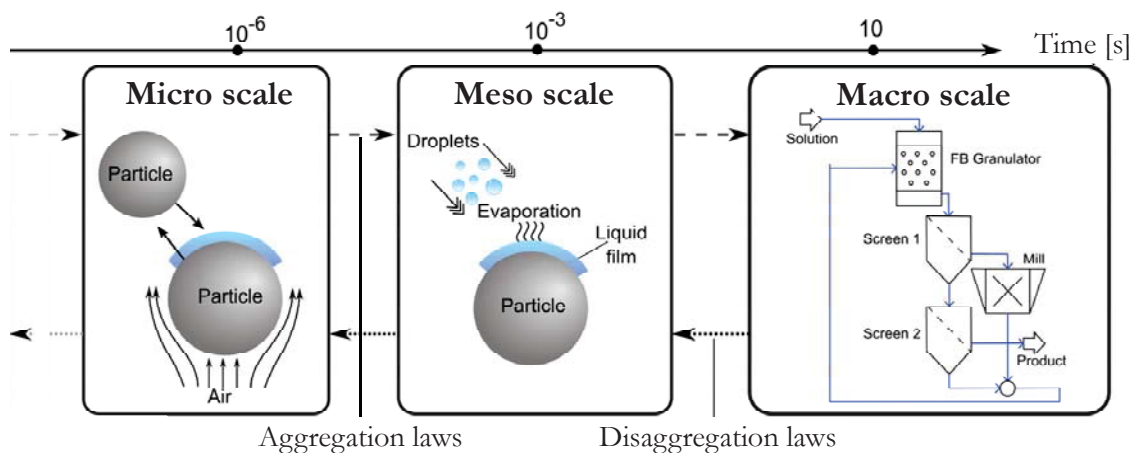


Figure 3-11: Structure of a multi scale model for fluidized bed agglomeration (based on Werther et al., 2011).

3.8.1 The micro scale

For lab-scale equipment geometry DPM simulations are performed for a short representative time interval (in the order of 10 seconds) to describe the fluid, particle and collision dynamics. Special attention is paid to the spray zone, where liquid droplets are injected into the system. Particle wetting can be described with the help of a discrete model of the cone-shaped spray



zone, which defines the amount of liquid deposited on each particle. Palzer (2000) described particle wetting in a rotating drum granulator using a discretized spray zone model. Kafui & Thornton (2008) applied this approach to a DPM simulation of a fluidized bed. The liquid deposited on a particle is assumed to form a film of constant thickness on the surface. Therefore, the moisture content can be expressed as the surface fraction covered by a liquid film. For further collisions the wetted surface fraction defines a probability whether the contact takes place at a wet or a dry spot. Wet collisions include additional energy dissipation according to Eq. 3-30 and 3-31.

To determine the adhesion rate, a sticking criterion is defined. If the initial kinetic energy of two particles involved in a collision is smaller than the sum of the plastic and viscous energy dissipation, they will coalesce. After an agglomeration event the primary particles are still tracked as two individual particles bound together by viscous adhesion forces. Therefore, further collisions with other particles or with the equipment walls will break the agglomerate structure, if the adhesion force is overcome. The sum of both the adhesion and breakage rates is defined as coalescence efficiency Ψ_{ij} . It is recorded as a function of the size of the involved primary particles.

Particle trajectories for the simulated reference time interval as well as the profile of the relative velocity between the particles and the gas are saved and transferred to the meso scale simulation.

3.8.2 The meso scale

Heat and mass transfer between the particles and the surrounding gas phase is difficult to include into the micro-scale simulation due to the longer time constants of the processes involved. While the particle dynamics can reach a steady state within few seconds of simulation time, it takes several minutes to reach the equilibrium regarding heat and mass transfer in a fluidized bed with liquid injection. Therefore, on the meso scale the representative particle trajectories obtained with the DPM are repeated in a loop to extrapolate the particle dynamics to longer time scales, relevant for heat and mass transfer. Also the profile of the relative velocities between gas and particles, which is used to calculate the heat and mass transfer coefficients, is obtained from the DPM simulations. Since they are exposed to the fluidization air flow, wet particles in the granulator are dried. By applying heat and mass transfer laws, the temperature and moisture content of each individual particle can be calculated, as presented in Werther et al. (2011). Local



heat and mass transfer coefficients are modeled according to Gnielinski (1980) using the relative velocity between the individual particle and the gas phase provided by the DPM simulation.

3.8.3 The macro scale

A one-dimensional population balance equation for a batch agglomeration process (no inlet and outlet streams, no nucleation, no breakage), using the particle diameter as internal coordinate, is given in Eq. 3-32.

$$\frac{\partial n(t, v)}{\partial t} = B_{agg}(t, v) - D_{agg}(t, v) \quad (3-32)$$

The number of particles n with size v changes due to the formation of agglomerates in this size interval (Birth) and due to loss of particles that are integrated in agglomerates in other size fractions (Death). The birth term B_{agg} and the death term D_{agg} are given by

$$B_{agg}(t, v) = \frac{1}{2N_{tot}(t)} \int_0^v \beta(t, v-u, u) \cdot n(t, u) \cdot n(t, v-u) du, \quad (3-33)$$

$$D_{agg}(t, v) = \frac{1}{N_{tot}(t)} \int_0^\infty \beta(t, v, u) \cdot n(t, u) \cdot n(t, v) du. \quad (3-34)$$

Here, N_{tot} is the total number of particles and β denotes the aggregation kernel, which is typically written as the product of a size-independent rate constant β_0 and a size dependent term β^* . An overview of different approaches for the aggregation kernel is given for example in Gantt et al. (2006) or Hampel (2010). The kernel defines the aggregation velocity of two particles with size u and $v-u$ to form an agglomerate of size v . This probability of aggregation of two particles can be extracted from the micro scale simulation, as proposed by Gantt et al. (2006). For this purpose the kernel should be written as the product of a collision rate f_c and the coalescence efficiency φ_A (Tan et al., 2004)

$$\beta_{ij} = f_c \cdot \varphi_A. \quad (3-35)$$

Both parameters are directly obtained from the micro scale simulation. For a relevant process time (in the order of 1 hour), the evolution of the particles size distribution in the fluid bed agglomerator is calculated. Growth has a strong influence on both the particle dynamics and the heat and mass transfer in a fluidized bed. Therefore, the updated particle size distribution is sent back to the DPM in order to perform a second iteration of the micro scale simulation. New



trajectories and collision frequencies may occur, which alter the results also on the meso and macro scale. The whole scheme is iterated, until the product size distribution converges to a constant result.



4 Material characterization for model parameters

In this chapter experimental results regarding the mechanical material characterization are presented. The mechanical behaviour of a material influences the contact mechanisms between particles and is governed by its supra-molecular structure. Two basic structures can be distinguished: amorphous and crystalline materials. While crystals consist of highly ordered molecular lattices, the molecules of amorphous substances are arranged statistically in a liquid-like manner. A heterogeneous mixture of different ingredients and the presence of polymer components prevent the formation of ordered molecular arrangements. Therefore, many food powders like vegetable and fruit powders, various sugars, milk, whey, meat and fish powders, protein hydrolysates, gluten, starch and flour contain high amounts of amorphous solids. Palzer (2005) gives a profound overview on the behaviour of amorphous food powders with respect to agglomeration processes. In this work spray-dried maltodextrin DE 21 (Glucidex 21, Roquette SA, France) made from wheat is used as model substance, since it can model the behaviour of other food powders that are processed in their amorphous state (Loret et al., 2004). Therefore, at first an introduction is given to the glass transition of maltodextrin DE 21. After that, results for the coefficient of restitution, the modulus of elasticity and the friction coefficient are presented, since they are required input parameters of the DPM. In order to achieve a realistic representation of the particle-particle interaction using the model, the knowledge of the mechanical material properties is essential.

4.1 Glass transition of amorphous maltodextrin

The mechanical properties of amorphous water-soluble food powders vary largely with temperature and moisture content. This is due to the 2nd order transition from the brittle glassy state to the rubbery state, which is introduced in this section.

The mobility of the molecules within an amorphous matrix increases with increasing temperature. Thus, the previously rigid glass-like substance is becoming first rubbery and later viscous-plastic.



During this transition the liquid-like (viscous) properties are more and more dominating over the solid-like (elastic) texture components (Ferry, 1980). This change is called the “glass transition”. The glass transition temperature can be measured as a function of the moisture content using differential scanning calorimetry (DSC). In this work the onset of glass transition is referred to as the glass transition temperature T_g .

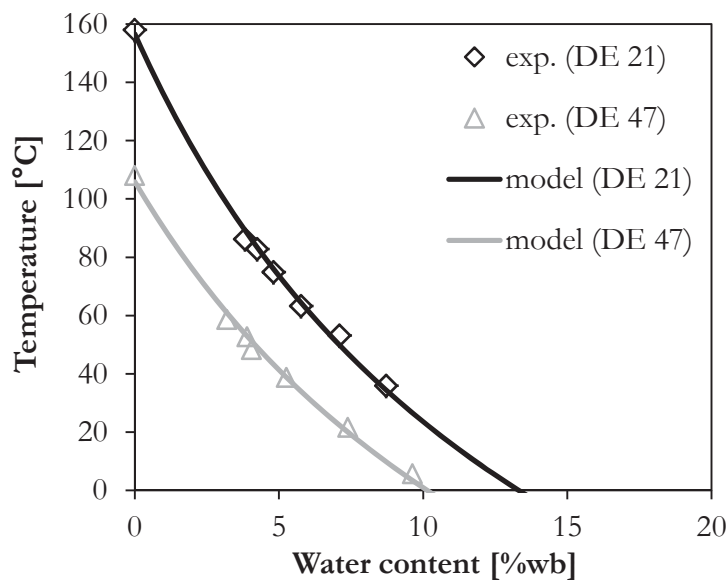


Figure 4-1: Glass transition temperature of maltodextrin (DE 21 and DE 47) as a function of the moisture content (Haider, 2010).

It can be seen in Fig. 4-1 that the glass transition temperatures of maltodextrin DE 21 and DE 47 decrease with increasing moisture content. The symbols refer to measurements by Palzer (2005) and the continuous line was calculated using the model by Gordon and Taylor (1952). Their approach for the glass transition temperature of a binary mixture is given in Eq. 4-1, where w denotes the wet based water content and k is the Gordon&Taylor constant, which is determined experimentally (Palzer, 2009).

$$T_g = \frac{w \cdot T_{g,w} + k \cdot (1-w) \cdot T_{g,s}}{w + k(1-w)} \quad (4-1)$$

The calculation was done with the glass transition temperature $T_{g,w} = -135^\circ\text{C}$ for pure water and $T_{g,s} = 157^\circ\text{C}$ for dry maltodextrin DE 21 (106°C for DE 47). The constant k was set to 7.5 for DE 21 maltodextrin and 7.0 for DE 47 maltodextrin according to the experimental data shown in Fig. 4-1.

In the glassy state amorphous substances react more elastically, while exposed to any stress. Due to glass transition, the viscosity decreases from 10^{12} Pas to 10^8 – 10^9 Pa s (Sperling, 1986). Above T_g the material starts to flow under applied stress and behaves more like a viscous liquid than like a solid. For this reason, the mechanical parameters described in this chapter will always be given as a function of $T-T_g$, where T denotes the temperature at which the measurements were performed.

4.2 Coefficient of restitution

The coefficient of restitution was determined as a function of the impact velocity and of the moisture content with the help of free fall tests, as described in section 2.4.1. Both agglomerates from the fluid bed agglomeration process and dense spherical beads were tested. Furthermore, the material of the target plate was varied in order to describe particle-wall interactions (impact on a steel plate) and particle-particle interactions (impact on a dense maltodextrin body). Wet particle interactions were investigated via impacts on a steel plate covered by a thin liquid film.

4.2.1 Free-fall tests with agglomerates

In order to describe the energy dissipation that occurs during impact, sample agglomerates taken from the fluidized bed were analyzed using the free-fall tester. The impact of one representative maltodextrin agglomerate onto a steel plate is illustrated in Fig. 4-2.

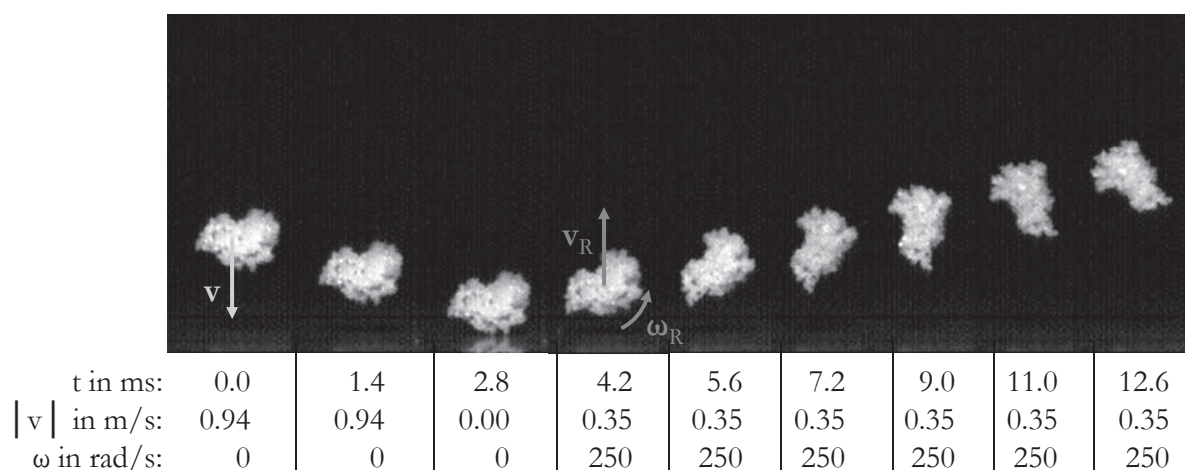


Figure 4-2: High-speed photographs of the impact of a maltodextrin agglomerate onto a steel plate (v : impact velocity, v_R : rebound velocity, ω_R : angular rebound velocity).



For the analysis agglomerates in a diameter range from 1.4 -2.0 mm of two different samples taken out after 5 min and after 30 min of liquid injection time were dried in a lab oven up to a residual moisture content of 3 % (wb). The tested agglomerates are therefore in the glassy state ($T-T_g = -80$ K).

The obtained restitution coefficient is shown as a function of the impact velocity in Fig. 4-3 for two different liquid injection durations. 100 repetitions were performed for each test scenario. It can be seen that the restitution coefficient increases with increasing injection time due to coefficient with increasing impact velocity can be observed, but the differences are not significant. Generally, the standard deviation of the results, which is indicated by the error bars in Fig. 4-3, is very high.

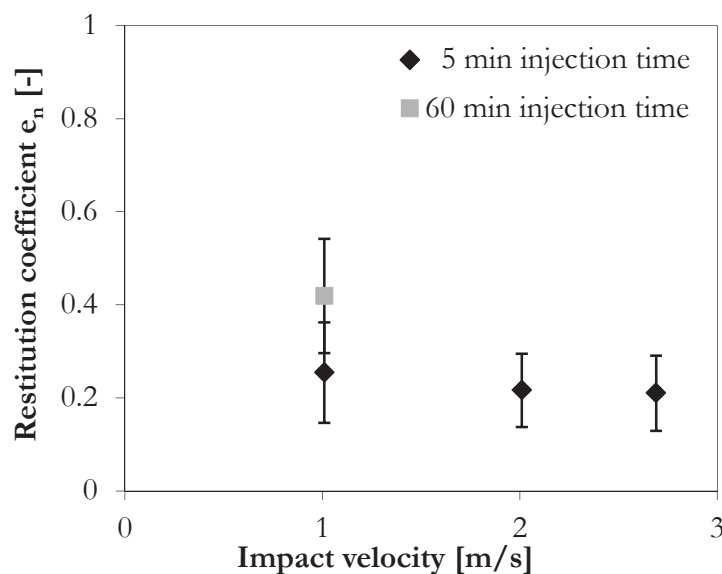


Figure 4-3: Restitution coefficient of maltodextrin agglomerates impacting on a steel plate.

Due to the intrinsically heterogeneous agglomerate structure each impact is different. Some branched agglomerates are partially disrupted during impact, some hit the target plate twice at different positions or rebound at very high rotational velocity. Therefore, the measured restitution coefficient is strongly influenced by the irregular shape of the agglomerates. The measured result is lower than the restitution of a spherical particle, where only plastic deformation is a significant source of energy dissipation. To describe the restitution coefficient as a material property of maltodextrin, free fall tests with agglomerates are therefore less suitable.



4.2.2 Free-fall tests with spherical beads

Dense spherical beads (1-2 mm in diameter) were produced to improve the reproducibility of the impact events and to eliminate the influence of the particle shape on the restitution coefficient. The beads can be seen as enlarged primary particles (see Fig. 4-4). They were equilibrated at different moisture content and tested on two different target plates: a metal plate and a dense maltodextrin body.

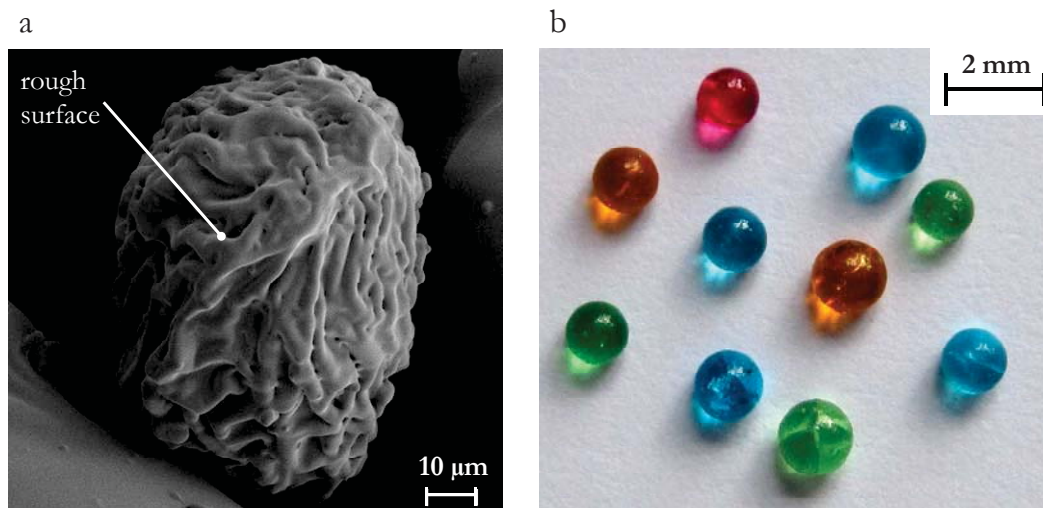


Figure 4-4: SEM picture of a maltodextrin DE21 primary particle at 1000x magnification (a) and dense spherical maltodextrin beads (b).

In Fig. 4-5 the restitution coefficient is shown as a function of the moisture content of the bead, which is expressed as the difference of the temperature T during test and the glass transition temperature T_g . For two different impact velocities the restitution coefficient is presented for the interaction between maltodextrin beads and a steel plate (Fig. 4-5 a) and between the beads and a maltodextrin body of equal moisture content. 700 repetitions were performed for each impact scenario. The error bars in Fig. 4-5 indicate the standard deviation of the results.

For the impact on a steel plate (Fig. 4-5) maltodextrin shows elastic-plastic material behaviour ($e = 0.8$). Both the impact velocity and the moisture content do not significantly affect the restitution coefficient within the investigated range, which is in the glassy state of the beads. It is expected that the restitution coefficient will decrease substantially above the glass transition temperature. Tests with beads above T_g were not successful so far, as the beads do not maintain their spherical shape during the equilibration. For the impact on a maltodextrin plate (Fig. 4-5) a restitution coefficient of approximately 0.65 was found in the experiments. A slightly decreasing tendency with increasing moisture content can be seen, while the impact velocity is not



significantly influencing the results. The results shown in Fig. 4-5 can directly be used as input parameters in a DEM contact model for the impact of dry maltodextrin particles against a wall ($e = 0.8$) or against other maltodextrin particles ($e = 0.65$).

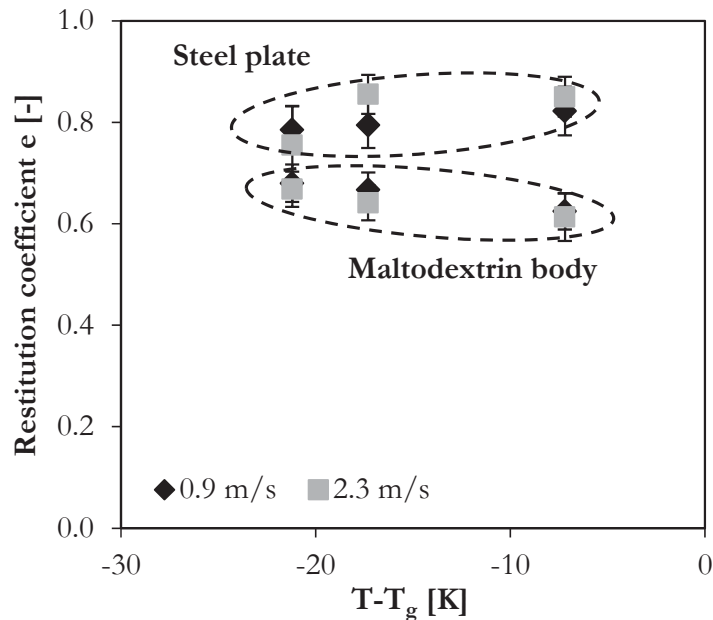


Figure 4-5: Restitution coefficient of glassy maltodextrin beads as a function of their moisture content for two different impact velocities (5 cm and 30 cm falling height). Impact on a steel plate and impact on a maltodextrin plate of equal moisture content.

4.2.3 Viscous energy dissipation in a liquid film

The impact of maltodextrin beads on a steel plate covered by a liquid film was investigated to describe the influence of viscous forces on the energy dissipation. In Fig. 4-6 the measured restitution coefficient is compared for two scenarios: the impact on a dry steel plate and on a steel plate covered by a thin water film (thickness $h = 300 \mu\text{m}$, viscosity $\eta = 10^{-3} \text{ Pa}\cdot\text{s}$, $T = 20^\circ\text{C}$). Obviously the additional energy dissipation in the liquid film leads to a reduction of the rebound velocity of almost 50% for the investigated case. For the wet impact scenario the error bars are larger due to the smaller number of repetitions (75) per experiment and due to small variations of the liquid film thickness. No significant differences are observed for the influence of the moisture content on the restitution coefficient in the glassy state of the maltodextrin beads.

According to Eq. 3-32 the viscous energy dissipation in the liquid film is a function of the fluid viscosity and of the impact velocity, but it is independent of the material properties of the solid



particle. Therefore it is suggested not to combine the plastic contact deformation and the viscous dissipation in a “wet” restitution coefficient. The two mechanisms should be kept separate.

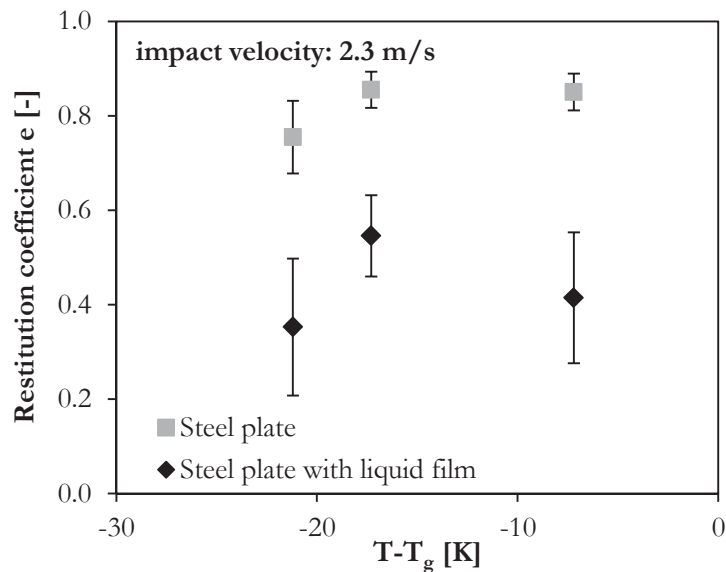


Figure 4-6: Restitution coefficient of glassy maltodextrin beads for dry and wet impact on a steel plate at 2.3 m/s impact velocity.

4.3 Modulus of elasticity

Three-point bending tests with dense homogeneous maltodextrin bars (DE 21 and DE 47) have been performed at the Nestlé Research Center in Lausanne in the framework of another project. For both materials the short-time modulus of elasticity was obtained as introduced in section 2.4.2 using maltodextrin bars equilibrated at different moisture content. The results are shown in Fig. 4-7. For glassy bars made of maltodextrin DE 21 a value of approximately 1 GPa is found (3 GPa for DE 47), which decreases continuously with increasing moisture content. At $T = T_g$ 0.7 GPa are measured (2 GPa for DE 47), at $T = T_g + 10$ K approximately 0.5 GPa are measured (1 GPa for DE 47).

For dry maltodextrin DE 21 particles a value of 1 GPa is therefore used as input parameter for the modulus of elasticity in the DPM.

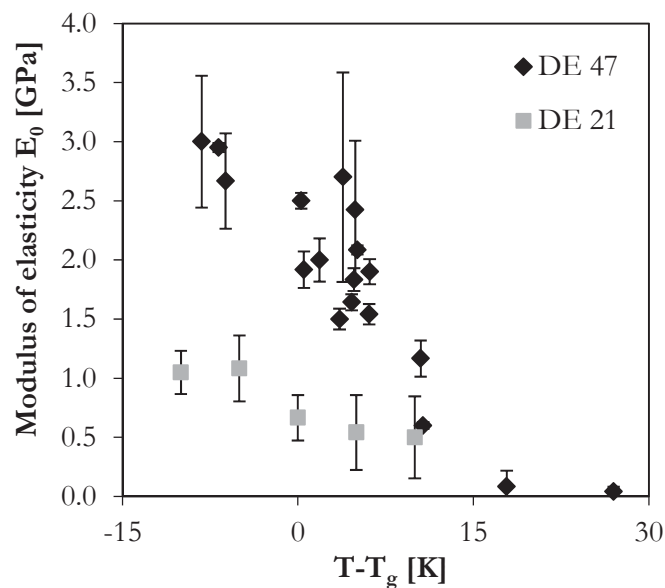


Figure 4-7: Short-time modulus of elasticity E_0 of maltodextrin DE 21 and DE 47 as a function of the moisture content, expressed as difference between the test temperature T and the glass transition temperature T_g of the sample (Haider, 2010).

4.4 Friction coefficient

Shear tests were performed with different fractions of the agglomerates produced in the spouted bed to investigate the influence of the process conditions on the flow behaviour of the agglomerates. Test setup and experimental procedure are presented in section 2.4.3. All agglomerate samples were dried to 4% moisture content (wet based) before the test. The pre-consolidation was performed at a normal stress of 9 kPa, which results in a density of the probe in the shear cell of 450 kg/m³. The second step of the consolidation was performed at 6.9 kPa. A representative yield locus curve is shown in Fig. 4-8. For the coefficient of inner friction μ_i a value of 0.9 is found for primary particles and 1.2 for agglomerates. For wall friction a value of 0.5 is found. These values are used as input parameters in the DPM simulations.

The results regarding the influence of particle size, process time and process temperature on the flow behaviour of maltodextrin agglomerates are summarized in Table 4-1.

At constant process temperature and particle size the cohesion of maltodextrin agglomerates is reduced with increasing injection time. This effect is expected due to consolidation of the agglomerates in the fluidized bed, which leads to a more compact and dense particle structure. A clear trend can also be seen regarding the influence of process temperature: At higher



temperature the cohesion is reduced. This effect can be related to the higher drying rate at high process temperature which limits the agglomeration probability in the fluidized bed and favours the formation of compact structures.

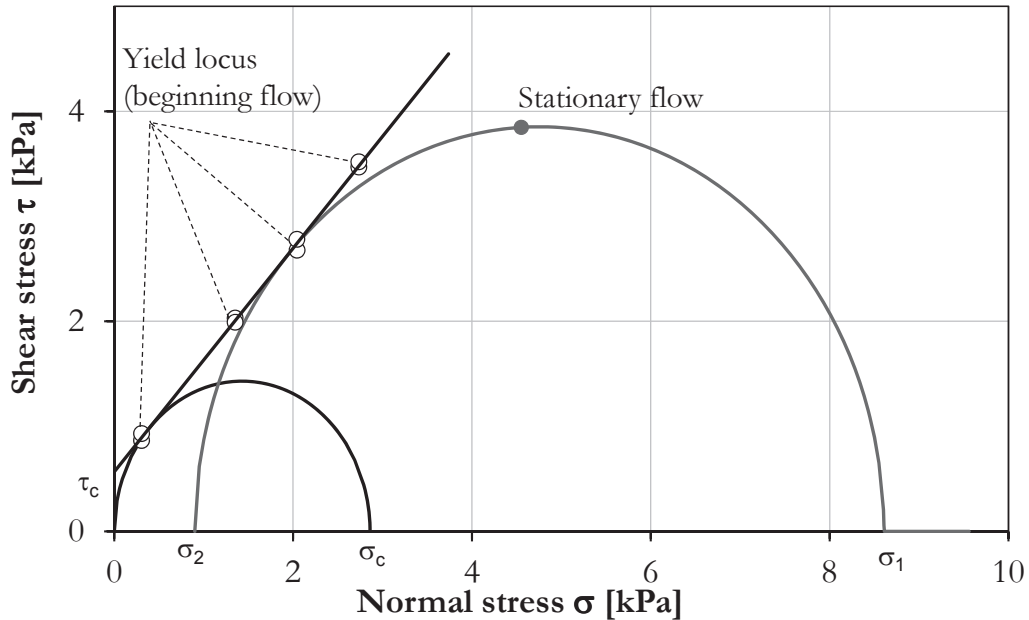


Figure 4-8: Yield locus for internal particle friction, measured with a Jenike shear cell for maltodextrin DE 21 agglomerates (moisture content: 4 % (wet based), mean particle diameter: 0.6 mm).

Table 4-1: Flow behaviour of maltodextrin DE21 agglomerates as a function of the process conditions measured via shear tests.

No.	Size fraction [mm]	Injection time [min]	Process temperature [°C]	Cohesion τ_c [kPa]	Inner friction coefficient μ [-]
1	0.01-0.2	0	-	0.82	0.90
2	0.25-0.8	5	50	0.96	1.27
3	0.25-0.8	30	50	0.66	1.25
4	0.25-0.8	60	50	0.51	1.22
5	0.8-1.25	60	50	0.77	1.33
6	1.25-2.0	60	50	0.93	1.31
7	0.25-0.8	30	70	0.55	1.13
8	0.25-0.8	30	90	0.30	1.10



Some unexpected effects are seen regarding the influence of particle size on the flow behaviour. The general purpose of the agglomeration process is to improve the flowability of the product, which is clearly achieved in this case, comparing the results for the primary powder and the smaller agglomerate fractions. Yet, with increasing agglomerate size the cohesion increases. This is probably related to the irregular shape of the agglomerates with large pores and branches structures, which hinders the free flow of the particles. It must be said additionally that the Jenike shear cell is designed to test the flowability of powders rather than agglomerates, which might affect the results obtained for the largest agglomerate fraction ($d_p > 1.25$ mm).



5 Characterization of a Wurster-coater

5.1 Introduction

Although micro scale processes in granulation determine the entire process dynamics including growth rate and structuration of the product, a detailed understanding on the influence of material and process parameters on the particle interactions in a fluidized bed granulator is still missing today. Therefore, a detailed simulation study was performed using the Discrete Particle Model. For the example of a Wurster-coater the sensitivity of mechanical material properties as well as the influence of various process parameters on the particle and collision dynamics are presented in this chapter. Combined with experimental results for the agglomeration of amorphous maltodextrin in a Wurster-coater with identical geometry, the predictions from the computational model can be correlated with measured properties of the product agglomerates.

This chapter is organized as follows: At first, the applied simulation conditions are introduced in section 5.1. In section 5.2 a simulation case study is presented regarding the sensitivity of material parameters, which are based on the measured material properties of glassy maltodextrin agglomerates (DE 21), on the particle and collision dynamics. Experimental results for the influence of process parameters on the agglomeration behaviour of amorphous maltodextrin are presented in section 5.3. An optimal set of process parameters is compiled for the agglomeration of maltodextrin in a Wurster-coater as a compromise between fast growth and process stability. Finally, in section 5.4 the DPM is extended by a description of the interaction between surface-wet particles based on additional viscous energy dissipation. The influence of viscous forces on the particle and collision dynamics is investigated for the example of a Wurster-coater.



5.2 Simulation conditions

Simulations were performed using the commercial simulation software EDEM 2.3 (DEM Solutions Ltd.) coupled with the software Fluent 12 (ANSYS Inc.) to describe the particle and fluid dynamics in a fluid bed granulator. The geometry of the GF3-insert with bottom-spray injection nozzle and Wurster tube (Fig. 2-4 b) was supplied by Glatt Ingenieurtechnik GmbH, Weimar, Germany and slightly simplified for the DPM simulations (Fig. 5-1 a). The gas flow profile is resolved on a mesh consisting of 12000 tetrahedral cells, as shown in Fig. 5-1 b. For each cell, the volume-averaged gas velocity is calculated.

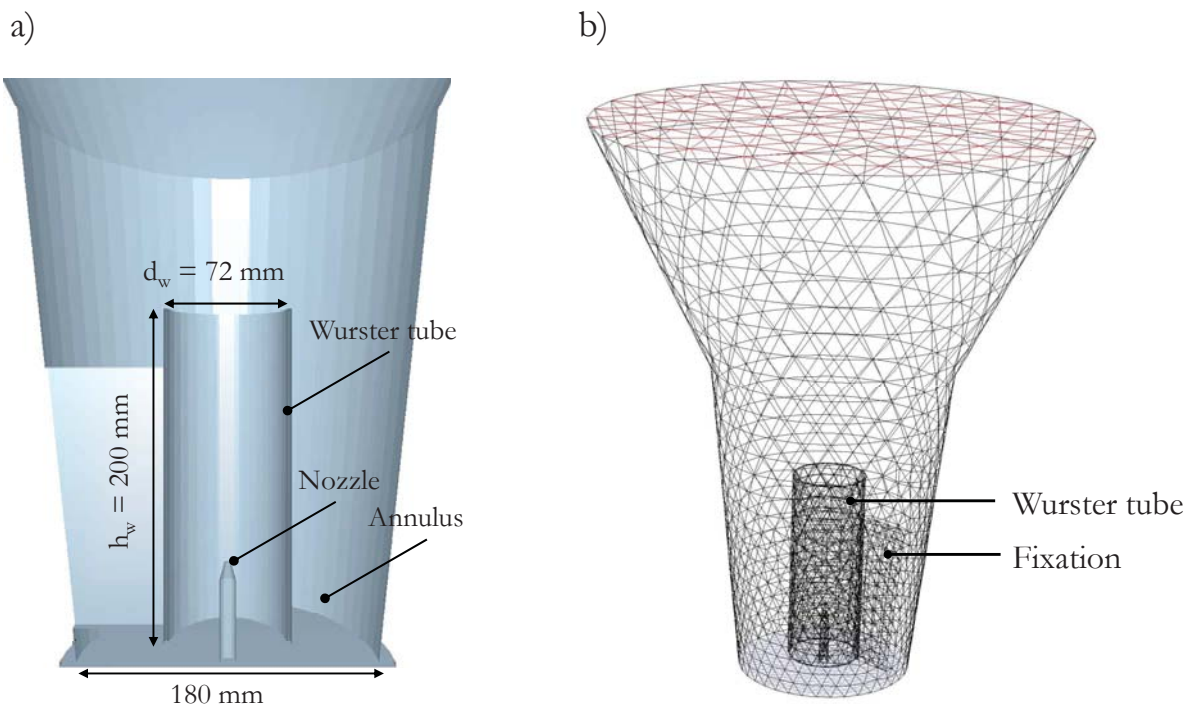


Figure 5-1: Cross-sectional view of the modeled Wurster-coater: (a) Glatt GF3 geometry, (b) simplified geometry for DPM simulations, (c) mesh for CFD simulation.

In the Wurster-coater, air enters the equipment through the bottom via a segmented distributor plate that consists of a perforated plate, as illustrated in Fig. 2-5. Below the Wurster tube (zone 1) the fluidization air velocity is higher than in the annulus (zone 2) due to a larger porosity of the plate (27 % in zone 1 compared to 7 % in zone 2). In zone 3 near the wall of the apparatus a slightly higher porosity of the plate (18 %) and therefore higher gas velocity is applied to avoid stagnant areas. Additionally, air is injected by a bottom-spray nozzle which is situated at the center inside the Wurster tube. The original layout of the bottom plate that is used in the

experiments (see Fig. 2-5) was simplified for the modeling according to the scheme shown in Fig. 5-2.

At the distributor plate, the gas inlet velocities were specified for each zone as boundary condition in the DPM simulation of the Wurster coater. The boundary conditions were set to match in each segment the gas flow rate through the perforated distributor plate of the Glatt GF3 granulator. The pressure drop correlation by Hunt and McAllister (Hunt et al., 1955; McAllister et al., 1958) was used to estimate the distribution of the air flow rate among the different segments of the plate. "No slip" boundary conditions at the walls were set for the gas, whereas the particle-wall friction is defined by the friction coefficient. At the outlet of the process chamber atmospheric pressure was assumed, using a pressure outlet boundary condition. The DPM simulation time step was chosen according to the procedure described in Antonyuk et al. (2011).

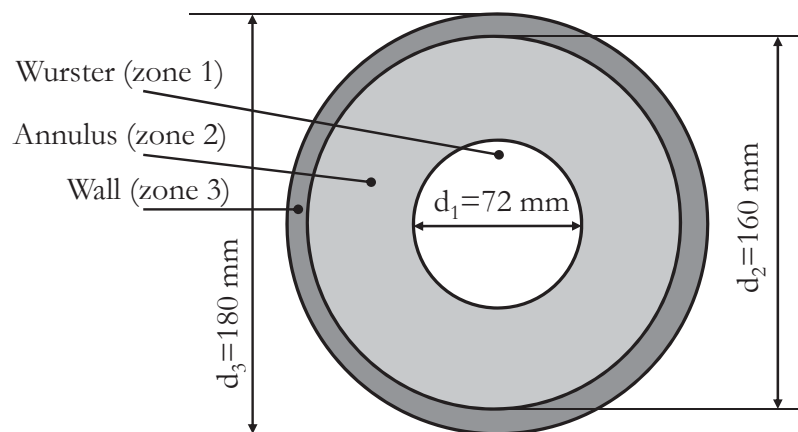


Figure 5-2: Segmented distributor plate of the Wurster-coater: representation with 3 homogeneous zones used in the simulations.

At the start of each simulation the particles are randomly positioned inside the equipment and allowed to settle to the bottom. Then, the air flow rate is increased following a ramp profile for 0.3 s until its steady state flow rate is reached. A stable fluidization regime is obtained within 1 s of simulation time. All test cases presented in this chapter were run for 1.5 s in the steady fluidization regime. Particle and collision velocities as well as all other kinetic parameters characterizing the particle dynamics were averaged over this representative time interval.



5.3 Numerical study on the influence of material properties on the particle and collision dynamics

In a comprehensive simulation study the influence of material properties on the particle dynamics is analyzed in this section. Based on the set of material parameters obtained for maltodextrin agglomerates, which was compiled according to the experimental results presented in chapter 4, a sensitivity analysis is performed to identify key influence parameters for the particle dynamics. Based on the simulation results the relevance of micro-scale particle properties on the structure of the final product particles is highlighted. Table 5-1 gives an overview on the applied simulation parameters. Bold numbers indicate the settings for the base case. In a parameter study, the elastic modulus, the restitution coefficient and the total bed mass (i.e. the number of particles) were varied individually, keeping all other parameters constant.

Table 5-1: Simulation conditions of the case study regarding the sensitivity of particle properties (bold numbers indicate settings of base case).

Parameter	Symbol	Unit	Range of values
Elastic modulus	E	GPa	0.25, 0.5, 1.00
Restitution coefficient	e	-	0.2, 0.4 , 0.6
Bed mass	m_{bed}	kg	0.25, 0.38 , 0.50
Particle diameter	d_p	mm	2.0
Sliding friction coefficient	μ	-	1.0
Particle density	ρ	kg/m ³	600
Gas velocity zone 1	u_{Wur}	-	$10 \cdot u_{\text{mf}}$
Gas velocity zone 2	u_{Ann}	-	$3.8 \cdot u_{\text{mf}}$
Gas velocity zone 3	u_{Wall}	-	$5.0 \cdot u_{\text{mf}}$
Atomizer gas velocity	u_{Jet}	-	$115 \cdot u_{\text{mf}}$
DEM simulation time step	Δt_{DEM}	s	$1 \cdot 10^{-6}$
CFD simulation time step	Δt_{CFD}	s	$5 \cdot 10^{-4}$
Total simulation time	t	s	2.5



5.3.1 Influence of the elastic modulus

The elastic modulus is a characteristic parameter for the contact stiffness of a particle. It determines the particle deformation during a collision and has a strong influence on the contact time. The influence of the elastic modulus on the particle and collision dynamics in a Wurster-coater is analyzed in this section. Experimentally, the elastic modulus of DE 21 maltodextrin was determined as a function of the moisture content (see section 4.3). In this case study the elastic modulus is varied from 1.0 GPa (for the glassy state) to 0.5 GPa (at $T_g + 10$ K) and 0.25 GPa.

In Fig. 5-3 typical snapshots of the particle positions are shown for the three cases. The particle velocity is indicated by the colour code. Since the fluidized bed is an inherently unstable dynamic system, small heterogeneities of the particle distribution like bubbles or particle clusters may emerge and disappear in a chaotic manner. A dominant influence of the elastic modulus on the particle positions and the elevation of the bed cannot be identified from Fig. 5-3. In the central vertical plane of the Wurster-coater ($y = 0$) the radial distribution of the particles was analyzed in the dense bottom zone ($z = 20$ mm) and at the upper end of the Wurster tube ($z = 220$ mm). By counting the average number of particles with their center of mass positioned inside rectangular control volumes with 20 mm side length and dividing the volume of the particles by the volume of the cube, the time-average solids volume fraction can be evaluated.

In Fig. 5-4 the time-averaged solids volume fraction is shown as a function of the x-coordinate at constant height $z = 20$ mm. The vertical position of the analyzed slice is indicated in the right part of Fig. 5-4. It can be seen that the average solids volume fraction is increasing from the outside towards the center in the dense bed up to a value of approximately $\epsilon_s = 0.4$ at $x = \pm 40$ mm, which corresponds to the position of the wall of the draft tube. Particles are transported towards the center in the bottom zone by the Venturi effect in order to become entrained by the spout. Since the gap distance between Wurster tube and the bottom plate limits the amount of particles that can enter the draft tube, the concentration is increasing radially. Below the Wurster tube the particle concentration is lower due to their acceleration in the spout. Due to the influence of the fixation of the draft tube (see Fig. 5-1), the concentration profile is slightly unsymmetrical.

A variation of the elastic modulus has only limited influence on the radial distribution of the particles. In Fig. 5-4 it can be seen that the solids volume fraction in the dense bottom zone generally increases slightly with increasing modulus of elasticity.

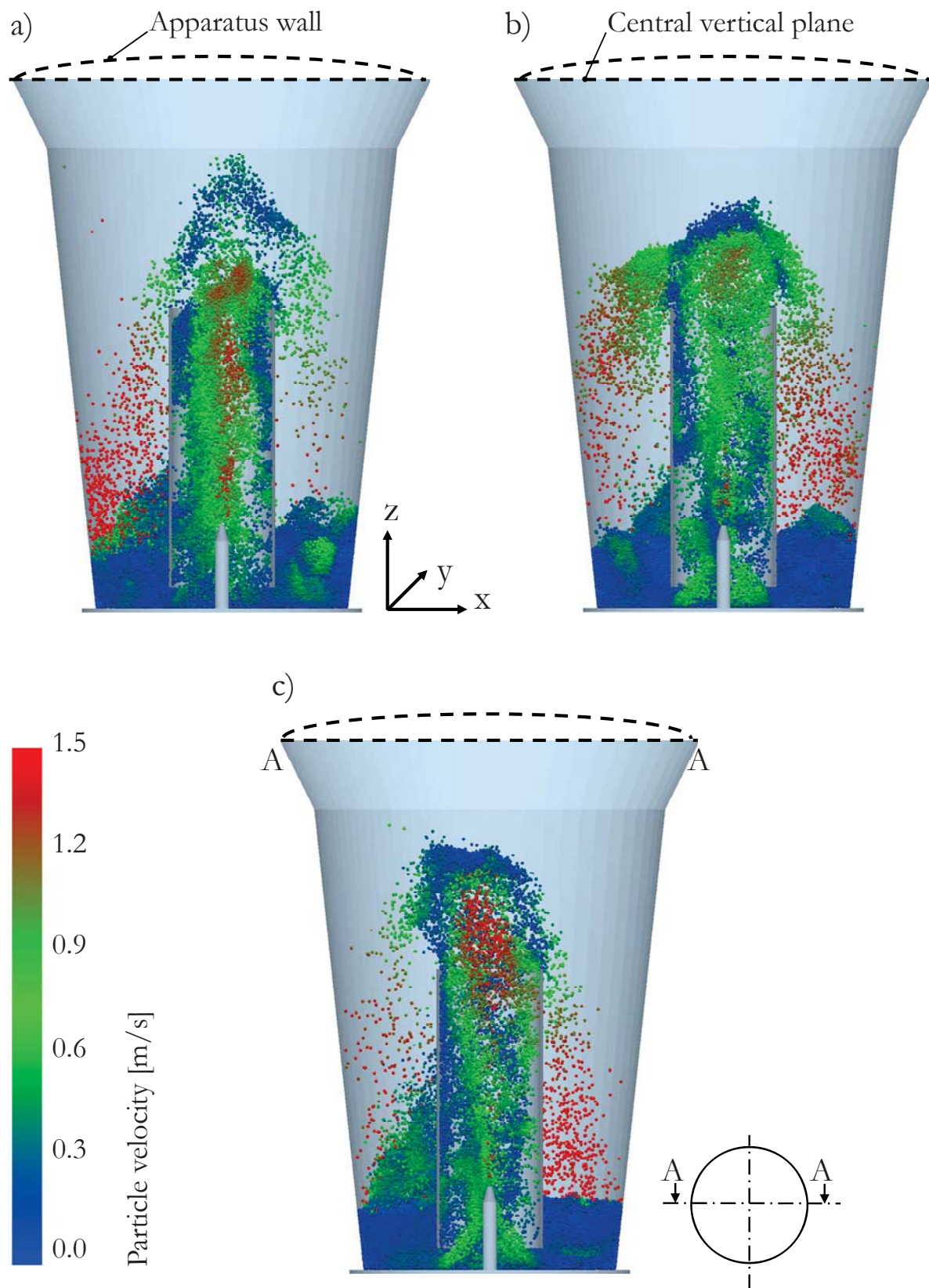


Figure 5-3: Instantaneous particle positions and velocity distribution at simulation time $t=2.0$ s for different values of the elastic modulus: a) 0.25 GPa, b) 0.5 GPa, c) 1.0 GPa.

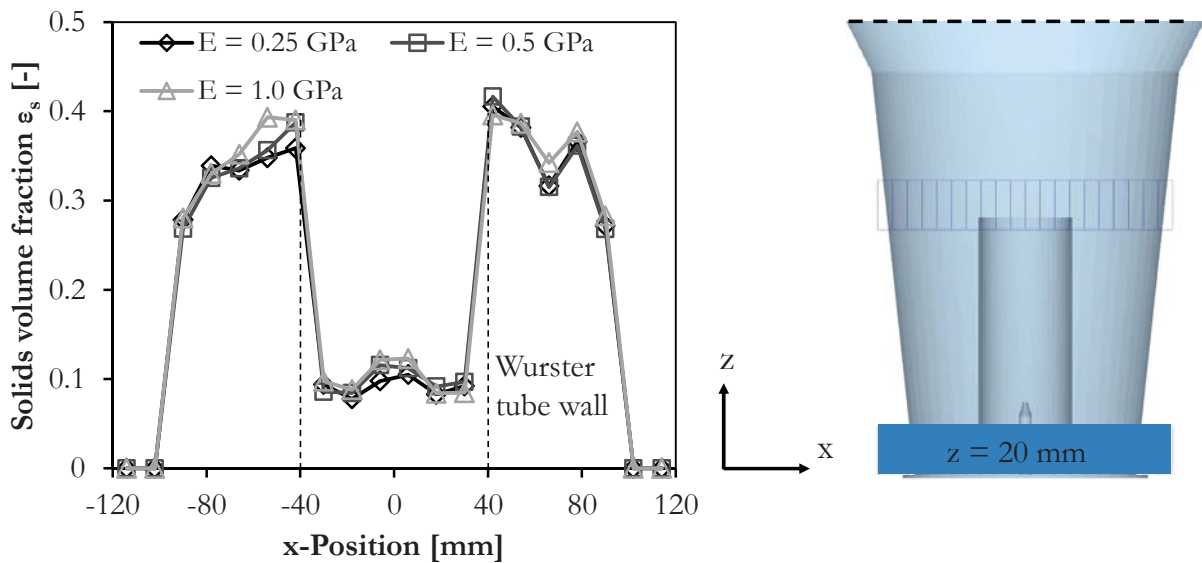


Figure 5-4: Time-averaged radial distribution of the particles in the Wurster-coater in the dense bottom zone ($z = 20$ mm) as a function of the elastic modulus of the particles.

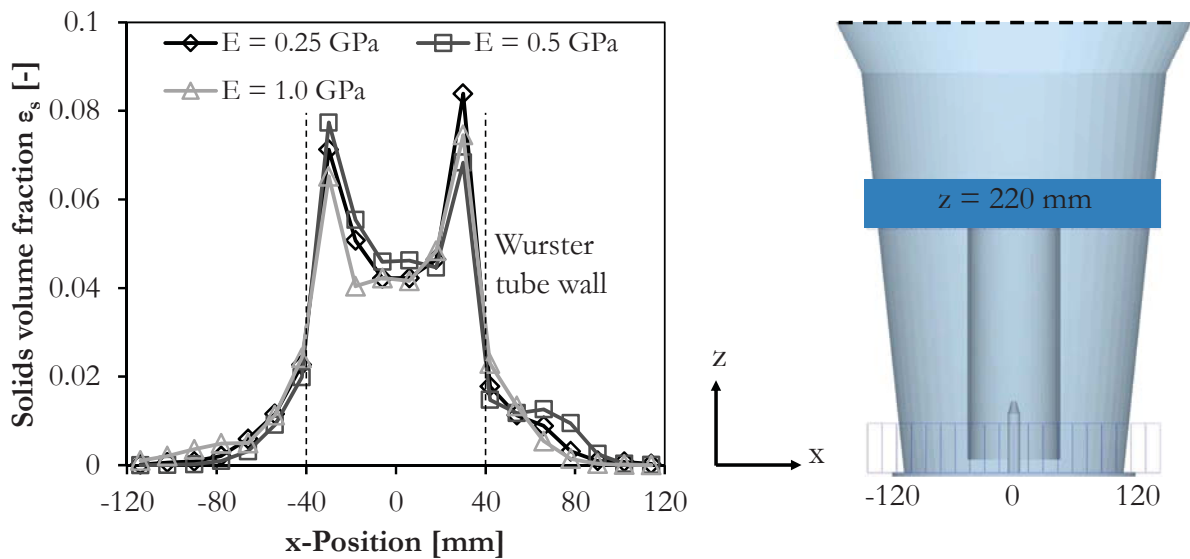


Figure 5-5: Time-averaged radial distribution of the particles in the Wurster-coater at the top of the draft tube ($z = 220$ mm) as a function of the elastic modulus of the particles.

At the top end of the Wurster tube (height $z = 220$ mm) generally lower particle concentrations are observed, as shown in Fig. 5-5. Inside the draft tube particles are transported upwards, where concentrations between 4 and 8 % are found on average. The solids volume fraction increases from the center to the inner wall of the Wurster tube. Outside the draft tube the particles are distributed over the full width of the expansion chamber before falling back down to the bottom zone. This results in low particle concentrations in the radial profile, which are decreasing



towards the outer walls of the equipment. A clear effect of the elastic modulus of the particles on their radial distribution in the upper region of the bed cannot be identified in Fig. 5-5.

Table 5-2: Influence of the elastic modulus, the restitution coefficient and the bed mass on the particle dynamics in a Wurster-coater.

Case	Mean particle velocity [m/s]	Mean angular velocity [rad/s]	Particle fraction in dense bed [%]	Particle fraction in Wurster [%]	Mean particle velocity Wurster [m/s]	Mean particle velocity Annulus [m/s]
E = 0.25 GPa	0.279	47.10	81.61	13.19	0.468	0.215
E = 0.50 GPa	0.280	46.72	81.40	12.32	0.484	0.210
E = 1.00 GPa	0.275	45.94	82.12	12.28	0.484	0.200
e = 0.2	0.269	47.09	82.19	12.80	0.461	0.201
e = 0.4	0.275	45.94	82.12	12.28	0.484	0.200
e = 0.6	0.276	48.10	81.21	12.96	0.482	0.208
m = 0.251 kg	0.218	43.50	81.36	13.95	0.371	0.164
m = 0.377 kg	0.275	45.94	82.12	12.28	0.484	0.200
m = 0.503 kg	0.339	48.85	81.51	11.68	0.590	0.254

For a quantitative analysis of the influence of material parameters on the particle dynamics Table 5-2 shows the time-averaged particle velocity and the particle distribution among the wetting and drying zones of the equipment, which were defined as the inside the draft tube and the dense bed ($\varepsilon_p > 0.1$) in the annulus, respectively. It can be seen that the elastic modulus is not a sensitive parameter for the overall average particle velocity and for the particle rotation. However, if the elastic modulus is increased, the mobility of the particles in the dense bed is reduced. Based on this effect the fraction of particles which is drawn into the Wurster tube is slightly decreased. Interestingly, the fraction of particles which is positioned inside the draft tube and in the dense bottom zone is nearly equal for all investigated cases. From this result it can be concluded the gas flow rate and other process-related parameters have a much greater influence on the distribution of the particles in the equipment than the material properties of the particles.

Unlike the time-averaged particle motion patterns, the collision dynamics show a strong sensitivity to changes in the elastic modulus of the particles. In Fig. 5-6 the number based density distribution (see appendix A2) of the average particle-particle collision velocity in the dense bed

and the particle-wall collision velocity is shown for three test cases with different elastic modulus. A monomodal distribution of the particle collision velocity is found with the mode at 0.01 m/s (see Fig. 5-6 a). Very low collision velocities prevail within the dense bed. If the elastic modulus is reduced, the distribution becomes wider, but the mode remains at the same value. For particle-wall collisions a wider velocity spectrum and higher average velocities are found (see Fig. 5-6 b). If the elastic modulus is decreasing, the frequency of collisions with very low relative velocity is reduced and the distribution is shifted to the right towards higher relative collision velocities.

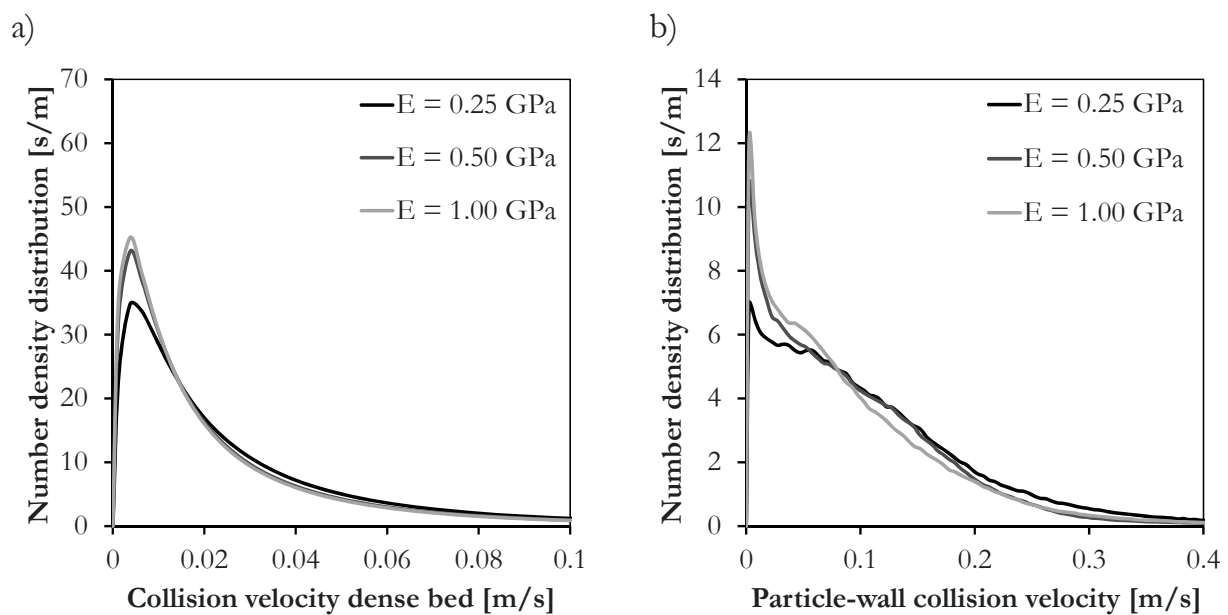


Figure 5-6: Influence of a variation of the elastic modulus on (a) the time-averaged number density distribution of the particle-particle collision velocity and (b) on the particle-wall collision velocity distribution in a Wurster-coater.

Regarding the influence of the elastic modulus it is found that an increase from 0.25 to 1.0 GPa leads to a decrease of the average particle-particle and particle-wall collision velocity of almost 20 %, which is shown in Fig. 5-7 a). Meanwhile the average collision frequency is increased by 30 % (see Fig. 5-7 b). Stiffer particles collide at higher frequency but lower average velocity. Due to the larger deformation of particles with low elastic modulus and due to their higher collision velocity, the average collision duration increases disproportionately. On average, each particle collides approximately 30 times more often with another particle than with the walls of the equipment for all investigated cases. For an increase of the elastic modulus a decreasing trend of the particle-wall frequency is found, as shown in Fig. 5-7 c).

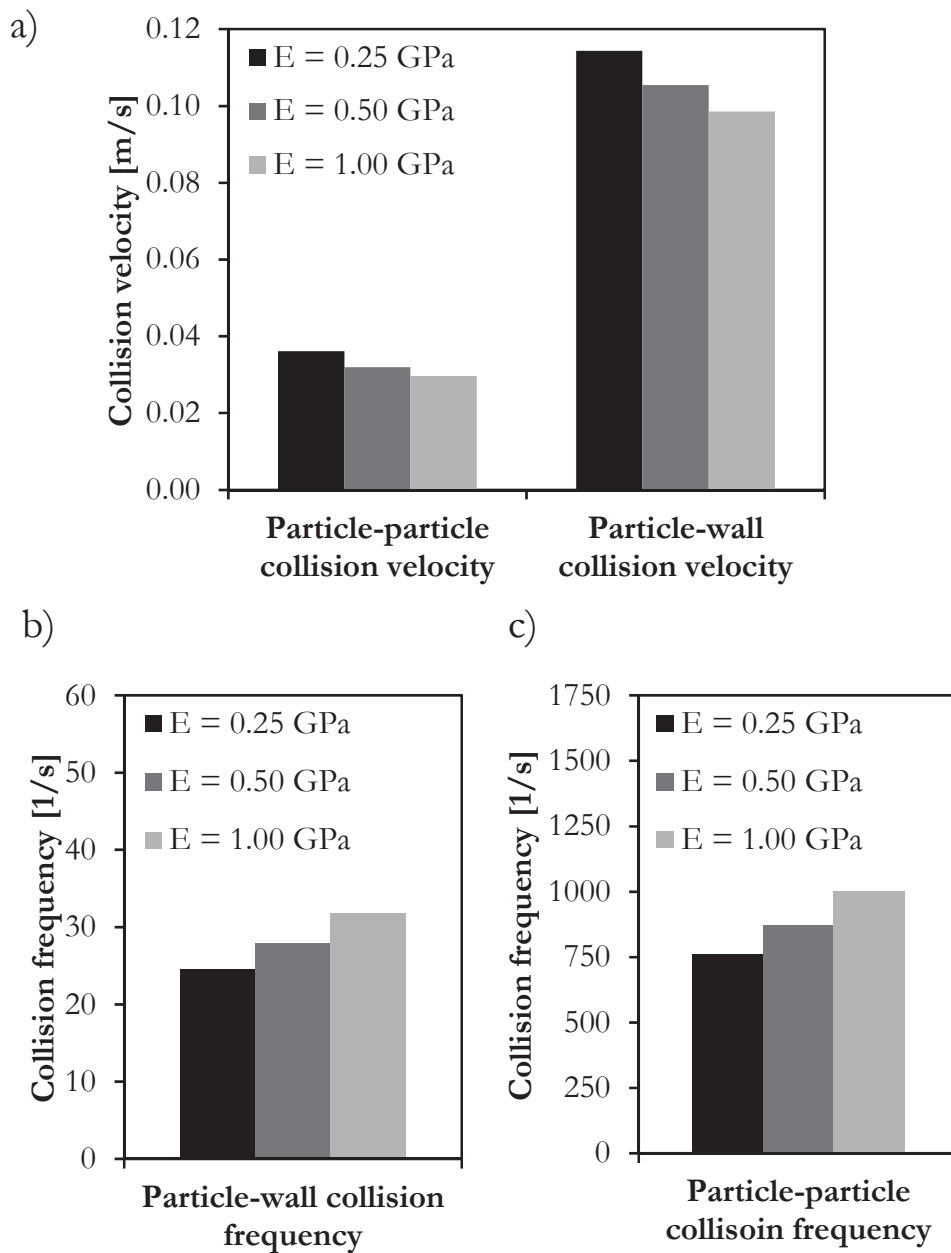


Figure 5-7: Influence of the elastic modulus on the collision velocity and the collision frequency in a Wurster-coater.

For all investigated case studies the influence of the material parameters on the collision dynamics is summarized in Table 5-3. Table 5-4 gives an overview on the influence of the material parameters on the collision frequency in the Wurster-coater.



Table 5-3: Influence of the elastic modulus, the restitution coefficient and the bed mass on the collision dynamics in a Wurster-coater.

Case	Mean particle-particle collision velocity [m/s]	Particle-particle collision velocity (inside draft tube) [m/s]	Particle-particle collision velocity (inside dense bed) [m/s]	Mean particle-wall collision velocity [m/s]	Mean collision duration [μ s]
E = 0.25 GPa	0.0361	0.1051	0.0345	0.1143	227
E = 0.50 GPa	0.0320	0.0902	0.0298	0.1054	175
E = 1.00 GPa	0.0297	0.0909	0.0282	0.0986	139
e = 0.2	0.0269	0.0798	0.0252	0.0989	201
e = 0.4	0.0297	0.0909	0.0282	0.0986	139
e = 0.6	0.0352	0.1416	0.0345	0.0974	91
m = 0.251 kg	0.0322	0.1007	0.0313	0.0747	126
m = 0.377 kg	0.0297	0.0909	0.0282	0.0986	139
m = 0.503 kg	0.0313	0.0705	0.0286	0.1273	145

The effect of the elastic modulus on the collision frequency is well visualized in Fig. 5-8 a). Generally, it can be seen that high collision frequencies occur mainly in the dense bottom zone of the bed, while in the dilute zone at a bed height greater than 100 mm the average collision frequency is approximately 5 times lower. This result is in a strong correlation with the solids volume fraction, which is shown in Fig. 5-8 b) as a function of the bed height. While the distribution of the particles along the bed height remains unchanged if the elastic modulus is varied in the investigated range, the collision frequency in the dense bed is largely increased.

In Fig. 5-9 radial profiles of the collision frequency at the central vertical plane ($y = 0$) are shown as a function of the elastic modulus for two different positions in the bed. The situation in the dense bottom zone of the bed (height $z = 20$ mm) is depicted in Fig. 5-9 a), while Fig. 5-9 b) shows the situation at the upper end of the Wurster tube (height $z = 220$ mm). The position of the investigated planes is illustrated in Fig. 5-4 and 5-5, respectively.

Very high collision frequencies up to 1500 s^{-1} are found in the annulus region of the dense bed, with peaks near the outer wall of the equipment and in the vicinity of the Wurster tube. The general trend towards higher collision frequencies with higher elastic modulus of the particles is confirmed in Fig. 5-9 a).



Table 5-4: Influence of the elastic modulus, the restitution coefficient and the bed mass on the collision frequency in a Wurster-coater.

Case	Mean particle-particle collision frequency [1/s]	Particle-particle collision frequency (inside draft tube) [1/s]	Particle-particle collision frequency (inside dense bed) [1/s]	Mean particle-wall collision frequency [1/s]
$E = 0.25$ GPa	761	147	920	24.6
$E = 0.50$ GPa	872	182	1062	27.9
$E = 1.00$ GPa	1002	188	1224	31.8
$e = 0.2$	938	217	1117	30.1
$e = 0.4$	1002	188	1224	31.8
$e = 0.6$	876	108	1019	33.7
$m = 0.251$ kg	712	113	802	30.4
$m = 0.377$ kg	1002	188	1224	31.8
$m = 0.503$ kg	1196	365	1515	35.4

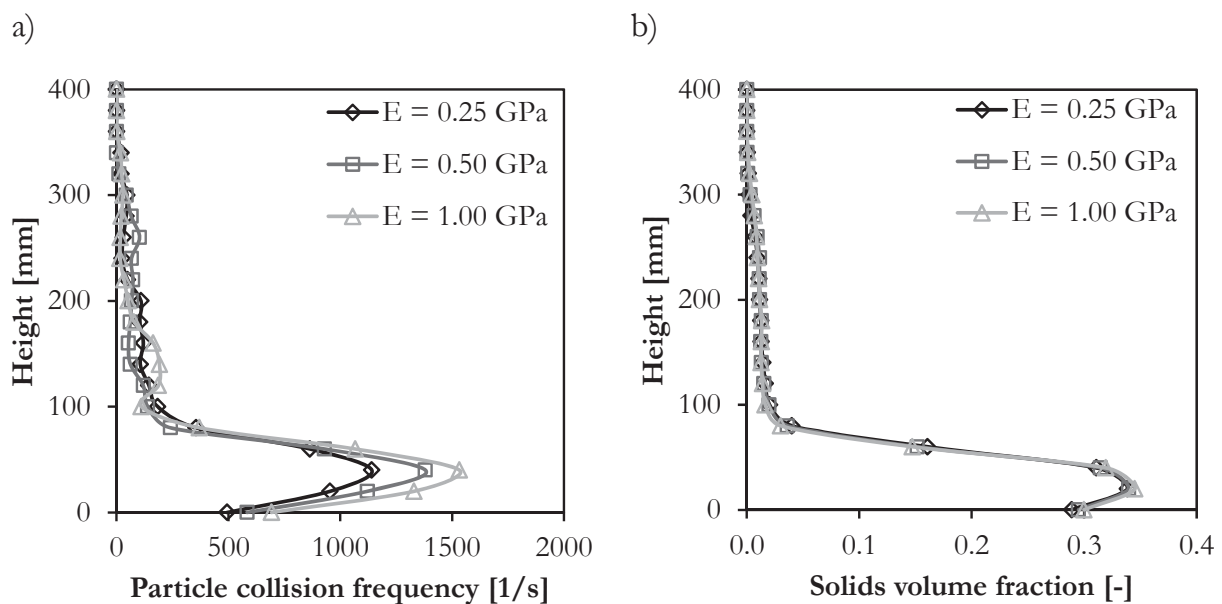


Figure 5-8: Influence the elastic modulus on the vertical profile of (a) the time-averaged particle-particle collision frequency and (b) the solids volume fraction in a Wurster-coater.

In the dilute zone at the top of the Wurster tube (Fig. 5-9 b), however, no clear influence of the elastic modulus on the collision frequency can be identified. Inside the draft tube the collision frequency is roughly 10 times smaller than in the dense annulus zone.

It can be concluded that an increase of the elastic modulus reduces largely the time-scale of the particle-particle interactions. Therefore, the simulation time step must be adapted to the stiffest particle which is present in the system.

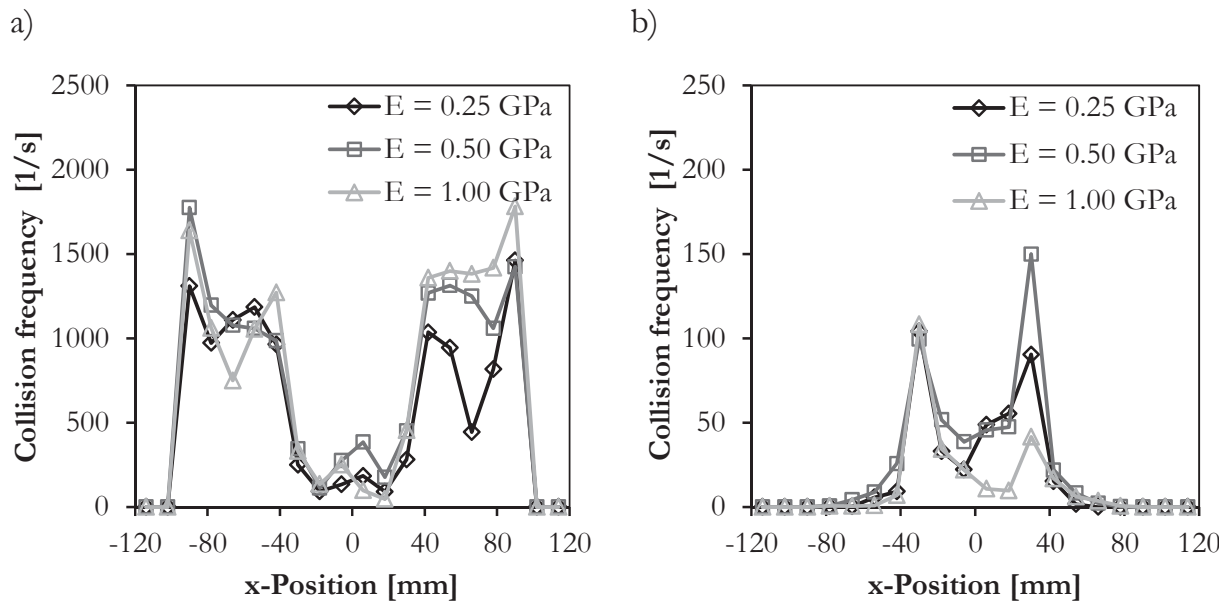


Figure 5-9: Influence of the elastic modulus on the radial distribution of the time-averaged particle-particle collision frequency in a Wurster-coater at different bed heights: a) $z = 20$ mm, b) $z = 220$ mm.

5.3.2 Influence of the restitution coefficient

The restitution coefficient determines the fraction of energy that is dissipated during a collision. In the applied visco-elastic Hertz-Mindlin contact model, energy dissipation is included via a viscous damping term. Due to their irregular shape and fragile structure, very low restitution coefficients were measured for maltodextrin agglomerates. In this section the sensitivity of the restitution coefficient relative to the particle and collision dynamics in a Wurster-coater is analyzed. In comparison to the base scenario with a restitution coefficient of $e = 0.4$, two variations are investigated. These variations correspond to a process which is operated closer to the glass transition temperature ($e = 0.2$) and a process where the particles are closer to the brittle state of dense primary particles ($e = 0.6$). In all cases the restitution coefficient investigated here is a property of the core particle material. The simulation does not include liquid layers or other



sources of viscous adhesive forces which lead to a decreasing restitution coefficient as well. Due to the reduced energy dissipation, higher average particle velocities are observed, if the restitution coefficient is increased in the simulations (see Table 5-2 and Fig. 5-10). In the Wurster-coater, this effect is more pronounced for particles at the inside the draft tube than for particles in the dense bed. Also the average rotational velocity is increasing in case of a larger restitution coefficient. No significant influence on the distribution of the particles among the dense bed and the wetting zone inside the draft tube can be observed in the investigated range of the restitution coefficient.

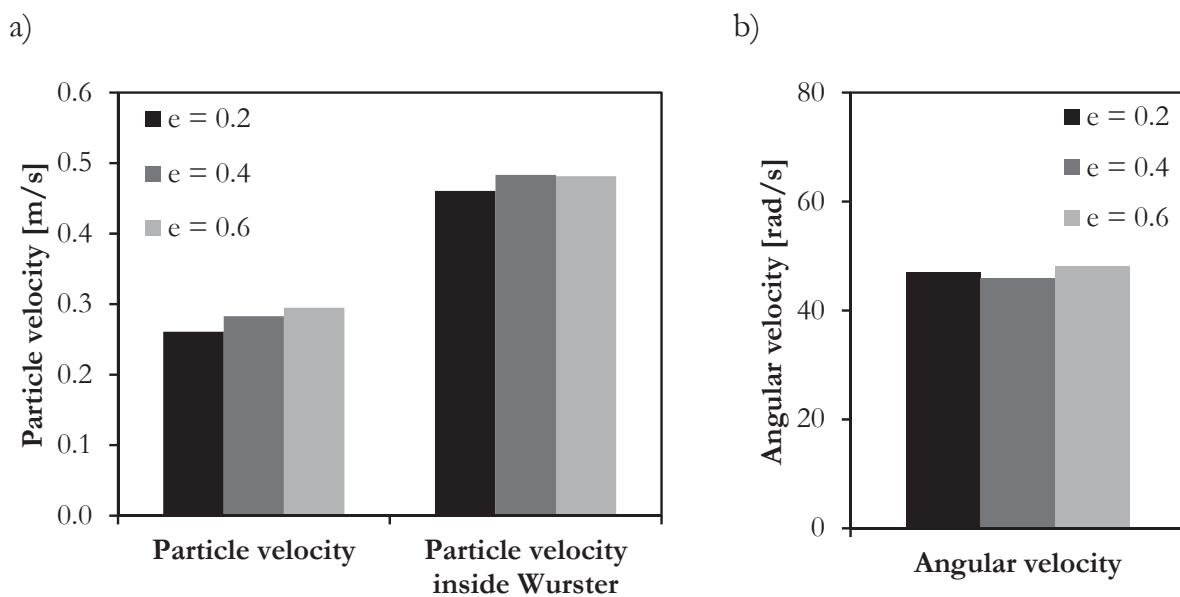


Figure 5-10: Influence of the restitution coefficient on the particle dynamics in a Wurster-coater.

A monomodal distribution of the average collision velocity, which is defined according to Eq. 3-15 at the first contact of two colliding particles, is found for all three cases as shown in Fig. 5-11. With increasing restitution coefficient the mode is shifted towards higher velocities and the distribution gets wider.

As presented in Table 5-3 and Fig. 5-12 a), the overall average collision velocity increases by more than 30 % for a restitution coefficient of 0.6 compared to the result at $e = 0.2$. Looking at collisions inside the Wurster tube only, the increase is even more pronounced (+70%). This trend cannot be observed for particle-wall collisions, where a slightly lower average collision velocity is found for increasing restitution coefficients. Furthermore it can be seen in Fig. 5-12 b) that the viscous component in the contact model has a dominant influence on the contact time. The



average duration of the collisions is reduced by more than 50%, if the restitution coefficient changes from 0.2 to a value of 0.6.

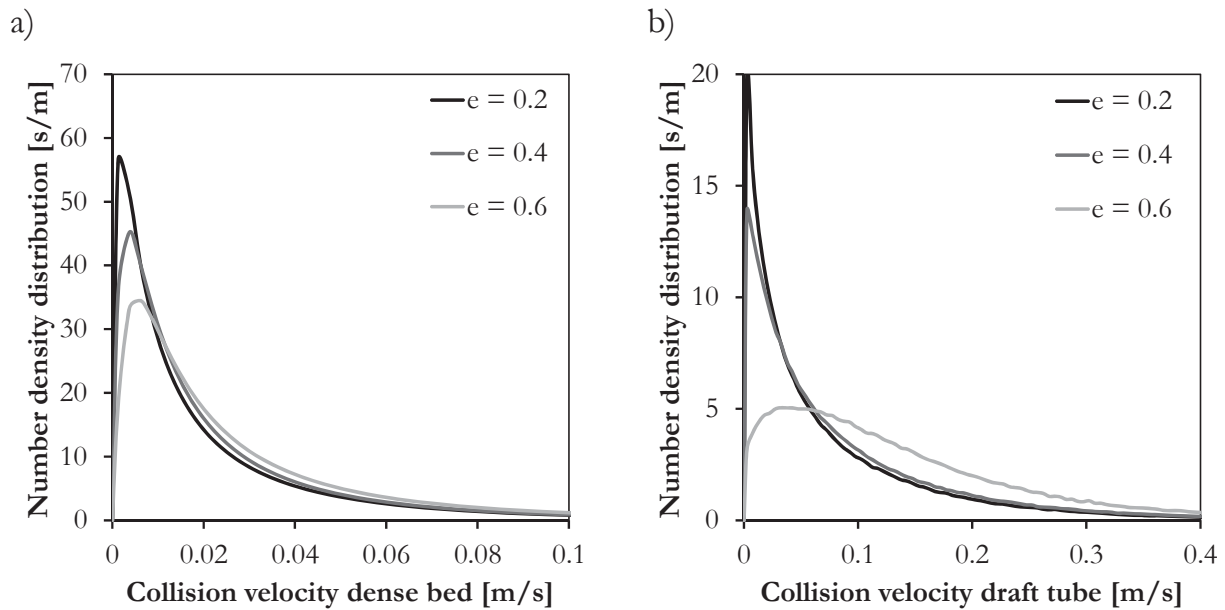


Figure 5-11: Influence of a variation of the restitution coefficient on (a) the time-averaged number density distribution of the particle-particle collision velocity and (b) on the particle-particle collision velocity distribution inside the draft tube of a Wurster-coater.

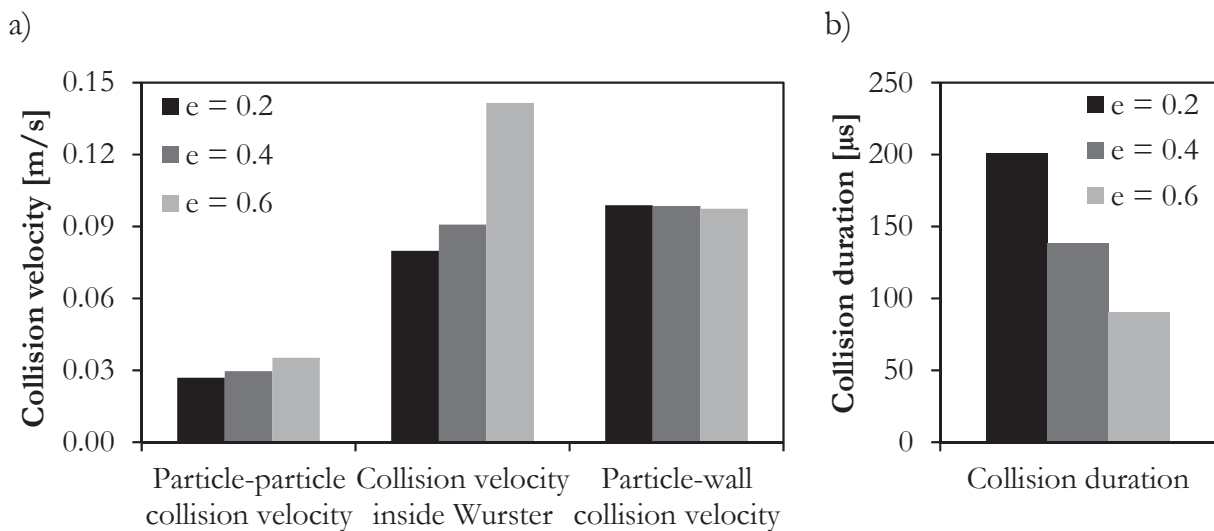


Figure 5-12: Influence of the restitution coefficient on the collision dynamics in a Wurster-coater.

Regarding the collision frequency, the influence of the restitution coefficient is less evident. As shown in Table 5-4 and Fig. 5-13 a), the highest average collision frequency occurs at $e = 0.4$, while for both $e = 0.2$ and $e = 0.6$ lower collision frequencies are found in the simulations. Inside



the draft tube a decreasing collision frequency is observed for increasing values of the restitution coefficient.

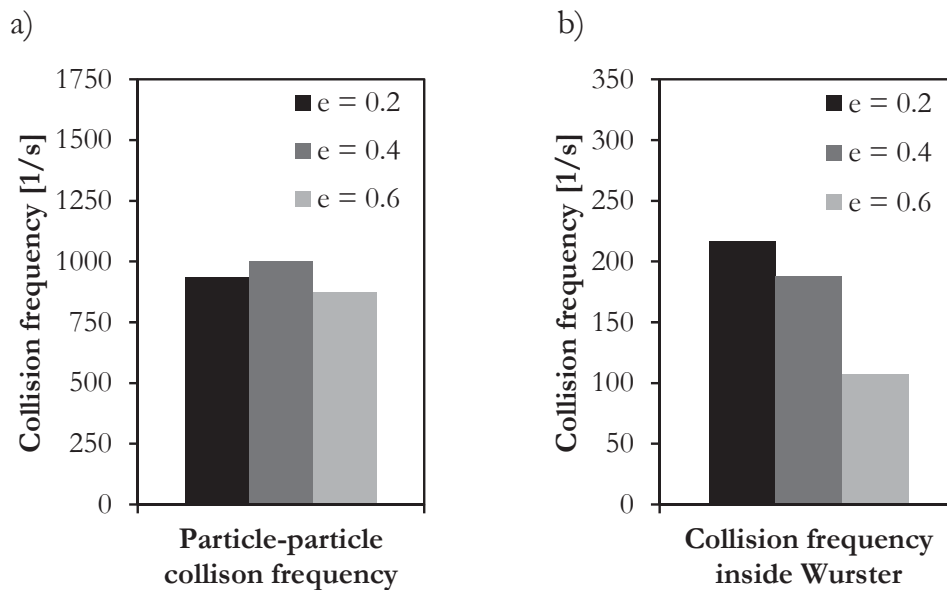


Figure 5-13: Influence of the restitution coefficient on the collision frequency in a Wurster-coater.

The profile of the collision frequency over the bed height (see Fig. 5-14 a) shows that higher collision frequencies at $e = 0.4$ compared to the other two cases are observed mainly in the dense bottom zone. This result can be explained by differences in the solids volume fraction, as shown in Fig. 5-14 b). On average, the solids volume fraction at the bottom of the bed (0 – 40 mm bed height) is higher at $e = 0.4$ compared to the other cases, while the bed expansion is lower. Due to the confined space the free path between particle collisions is lower and the average collision frequency is higher, if the particles move at comparable velocity. In the dilute regions above 100 mm bed height and at the inside of the draft tube the collision frequency is increasing with decreasing restitution coefficient.

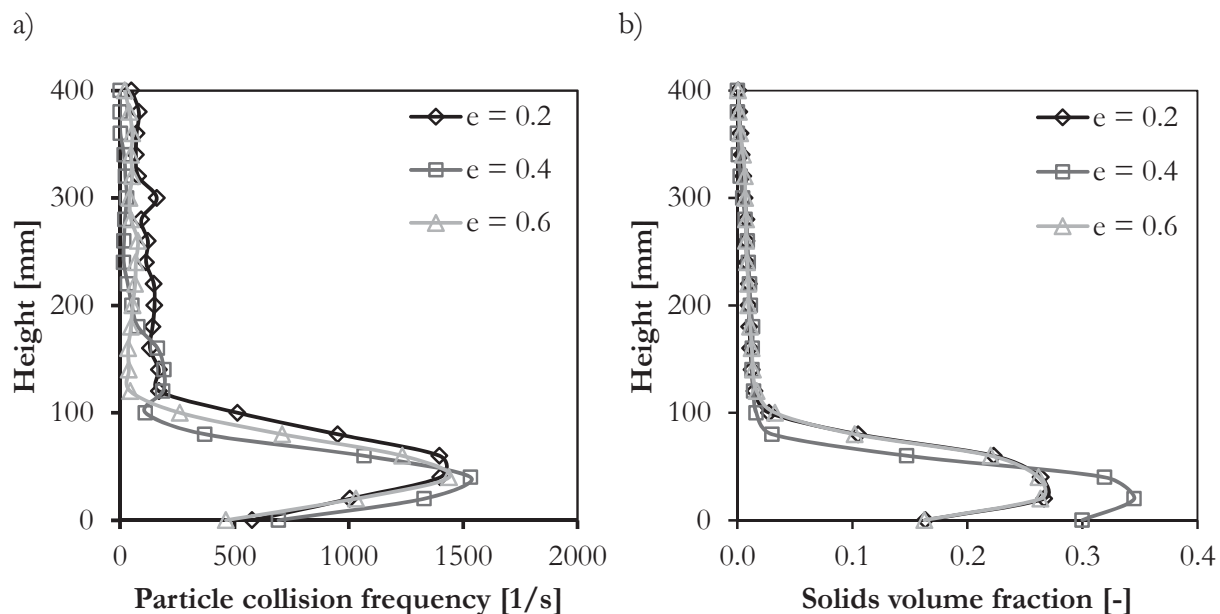


Figure 5-14: Influence of a variation of the restitution coefficient on the profile of (a) the time-averaged particle-particle collision frequency and (b) the solids volume fraction over the bed height in a Wurster-coater.

5.3.3 Influence of the bed mass

At equal material properties and process parameters (base scenario, see Table 5-1) the number of particles in the granulator was varied. Three different batch sizes are compared in this section: 0.251 kg (corresponding to 100 000 spherical particles of 2 mm diameter), 0.377 kg and 0.503 kg. The aim of the study is to understand better and in more detail the influence of the filling level of a Wurster-coater on the particle and collision dynamics.

In Fig. 5-15 snapshots of the particle positions and their velocity distribution are shown for the three test cases with different bed mass. It can be seen that the elevation of the dense bed in the annulus is increasing with increasing bed mass. Furthermore, the particle concentration inside the draft tube is enlarged and the particle fountain above the Wurster tube reaches to higher levels. Although the flow rate of the fluidization air and of the atomizer are kept constant, higher velocity gradients are observed and the average particle velocity increases by more than 50 % if the bed mass is doubled from 0.251 kg to 0.503 kg (see Table 5-2 and Fig. 5-16 a).

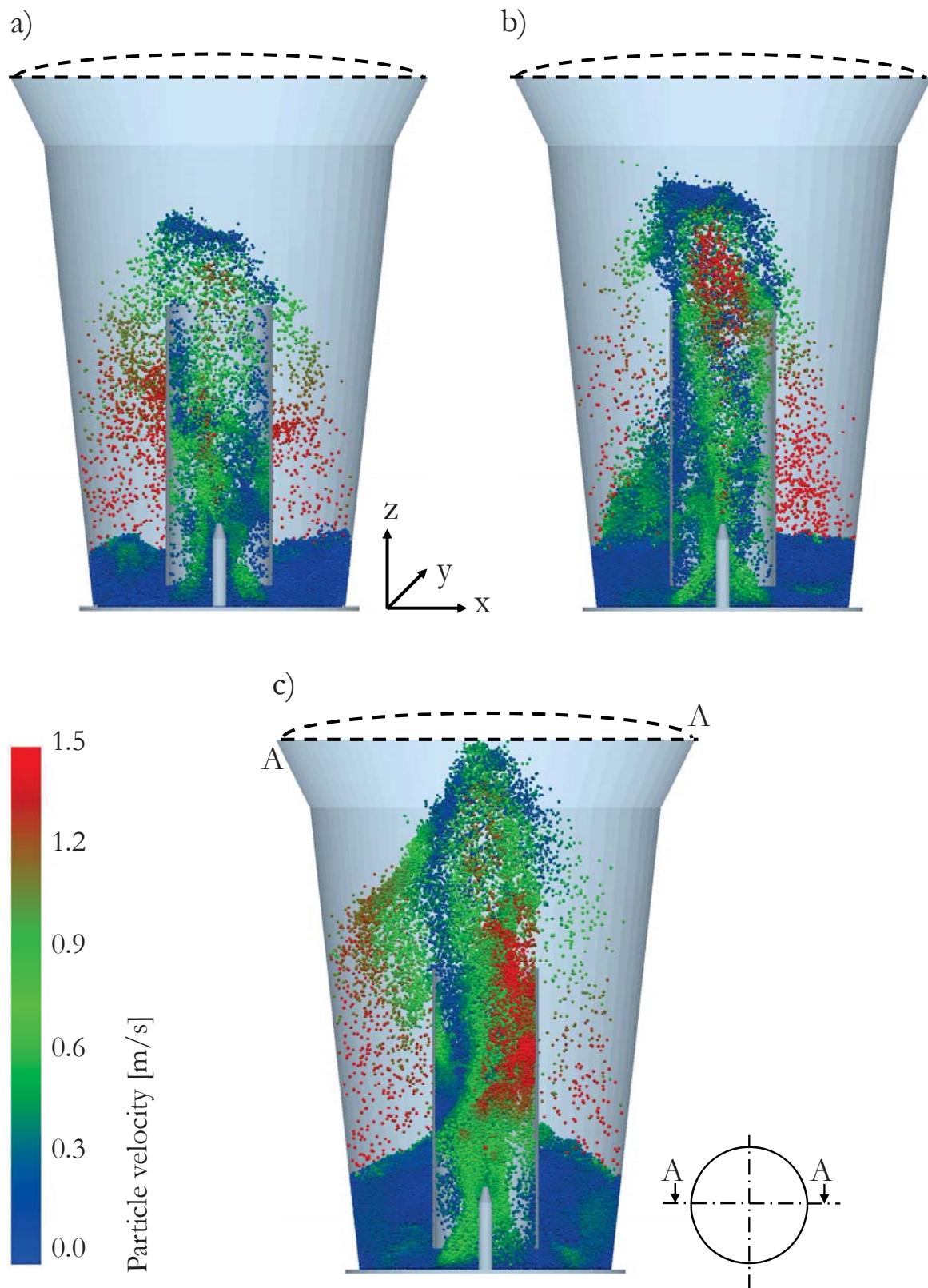


Figure 5-15: Instantaneous particle positions and velocity distributions at simulation time $t = 2.0$ s for different values of the bed mass: a) 0.251 kg (100 000 particles), b) 0.377 kg (150 000 particles), c) 0.503 kg (200 000 particles).

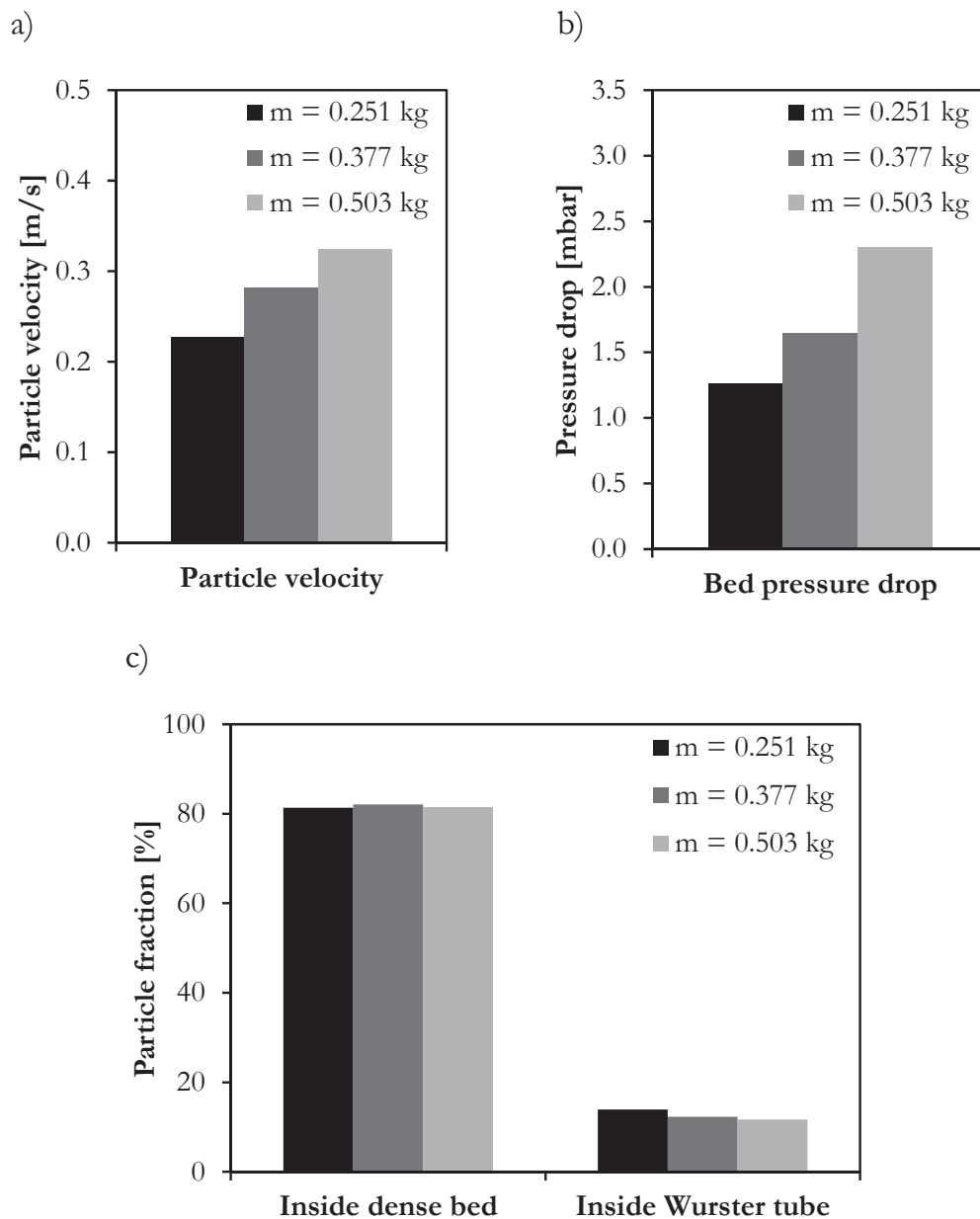


Figure 5-16: Influence of the bed mass on the particle dynamics in a Wurster-coater.

The main reason for this behaviour is the elevated pressure drop of the bed (see Fig. 5-16 b), which forces a larger fraction of the gas to flow through the draft tube, where it entrains the particles in the spout. While the fraction of particles positioned in the dense bed is similar as in the other simulation cases, the particle fraction inside the Wurster tube is reduced if the bed mass is increased, as shown in Fig. 5-16 c). Note that the absolute number of particles inside the draft tube is increasing, but not to the same extent as the bed mass. Therefore the particle fraction inside the draft tube is reduced. The “missing” particles are positioned in the expansion chamber above the draft tube.



Opposite to the particle dynamics, the characteristic figures for the collision dynamics, which are summarized in Table 5-3, are not significantly influenced by an increase of the bed mass. In the Wurster-coater the average particle-particle collision velocity and its distribution (see Fig. 5-17 a) and Fig. 5-18 a) are insensitive to changes of the bed mass in the investigated range. Also the average collision duration is not affected by a change of the bed mass, as shown in Fig. 5-18 b).

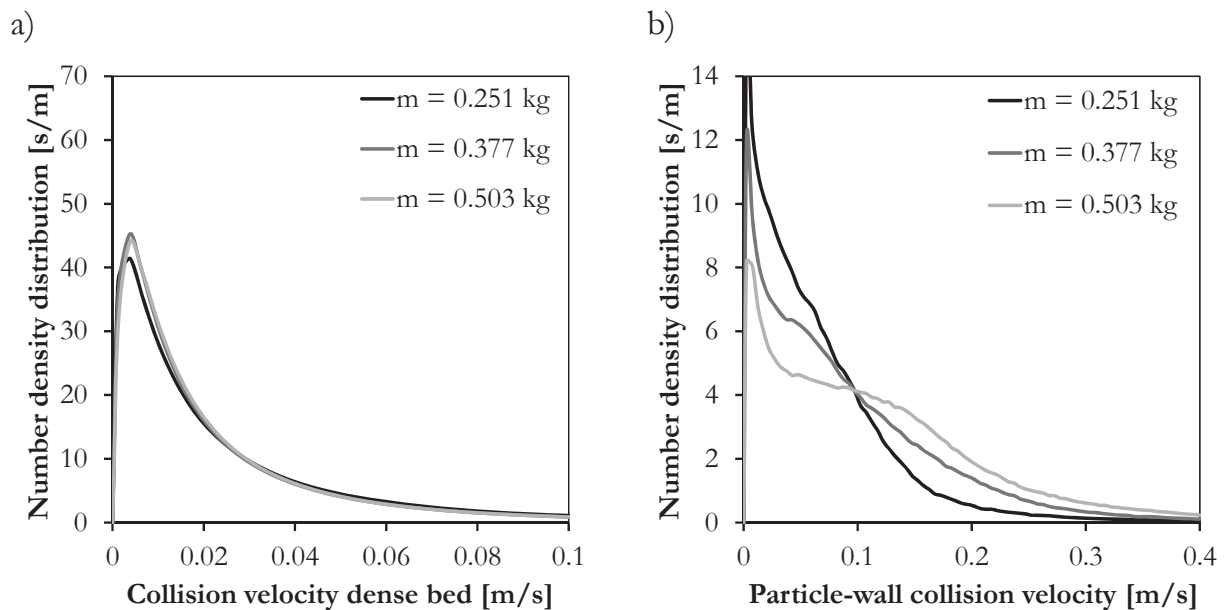


Figure 5-17: Influence of a variation of the bed mass on (a) the time-averaged number density distribution of the particle-particle collision velocity and (b) on the particle-wall collision velocity distribution in a Wurster-coater.

Looking at the interactions between particles and the walls, however, an increasing average collision velocity is found (see Table 5-3 and Fig. 5-17 b). This can be related to higher particle velocities inside the draft tube, where more energetic collisions with the wall occur as a consequence.

Higher particle velocities and higher particle concentrations lead to a pronounced increase of the collision frequency of the particles in the Wurster-coater, if the bed mass is enlarged (see Table 5-4 and Fig. 5-19). The dense bed is more agitated, which leads to an 80 % increase of the collision frequency, if the bed mass is doubled. Inside the Wurster tube this effect is even stronger, since both the average particle velocity and the solids volume fraction increase with rising particle number in the bed. The collision frequency increases by a factor of 3 for the investigated case. As shown in Fig. 5-19 b), however, the particle-wall collision frequency is not affected significantly by an increase of the bed mass, due to the constant surface area of the walls.

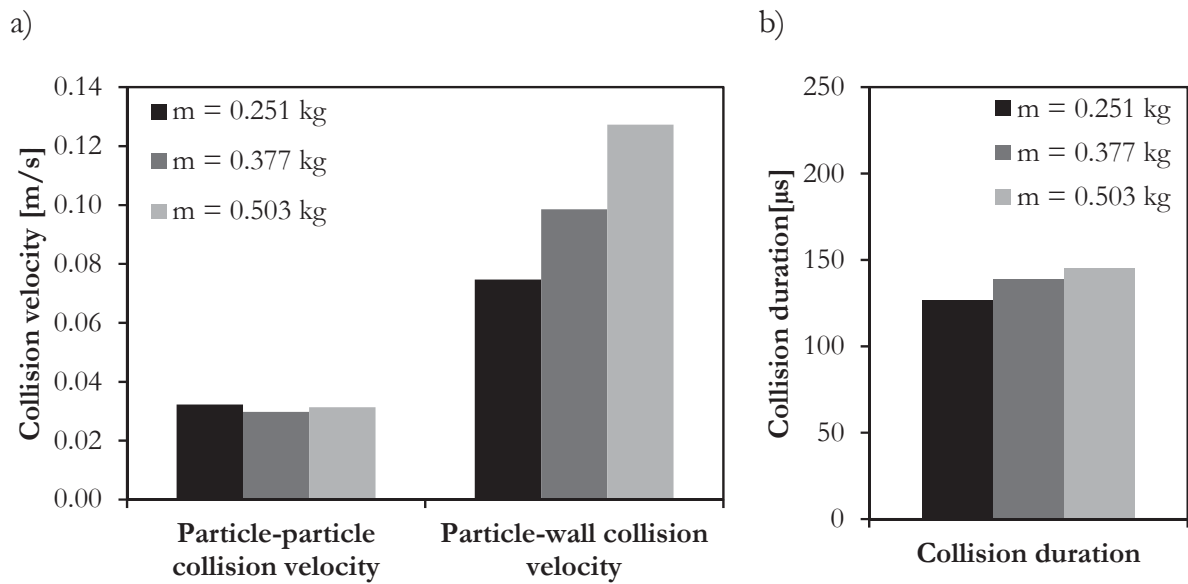


Figure 5-18: Influence of the bed mass on the collision dynamics in a Wurster-coater.

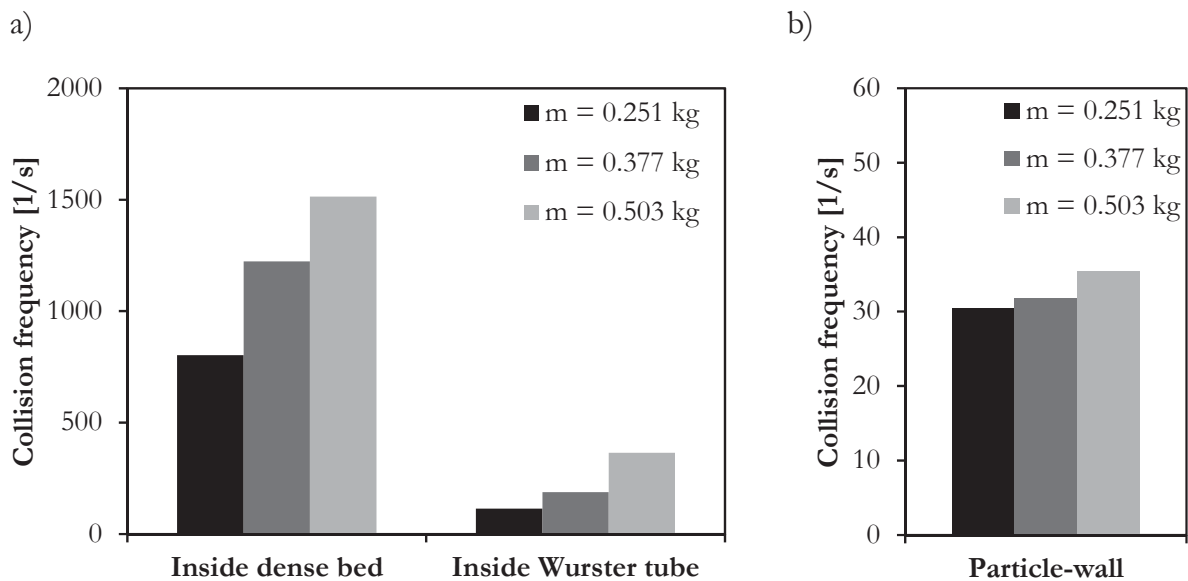


Figure 5-19: Influence of the bed mass on the collision frequency in a Wurster-coater.

Regarding the profile of the collision frequency over the bed height in Fig. 5-20 a, it can be seen that the increased collision frequency applies to all levels of the bed. The profile of the solids volume fraction, shown in Fig. 5-20 b, reveals that the dense bed expands for higher bed mass, but the density of the packing remains unchanged. Therefore the increase of the collision frequency can entirely be related to the accelerated particle motion in case of a higher bed mass. At equally confined space the particles move faster, which leads to a higher collision frequency.

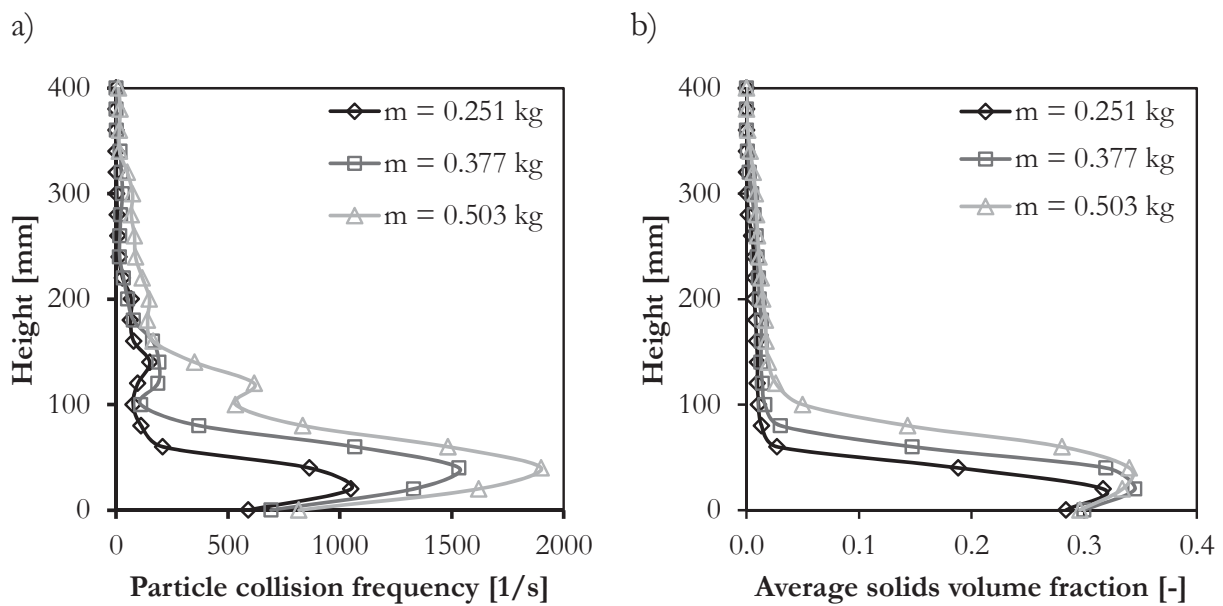


Figure 5-20: Influence of a variation of the bed mass on the profile of (a) the time-averaged particle-particle collision frequency and (b) the solids volume fraction over the bed height in a Wurster-coater.

5.3.4 Conclusion

In a detailed simulation study the influence of the elastic modulus, the restitution coefficient and the bed mass on the particle and collision dynamics in a Wurster-coater was analyzed. All particle properties were chosen to represent the behaviour of amorphous maltodextrin agglomerates, which were analyzed experimentally. While the mechanical material properties have a strong influence on the collision dynamics, especially the relative collision velocity and the contact time, the motion and distribution of the particles inside the equipment remains almost unchanged. Opposite to that, at identical particle properties an increase of the bed mass dramatically changes the particle dynamics and the elevation of the bed, although the gas flow rate is not changed. While the average collision velocity remains almost constant, the collision frequency is strongly influenced by a change of the bed mass due to differences regarding the intensity of particle agitation.

Transferred to the structuration of maltodextrin agglomerates in a Wurster-coater, the simulation results suggest that an operational setpoint closer to the glass transition temperature will favour the formation of compact and dense agglomerates as the contact deformation and the viscous energy dissipation are increased. Higher average particle-wall collision velocities promote compaction and breakage events. Furthermore, the average contact time is largely increased,



which will increase the agglomeration rate. Changing the bed mass has a less important effect on the particle structuration, as the collision dynamics are not strongly influenced. However, an increase of the bed mass leads to less regular particle circulation patterns and longer cycle times. Along with a higher bed mass the absolute particle concentration inside the draft tube is increased, but the fraction of particles positioned inside the draft tube is decreased. Therefore, the homogeneity of particle wetting will be negatively affected, if the bed mass is increased.

5.4 Experimental and computational study of the influence of process parameters on particle dynamics and product design

The agglomeration of food powders in fluidized beds is a well-established continuous process running at large scales in the food industry. Yet, the influence of numerous process parameters on the complex system of micro-mechanisms, which determine the agglomeration dynamics, is still not fully understood. To develop a better understanding of the influence and sensitivity of process parameters on the agglomeration of amorphous food powders, fluidized bed agglomeration experiments were performed in a Wurster-coater using amorphous spray-dried dextrose syrup DE 21. Pure water was injected as plasticizing agent to induce the agglomeration. An optimized set of process parameters was defined as a compromise between fast agglomerate growth and the overall process stability. An overview of the effect of different process variables is presented in this chapter. The applied experimental conditions are given in Table 5-5.

Table 5-5: Experimental conditions.

Parameter	Symbol	Unit	Value
Bed mass	m_{bed}	kg	1
Average primary particle diameter	$d_{p,0}$	mm	0.15
Fluidization air flow rate	\dot{V}_F	m^3/h	70 - 120
Atomizer flow rate	\dot{V}_{spout}	m^3/h	1.7 - 2.8
Temperature in the process chamber	T	$^{\circ}\text{C}$	30 - 90
Liquid injection rate	\dot{m}_{liq}	g/min	6 - 18
Injection time	t	min	0 - 80
Gap distance below Wurster tube	h_{gap}	mm	10 - 30



A detailed understanding of the influence of process parameters on the particle dynamics can be achieved using the DPM. Together with the experimental results, two simulation case studies are presented in this chapter analyzing the influence of the atomizer flow rate and of the gap distance between the bottom plate and the Wurster tube on the particle circulation. Combined with the experimental findings, the DPM is a valuable tool to improve the understanding of the agglomeration process. The applied simulation conditions are summarized in Table 5-6.

Table 5-6: Simulation conditions.

Parameter	Symbol	Unit	Value
Number of particles	N	-	150 000
Particle diameter	d_p	mm	2
Particle density	ρ_p	kg/m ³	1500
Normal coefficient of restitution	e_n	-	0.8
Sliding friction coefficient	μ	-	0.1
Poisson ratio	ν	-	0.25
Elastic modulus	E	GPa	0.25
Fluidization velocity (zone 1, below draft tube)	$u_{F,W}$	m/s	8 (= 10.1 u_{mf})
Fluidization velocity (zone 2, below annulus)	$u_{F,ann}$	m/s	3 (= 3.8 u_{mf})
Fluidization velocity (zone 3, near wall)	$u_{F,wall}$	m/s	4 (= 5.1 u_{mf})
Total particle mass	m_p	kg	0.94
Fluidization air flow rate	\dot{V}_F	m ³ /h	440
Atomizer air flow rate	\dot{V}_{spout}	m ³ /h	0.9 – 7.2
Time step for DEM simulation	Δt_{DEM}	s	$1 \cdot 10^{-6}$
Time step for CFD simulation	Δt_{CFD}	s	$1 \cdot 10^{-4}$
Total simulation time	t	s	3

The minimum fluidization velocity u_{mf} was approximated using the correlation proposed by Wen & Yu (1966a).



5.4.1 Influence of the fluidization air flow rate

The flow rate of the fluidization air affects both the particle dynamics (bed expansion, collision dynamics, mixing quality) and the heat and mass transfer kinetics in the fluidized bed. It is therefore an important influence factor for the agglomeration process. The effect of the fluidization air flow rate on the mean agglomerate diameter and on the stability of the process is shown in Table 5-7 for the agglomeration of maltodextrin in a Wurster-coater. The Sauter diameter of samples taken from the fluidized bed after 10 minutes of liquid injection is decreasing if the air flow rate is increased. This can be related to the higher drying potential of the fluidization air, limiting the availability of wet sticky particle surfaces. Furthermore, the agglomeration rate is reduced due to more intense agitation of the bed, which promotes disruptive mechanisms such as breakage and attrition.

Table 5-7: Influence of the fluidization air flow rate on growth rate and process stability.

Fluidization air flow rate	70 m ³ /h	100 m ³ /h	120 m ³ /h
Mean agglomerate diameter d_{32} at $t = 10$ min	450 μm	437 μm	396 μm
Stable process time	20 min	60 min	> 80 min

To maintain a stable fluidization of the growing agglomerates a certain minimum gas flow rate must be maintained, though. Otherwise the mixing in the bed is no longer homogeneous and the bed may collapse. For the given process conditions, the fluidization air flow rate should be kept at 100 m³/h, which is equivalent to a superficial gas velocity of approximately 4 times the minimum fluidization velocity of an agglomerate of 1 mm in diameter.

5.4.2 Influence of the process temperature

In an experimental study the influence of the process temperature on the agglomeration behaviour of amorphous maltodextrin was analysed. Two opposed effects are expected:

- The higher the process temperature, the faster is the evaporation of water from the particles. The availability of liquid binder is reduced and plasticized spots on the particle surface will dry out faster. Possibly also a larger fraction of the injected spray droplets will dry out to before being deposited on a particle. This should decrease the aggregation rate.

- The glass transition temperature of the amorphous material marks the onset of stickiness. If the operating temperature is increased, a larger fraction of the bed material will undergo glass transition and potentially form agglomerates. This should increase the aggregation rate.

Fig. 5-21 shows the evolution of the Sauter mean diameter of the agglomerates with time at 50°C, 70°C and 90°C process temperature. Obviously the agglomerate growth rate is very fast during the first 10 minutes, especially for the Wurster-coater. The build-up of agglomerates is the dominant mechanism during this initial phase of the process. After 10 minutes the growth rate decreases due to agglomerate breakage and attrition, which become more and more important.

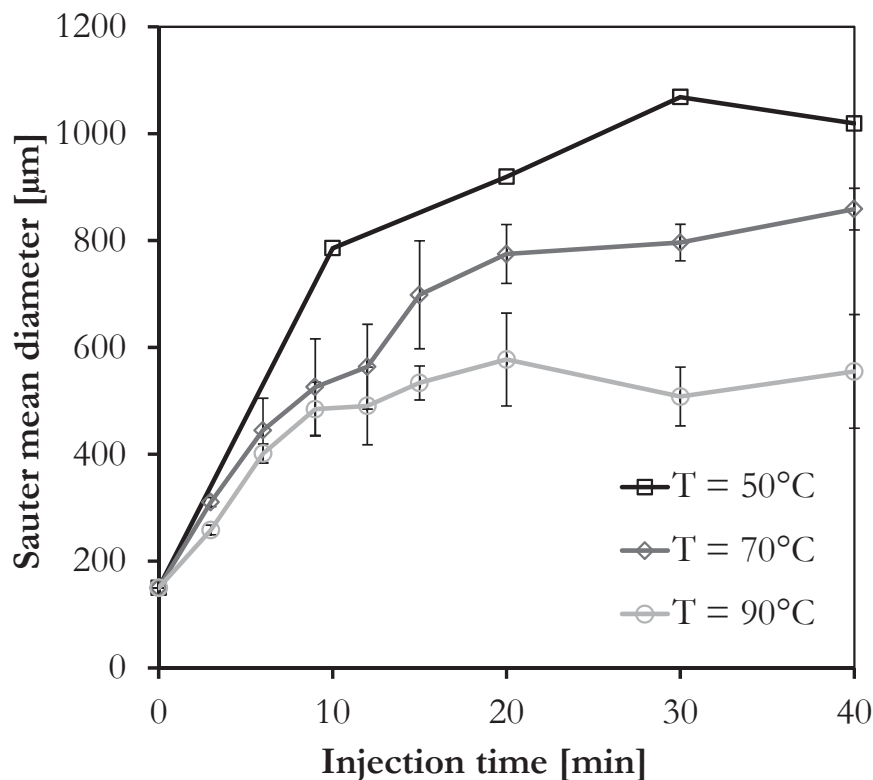


Figure 5-21: Measured effect of process temperature on the Sauter mean diameter of the agglomerates.

After 40 minutes of process time, the equilibrium between growth by agglomeration and size reduction through breakage seems to be reached. Breakage and compaction of the particles limit the growth rate afterwards. Regarding the influence of process temperature it can be seen in Fig. 5-21 that the Sauter mean diameter (see appendix A3) decreases, if the operating temperature is increased. This shows that the drying rate is the limiting factor for the growth kinetics of maltodextrin under the given process conditions. Especially at high process temperature many



spray droplets dry out, before they hit a particle, which results in slow particle growth. For the stickiness of the particles their surface moisture content is decisive. Higher temperature of the fluidization air increases the drying rate and reduces the equilibrium moisture content of the particles. Yet, the process becomes also more stable and a bed collapse can be avoided, if the operating temperature is kept above 70°C, which is in agreement with the experimental results of Palzer (2009).

The influence of the process temperature on the agglomerate strength is shown in Fig. 5-22 and Fig. 5-23 for two different size classes. Error bars indicate the 95 % confidence interval of the average value based on the number of tested samples (see Table 5-8). The tested agglomerates were sampled after 15 minutes of liquid injection. Since all agglomerates are in the glassy state, the impact of the process temperature on the mechanical behaviour is not as strong as expected. Still, due to the different drying potential in the process, the agglomerate structure and the thickness of the solid bridges vary, which is reflected by the results.

Table 5-8: Water content of the tested maltodextrin agglomerates as a function of the operating temperature. The corresponding glass transition temperature was calculated according to the model by Gordon & Taylor (1952), (Eq. 4-1).

Process temperature	50°C	60°C	70°C	80°C	90°C
Water content	6.4%	5.9%	5.1%	4.5%	3.7%
T_g according to Gordon & Taylor	57 °C	63 °C	72 °C	80 °C	92 °C
$T - T_g$ (at 25°C)	-32 K	-38 K	-47 K	-55 K	-67 K
Number of tested samples	150	159	123	118	133

For the breakage force (Fig. 5-22 a) and breakage energy (Fig. 5-23 b) an increasing trend can be observed with increasing temperature, up to a maximum between 60°C and 80°C. This finding can be correlated with an optimum for the viscous flow on the particle surface (sintering). At low temperature the viscosity is higher and the glass transition temperature may not be exceeded, which is a precondition for sintering. At high temperature, the drying rate is faster, which limits the time available for bridge stabilization. No clear dependency of breakage force on the agglomerate size was found. The process temperature does not show a significant influence on the contact stiffness of the solid bridges, as shown in Fig 5-22 b). The contact stiffness is a material property which should be independent of the process conditions.

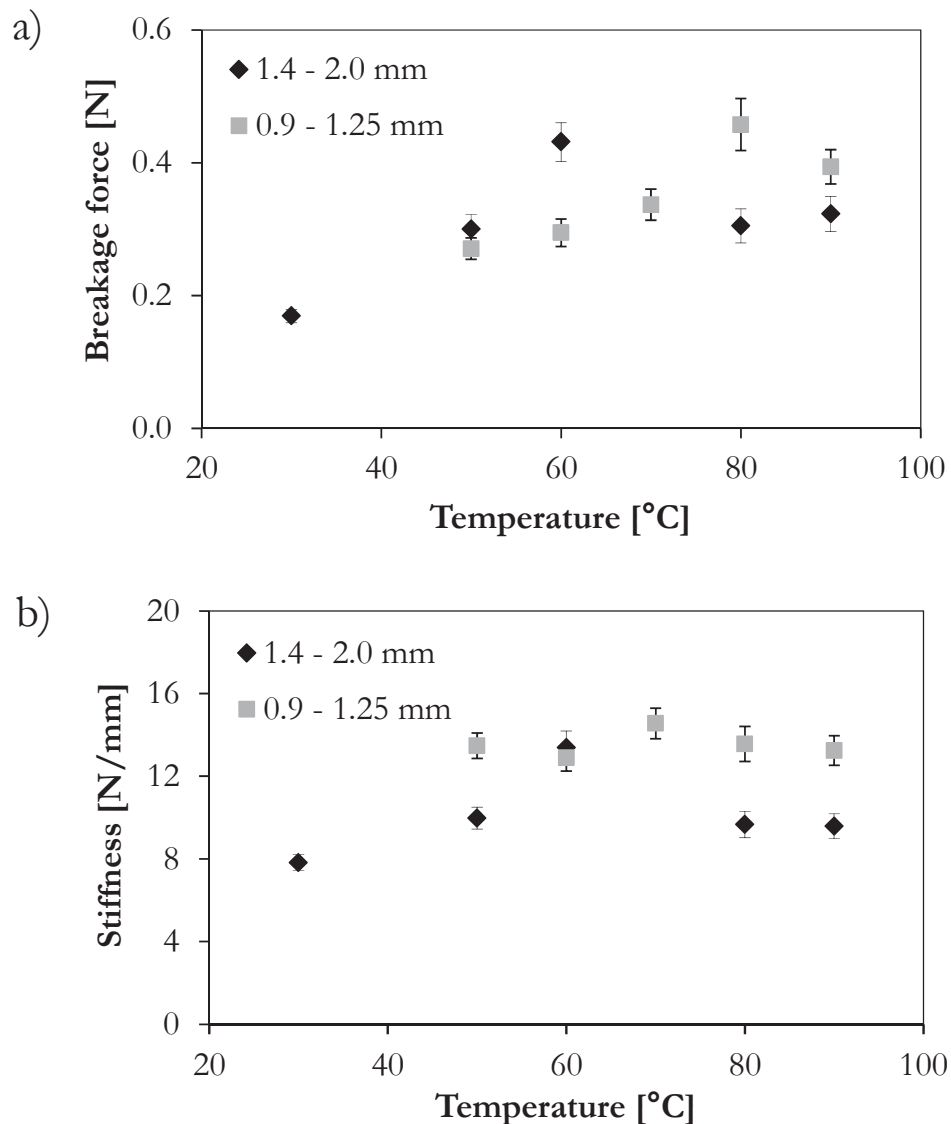


Figure 5-22: Measured average breakage force (a) and contact stiffness (b) as a function of the process temperature at an injection time of 15 min.

However, due to size-dependent differences in porosity and inner structure of the agglomerate network, the contact stiffness depends on the particle size, which is shown in Fig. 5-22 b). Small agglomerates are generally stiffer than large agglomerates. The displacement increment (see Fig. 5-23 a) is not significantly influenced by either the process temperature or the agglomerate size. The maximum deformation a solid bridge can withstand is relatively constant at 0.015 mm for the applied process conditions.

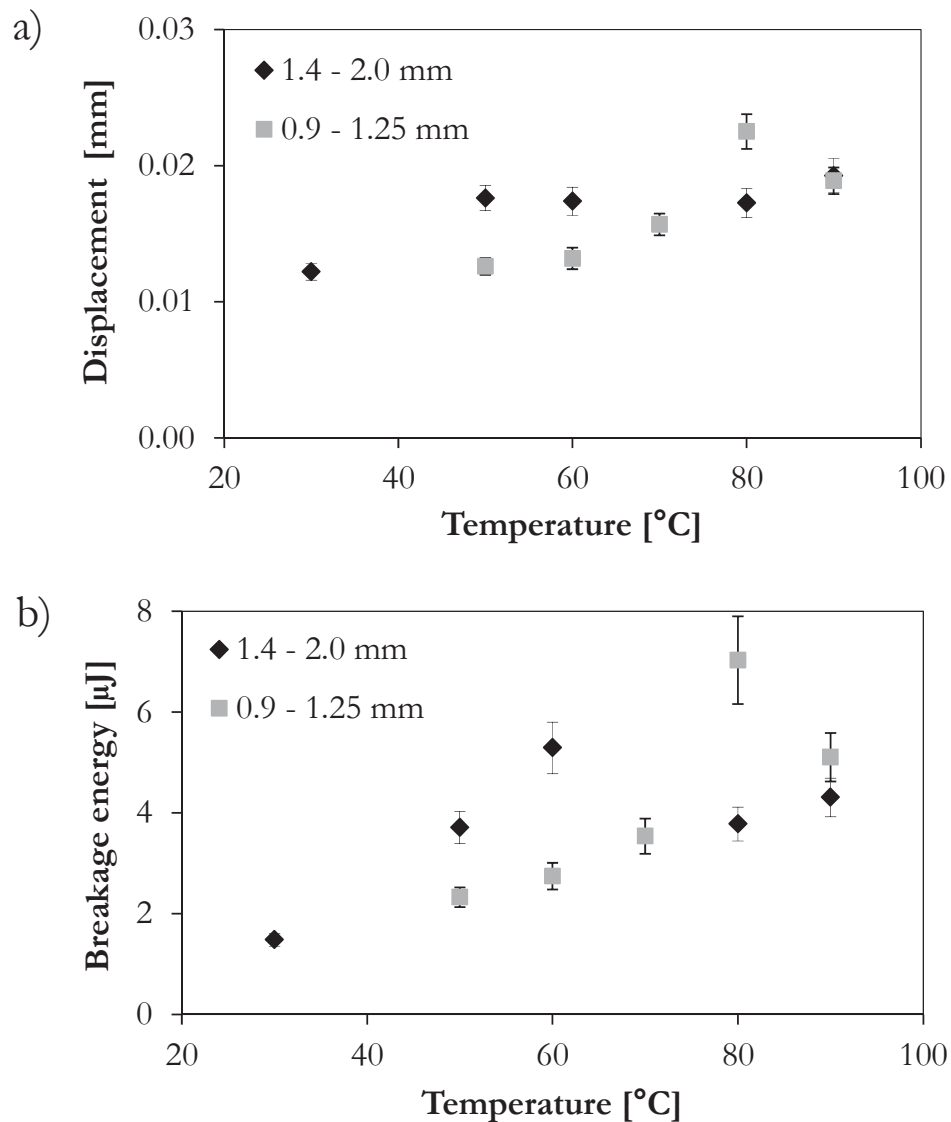


Figure 5-23: Measured average displacement increment (a) and breakage energy (b) as a function of the process temperature at an injection time of 15 min.

5.4.3 Influence of the liquid injection rate

For the agglomeration of food powders in fluidized beds the liquid injection rate is a decisive parameter, since viscous liquid layers are required to initiate the adhesion of particles. If the glass transition temperature is exceeded locally due to the addition of liquid droplets, the particle surface becomes sticky and colliding particles may adhere. Depending on the liquid injection rate, the availability of activated adhesive particle surfaces is limited to smaller or larger regions throughout the bed. The overall agglomeration rate is therefore expected to be dependent on the specific amount of liquid binder added to the process per unit of time. Growth rate and



throughput of the process are driven by the liquid injection rate. The more intense the solid agitation and mixing is in the granulator, the higher is the acceptable liquid injection rate, but local overwetting will provoke the formation of large lumps, which can even cause the collapse of the entire bed. Therefore, the liquid injection rate must be chosen as a compromise between fast agglomerate growth and process stability.

In this work the liquid injection rate was varied in a range of 6 - 18 g/min (0.6 - 1.8 % of the bed mass per minute). It was found that the growth rate during the first 10 minutes of liquid injection is not strongly influenced, but the process stability for longer process times is largely dependent on the liquid injection rate. An injection rate of 12 g/min (1.2 % of the bed mass per minute) allows the process to remain stable without lump formation for approximately 60 min. This injection rate is therefore used as reference in all other parameter studies.

5.4.4 Influence of the atomizer gas flow rate

In a combined experimental and numerical study the influence of the atomizer gas flow rate on the dispersion of the spray liquid added to the bed and on the particle dynamics in a Wurster-coater is analyzed. The distribution of the liquid among the particles plays a key role for the agglomeration in fluidized beds. In the Schlick Series 970 two-fluid nozzle (see Fig. 2-4), which is used in the experiments, compressed air is applied to disperse the liquid into small droplets. The atomizer gas flow rate can be adjusted in the experiments via a pressure valve and a rotameter. As shown in Fig. 5-24 the atomizer pressure and the capillary tip height h_D (see Fig. 2-4) have a strong effect on the mean droplet diameter, which was measured by laser diffraction (Sympatec Helos 12 LA). The higher the atomizer pressure, the smaller are the droplets. All scenarios regarding the atomization of the liquid phase in this work have in common that the mean droplet size is much smaller than the average particle diameter.

Increasing the atomizer flow rate is expected to inhibit the agglomeration, as small droplets dry out faster and are less likely to collide with particles. This suggests higher overspray rates. Furthermore, only small parts of a particle surface are wetted and become sticky, if the impacting droplet is small. The active sticky surface dries out fast and will become inactive, before the particle has reached the dense bottom zone of the bed. Therefore, smaller liquid droplets are expected to decrease the growth rate of the agglomerates. On the other hand the stability of the process may be improved, as higher atomizer flow rates lead to a more homogeneous liquid distribution in the system.

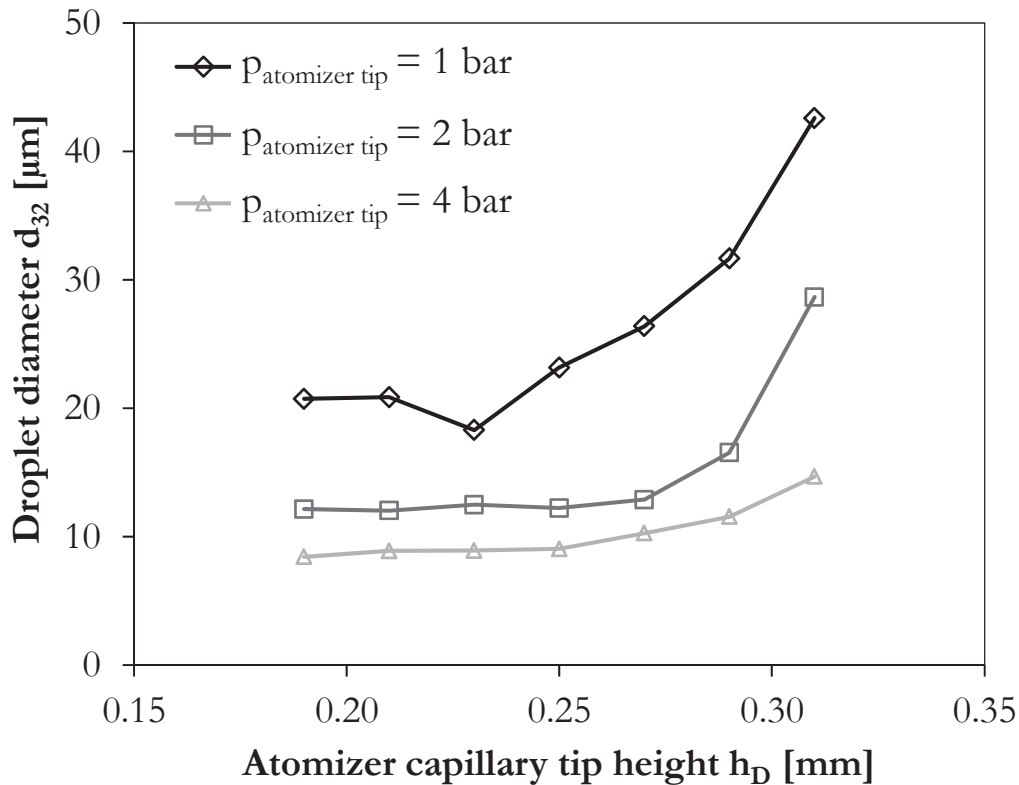


Figure 5-24: Measured Sauter mean diameter (d_{32}) of water droplets as a function of the atomizer pressure and the tip height h_D using a Schlick Series 970 two-fluid nozzle.

DPM simulation results show that the jet injection via the nozzle has a strong influence on the particle dynamics in the granulator. Three different scenarios are compared, fixing the atomizer gas flow rate to $0.9 \text{ m}^3/\text{h}$ (case 1), $4.5 \text{ m}^3/\text{h}$ (case 2) and $7.2 \text{ m}^3/\text{h}$ (case 3). The atomizer flow rates are calculated at atmospheric conditions (1 bar, $20 \text{ }^\circ\text{C}$). In Fig. 5-25, snapshots of the particle positions and their velocities are displayed. The colour indicates the particle velocity magnitude: blue particles move slowly ($v < 0.5 \text{ m/s}$) and red particles are fast moving ($v > 1.5 \text{ m/s}$). It can be seen that a higher jet flow rate provokes higher particle velocities inside the Wurster tube. Accordingly the height of the particle fountain increases with higher spout velocity from 430 mm above the nozzle tip in case 1 to 490 mm in case 3.

The particle movement is directed upwards inside the draft tube and downwards in the annulus. This indicates that the circulating regime is intact in a wide fluidization range. At the top of the Wurster tube a deceleration of the particles can be observed and for low atomizer flow rates, as in case 1. Here, some particles are moving downwards at the inside of the Wurster tube, which indicates unwanted backmixing. This is in accordance with the experimental results for low atomizer flow rates: Back-mixing leads to inhomogeneous wetting, which can cause the formation of lumps.

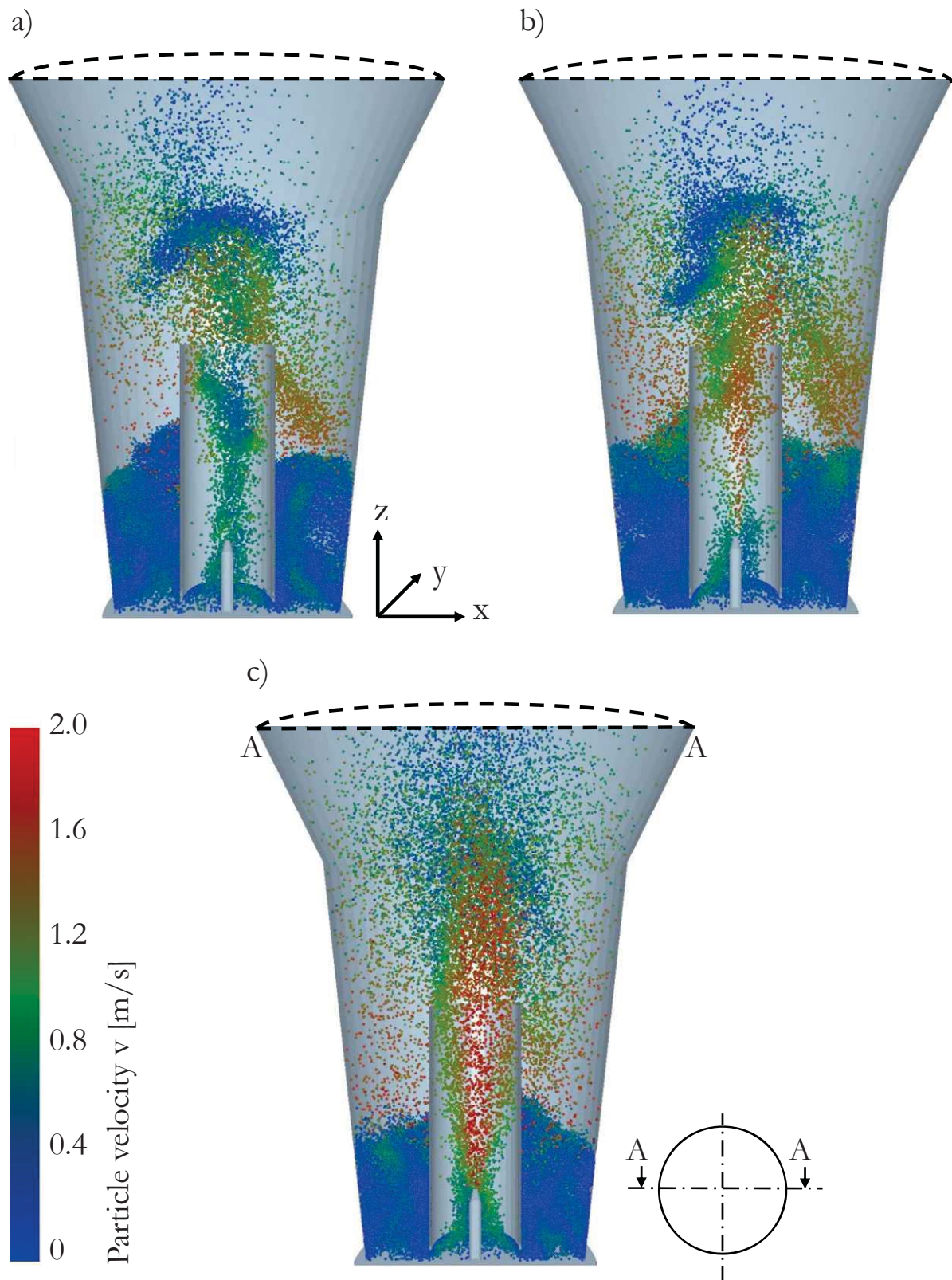


Figure 5-25: Influence of the atomizer flow rate on instantaneous particle positions and particle velocity distributions in the Wurster-coater: a) $0.9 \text{ m}^3/\text{h}$ (case 1), b) $4.5 \text{ m}^3/\text{h}$ (case 2), c) $7.2 \text{ m}^3/\text{h}$ (case 3).

**Table 5-9: Parameters characterizing the particle motion inside the Wurster tube for simulation cases 1 to 3.**

Parameter	Symbol	Unit	Case 1	Case 2	Case 3
Average solids volume fraction	ε_s	%	5.9	5.1	5
Average particle velocity	$v_{p,\text{mean}}$	m/s	0.71	0.88	0.94
Particle-particle collision frequency	f_c	s^{-1}	102	80	64
Average particle-particle collision velocity	v_c	m/s	0.26	0.29	0.35
Average contact time	t_c	μs	69	65	63

With the help of a detailed analysis of the DPM data on the particle motion inside the Wurster tube, the visual observations concerning the particle distribution in the granulator from Fig. 5-25 can be quantified (see Table 5-9). By increasing the jet velocity, the average solids volume fraction inside the draft tube is reduced up to a certain limit. If the fluid dynamic conditions create a stable particle circulation, the quantity of particles dragged into the tube is controlled by the gap distance below the Wurster tube (case 2 and 3). If a stable circulating regime is not established, the average particle residence time in the Wurster tube increases (case 1). Particles that are stagnant or fall back downwards in the Wurster tube due to the insufficient gas velocity cause an increase of the solids volume fraction. Higher particle concentrations in the draft tube will increase the wetting efficiency and cause agglomeration rates. The atomizer flow rate shows a clear correlation with the average particle velocity $v_{p,\text{mean}}$. The collision frequency f_c on the other hand decreases with increasing jet velocity. Both results indicate a higher agglomeration probability for low atomizer flow rates. The reduction of the collision frequency with higher jet flow rates can be related to the fact that regions of high solids volume fraction along the wall of the draft tube are formed less often and that the particle flow follows more uniform parallel trajectories. Collisions between wet particles inside the Wurster tube are particularly important to predict agglomeration events. To build up agglomerates, the kinetic energy of the collision partners must be dissipated by viscous forces. Increasing the relative collision velocity v_c and decreasing the contact time t_c will prevent the formation of agglomerates (Ennis et al., 1991; Antonyuk et al., 2009).

Based on the experimental findings for the mean droplet size and the simulation results for the particle dynamics it is expected that the agglomeration rate decreases with higher atomizer flow rates. This behaviour could be verified experimentally. In Fig. 5-26 the effect of the atomizer



flow rate on the growth of the agglomerates is shown. Obviously, the growth rate during the initial phase of the process is strongly dependent on the jet injection at the nozzle.

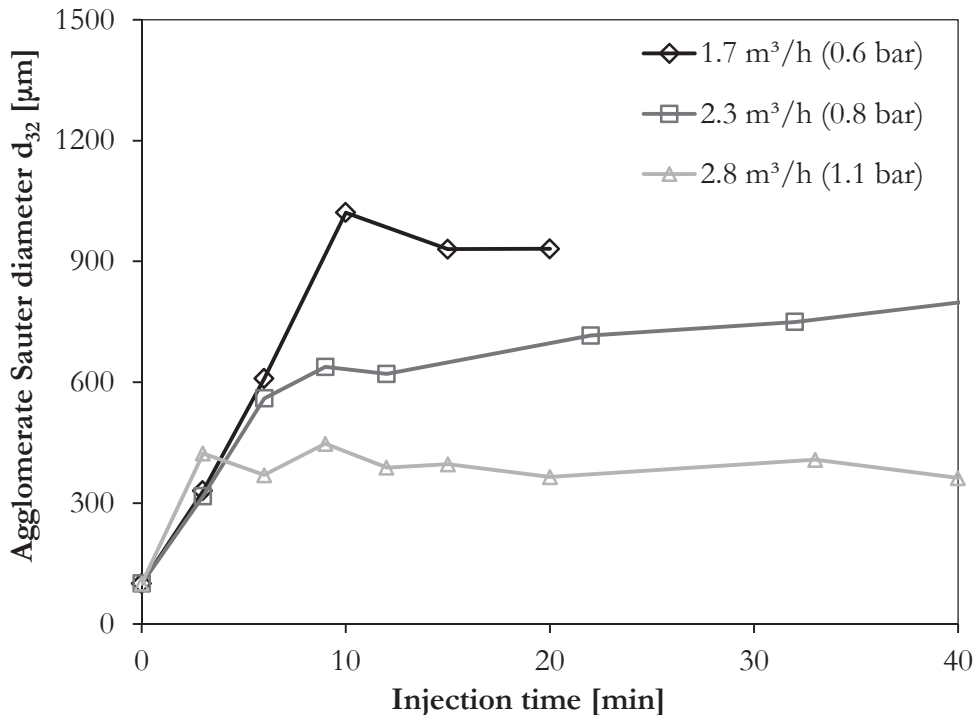


Figure 5-26: Measured mean agglomerate diameter as a function of the injection time for different atomizer gas flow rates in the Wurster-coater. Wurster gap distance: 30 mm, atomizer capillary tip height h_D : 0.29 mm.

For the lowest atomizer flow rate in the experiments (1.7 m³/h), the Wurster tube was blocked by large lumps after 20 min. A sufficiently high atomizer flow rate is therefore necessary to maintain homogeneous wetting conditions and to keep the agglomeration process stable.

It can be concluded from the experiments and the simulation results that the momentum of the jet injection can be used to control or to prevent agglomeration in a Wurster-coater. The atomizer flow rate must be kept above a minimum level, as intense mixing and agitation are needed inside the draft tube to break up larger lumps once they are formed. A further increase of the atomizer flow rate reduced the wetting efficiency and leads to slower particle growth. In addition the mechanical properties of the material and their distribution amongst the particle bulk and single particles have to be considered.



5.4.5 Influence of the gap distance between Wurster tube and bottom plate

A specific process parameter of the Wurster-coater is the gap distance below the Wurster tube. Based on experience the supplier of the equipment (Glatt Ingenieurtechnik GmbH, Weimar) recommends as a rule of thumb to choose the gap distance in the range of 5-10 times the average particle diameter of the product. In this work the effect of the gap distance on the particle circulation and on the particle concentration in the spray zone is analyzed in detail with the help of DPM simulations. An experimental study is presented to verify the predictions obtained from the model.

The gap distance between the distributor plate and the Wurster tube is a parameter that strongly influences the particle dynamics inside the granulator as it controls the recirculation of particles into the spout. Gap distances of 10, 20 and 30 mm were compared in the case studies 3 to 5. These distances are equal to 5, 10 and 15 times the particle diameter. The simulation parameters are given in Table 5-6. By adjusting the gap distance below the Wurster tube, the number of particles that are dragged into the draft tube can be controlled. It can be seen in Fig. 5-27 that larger gap sizes increase the particle concentration in the Wurster tube.

In case 3, particles are only present at the center of the tube. All particles rise at a velocity above 1 m/s, which is indicated by green and red colour. Contrary to that, particles can be found spread over the whole diameter of the Wurster tube if the gap distance is increased (case 4). Near the wall of the tube particles move at low velocity, indicated by blue colour. Particles are slowed down, but the circulating fluidization regime is still intact. In case 5 the particle concentration inside the draft tube is further increased. The entire cross section of the Wurster tube is filled. In the center the particles are accelerated by the jet and move at high velocity (red colour). However, along the walls particle strands slide downwards, which clearly indicates unwanted backmixing. The simulations show that at gap distances larger than 10 times the particle diameter (case 5), the circulating regime is no longer intact. The overall flow regime is less homogeneous and tends to become unstable.

A quantitative analysis of the effects of an increased gap distance below the Wurster tube is presented in Table 5-10. It is found that the average solids volume fraction inside the draft tube increases by 70 % from case 3 to case 5. At the same time, the average particle velocity is reduced, which is again mainly related to the formation of particle strands at the wall of the tube. In these regions of high solids volume fraction the frictional energy dissipation is increased, leading to lower average particle velocities. For the collision frequency, no clear trend is



observed. Along with the reduced particle velocity, also the average relative collision velocity decreases, as most collisions occur among slowly moving clustered particles.

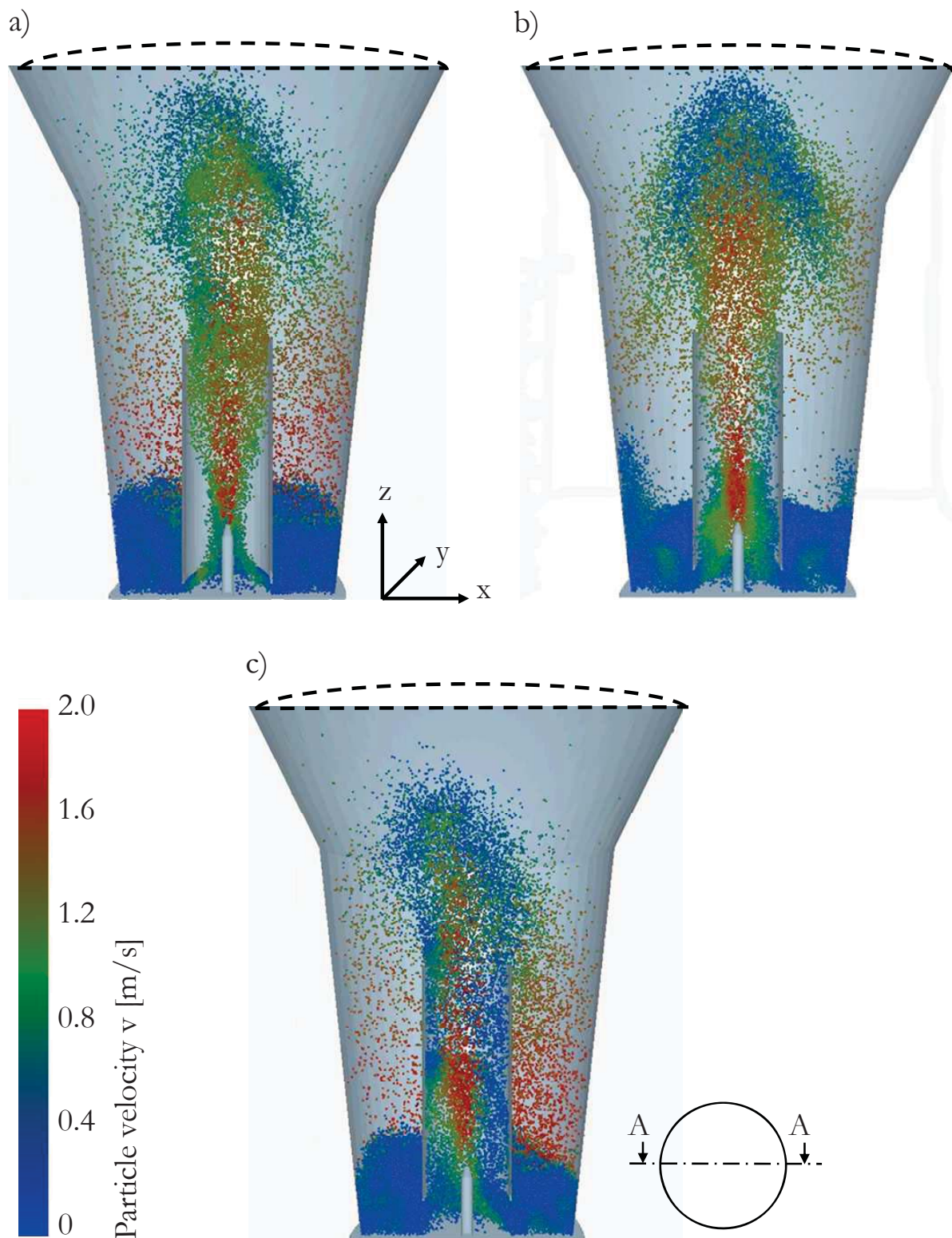


Figure 5-27: Instantaneous particle positions and particle velocity distributions in the Wurster-coater for different gap distances: a) 10 mm (case 3), b) 20 mm (case 4), c) 30 mm (case 5).



Finally, an increasing average contact is found with increasing gap distance, which may promote the agglomeration of sticky particles.

Table 5-10: Parameters characterizing the particle motion in the Wurster tube for simulation cases 3 to 5.

Parameter	Symbol	Unit	Case 3	Case 4	Case 5
Average solids volume fraction	ϵ_s	%	5.1	6.6	8.8
Average particle velocity	$v_{p,\text{mean}}$	m/s	1.06	0.86	0.7
Particle-particle collision frequency	f_c	s^{-1}	91	71	87
Average particle-particle collision velocity	v_c	m/s	0.34	0.32	0.28
Average contact time	t_c	μs	63	65	68

From the simulation results an increased agglomeration rate can be expected for larger gap distances below the Wurster tube due to more efficient wetting and less overspray. On the other hand, adverse effects such as backmixing of particles falling into the Wurster tube from the top, degradation of the particle circulation patterns and a broader residence time distribution of the particles in the spray zone were observed for gap distances larger than 10 times the mean particle diameter. Inhomogeneous wetting is expected to produce a wider agglomerate size distribution. Furthermore, the fluidized bed may collapse, if large agglomerates cannot be transported out of the tube by the gas jet.

Experimentally the influence of the gap distance below the Wurster tube on the growth rate of maltodextrin agglomerates was investigated. If the gap distance is small, a lower growth rate was found as shown in Fig. 5-28. On the other hand, gap distances larger than 30 mm lead to overwetting and lump formation in the investigated case. This is in good agreement with the predictions of the DPM.

However, the size of the gap between bottom plate and Wurster tube has to be larger in the experiments than 10 times the mean particle diameter, which was predicted as optimum for a stable circulation in the DPM simulations. For irregular shaped particles such as maltodextrin agglomerates the tendency to block the gap is very high due to interlocking of the complex particle structures. Since only spherical particles were considered in the simulations, this behaviour cannot be represented by the DPM so far.

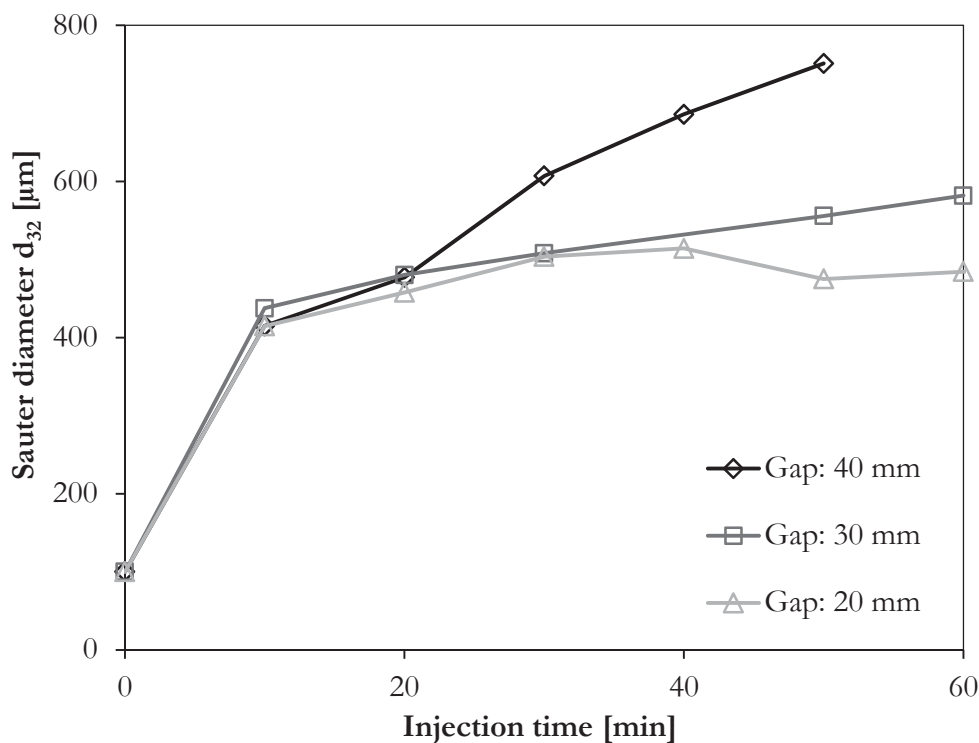


Figure 5-28: Measured evolution of the Sauter diameter (d_{32}) of the agglomerates (DE 21 maltodextrin) as a function of the injection time for different gap distances.

5.4.6 Conclusion

In this section the influence of different process parameters relevant for the agglomeration of amorphous water-soluble food powders in a Wurster-coater was investigated in a combined experimental and numerical study. The fluidization air flow rate, the process temperature, the liquid injection rate, the atomizer air flow rate and the gap distance between bottom plate Wurster tube were considered individually regarding their influence on agglomerate growth rate and overall process stability. It can be concluded for all considered parameters that one always has to compromise between fast growth at intensive particle wetting conditions and long term process stability. For the economics of an agglomeration process it is desirable to reduce the total process time necessary to build up agglomerates of a defined size and strength. This can be achieved by increasing the spray rate and simultaneously increasing the particle flux through the spray zone in order to avoid over-wetting and subsequent agglomeration. Another option would be to increase both the spray rate and the temperature of the fluidization air.

DPM simulations have proven to be an excellent tool to develop a better understanding of the effect of process parameters on the particle dynamics, which are hard to obtain experimentally.



Based on the presented results, an optimal set of process parameters for the agglomeration of maltodextrin DE 21 in a Glatt GF3 Wurster coater was compiled, which is summarized in Table 6-7. These process conditions are used as reference in further experiments for the investigation of the effect of the granulator geometry on the agglomeration behaviour.

Table 5-11: Optimal process conditions for the agglomeration of DE 21 maltodextrin in a Glatt GF3 Wurster-coater.

Parameter	Unit	Value
Fluidization air	m ³ /h	100
Bed temperature	°C	70
Atomizer flow rate	m ³ /h	2.3
Liquid injection rate	g/min	12
Mean droplet diameter	µm	40
Wurster gap distance	mm	30

Although these optimum process conditions strictly apply only for the used bed material and the used lab scale equipment, the observed phenomena are valid for any amorphous food powder being agglomerated in a fluidized bed.



5.5 Numerical study on the influence of viscous energy dissipation

Viscous forces in a liquid film contribute significantly to the energy dissipation in case of a collision between surface-wet particles, as shown experimentally in section 4.2.3. So far, only dry particle interactions were considered using the DPM. In this section, the effect of an additional viscous force on the particle and collision dynamics in a Wurster-coater is investigated.

5.5.1 Simulation conditions

For this purpose the DPM is extended by a viscous force model according to Popov (2010), as described in section 3.7. The following assumptions are made for the simulation study presented in this section:

- The liquid is present on the particle surface, forming a film with constant thickness h .
- The properties of the core particle are not altered due to the presence of a liquid film.
- The probability of a collision is equal at all positions on the particle surface, no matter if the position is wet or dry.
- Viscous forces are active, if one or both contact surface positions are wet. The probability for this is given by the wetted surface fraction Φ , which is defined as the ratio between the area covered by a liquid film and the total particle surface.
- No liquid is exchanged between particles during collisions.
- The liquid mass is spread homogeneously among all particles in the system ($\Phi = \text{const.}$).

The applied simulation conditions are summarized in Table 5-12. Further simulation parameters and gas flow properties are given in Table 5-1.

In comparison to a dry reference (case 1), three simulation cases regarding the influence of viscous energy dissipation on the particle and collision dynamics in a Wurster-coater are analyzed in this section. In case 2 the wetted surface fraction is set to $\Phi = 10\%$, which is a realistic value for fluidized bed granulation (Heinrich, 2001). The viscosity of the liquid film is defined as $\eta_{\text{liq}} = 0.01 \text{ Pa s}$, which corresponds approximately to the value found for whipping cream. In case 3 the viscosity of the liquid film is increased to $\eta_{\text{liq}} = 0.1 \text{ Pa s}$, which corresponds



approximately to the behaviour of olive oil at room temperature. In case 4 the wetted surface fraction is reduced to $\Phi = 5\%$, keeping the liquid viscosity at $\eta_{\text{liq}} = 0.1 \text{ Pa s}$.

Table 5-12: Simulation conditions for the case study including viscous energy dissipation.

Parameter	Symbol	Unit	Value
Elastic modulus	E	GPa	1.0
Restitution coefficient	e	-	0.4
Particle diameter	d_p	mm	3.0
Bed mass	m_{bed}	kg	0.377
Number of particles	N	-	44500
Sliding friction coefficient	μ	-	1.0
Wetted surface fraction	ϕ	%	0, 5, 10
Liquid film viscosity	η_{liq}	Pa s	0.01, 0.1
Liquid film thickness	h	μm	50

5.5.2 Influence of viscous forces on the particle dynamics

For all 4 investigated simulation cases, snapshots of the particle positions and the velocity distributions at the simulation time $t = 2.2 \text{ s}$ are shown in Fig. 5-29.

While in the dry reference case (Fig. 5-29 a) particles are pushed up to approximately 150 mm above the top end of the draft tube in the spout, the elevation of the particle fountain is smaller in the three cases involving viscous forces. This can be explained by the additional energy dissipation introduced by viscous forces, which reduce the kinetic energy of the particles inside the Wurster-coater. Regarding the particle positions, the results obtained in the three cases including viscous forces (Fig. 5-29 b-d) are very similar.

A quantitative analysis of the influence of viscous forces on the particle dynamics is given in Table 5-13. It can be seen that the additional viscous forces lead to a reduction of the average particle velocity of 12 %. This effect is more pronounced for particles positioned inside the dense bed (-13.5 %) than for those inside the Wurster tube (-7 %). If viscous forces are considered, the fractions of particles positioned in the dense bed and inside the Wurster tube is slightly increased, since fewer particles are pushed up into the expansion chamber (see also Fig. 5-29).

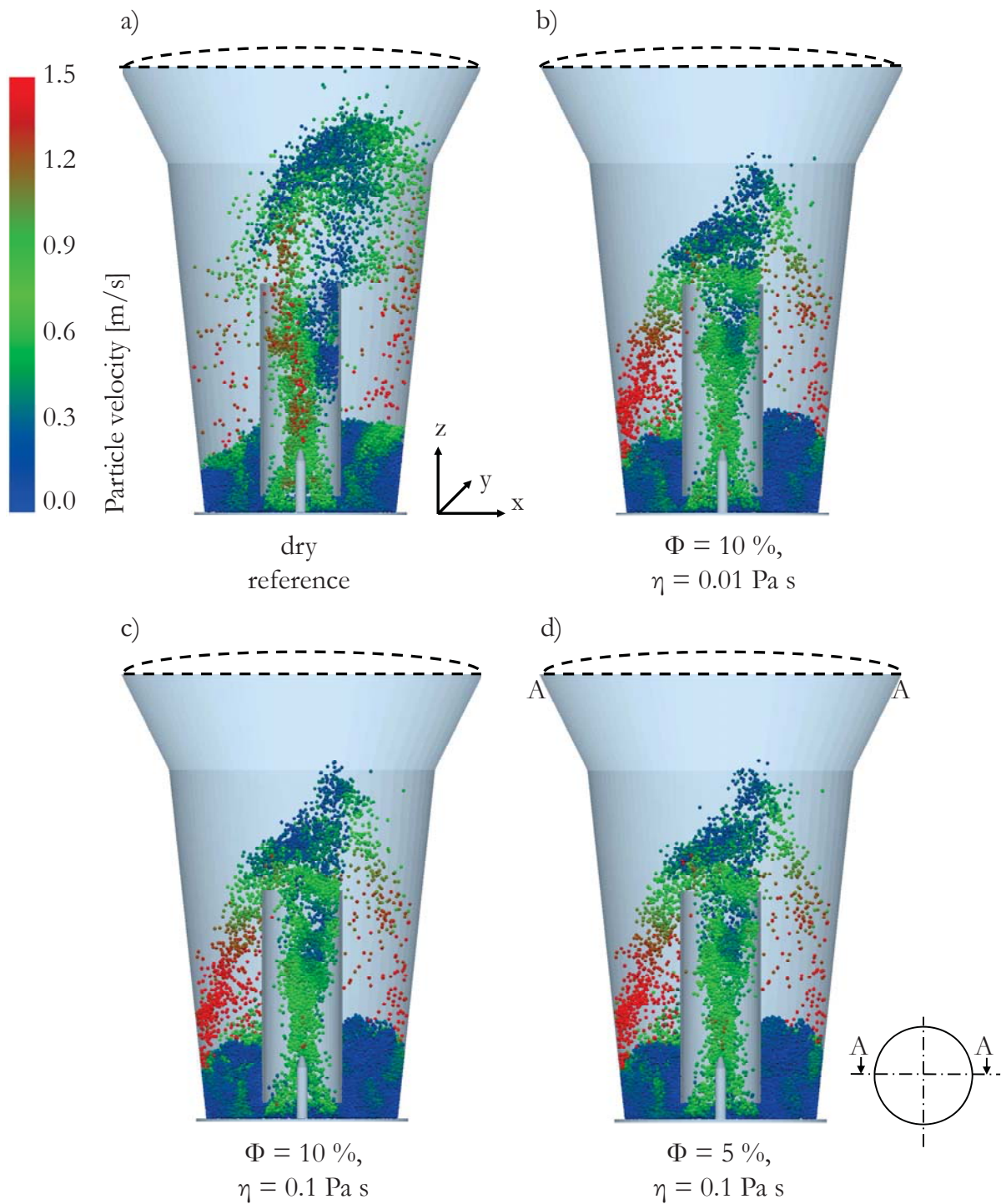


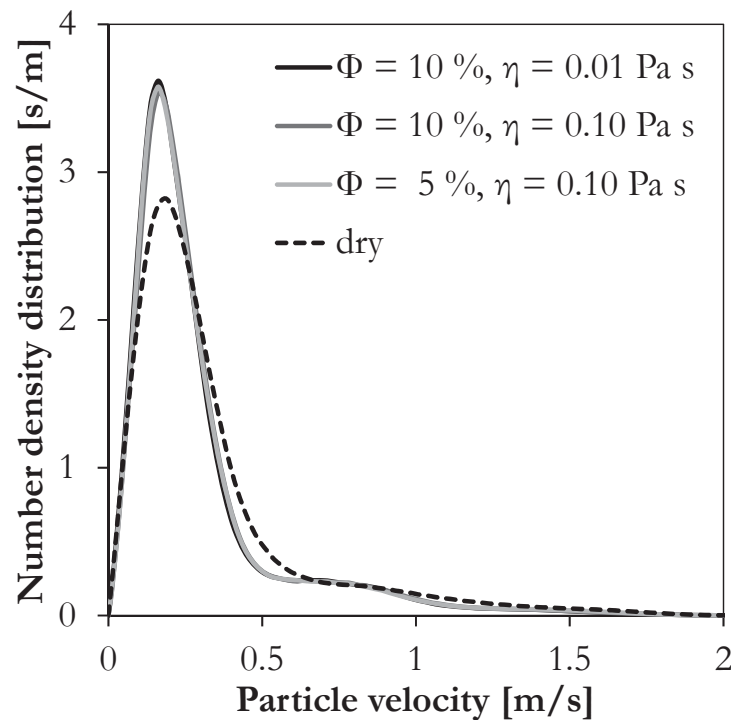
Figure 5-29: Instantaneous particle positions and velocity distributions in the Wurster-coater at simulation time $t = 2.2 \text{ s}$ for different scenarios involving viscous forces: a) case 1 (dry reference), b) case 2 ($\Phi = 10\%$, $\eta_{\text{liq}} = 0.1 \text{ Pa s}$), c) case 3 ($\Phi = 10\%$, $\eta_{\text{liq}} = 0.01 \text{ Pa s}$), d) case 4 ($\Phi = 5\%$, $\eta_{\text{liq}} = 0.1 \text{ Pa s}$).


Table 5-13: Influence of viscous forces on the particle dynamics in a Wurster-coater.

Case	Mean particle velocity [m/s]	Mean angular velocity [rad/s]	Particle fraction in dense bed [%]	Particle fraction in Wurster [%]	Mean particle velocity Wurster [m/s]	Mean particle velocity Annulus [m/s]
dry	0.343	44.96	76.70	7.27	0.778	0.248
$\Phi = 10 \%$, $\eta = 0.01 \text{ Pa s}$	0.296	40.43	78.85	7.75	0.720	0.213
$\Phi = 10 \%$, $\eta = 0.10 \text{ Pa s}$	0.301	41.77	78.84	7.75	0.728	0.217
$\Phi = 5 \%$, $\eta = 0.10 \text{ Pa s}$	0.301	41.17	79.15	7.64	0.723	0.215

Significant differences between the 3 cases including viscous forces cannot be observed except for the angular particle velocity. In the investigated range of parameters the particle dynamics are not very sensitive to the viscosity of the liquid film and to the wetted surface fraction.

In Fig. 5-30 the density distribution of the particle velocities inside the Wurster-coater is shown for all 4 simulation cases. Two contributions related to particles positioned inside the dense bed (peak at 0.2 m/s) and to particles in the spout channel (small peak at 0.7 m/s) can be found. The distribution is clearly shifted towards lower velocities, if viscous forces are considered. Again, differences between the cases 2-4 are not significant.


Figure 5-30: Influence of viscous forces on the particle velocity distribution in a Wurster-coater.



For the simulation cases 1, 2 and 3 the vertical profile of the solids volume fraction and of the particle velocity is shown in Fig. 5-31. While the particle concentration inside the dense bed and also the expansion of the dense bed are not significantly influenced by viscous forces (see Fig. 5-31 a), the average particle velocity is lower for the entire range of the profile, if viscous forces are taken into account. Furthermore it can be seen in Fig. 5-31 b) that the expansion of the bed in the dilute zone above the Wurster tube is reduced in the cases 2 and 3.

The radial distribution of the particles and their velocity is shown in Fig. 5-32 for the dense bed (height $z = 20$ mm, analogue to Fig. 5-4) and in Fig. 5-33 for the upper end of the Wurster tube (height $z = 220$ mm, analogue to Fig. 5-5).

For both the solids volume fraction (Fig. 5-32 a) and the particle velocity (Fig. 5-32 b), a clear separation can be seen between the dense annulus zone with low particle velocity and the spout zone at the center of the Wurster-coater, where the particles are accelerated. The separation between the two zones is enforced by the walls of the draft tube, which are positioned at $x = \pm 40$ mm at the center of the equipment. Differences between the dry reference simulation case and the cases including viscous forces can be identified, but quantitatively the effects are small. At a higher position in the Wurster-coater (height $z = 220$ mm), the effect of viscous forces on the particle dynamics can be seen more clearly, as shown in Fig. 5-33. If viscous forces are included in the simulation, higher average particle concentrations are found at the center ($x = 0$) and at the right side of the annulus ($x = 60$ mm). The lack of symmetry in the radial particle concentration profile may be related to the influence of the fixation of the draft tube (see Fig. 5-1). For the upper region of the bed clear differences of the average particle velocity are observed in Fig. 5-33 b between the dry reference case and the simulations including viscous forces. In the center of the Wurster tube ($x = 0$) as well as in the annulus, higher particle velocities are found in the reference case compared to cases 2-4. This corresponds to the image of a stagnant bed at the upper end of the Wurster tube, as seen in Fig. 5-29 b, c and d.

It can be concluded that viscous forces have a clear effect on the particle dynamics, as the average particle velocity and the expansion of the bed are reduced. However, in the investigated range the particle motion inside the Wurster-coater was found to be mostly insensitive to variations of the viscosity of the liquid film as well as of the wetted surface fraction.

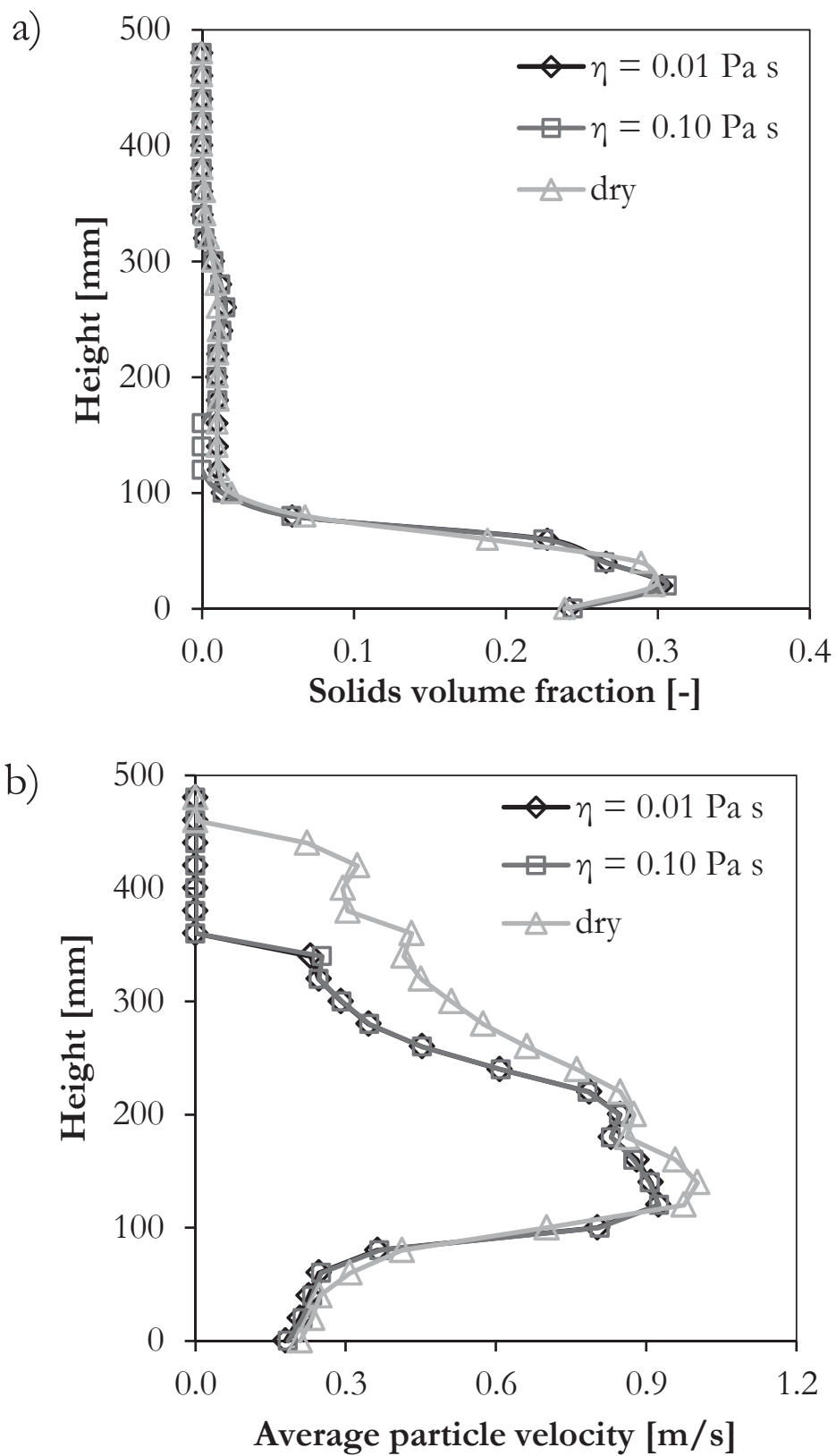


Figure 5-31: Influence of the viscosity of the liquid film on the vertical profile of the particle concentration (a) and of the particle velocity (b) in a Wurster-coater. Wetted surface fraction $\Phi = 10\%$.

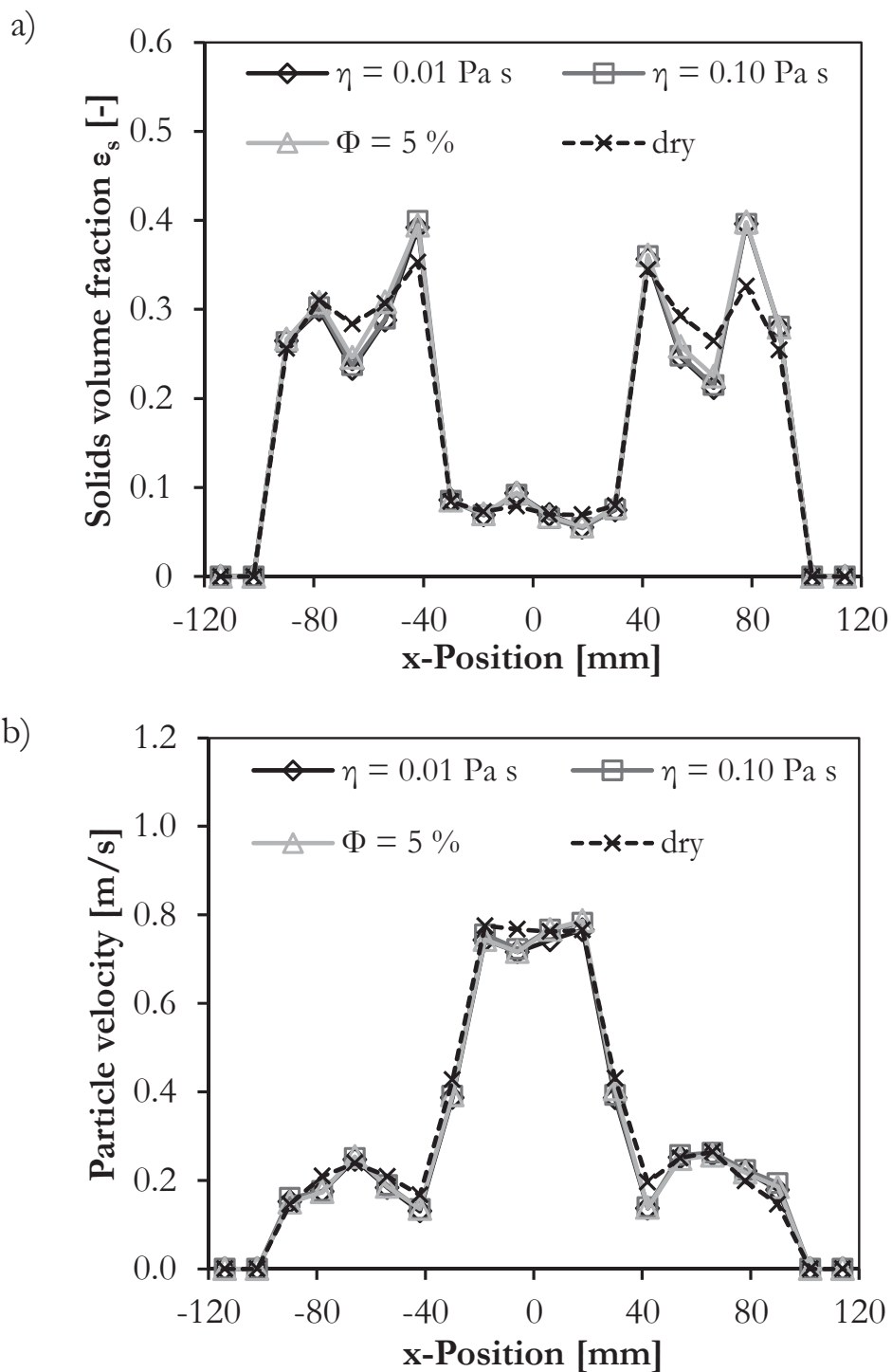


Figure 5-32: Influence of viscous forces on the radial particle distribution (a) and the particle velocity profile (b) in the dense bed of a Wurster coater (height $z = 20$ mm, as indicated in Fig. 5-4).

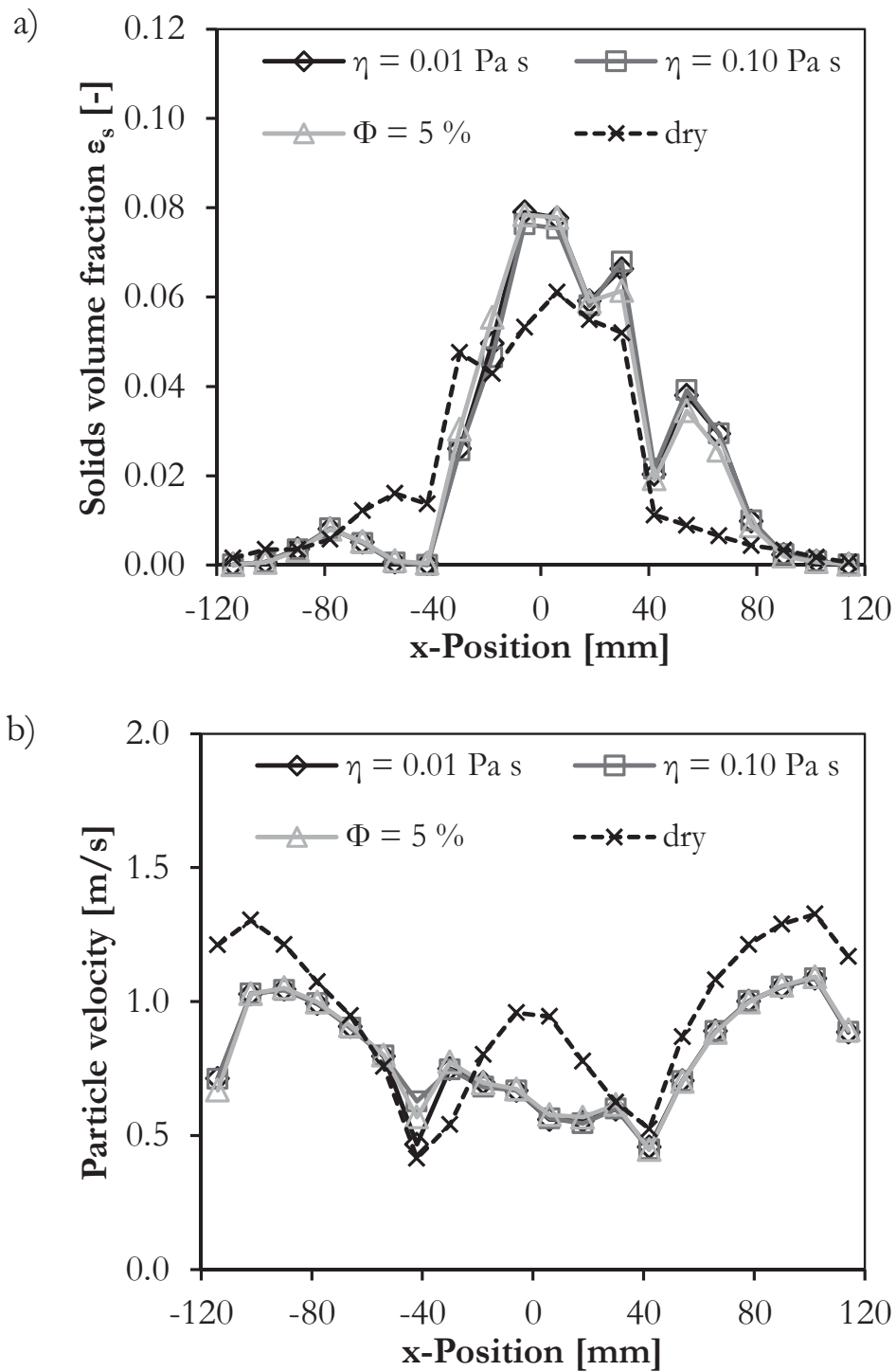


Figure 5-33: Influence of viscous forces on the radial particle distribution (a) and the particle velocity profile (b) at the upper end of the Wurster tube (height $z = 220$ mm, as indicated in Fig. 5-5).



5.5.3 Influence of viscous forces on the collision dynamics

The introduction of additional viscous energy dissipation has very strong effects on the collision dynamics in a Wurster-coater, which are discussed in this section. An overview on these influences is given in Table 5-14 for the dry reference case and the 3 simulation cases including viscous forces.

As described in section 3.6, collisions are defined as pairwise encounters of particles, which come into contact, stay in contact for a certain duration and separate again. Throughout the duration of the collision adhesive and repulsive forces are calculated according to the contact model equations. It is important to note that the encounter of two particles is only counted as collision, if they separate again after their contact. This means that the repulsive contact forces must be larger than the adhesive forces. At this point, the viscous forces play a dominant role, especially in the dense bed of a Wurster-coater, where the majority of the particle encounters happen at very low relative velocity in the order of 0.05 m/s (see Table 5-14). For these encounters at low kinetic energy, viscous forces can overcome the repulsive contact forces, which means that the particle stay in contact and form loose agglomerates. As long as the aggregated particles stay in contact (i.e. the overlap remains greater than zero), the encounter is not counted as a collision.

Table 5-14: Influence of viscous forces on the collision dynamics in a Wurster-coater.

Case	Mean particle- particle collision velocity [m/s]	Particle-particle collision velocity (inside draft tube) [m/s]	Particle-particle collision velocity (inside dense bed) [m/s]	Mean particle- wall collision velocity [m/s]	Mean collision duration [μs]
dry	0.0465	0.2087	0.0455	0.1489	175
$\Phi = 10 \%$, $\eta = 0.01 \text{ Pa s}$	0.1618	0.2362	0.1475	0.3178	21353
$\Phi = 10 \%$, $\eta = 0.10 \text{ Pa s}$	0.1636	0.2431	0.1490	0.3209	23351
$\Phi = 5 \%$, $\eta = 0.10 \text{ Pa s}$	0.1647	0.2388	0.1505	0.3299	21887

Therefore, the consideration of viscous contact forces has a very strong influence on the average collision velocity and on the collision duration, as shown in Table 5-14. Since in the dense bed more than 90 % of the collisions occur at a kinetic energy below the separation threshold, viscous forces reduce the number of counted collisions accordingly. Since all particle impacts at low relative velocity are not counted as collisions due to the missing separation step, the average relative impact velocity of those collisions that are taken into account is increased from 0.05 m/s



for the dry reference case to 0.16 m/s for the simulation cases 2, 3 and 4. Inside the Wurster tube the average impact velocity is higher, so that the separation threshold is exceeded for 65 % of the collisions. Viscous contact forces also largely increase the duration of particle collisions. On the one hand they act as damping mechanism which reduces the relative particle motion and therefore increases the contact time. On the other hand, all particle encounters which lead to the formation of agglomerates are cumulating their contact time up to the point, where the particles separate due to further collisions with other particles or the equipment walls. Therefore, the average duration of a collision is increased by a factor of 125, if viscous forces are taken into account in the DPM simulation.

In Fig. 5-34 the density distribution of the relative collision velocity is shown for all particle-particle collisions inside the dense bed of the Wurster-coater.

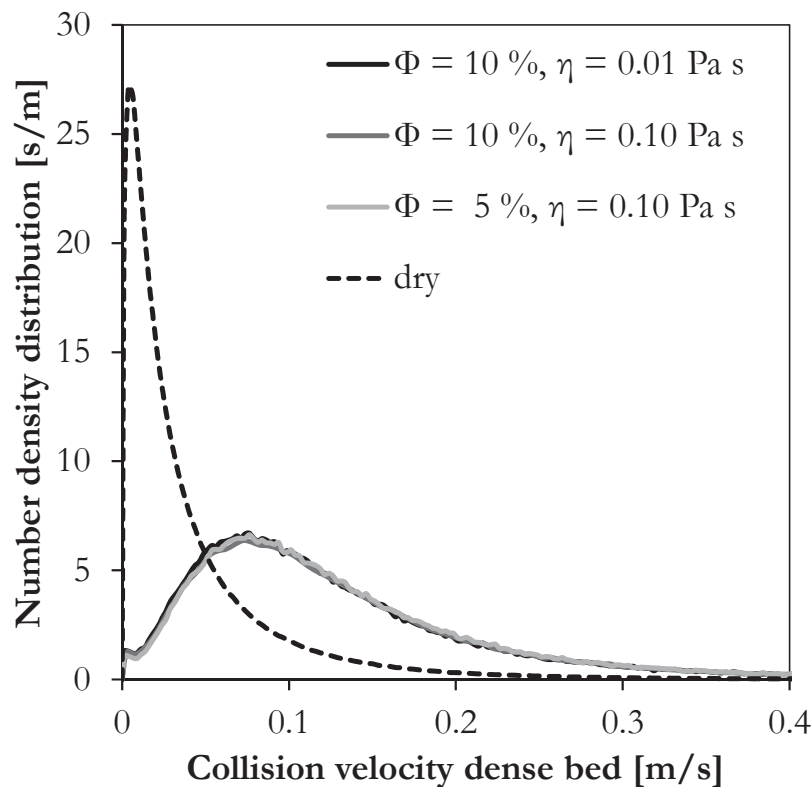


Figure 5-34: Influence of viscous forces on the collision velocity distribution in the dense bed of a Wurster-coater.

The distribution is shifted to larger velocities in case viscous forces are considered in the simulation. Since particle encounters at low impact velocity lead to adhesion, they are only considered as collisions, if the aggregate structure is broken again. Since this may take a long time in the dense bed of the Wurster-coater, impact velocities below 0.02 m/s, which are the most



frequent fraction in the dry case, are mostly eliminated from the velocity distribution, if viscous forces are considered in the simulation. As seen before for the particle dynamics, a significant influence of the liquid viscosity and of the wetted surface fraction is not revealed by the simulation results.

Information on the influence of viscous forces on the collision frequency in a Wurster-coater is summarized in Table 5-15. It can be seen that the adhesive effects induced by viscous contact forces reduce the overall collision frequency in the Wurster-coater by more than 90 %.

Table 5-15: Influence of viscous forces on the collision frequency in a Wurster-coater.

Case	Mean particle- particle collision frequency [1/s]	Particle-particle collision frequency (inside draft tube) [1/s]	Particle-particle collision frequency (inside dense bed) [1/s]	Mean particle- wall collision frequency [1/s]
dry	563	54	674	34.8
$\Phi = 10 \%$, $\eta = 0.01 \text{ Pa s}$	41	34	48	2.3
$\Phi = 10 \%$, $\eta = 0.10 \text{ Pa s}$	42	34	49	2.4
$\Phi = 5 \%$, $\eta = 0.10 \text{ Pa s}$	44	36	51	2.4

Due to different distributions of the relative collision velocity in the dense bed (average impact velocity in case 1: 0.05 m/s) and inside the Wurster tube (average in case 1: 0.21 m/s), the collision frequency inside Wurster tube is reduced by only 35 %. It can be seen in Table 5-15 that also the frequency of particle-wall collisions is reduced by more than 90 %, if viscous forces are included in the simulation.

Profiles of the collision frequency along the height of the granulator as well as in x-direction in the central plane at height $z = 20 \text{ mm}$ are shown in Fig. 5-35. These profiles illustrate very well the fundamental influence of viscous forces on the collision frequency, especially in the dense bed of the Wurster-coater. While the profile for the dry reference case peaks at up to 1500 collisions per particle pair and second in the dense bed near the outer wall of the equipment, the collision frequency in the cases including viscous forces hardly exceed 50 collisions per particle pair and second.

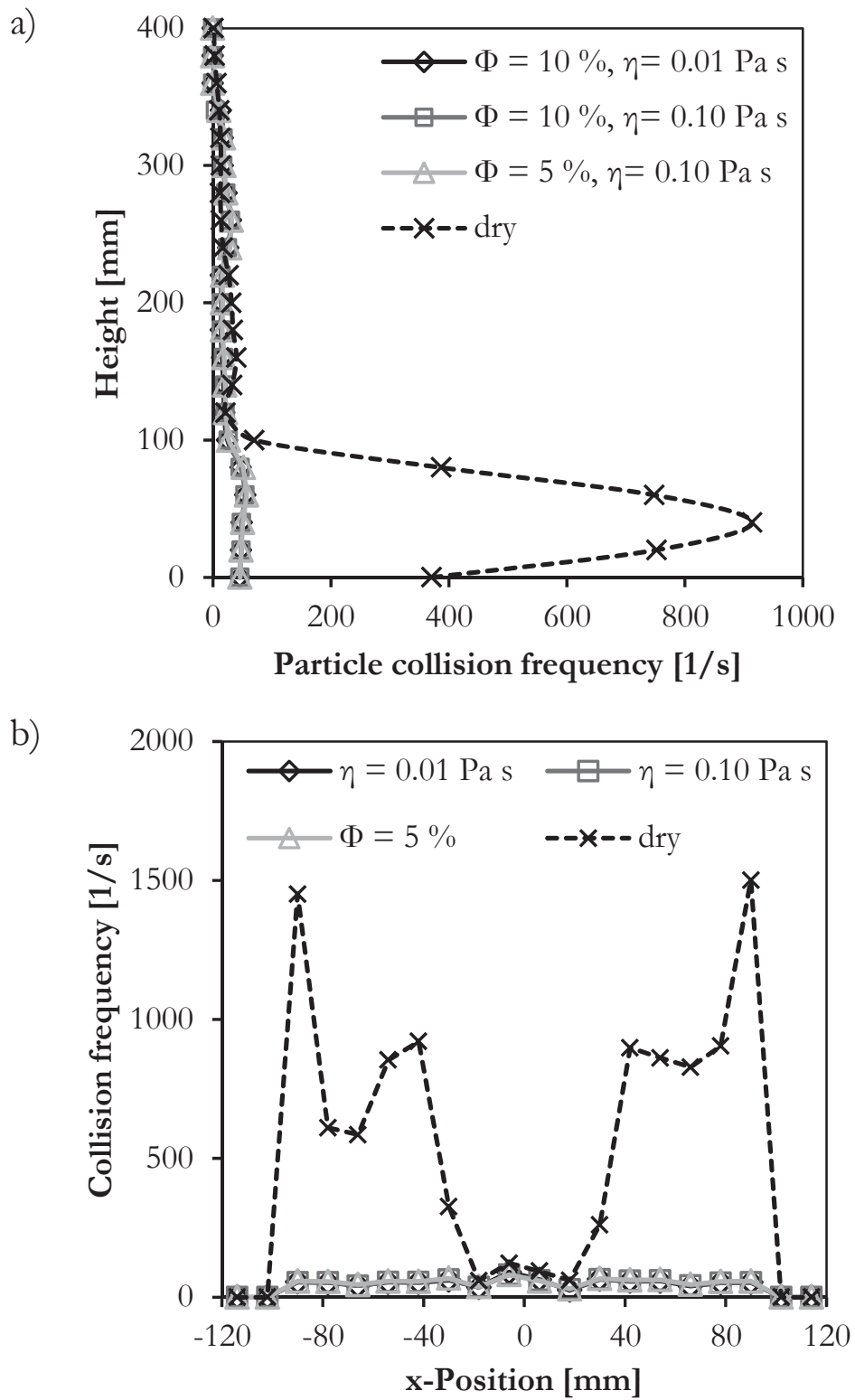


Figure 5-35: Influence of viscous forces on the collision frequency in a Wurster-coater. Vertical profile (a) and radial profile at height $z = 20\text{ mm}$ (b).



5.5.4 Conclusion

In this section the effect of viscous energy dissipation related to liquid films, which partially cover the particle surfaces, on the particle and collision dynamics in a Wurster-coater was analyzed. For the applied simulation conditions a small reduction of the average particle velocity and of the expansion of the bed was observed, due to additional energy dissipation. Apart from that viscous contact forces have a dominant influence on the particle collision kinetics. Inside the dense bottom zone of the Wurster-coater more than 90 % of the collisions occur at insufficient kinetic energy in order to overcome the viscous force. The particles therefore stay in contact and form loose aggregates, until a sufficiently energetic collision breaks the aggregate structure. This leads to a reduction of the collision frequency of more than 90 %.

Comparing different simulation scenarios under variation of the viscosity of the liquid film and of the wetted surface fraction do not significantly influence the particle and collision dynamics in the investigated range.



6 Comparison of different granulator geometries

The geometry of the equipment has a strong influence on the particle dynamics and therefore on the final product properties. In a combined numerical and experimental study the influence of the geometry of the granulator equipment on the agglomeration process dynamics is analyzed in this chapter. Three different granulator configurations are compared: a top-spray granulator, a Wurster-coater and a spouted bed. The original geometry of the equipment is used, as supplied by Glatt Ingenieurtechnik GmbH, Weimar. The objective of this chapter is to assess the ability of the Discrete Particle Model to study the fluid and particle dynamics in a fluidized bed granulator and to predict their implications on the final product properties.

This chapter is organized as follows: In section 6.1 DPM simulation results regarding the particle and collision dynamics as well as the residence time distribution of the particles in the spray zone are presented for three different granulator configurations. In section 6.2 the agglomerate growth rate is analyzed experimentally as a function of the injection time for the same equipment geometries as used in the DPM. Structure and strength of the agglomerates produced at equal process conditions in different equipment geometries are discussed in section 6.3. Finally, the verification of the predictions of the DPM on growth rate and strength of the agglomerates is elaborated in section 6.4.

6.1 Numerical study on the influence of the equipment geometry

In this section a top-spray granulator, a Wurster-coater and a spouted bed are compared regarding the gas, particle and collision dynamics. These kinetic values are characteristic for the applied process conditions and the geometry of the apparatus. Specifics of the three granulator configurations, which affect the granulation process dynamics and thus the structure and strength of the product, are analyzed in this section, based on the results of DPM simulations. A special

focus is put on the particle circulation patterns, which have a strong effect on the homogeneity of particle wetting.

6.1.1 Simulation conditions

An overview on the applied simulation conditions is given in this section. Simulations were performed using 150 000 monodisperse spherical particles of 2 mm diameter, which corresponds to a batch size of 0.94 kg at a particle density of 1500 kg/m³. A constant coefficient of restitution of 0.8 was set in this study, according to experimental results obtained by Antonyuk et al. (2010) for γ -Al₂O₃. All used simulation parameters are listed in Table 6-1.

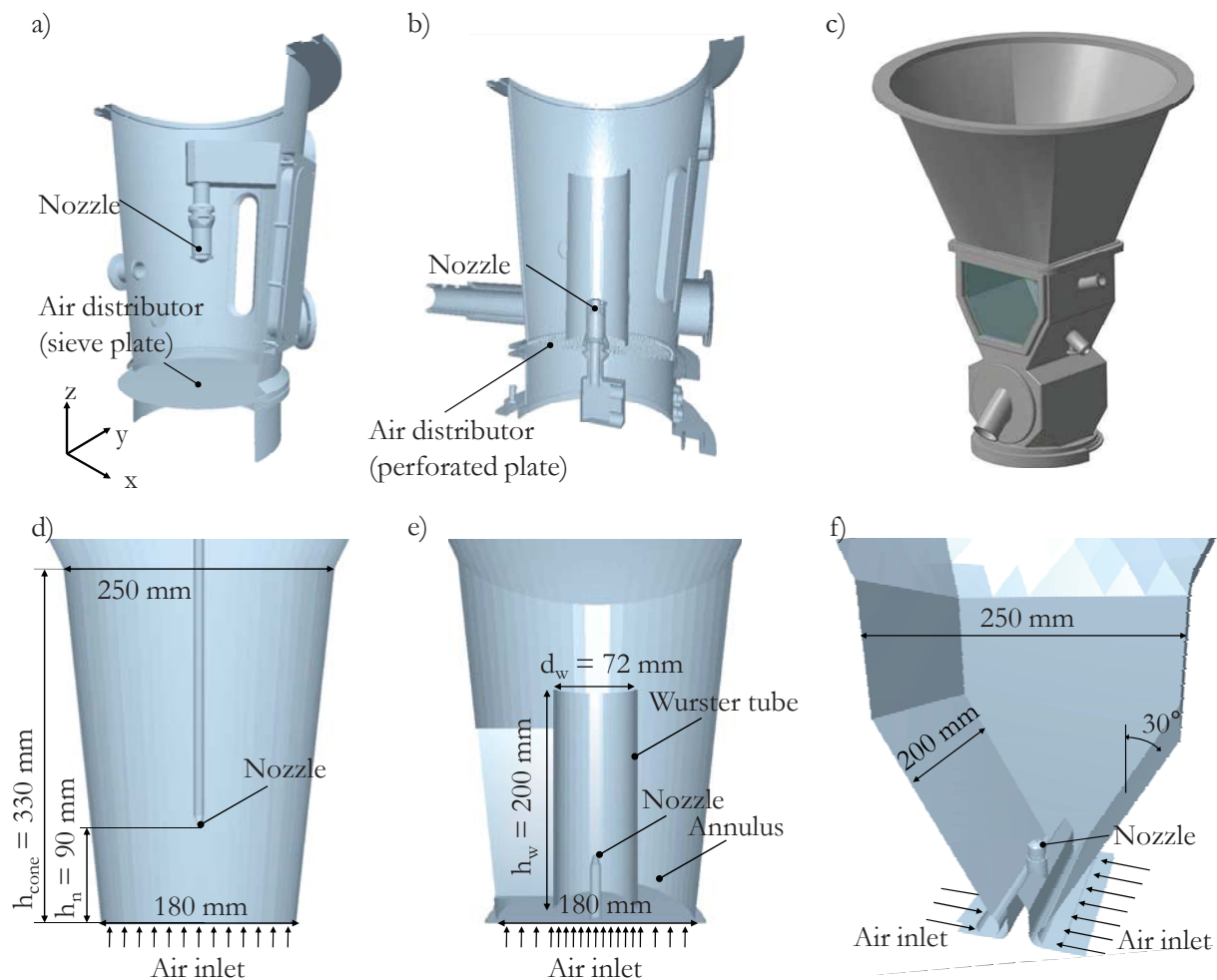


Figure 6-1: Cross section of the used fluidized bed granulator geometries: (a) & (d) Top-spray granulator (Glatt GF3), (b) & (e) Wurster-coater (Glatt GF3), (c) & (f) Spouted bed (Glatt ProCell 5).

The geometries of the GF3-insert with top-spray injection nozzle (Fig. 6-1 a) with bottom-spray injection nozzle and Wurster tube (Fig. 6-1 b) and the ProCell 5 insert (Fig. 6-1 c) were supplied



by Glatt Ingenieurtechnik GmbH, Weimar, Germany and slightly simplified for the DEM-CFD simulations (Fig. 6-1 d, e and f). The geometry of the Wurster-coater is identical to the one which was characterized in chapter 5. An enlarged view of the air inlet slots and the central T-profile, which diverts the air flow towards the top, are shown in Fig. 6-2.

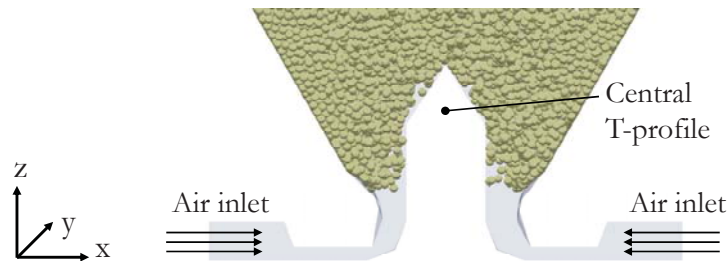


Figure 6-2: Air inlet slots of the spouted bed in the DPM.

Simulations were performed at equal fluidization gas flow rate in all three granulators to allow a fair comparison of the particle dynamics. Also during the experiments the gas flow rate was fixed, in order to compare the devices at equal drying potential η , which is defined as the difference between the dry based saturation gas humidity Y^* and the humidity at the outlet Y divided by the difference of the saturation humidity and the humidity at the inlet Y_{in} .

$$\eta = \frac{Y^* - Y}{Y^* - Y_{in}} \quad (6-1)$$

At the gas inlet boundary the velocities were specified. "No slip" boundary conditions at the walls were set for the gas, whereas the particle-wall friction is defined by the sliding friction coefficient (see Table 6-1). At the outlet of the bed atmospheric pressure was assumed. The DEM simulation time step was chosen according to the procedure described in Antonyuk et al. (2011).

Particle wetting is a key mechanism in granulation and agglomeration. Therefore, the particle and collision dynamics specifically for particles positioned inside the spray zone are analyzed in section 6.1.4. The biconical spray zone was defined in the simulations as shown in Fig. 6-3.

A constant length L of 45 mm was used based on the jet injection depth found in DPM simulations of the Wurster-coater (Fries et al., 2011a). The biconical shape of the spray zone is related to DPM simulations of droplet deposition according to Link et al. (2007). Throughout the simulations the spraying angle φ was kept constant at 40° . The applied simulation conditions are summarized in Table 6-1.

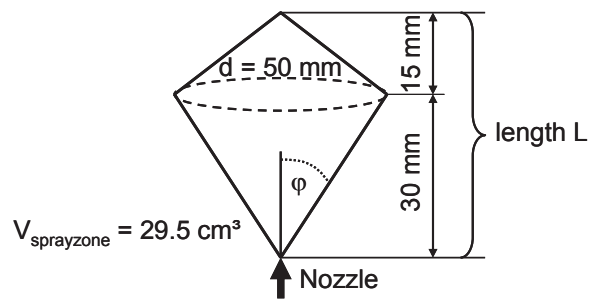


Figure 6-3: Geometry of the spray zone.

Table 6-1: Overview on simulation parameters.

Parameter	Symbol	Unit	Value
Fluidisation air flow rate	\dot{m}_F	kg/h	360
Atomizer flow rate	\dot{m}_{spout}	kg/h	5.7
Gap distance below Wurster	h_{gap}	mm	30 (= 15 \cdot d_p)
Normal coefficient of restitution	e_n	-	0.8
Sliding friction coefficient of particles	μ	-	0.1
Rolling friction coefficient of particles	m_R	-	0.05
Poisson's ratio of particles	ν	-	0.25
Shear modulus of particles	G	Pa	$1 \cdot 10^8$
DEM simulation time step	Δt_{DEM}	s	$1 \cdot 10^{-6}$
CFD simulation time step	Δt_{CFD}	s	$1 \cdot 10^{-4}$
Total simulation time	t	s	4
Number of particles	N_p	-	150 000
Number of grid cells (CFD)	N_{cell}	-	9600 - 17600

6.1.2 Particle dynamics

Typical snapshots of the particle positions and their velocity distribution, which is indicated by the colour code, are shown in Fig. 6-4 for the three investigated granulator configurations. The top-spray granulator and the Wurster-coater were cut along the central vertical plane in order to show the particles at the center of the granulator. The images illustrate well the different particle motion patterns in the three granulators. An agitated dense bed with particle eruptions caused by bubble breakup at the top of the bed is found for the top-spray granulator (Fig. 6-4 a) and the



spouted bed (Fig. 6-4 c). In the Wurster-coater a dense bed with low particle motion is seen in the lower annulus region, while the particles are transported upwards in a spout inside the draft tube.

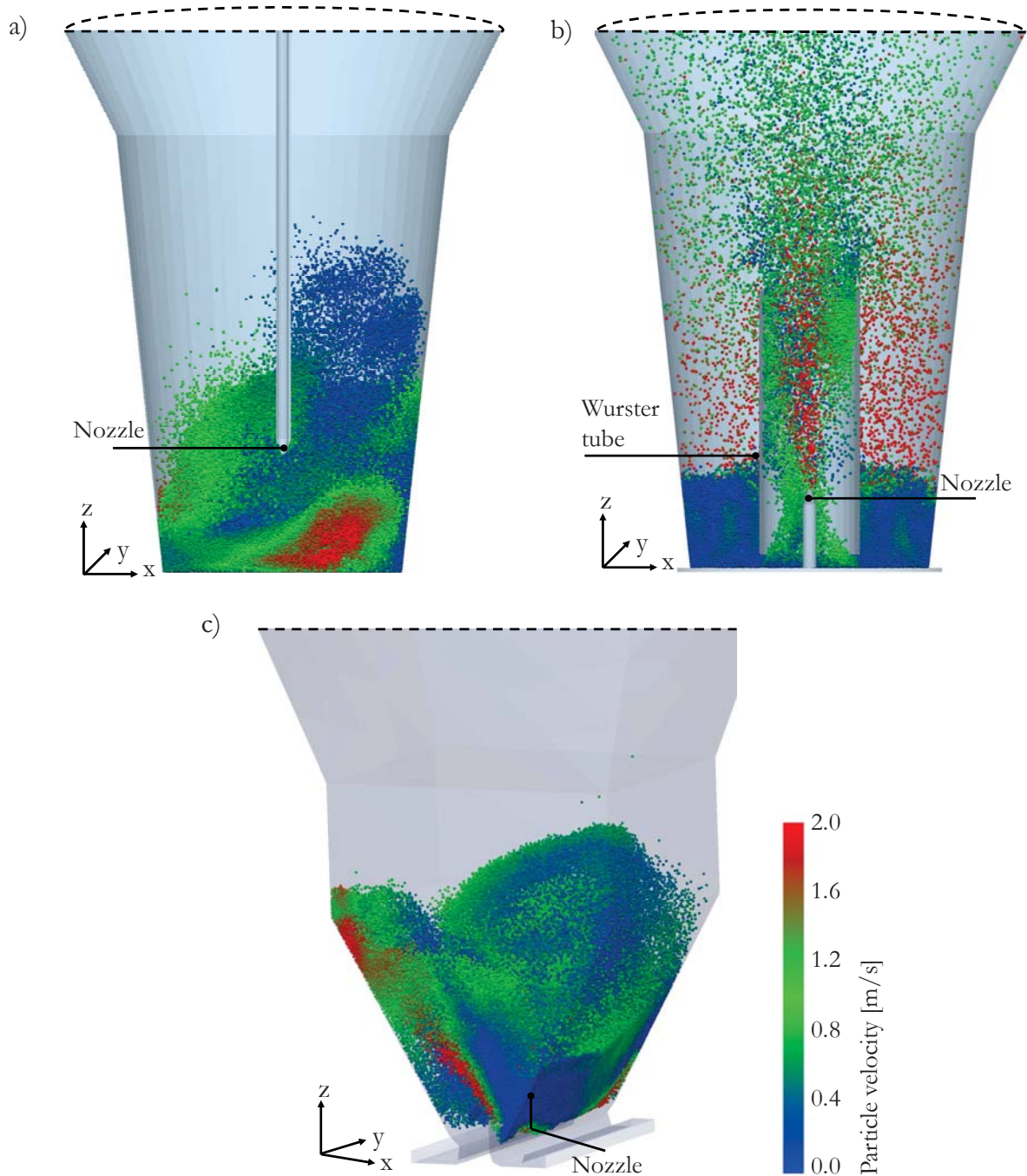


Figure 6-4: Instantaneous particle positions and particle velocity distribution at identical process conditions for the top-spray granulator (a), the Wurster-coater (b) and the spouted bed (c). Colours indicate the particle velocity.



Quite a few particles are present in the dilute region above the bed in the Wurster-coater, while no particles rise higher than 300 mm above the bottom of the bed in the top-spray granulator and the spouted bed.

In Fig. 6-5, time-averaged contour plots of the gas velocity and the solids volume fraction are shown. Three representative slices positioned at $x = 0$ mm (at the center of the granulator), $\Delta x = 50$ mm and $\Delta x = 100$ mm were cut out of the fluid volume for each apparatus. As indicated by the legend, the colour code refers to the mean gas velocity (averaged over 7 s of simulation time) for the left column and to the mean solids volume fraction in the right column.

In the top-spray granulator (Fig. 6-5 a) the gas velocity profile is symmetric in radial direction. Due to the conical shape of the granulator the gas velocity is decreasing towards the top. At the nozzle tip, a small jet zone with gas velocities above 15 m/s can be seen. The solids volume fraction in the dense bed at the bottom is largely influenced by the atomizer, creating a zone with higher porosity at the center of the bed.

In the Wurster-coater (Fig. 6-5 b) very high gas velocities are found inside the draft tube due to the structure of the segmented distributor plate with larger orifices at the center and due to the cocurrent injection at the atomizer. Even in the expansion chamber above the Wurster tube, the gas velocity reaches 5 m/s compared to a maximum of 0.5 m/s in the top-spray granulator and the spouted bed at the same height. In the central cross section, the support of the Wurster tube can be seen as a white zone to the right. The solids volume fraction in the dense bed is higher on average in the Wurster-coater than in the top-spray granulator. Inside the draft tube, the particles are drawn towards the center by the gas flow.

In the spouted bed (Fig. 6-5 c) the gas velocity profile is not symmetric, despite the averaging over 7 s of simulation time. This expresses the dominant influence of velocity fluctuations on the spout fluidization regime. The bed is very dense at the bottom, especially towards the inlet slots along the inclined side walls of the granulator.

For a quantitative analysis the average velocity magnitude of all particles is presented in Fig. 6-6 a) as a function of the simulation time. While the average particle velocity in the Wurster-coater is almost constant, fluctuations of approximately 0.2 m/s are found in the spouted bed and the top-spray granulator. A very stable particle circulation is immediately established in the Wurster-coater, while periodic particle eruptions caused by large bubbles dominate the particle motion pattern in the other granulator configurations at equal fluidization and atomizer gas

throughput. Averaged over the total simulation time, the particle velocity in the Wurster-coater is 23 % lower than the particle velocity in the spouted bed and in the top spray granulator.

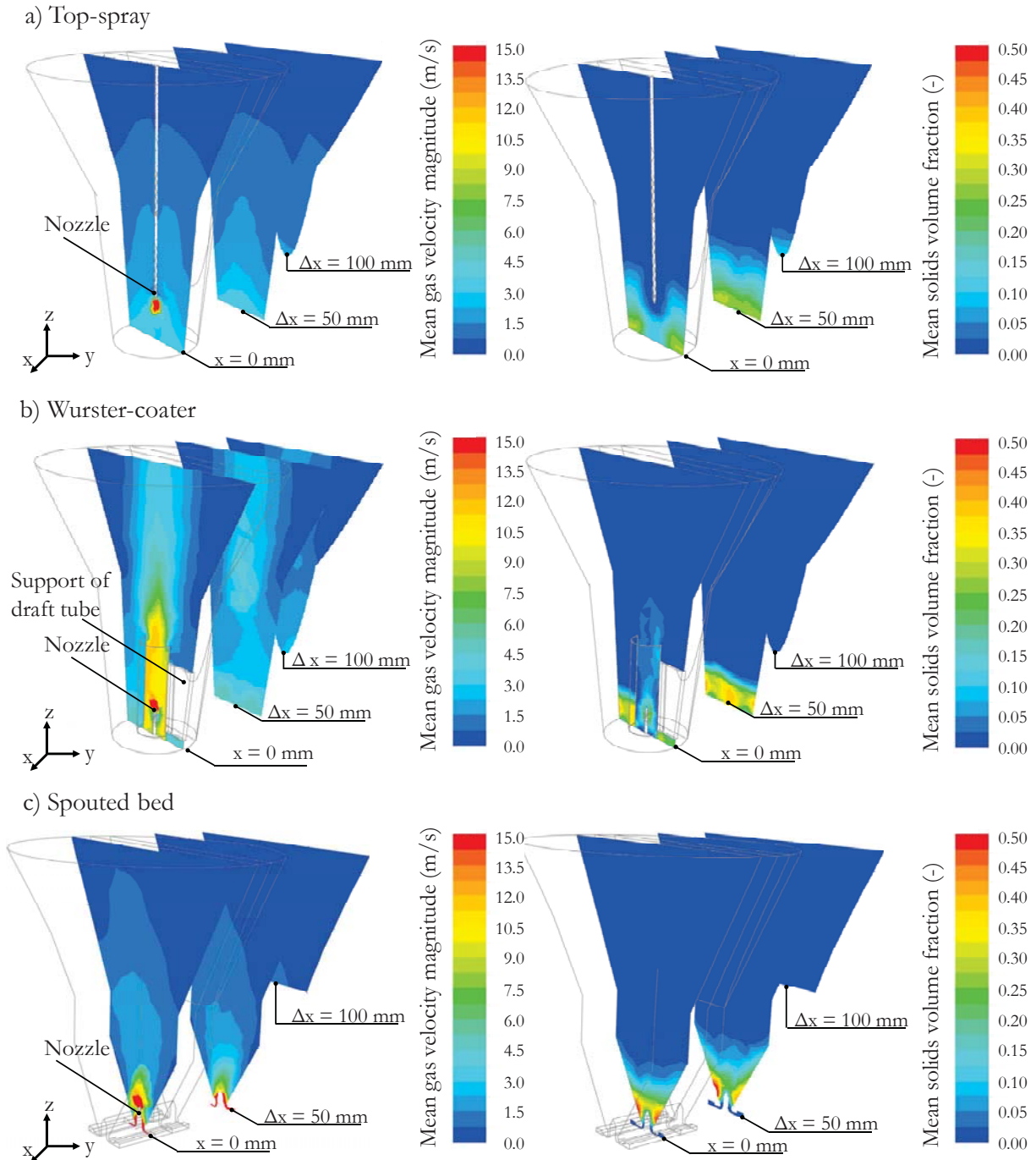


Figure 6-5: Time-averaged gas velocity and solids volume fraction in three slices (positioned at $x=0$, $x=50$ and $x=100$ mm).

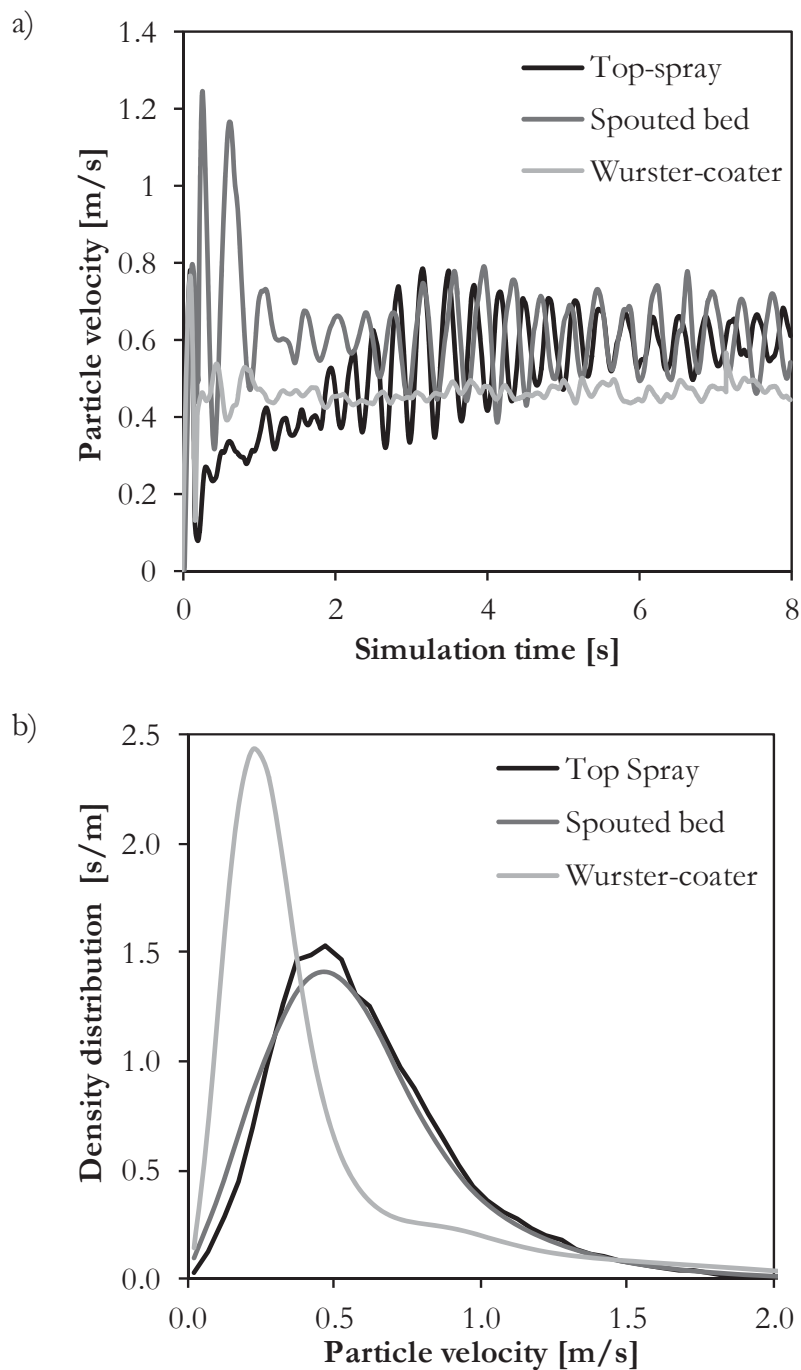


Figure 6-6: Transient profile of the average particle velocity in the top-spray granulator, the spouted bed and the Wurster-coater, (b) density distribution of the time-averaged particle velocity.

This is mainly due to lower particle motion in the dense bed in the annulus of the Wurster-coater. The small gap distance between the bottom plate and the draft tube limits the number of particles which enter into the Wurster tube, where they are accelerated. It can be seen in Fig. 6-6 a) that a stable fluidization regime is established within 1-2 s of simulation time in the



Wurster-coater and the spouted bed, while it takes 4 s until the mean particle velocity reaches its stationary value in the top-spray granulator. A comparison of the time-averaged particle velocities is given in Table 6-2.

In Fig. 6-6 b) the time-averaged density distribution (see appendix A2) of the particle velocity is shown for the three investigated granulator configurations. The stable fluidization regime (4-8 s simulation time) was taken into account for the averaging. While the distributions obtained in the simulations of the spouted bed and the top-spray granulator are very similar with one mode at $v = 0.5$ m/s, for the Wurster-coater a clear mode is found at $v = 0.25$ m/s for the particles in the annulus and a second mode at $v = 0.85$ m/s for the particles inside the Wurster tube.

It is also interesting to analyze the average particle velocity as a function of the height of the granulator, which is presented in Fig. 6-7 a). For this purpose the granulators were discretized along the vertical axis into 25 slices of 20 mm thickness, starting at height $h = 0$ at the bottom plate. For comparison, the solids volume fraction along the height of the granulator is shown in Fig. 6-7 b). It can be seen that the particle velocity in the top-spray granulator and the spouted bed is almost constant over the height in a range of 0.4 - 0.6 m/s. Different to that the average particle velocity in the Wurster-coater is much lower at around 0.3 m/s in the dense bottom zone ($h = 0 - 80$ mm), but in the dilute regions above the bed it reaches 1.0 - 1.5 m/s, which is due to the acceleration of the particles in the spout.

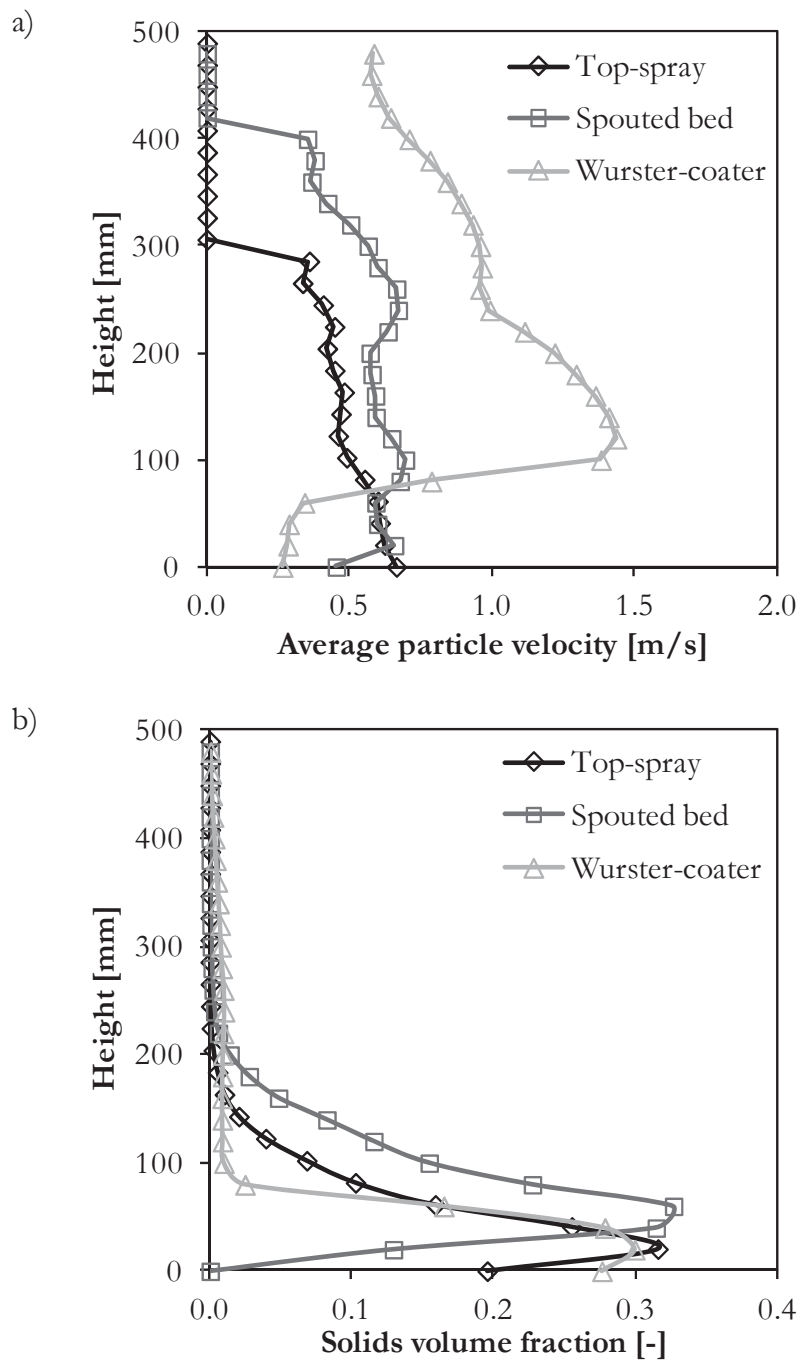


Figure 6-7: Time-averaged velocity profile (a) and solids volume fraction (b) along the height of the granulator.



6.1.3 Collision dynamics

One of the most interesting possibilities of a detailed DEM simulation is the analysis of the particle collision dynamics. In a fluidized bed granulator the agglomeration rate is strongly dependent on the particle collision velocity and the collision frequency. Colliding particles will rebound, if the kinetic energy of the contact partners will not be fully dissipated by plastic contact deformation, viscous or capillary forces. Below a certain critical impact velocity, the particles will stick to each other and form agglomerates (Ennis et al., 1991; Thornton & Ning, 1998; Antonyuk et al., 2009). In Table 6-2 the collision frequency for particle-particle and particle-wall collisions is given for the three investigated granulator configurations.

In Fig. 6-8 the average relative collision velocity for particle-particle collisions (a) and particle-wall collisions (b) is shown as a function of the simulation time. The information about collisions was tracked for a representative interval of 1 second within the stable fluidization regime. It can be seen that the particle-particle collision velocity is nearly constant over time in the investigated range for all granulator configurations. In the Wurster-coater the average particle-particle collision velocity is 0.127 m/s, which is 16 % higher than in the spouted bed and 59 % higher than in the top-spray granulator for the given simulation conditions. For the spouted bed and the top-spray granulator the evolution of the average relative velocity of particle-wall collisions (see Fig. 6-8 b) shows oscillations which correspond to the fluctuations of the average translational particle velocity (see Fig. 6-6 a).

The average particle-wall collision velocity in the spouted bed is 0.5 m/s, which is nearly twice as high as the one in the Wurster-coater and 27 % higher than the one in the top-spray granulator. Many particles collide at high velocity with the central T-profile (see Fig. 6-2) in the spouted bed, whereas only few collisions of particles with the Wurster tube are observed. Due to the elevated particle-wall collision velocity, granules produced in the spouted bed are expected to show a higher consolidation and therefore higher strength than those produced in the Wurster-coater, based on the simulation results.

For all three granulator configurations the time-averaged distribution of the relative collision velocity is displayed in Fig. 6-9 a) for particle-particle collisions and in Fig. 6-9 b) for particle-wall collisions. The distribution of the particle-wall collision velocity (Fig. 6-9 b) differs between the three granulator configurations.

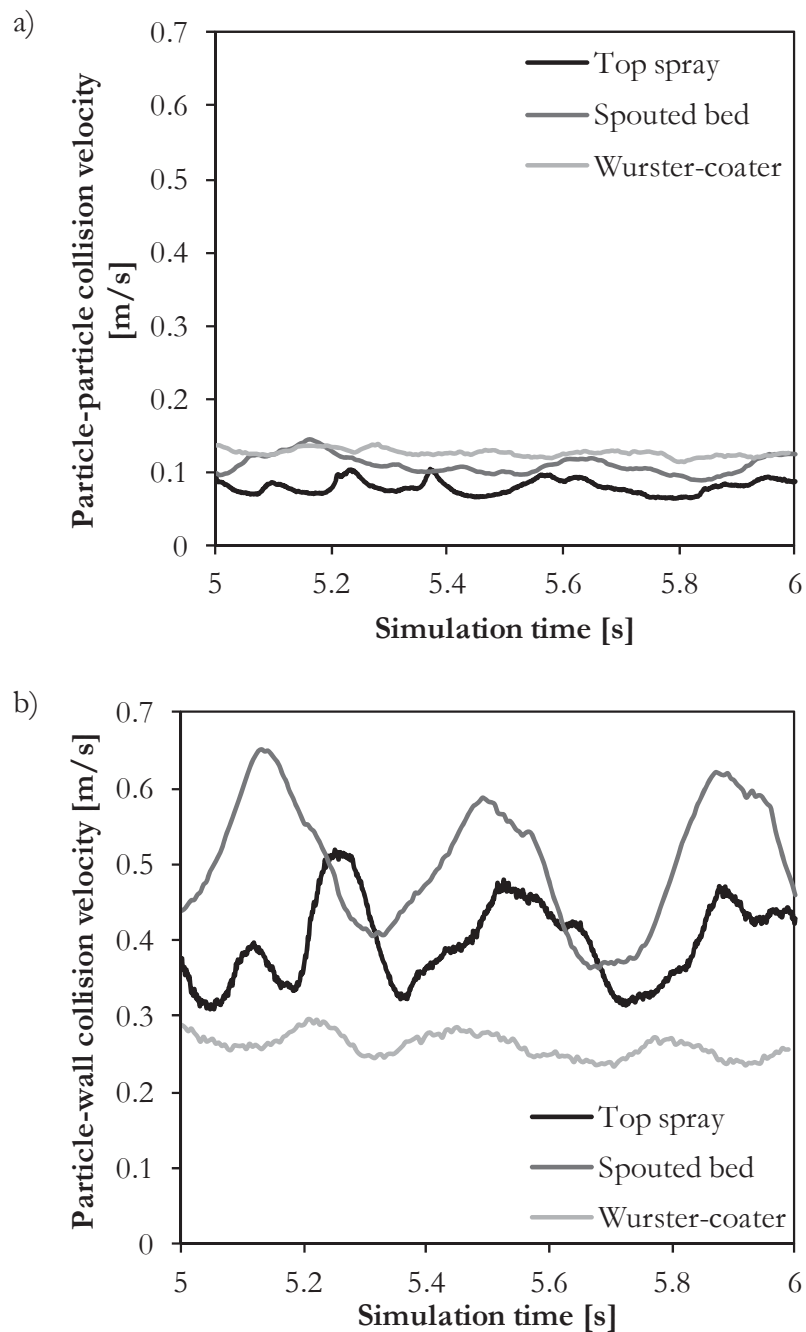


Figure 6-8: Transient profile of the average particle-particle collision velocity in the top-spray granulator, the spouted bed and the Wurster-coater, (b) average particle-wall collision velocity as a function of the simulation time.

While a narrow monomodal distribution with the mode at 0.18 m/s is found for the Wurster-coater, a wider distribution with the mode at 0.41 m/s is observed for the top-spray granulator and a bimodal distribution with modes at 0.08 m/s and 0.49 m/s is found for the spouted bed for the applied simulation conditions. Due to the directed flow profile of the particles in the



Wurster-coater, which is characterized by a stable circulation around the Wurster tube, particle wall collisions occur less frequently and at lower relative velocity in this type of granulator.

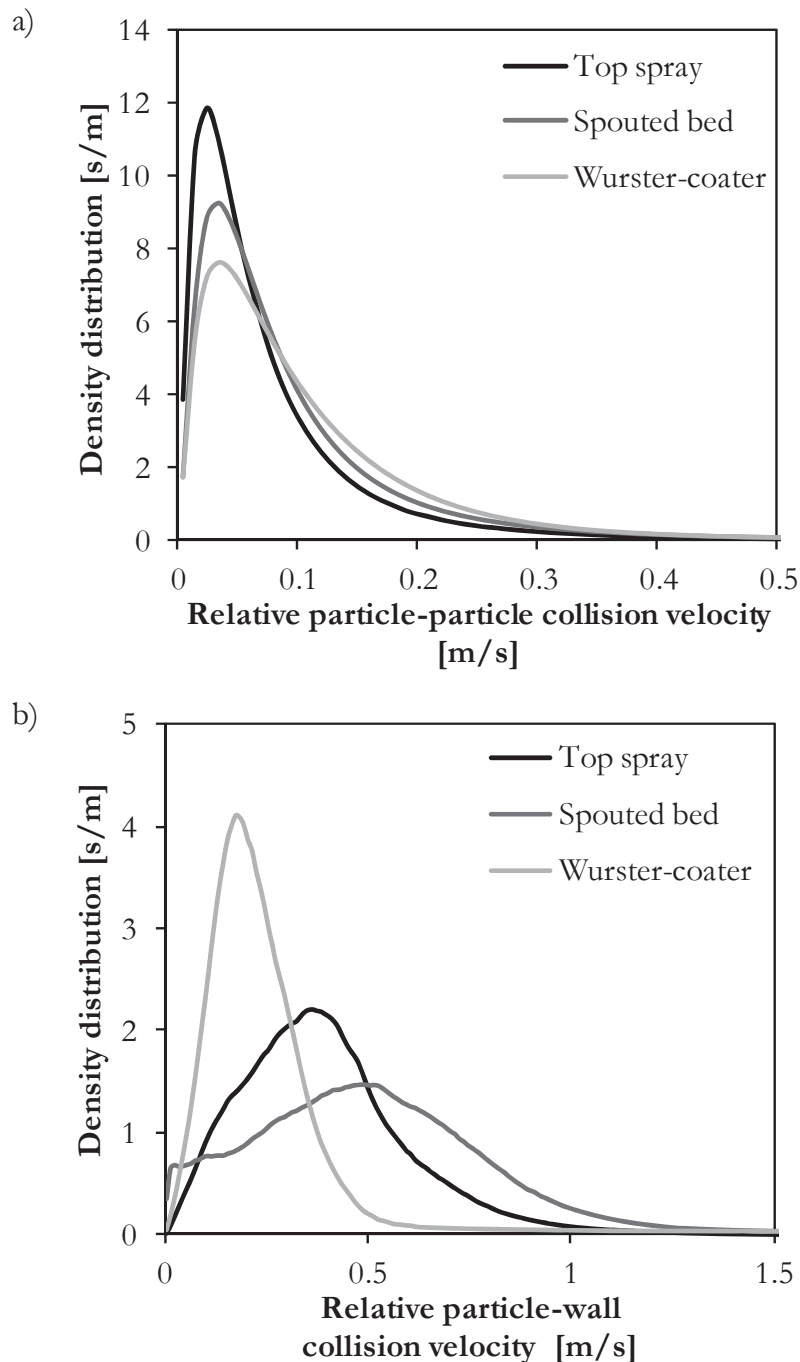


Figure 6-9: (a) Density distribution of the relative collision velocity of all particle-particle collisions in the reference time interval ($t = 5-6$ s simulation time) for three different granulator configurations, (b) density distribution of the particle-wall collision velocity.



In the spouted bed, where the granulator walls play a stronger role for the direction of the particle circulation and in the top-spray granulator, where the particle motion is mostly stochastic with large bubble-induced fluctuations, particle-wall collisions occur at higher relative velocity and higher frequency (see Table 6-2). Fluctuations of the particle and collision dynamics indicate that the spouted bed was not operated in a stable regime, as defined by Gryczka et al. (2008).

Table 6-2: Time-averaged particle and collision velocity and collision frequency (collisions per particle pair per second) in the Wurster-coater, the spouted bed and the top-spray granulator.

Parameter	Unit	Wurster-coater	Spouted bed	Top-spray
Particle velocity	m/s	0.47	0.61	0.60
Particle velocity in dense bottom zone ($\epsilon_p > 0.1$)	m/s	0.29	0.64	0.61
Particle fraction in dense bottom zone ($\epsilon_p > 0.1$)	%	75	75	84
Relative collision velocity (particle-particle)	m/s	0.13	0.11	0.08
Relative collision velocity (particle-wall)	m/s	0.26	0.51	0.40
Time-averaged maximum kinetic energy of particle collisions	μJ	34.9	51.5	12.6
Time-averaged maximum energy dissipation	μJ	7.1	8.0	2.6
Time-averaged maximum contact force	N	0.44	0.41	0.27
Time-averaged maximum deformation (overlap)	mm	0.017	0.019	0.013
Collision frequency (particle-particle)	s^{-1}	357	1149	1300
Collision frequency (particle-particle) in dense bottom zone ($\epsilon_p > 0.1$)	s^{-1}	492	1411	1462
Collision frequency (particle-wall)	s^{-1}	19	63	48

Based on the information about particle collisions, the DPM simulations can give exact data on the mechanical stress the particles are subject to in a fluidized bed granulator. Combined with the observed collision frequencies this gives a good indication on the intensity of consolidation and breakage of the particles. A comparison of the three tested granulator configurations is given in Table 6-2 and in Fig. 6-10. For each time step the maximum kinetic energy of all particle collisions as well as the corresponding energy dissipation are recorded and then averaged over the total simulation time. It is assumed that consolidation and breakage are determined by the maximum energy dissipation that a particle encounters in the process, rather than by the overall average value. Few hard collisions have a stronger impact on the strength of a particle than many gentle collisions. It can be seen in Fig. 6-10 a) that the time-averaged maxima of the kinetic

collision energy and the collisional energy dissipation are by a factor of 3 lower in the top-spray granulator than in the other configurations. This suggests a lower strength of agglomerates produced in the top-spray granulator, while the highest strength is expected for the spouted bed. For the time-averaged maximum contact force (see Fig. 6-10 b) the highest value is obtained in the Wurster-coater. This suggests that particles produced in the Wurster-coater can withstand the highest force before they break. Accordingly, the highest allowable deformation is expected for particles produced in the spouted bed, since the largest maximum particle deformation due to collisions is observed in this device, as shown in Fig. 6-10 c).

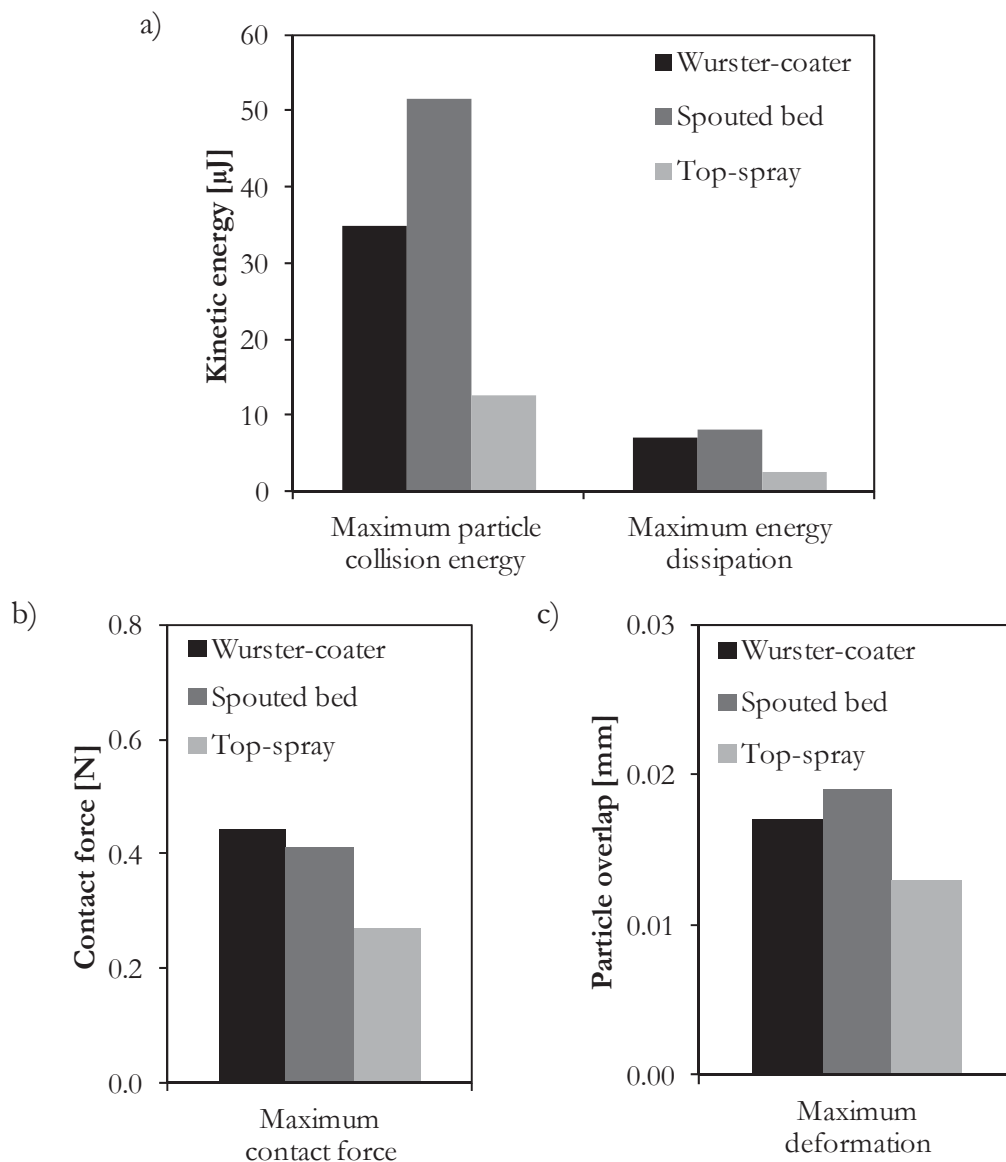


Figure 6-10: Comparison of time-averaged maxima of the collision energy (a), the energy dissipation (b) and the particle deformation (c) in the Wurster-coater, the spouted bed and the top-spray granulator.

Fig. 6-11 presents the collision frequency (collisions per particle pair per second), which was recorded in the DPM simulations. Particle-particle collisions (Fig. 6-11 a) are recorded approximately one order of magnitude more frequently than particle-wall collisions (Fig. 6-11 b) in all granulators. Mainly the dense fluidized bed regions of the investigated granulators account for the high collision frequency.

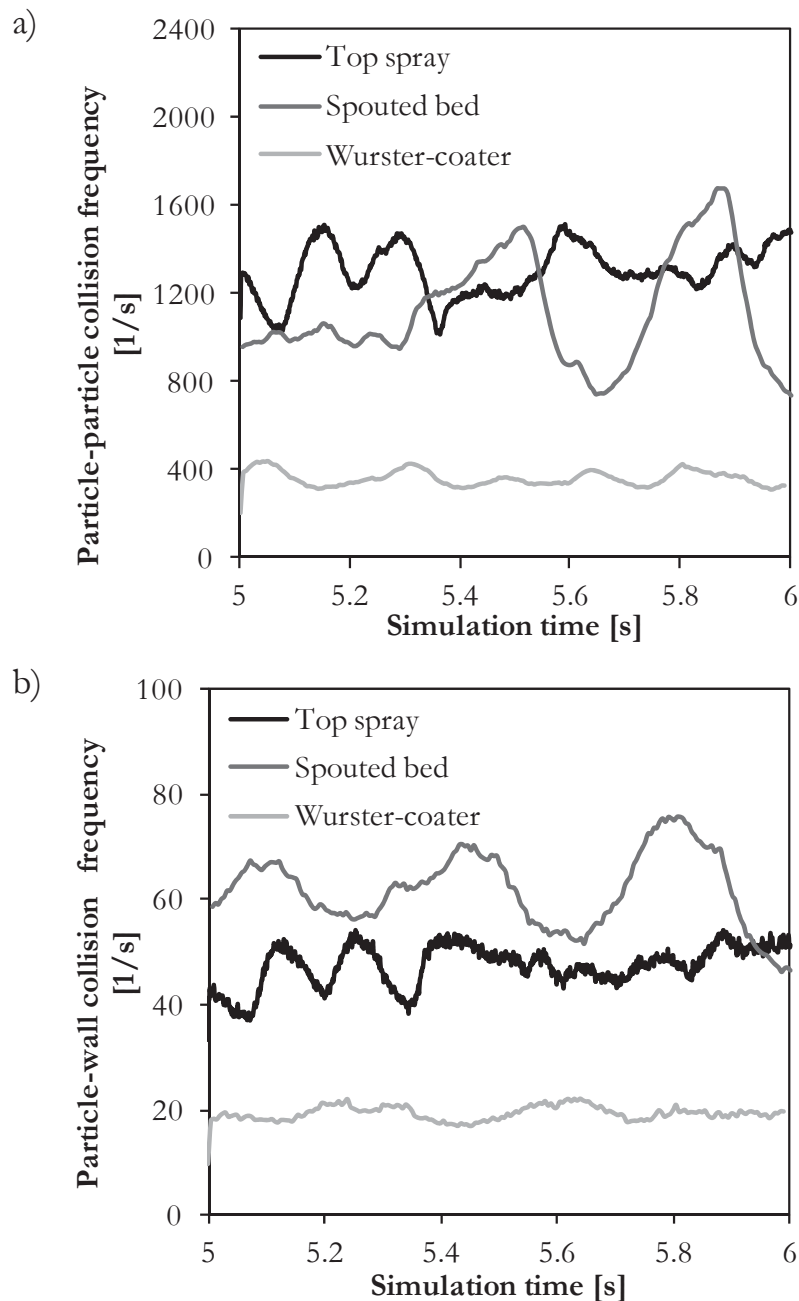


Figure 6-11: Collision frequency (collisions per particle pair per second) as a function of the simulation time for (a) particle-particle collisions, (b) particle-wall collisions.



On average the particle-particle collision frequencies in the top-spray granulator (1300 s^{-1}) and the spouted bed (1149 s^{-1}) are 3 times higher than the frequency observed in the Wurster-coater (357 s^{-1}), which is mainly caused by the differences in the particle dynamics inside the dense bottom zone (see Table 6-2). In the Wurster-coater the average particle velocity in the dense bottom zone is only 0.29 m/s , which is 40 % lower than its overall average particle velocity and 50 % lower than the average particle velocity in the bottom zone of the other two granulators. In the spouted bed and the top-spray granulator the bottom zone is more agitated so that the average particle velocity in the dense bed equals the overall average. The very high average collision frequency in the top-spray granulator can furthermore be related to the fact that 84 % of the particles reside in the dense bed in this device compared to 75 % in the other granulators. Large fluctuations of the particle-particle collision frequency can be seen for the spouted bed, which are related to the formation of large bubbles in the bed causing particle eruptions (low collision frequency) and contractions of the bed (high collision frequency). To a smaller extent, this behaviour is seen in the top-spray granulator as well, while the collision dynamics in the Wurster-coater are very stable over time.

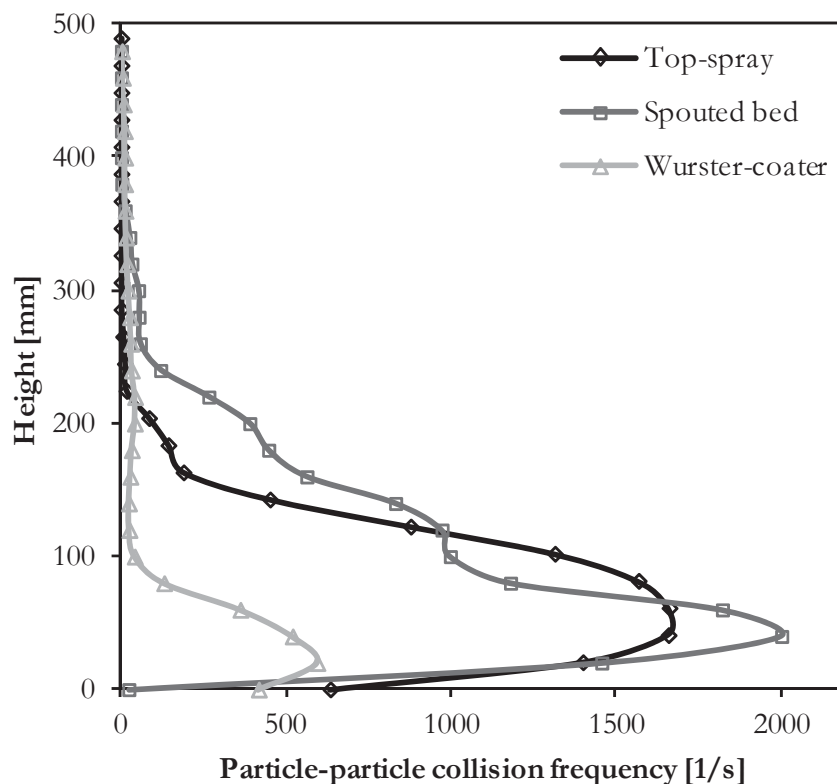


Figure 6-12: Time-averaged particle-particle collision frequency (collisions per particle pair per second) along the height of the granulator.



Zones in the granulator with high or low average collision frequency can be identified by analysing the frequency as a function of the bed height, as displayed in Fig. 6-12. The simulation results show very high collision frequencies in the dense bottom zones of the top-spray granulator and the spouted bed. Above the dense bed ($\epsilon_p < 0.1$), the average collision frequency is 2 orders of magnitude lower than in the bottom zone ($\epsilon_p > 0.1$).

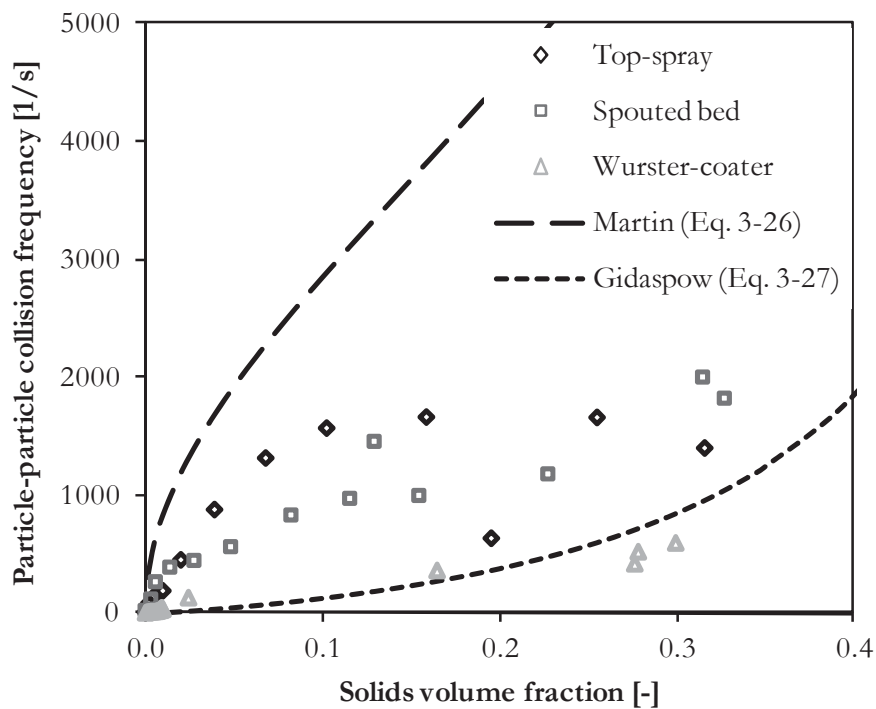


Figure 6-13: Time-averaged particle-particle collision frequency (collisions per particle pair per second) as a function of the average solids volume fraction, in comparison to the kinetic theory based models by Martin (1980) and Gidaspow (1994).

Generally the particle-particle collision frequency is in correlation with the solids volume fraction, which is presented in Fig. 6-13. Obviously this correlation is different for the three investigated fluidized bed granulators. At equal solids volume fraction, the particle-particle collision frequency is three times as high in the spouted bed and the top-spray granulator as in the Wurster-coater. This behaviour can be explained by the differences in the average particle velocity which were reported in Fig. 6-6 a) and Table 6-2. The locally averaged velocity fluctuation c , defined as the standard deviation of the velocity of all particles positioned in the same layer (thickness: 20 mm), is 0.2 m/s in the Wurster-coater and 0.3 m/s in the other two granulators. The model by Martin (Eq. 3-28) largely overestimates the collision frequency compared to the DEM results except for very dilute systems. The mean velocity fluctuation is much lower in the analysed fluidized bed systems than predicted by Martin's model. The formulation of the kinetic theory of granular flow



by Gidaspow (Eq. 3-29) on the other hand is in good agreement with the results found for the Wurster-coater, but it predicts lower collision frequencies than those found in the top-spray granulator and in the spouted bed, especially for the dilute regions. The model parameters given in Table 6-3 were chosen according to the DEM simulation results.

Table 6-3: Parameters for Martin's and Gidaspow's models.

Parameter	Symbol	Unit	Value
Particle diameter	d_p	mm	2
Solids volume fraction at minimum fluidization condition	ϵ_{mf}	-	0.6
Mean local velocity fluctuation	c	m/s	0.2

6.1.4 Particle interactions inside the spray zone

Especially for coating processes, particle rotation is a very important feature which affects the homogeneity of the applied coating layer. Particles must come into contact with spray droplets from all sides in order to allow homogeneous coating. Fast particle rotation inside the spray zone is therefore desirable, since it assures a homogeneous distribution of the spray liquid over the particle surface. In the DEM simulations it is found that particle rotation mainly arises from particle collisions, wall friction and gas velocity gradients. In Fig. 6-14 a) the ensemble-averaged angular velocity of the particles (defined according to Eq. 3-2), which are positioned inside the spray zone, is plotted as a function of the simulation time. While the average angular velocity of particles inside the spray zone in the Wurster-coater is nearly stationary, fluctuations between 60 and 100 rad/s are seen in the spouted bed. The transient profile of the average angular velocity in the top-spray granulator is also fluctuating, but at a lower overall level between 20 and 40 rad/s. At the chosen simulation conditions the Wurster-coater shows a stable particle circulation, whereas in the spouted bed and in the top-spray granulator periodic pulsations occur. Regarding the entire bed of particles the time-averaged angular velocity of the particles in the spouted bed is 65 rad/s, which is 74 % higher than in the Wurster-coater and 3.8 times higher than in the top-spray granulator (see Table 6-4). The spout fluidization via the two slots at the bottom promotes particle rotation as well as the inclined side walls of the spouted bed granulator, where the particles are rolling downwards. Furthermore, the bottom spray nozzle position increases the average particle rotation, since the nozzle jet region, where very strong gas velocity gradients are observed, has a much stronger influence on the particle dynamics in the dense bed compared to

the top-spray configuration, where the jet is in a dilute region of the bed. Looking only at particles inside the spray zone, where the influence of the gas jet is dominant, the average rotational velocity in the spouted bed is 74 rad/s, which is 68 % higher than in the Wurster-coater and 2.1 times higher than in the top-spray granulator.

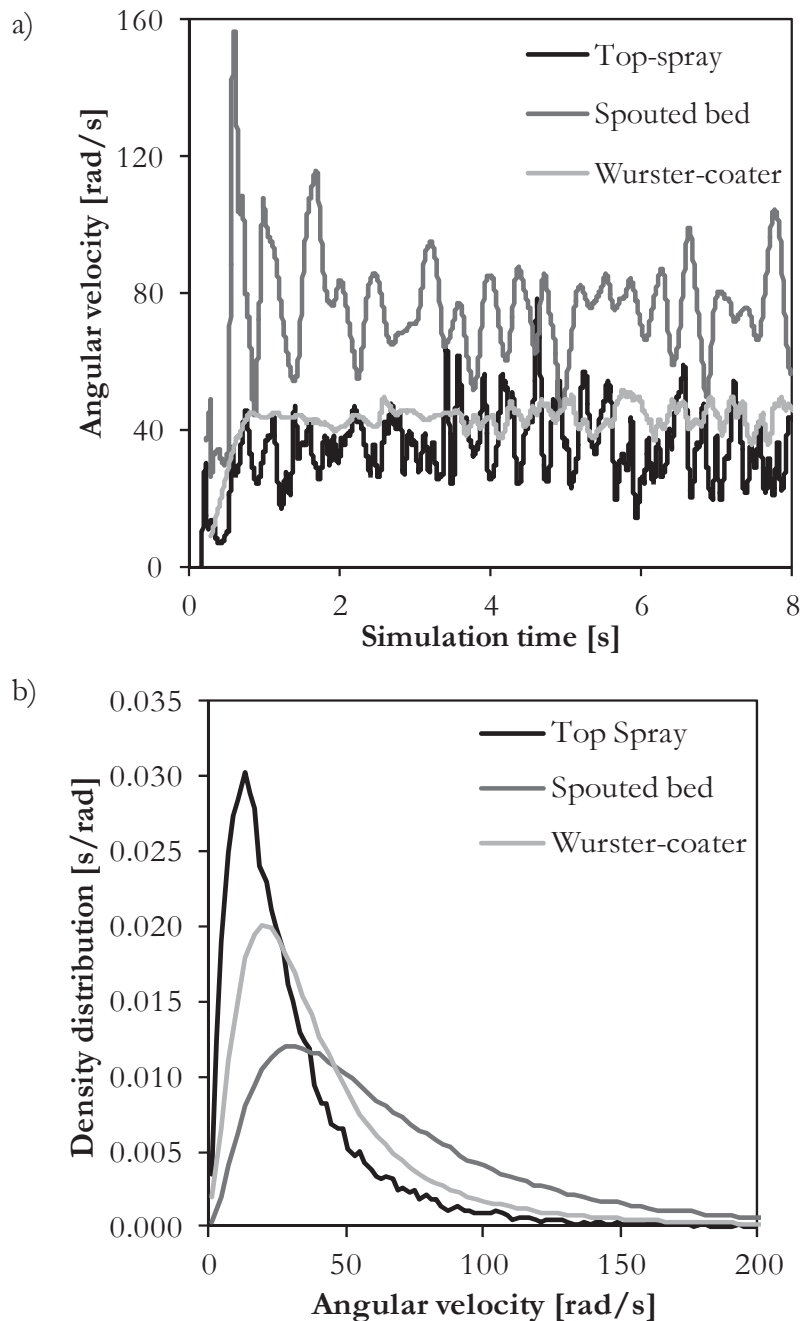


Figure 6-14: (a) Average angular velocity of particles positioned inside the spray zone in the top-spray granulator, the spouted bed and the Wurster-coater as a function of the simulation time, (b) density distribution of the time-averaged angular velocity of particles in the spray zone.



Regarding the density distributions of the angular particle velocity in Fig. 6-14 b), the largest spread is seen for the spouted bed, while the distribution for the top-spray granulator is narrow.

For the given conditions the particle rotation is very stable in the Wurster-coater. Based on these results particle wetting in the Wurster-coater is expected to be more homogeneous than in the spouted bed and in the top-spray granulator. On the other hand the average rotational velocity is much higher in the spouted bed, which will compensate for the negative effects of the velocity fluctuations. Both the Wurster-coater and the spouted bed are therefore recommended for coating purposes, while the top-spray granulator should rather be used for granulation and agglomeration purposes, according to the presented simulation results. Along with the higher angular velocity of the particles, the frictional energy dissipation should be much higher in the spouted bed compared to the top-spray granulator and the Wurster-coater. This aspect should limit the growth rate and favour the formation of compact agglomerates in the spouted bed, since attrition of fragile branched agglomerates is expected to be more important.

Particle collisions inside the spray zone are particularly relevant for the process dynamics, since interactions between surface-wet particles are the main driver for particle agglomeration. Looking at collisions of particles positioned inside the spray zone only, large differences between the granulator configurations are found. Opposite to the result obtained for the entire granulator, the average collision velocity of particles positioned inside the spray zone of the Wurster-coater is 0.40 m/s, which is 70 % higher than the average relative velocity in the spouted bed and 38 % higher than in the top-spray granulator (see Table 6-4).

Table 6-4: Time-averaged particle and collision velocity and collision frequency inside the spray zone (collisions per particle pair per second) in the Wurster-coater, the spouted bed and the top-spray granulator.

Parameter	Unit	Wurster-coater	Spouted bed	Top-spray
Particle fraction inside spray zone	%	0.44	0.71	0.35
Angular velocity (whole bed)	rad/s	37.3	65.1	17.0
Angular velocity (spray zone)	rad/s	44.1	74.1	35.0
Particle-particle collision frequency	s ⁻¹	136	433	73
Relative collision velocity	m/s	0.40	0.23	0.29



This effect can be related to the directed flow profile in the Wurster-coater, where the particles are accelerated inside the draft tube. In the Wurster-coater the wetting zone above the bottom spray nozzle is protected by the draft tube from lateral particle motion into the spray zone. Since this is not the case in the spouted bed, the particle trajectories are less regular, which causes a lower average collision velocity and higher collision frequency.

For all granulator geometries the particle-particle collision frequency is lower inside the spray zone than the average frequency in the whole granulator. In the top-spray granulator this effect is particularly strong, since the particle concentration inside the spray zone is very low and therefore also the collision frequency is low. In the top-spray granulator the collision frequency inside the spray zone is 17.8 times lower than the average value for the whole granulator, while this ratio is 2.6 for both the Wurster-coater and the spouted bed.

The density distribution of the relative particle-particle collision velocity inside the spray zone, which is shown in Fig. 6-15, has a monomodal shape for all three granulators. The highest average velocity is found in the Wurster-coater, where 7 % of the collisions occur at 1 m/s or higher relative velocity.

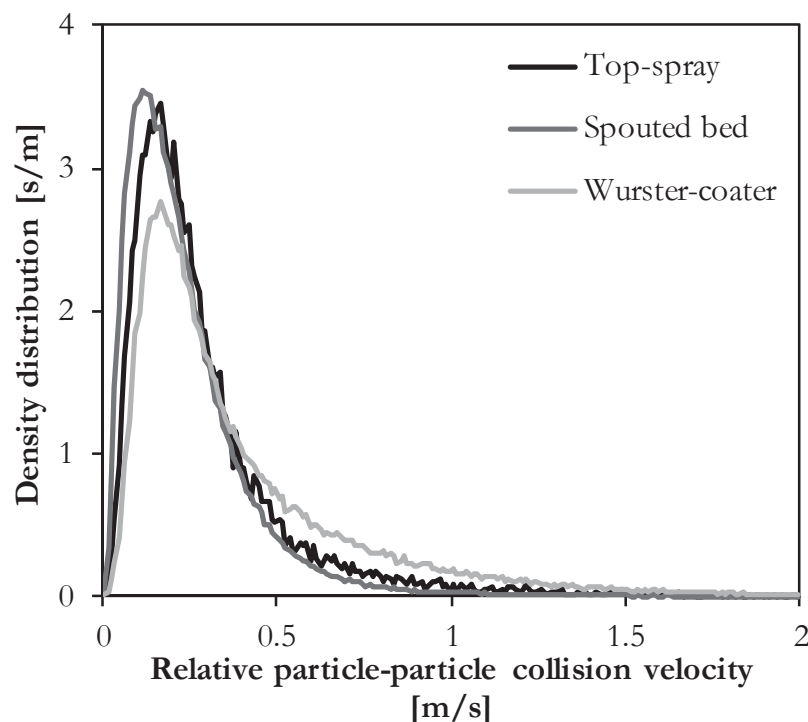


Figure 6-15: Time-averaged density distribution of the particle-particle collision velocity of particles positioned inside the spray zone.



Since particles inside the spray zone are surface-wet, the relative collision velocity in this zone is an indicator for the agglomeration rate. The lower the average collision velocity in the spray zone, the higher is the agglomeration probability. Based on the simulation results a lower agglomeration probability is expected for the Wurster-coater than for the spouted bed and the top-spray granulator. Agglomerates formed in the spouted bed should be stiffer and more compact in shape. Assuming that the spray zone plays a key role for agglomeration, since droplets deposited on the particle surface dry out quickly, low agglomeration efficiency can be expected in the top-spray granulator based on the DPM simulation results for the collision frequency. Agglomeration can only occur, if surface wet particles collide. In the top-spray granulator a larger fraction of the spray liquid will leave the system as overspray compared to Wurster-coater and spouted bed, since the average particle fraction inside the spray zone is lower (see Table 6-4). This increases the probability of the droplets to dry out before they impinge on a particle. As a limitation for these conclusions it should be kept in mind that the influence of moisture on the particle properties is neglected in the present simulation.

6.1.5 Residence time distribution in the spray zone

In order to quantify the homogeneity of particle wetting in the different fluidized bed granulator configurations, the residence time of the particles inside the spray zone is a useful indicator. Since liquid droplets injected via the nozzle are either immediately deposited on a particle inside the spray zone or evaporated, the particle wetting mechanism can be limited geometrically to the spray zone. Again the DEM simulation is an excellent tool, as the moisture content of individual particles in a fluidized bed is not accessible via experiments.

In Fig. 6-16 a) the density distribution of the residence time of the particles inside the spray zone is shown for 7 s of simulation time. While many particles remain almost dry for this limited simulation time interval, the distribution of those which were wetted varies largely between the three investigated granulator configurations.

In both the top-spray granulator and the spouted bed a wide distribution of the particle residence time inside the spray zone is observed. For the top-spray granulator this behaviour was expected, since the particle motion is purely stochastic, without any preferred particle paths. Additionally, the jet plays a less important role for the agitation of the bed than in the other two granulator configurations. Particles migrate slowly through the bed, so that some stay relatively long inside



the spray zone (up to 13 % of the total simulation time), while more than 50 % of the particles are not wetted during 7 s of simulation time.

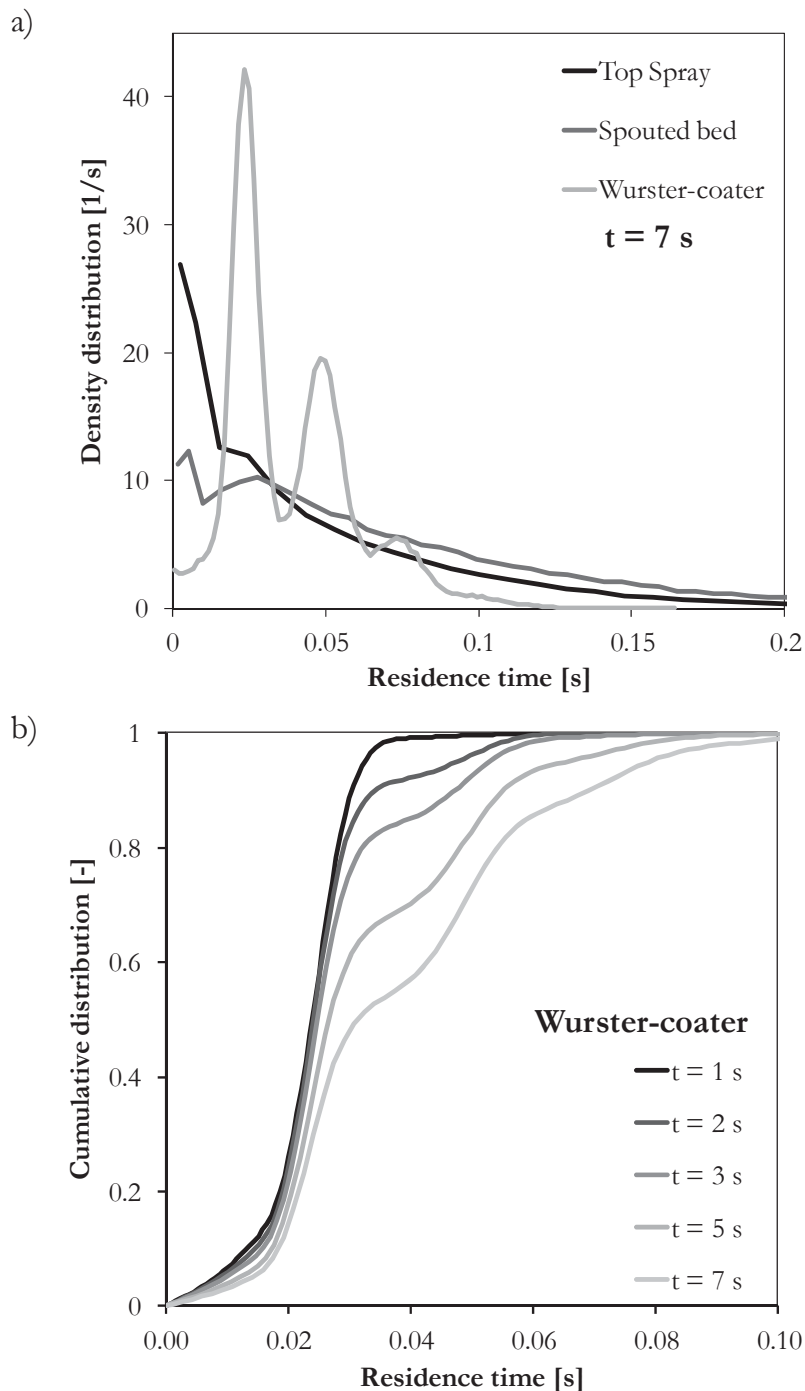


Figure 6-16: a) Density distribution of the residence time of the particles inside the spray zone for Wurster-coater, spouted bed and top-spray granulator after 7 s of simulation time, b) cumulative distribution of the residence time inside the spray zone for the Wurster-coater as a function of time.



Transferred to particle wetting, the residence time distribution observed in the simulations of the top-spray granulator suggests an inhomogeneous moisture distribution among the particles, possible formation of large lumps due to local overwetting and an overall slow growth rate, since the average residence time inside the spray zone is the lowest of all three granulators (see Table 6-5). Assuming that particle wetting can be derived from the residence time of the particles inside the spray zone and knowing the air temperature and velocity, the moisture content of each individual particle can be calculated by integrating over the particle trajectories. This was presented exemplarily for a small scale top-spray granulator in (Fries et al., 2011b).

For the spouted bed the residence time distribution shown in Fig. 6-16 a) is also wide, with no clear peak. Although the granulator geometry and the air flow profile clearly cause an internal particle circulation in the spouted bed, cyclic particle wetting or a preferred residence time per pass through the spray zone cannot be observed in Fig. 6-16 a). For the given simulation conditions the particle circulation in the spouted bed is obviously not stable enough to ensure homogeneous particle wetting. Fluctuations in the particle dynamics, which were also seen in Fig. 6-6 a) for the spouted bed, apparently dominate over the regular particle circulation. The average residence time in the spray zone in the spouted bed is twice as high as in the top-spray granulator and only one third of the particles were not wetted at all within 7 s of simulation time.

Table 6-5: Average and maximum residence time of the particles in the spray zone (percentage of the simulation time) for the Wurster-coater, the spouted bed and the top-spray granulator after 7 s of simulation time.

Parameter	Unit	Wurster-coater	Spouted bed	Top-spray
Average residence time	%	0.44	0.71	0.35
Maximum residence time	%	2.37	8.49	13.39
Fraction of dry particles	%	21.34	34.28	51.75

The residence time distribution found in the simulation of the Wurster-coater shows clear peaks at multiples of 25 ms, which is the preferred residence time per pass of the particles through the spray zone. The density distribution shows clearly the particle fractions which crossed the spray zone once, twice or three times during 7 s of simulation time. This is underlined by the cumulative residence time distribution (see appendix A1) shown in Fig. 6-16 b) for the Wurster-coater as a function of the simulation time. After 1 s, all wetted particles crossed the spray zone only once. With time the fraction of those passing through the spray zone twice is increasing,



while the absolute value of the residence time per pass is almost constant. The distribution is very narrow, which indicates homogeneous particle wetting. This feature of the Wurster-coater is underlined regarding Table 6-5: Almost 80 % of the particles have been wetted within 7 s of simulation time, while the maximum residence time in the spray zone is only 2.37 % of the simulation time.

It can be concluded that the Wurster-coater geometry has very clear advantages regarding the homogeneity of particle wetting. If coating quality is the critical process requirement or if sticky material must be handled, which is sensitive to the moisture content, then, based on the presented simulation results, the Wurster-coater is the best choice.

6.2 Experimental verification of the Discrete Particle Model

This section is focused on the verification of the predictions of the DPM regarding the influence of the particle and collision dynamics on the final product properties in the fluidized bed agglomeration process. As reliable non-intrusive measurement techniques for particle trajectories in fluidized beds are available today, DPM simulation of the flow regimes in bubbling fluidized beds (Goldschmidt, 2001), spout fluidized beds (van Buijtenen, 2011) and spouted beds (Link, 2006) have successfully been validated against experimental results using particle image velocimetry (PIV) or positron emission particle tracking (PEPT). Many other experimental techniques for particle monitoring have been used by different authors, which are referenced in section 1.3.3. Yet, information on particle rotation and on the particle collision frequency remains still experimentally inaccessible. Since particle collision dynamics are believed to be a key micro mechanism for both build-up and breakage of agglomerates in fluidized beds, they are considered extensively using the model. The fluidization regime has a dominant impact on the structuration of the product during the agglomeration. Therefore, the model can be used to predict growth rate and strength of the agglomerates, which both depend fundamentally on the particle and collision dynamics. An indirect verification of the model predictions is pursued in this work, based on the measured size, structure and strength of product agglomerates produced in the fluidized bed.



6.2.1 Comparison of the agglomeration rate in different granulator configurations

Batch agglomeration experiments were performed in a lab-scale fluidized bed granulator to compare the agglomeration behaviour of amorphous spray dried maltodextrin powder in three different granulator geometries (GF3 top-spray, GF3 Wurster-coater and ProCell 5 spouted bed, all supplied by Glatt Ingenieurtechnik GmbH, Weimar). Pure water was injected as plasticizing agent. The equipment geometries used in the experiments are identical to the granulator configurations that were compared using the DPM. To identify the influence of the equipment geometry on the growth rate of the agglomerates, all process parameters were kept constant throughout the experimental study. The set of parameters defined as optimum for the Wurster-coater (see section 5.4.6, Table 5-11) was used for all three devices, although these parameters do not necessarily define the optimum process conditions for the top-spray granulator and the spouted bed. This procedure allows isolating effects related to the equipment geometry and the specific flow conditions on the product properties. To track the evolution of the particle size with process time, every 5 minutes samples were taken from the fluidized bed and analysed by sieving. 5 repetitions were performed for each experiment.

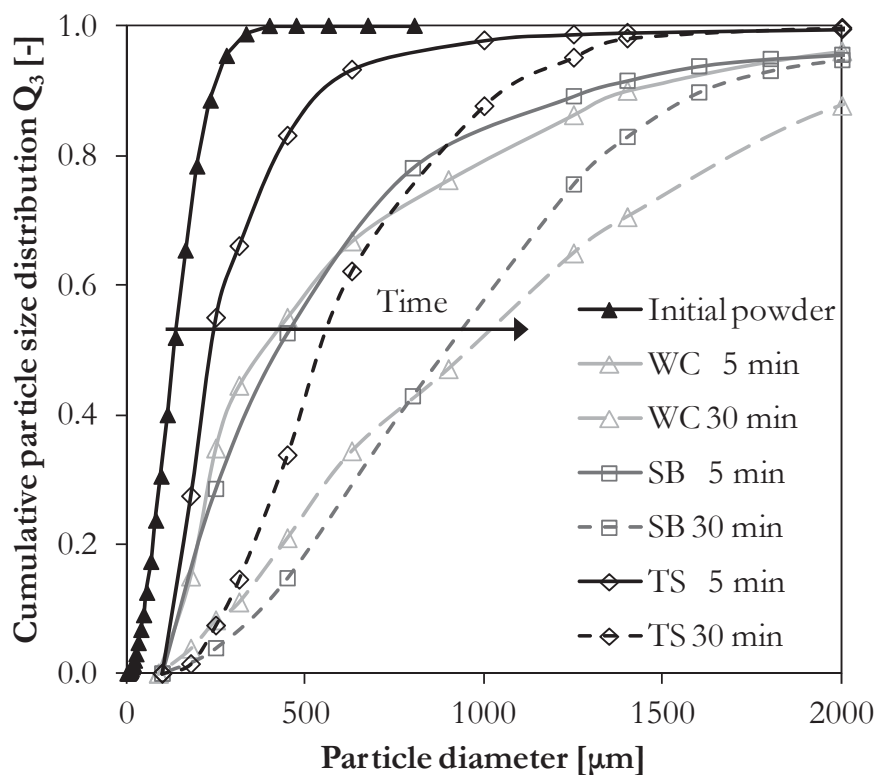


Figure 6-17: Cumulative mass-based size distribution of the agglomerates as a function of the process time.



It can be seen in Fig. 6-17 that the particle size distribution (see appendix A1) is continuously shifted towards larger particle diameters with progressing injection time, starting with the initial powder which has a Sauter mean diameter ($d_{32,0}$) of 150 μm . For each granulator the mass-based cumulative size distribution of the agglomerates is shown after 5 minutes and after 30 minutes of liquid injection. At identical process conditions (see Table 5-11) the Wurster-coater is characterized by a slightly higher growth rate than the spouted bed. This is probably related to a higher breakage rate in the spouted bed. In comparison to the other granulators, very low particle growth rates are obtained in the top spray granulator, which is most likely due to a higher overspray rate (less efficient wetting). Differences between the granulator configurations are found especially for agglomerates larger than 1.4 mm, where the mass fraction is twice as high in the Wurster-coater compared to the spouted bed granulator, while no agglomerates at all occur in this fraction in the top-spray granulator.

Local overwetting and lump formation are major risks when the top-spray configuration is used. Due to the stochastic particle motion in the bubbling fluidized bed with low average particle velocities a wide residence time distribution of the particles inside the spray zone occurs, which was shown in section 6.1.5 using the DPM. Few large lumps of approximately 20 mm in diameter were found in the experiments using the top-spray granulator after 60 min of liquid injection, but due to their weight they settle to the bottom and do not appear in the samples taken from the bed. To minimize lump formation the top-spray granulator has to be run very carefully using an elevated position of the nozzle above the bed (21 cm above the distributor plate). Due to this conservative but stable mode of operation, the overall efficiency of the top spray granulator is low compared to the other two configurations in this test. The growth rate is slower and a higher fraction of the spray liquid is lost as overspray.

The mean agglomerate size (Sauter diameter, see appendix A3) is shown in Fig. 6-18 as a function of time for the three tested granulator configurations. Error bars indicate the standard deviation of the results on the basis of five repetitions for each agglomeration experiment. The fastest growth rate but also the largest variance of the results is found for the Wurster-coater. At the defined process conditions the efficiency of the spouted bed and the top-spray granulator is lower, but the process is also more stable. Due to the irregular agglomerate shape, the equivalent particle size obtained by sieving is only an approximation of the true product properties. Differences in the agglomerate structure, which also affect the measured particle size, are presented in the next section.



The experimental results for the growth rate (see Fig. 6-19) are in good agreement with the expectations from the DPM simulations. A high agglomeration probability is expected if the collision frequency in spray zone is high and if the relative collision velocity in spray zone is low. A large average solids volume fraction in spray zone indicates intensive wetting. Both the agglomeration probability and the consolidation and breakage rate add up to the total agglomeration rate. If the dense bed is intensively agitated, with high average particle-particle and particle wall collision velocities, then the equilibrium between growth and compaction is shifted towards smaller agglomerates.

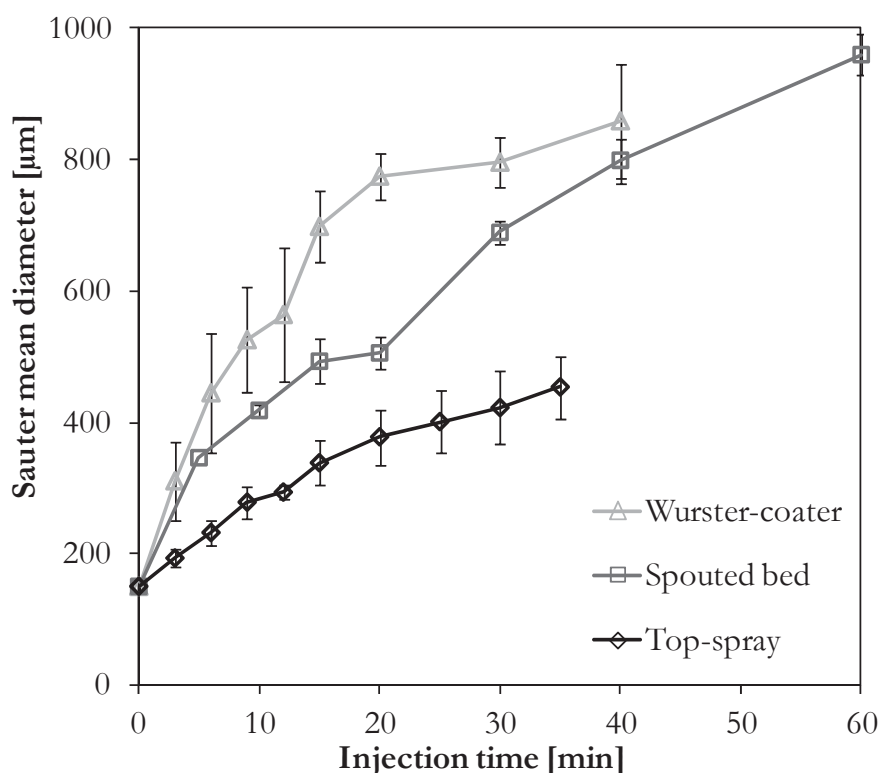


Figure 6-18: Evolution of the Sauter mean diameter of the agglomerates with time.

On this basis an intermediate growth rate is expected in the spouted bed since both the agglomeration probability and the breakage rate are expected to be very high. In the Wurster coater a lower agglomeration probability is expected due to less frequent and more energetic collisions in the spray zone. On the other hand, the breakage rate is also very low, which should result in a fast growth rate and the formation of fragile loosely structured agglomerates. According to the simulation results the top spray granulator is characterized by a low growth rate due to the low solids volume fraction and collision frequency of particles in the spray zone. The



agglomeration probability is expected to be particularly low due to the low wetting intensity, which is validated by the experiments.

The simulation results show that the presence and collision frequency of particles in the spray zone and therefore the agglomeration probability are particularly low in the top-spray granulator. This is confirmed by the experimental findings.

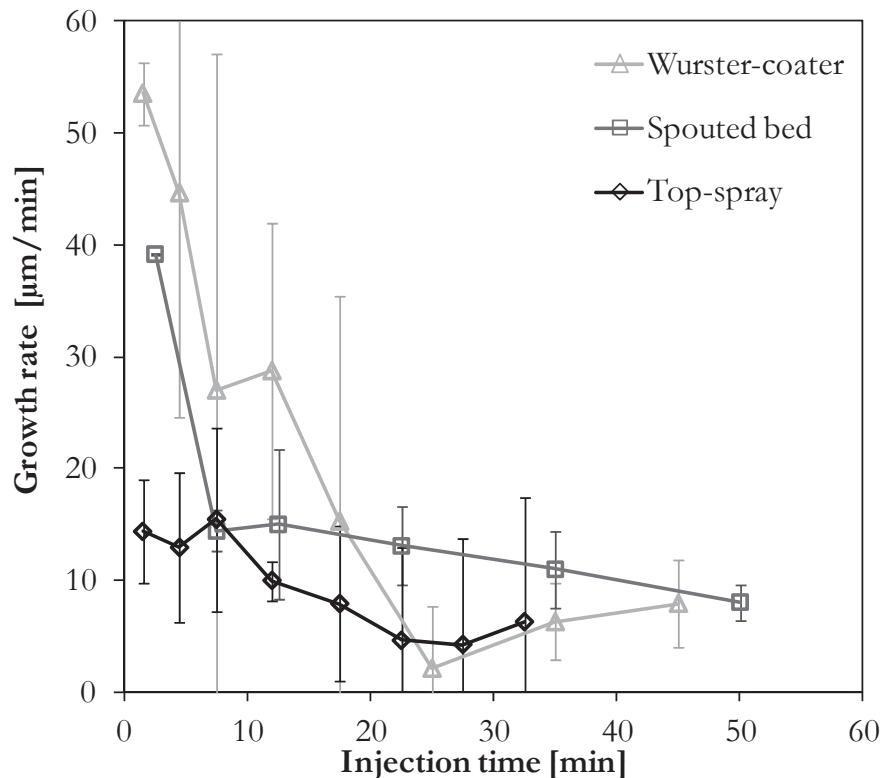


Figure 6-19: Evolution of the growth rate of the agglomerates with time.

6.2.2 Comparison of structure and strength of agglomerates from different granulator configurations

Throughout the agglomeration process the structure of maltodextrin agglomerates is continuously evolving. Compaction and breakage mechanisms are continuously competing with the build-up of larger structures due to agglomeration. These mechanisms are driven by the particle-particle interactions in the fluidized bed. Therefore, the agglomerate structure and strength is largely dependent on the flow conditions and the geometry of the granulator.



6.2.2.1 Agglomerate structure

Characteristic steps for the formation and consolidation of maltodextrin agglomerates can be identified in the SEM pictures shown in Fig. 6-20: During the initial minutes of the process loosely packed aggregates of primary particles are formed, which are bonded by thin solid bridges (Fig. 6-20 a). These bridges grow in the course of the process due to viscous flow on the plasticized particle surface (sintering). In Fig. 6-20 b) the smooth wetted areas can be seen, where dry primary particles are attached. This illustrates very well the agglomeration mechanisms: Some particles come into contact with liquid droplets, which creates a viscous (plasticized) film on the particle surface. When these surface-active particles collide with others, the kinetic energy of the collision may be dissipated in the viscous liquid film, which leads to adhesion. With time, sinter necks grow between the individual particles in the aggregate due to viscous flow on the particle surface and due to partial dissolution of the attached particle in the liquid film (see Fig. 6-20 c). Once the viscous bridges are dried by the fluidization air, stable solid bridges are formed. Repeated wetting and drying steps and multiple collisions promote consolidation of the agglomerates for longer process times.

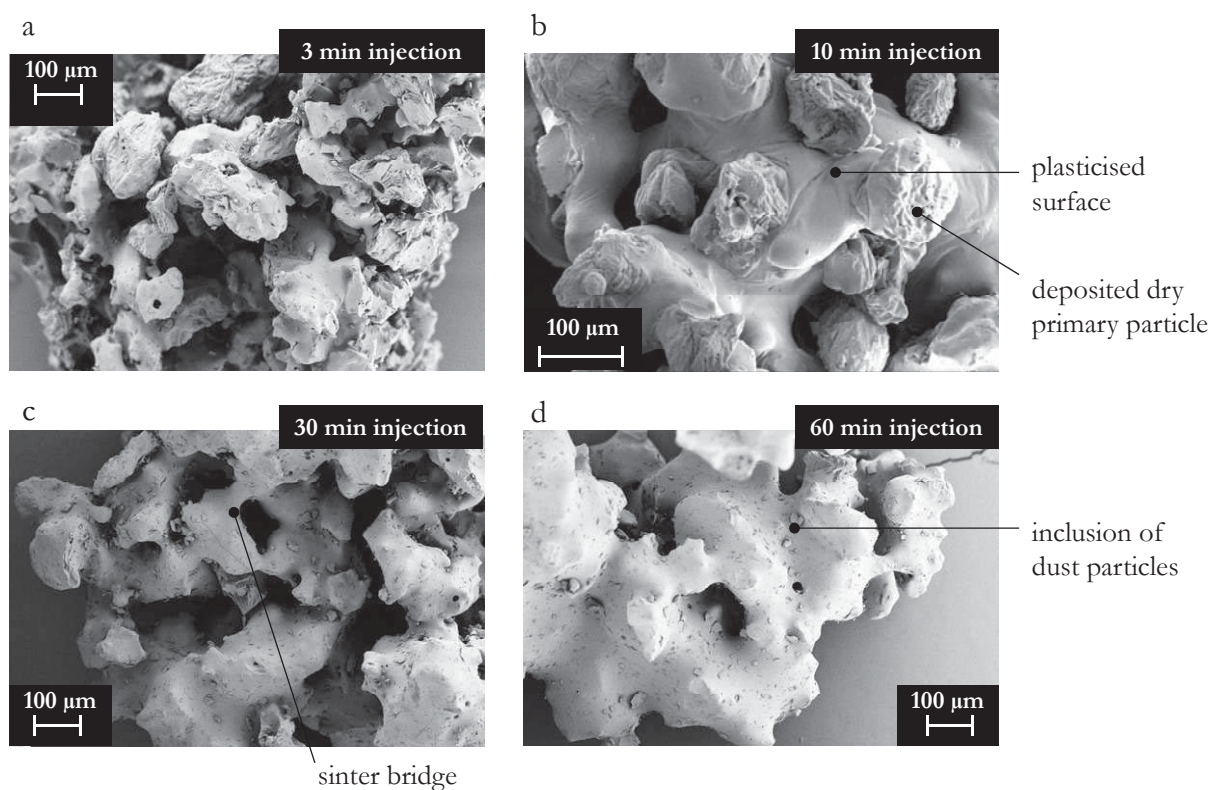


Figure 6-20: SEM images of maltodextrin agglomerates produced in the Wurster-coater at 70°C.



After 60 minutes a dense closed surface structure has grown, where primary particles and solid bridges can no longer be distinguished (Fig. 6-20 d). Due to breakage and attrition, more and more dust particles cover the agglomerate surface.

In Fig. 6-21 the evolution of the agglomerate structure with time, which is characteristic for the used granulator configuration, is compared for agglomerates produced in the spouted bed and in the Wurster-coater. After 5 minutes of liquid injection the formed agglomerate structures in both granulators are similar. The agglomerates produced in the spouted bed are slightly more compact and show less branched structures on the surface. For longer process times compact and dense agglomerates are found in the spouted bed. Smooth plasticized areas cover almost the entire agglomerate surface, whereas the particles taken from the Wurster-coater show a rough surface, where primary particles can still be identified. This indicates a less homogeneous liquid distribution among the particles in the spouted bed compared to the Wurster-coater and more intensive consolidation due to particle-particle interactions. Both effects are in excellent agreement with the predictions by the DPM.

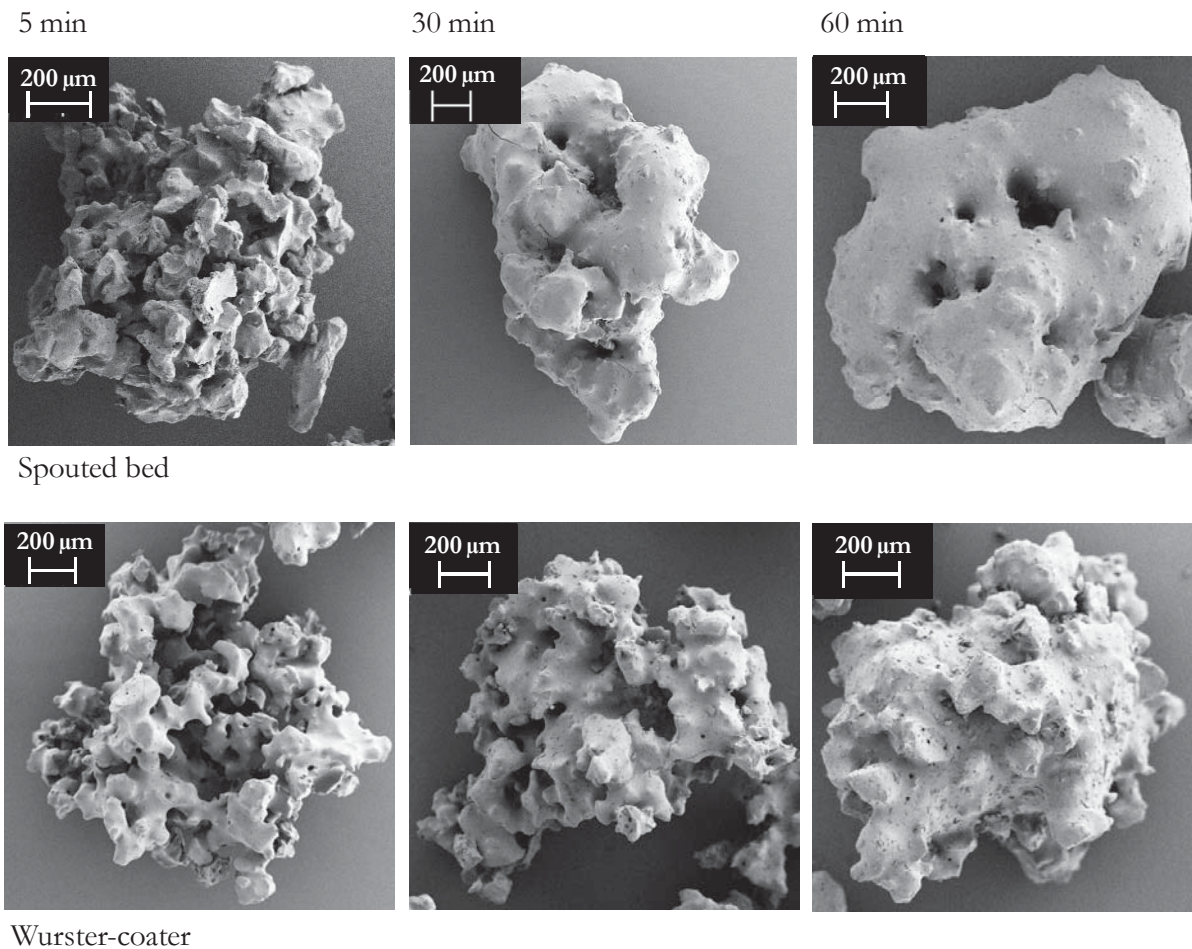


Figure 6-21: SEM images of maltodextrin agglomerates produced in the spouted bed and Wurster-coater: Evolution of the agglomerate structure with process time.

With the help of X-ray tomography the three-dimensional particle structure can be analyzed, which is very useful to describe also the inner structure of the agglomerates. Fig. 6-22 shows two slices cut out of an agglomerate bulk. Obviously, a filigree network with large interconnected voids dominates throughout the entire agglomerate structure. A comparison of the structures obtained after 5 minutes and 30 minutes of liquid injection reveals an increasing structure thickness with time, which is most probably due to sintering processes. Solid bridges between two particles in contact grow with time due to viscous material flow at the surface.

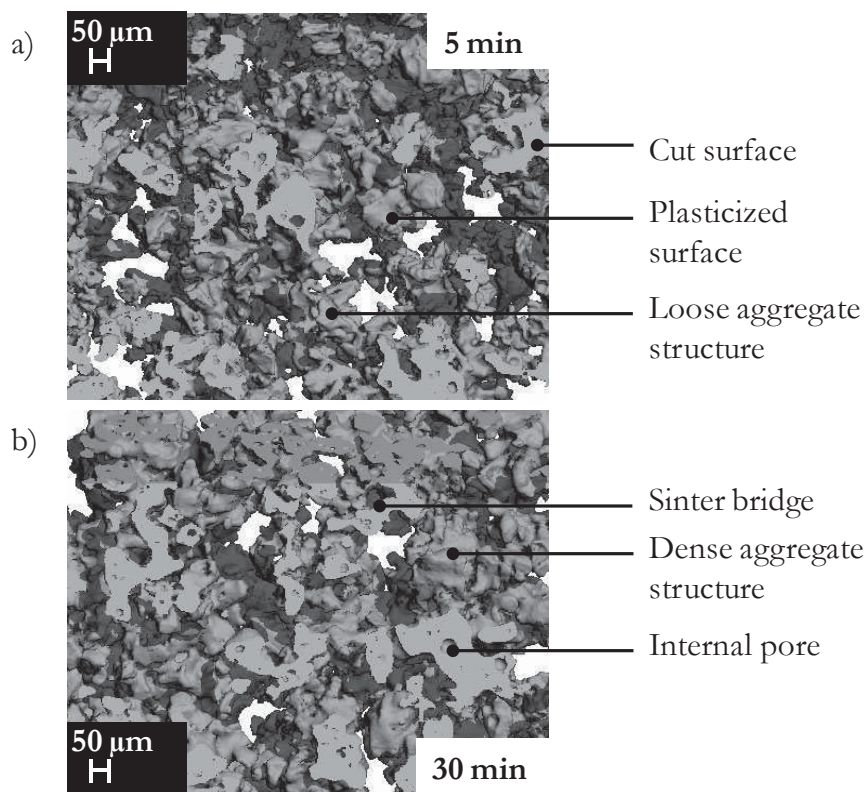


Figure 6-22: X-ray tomographic images of the 3D structure of maltodextrin agglomerates produced in the Wurster-coater. a) 5 min. liquid injection time, b) 30 min. liquid injection time.

The density distribution of the volume-based 3-dimensional structure thickness, defined according to Hildebrand & Rüeggsegger (1997) (see appendix D) is plotted in Fig. 6-23. The structure thickness can be obtained directly from analysis of 3D images recorded by an X-ray tomograph. The distribution of the structure thickness is shifted to the right with time, indicating the growth of sinter bridges and the compaction of the agglomerate structure along with the process time. The average structure thickness increases from 0.036 mm after 5 minutes to 0.040 mm after 30 minutes.

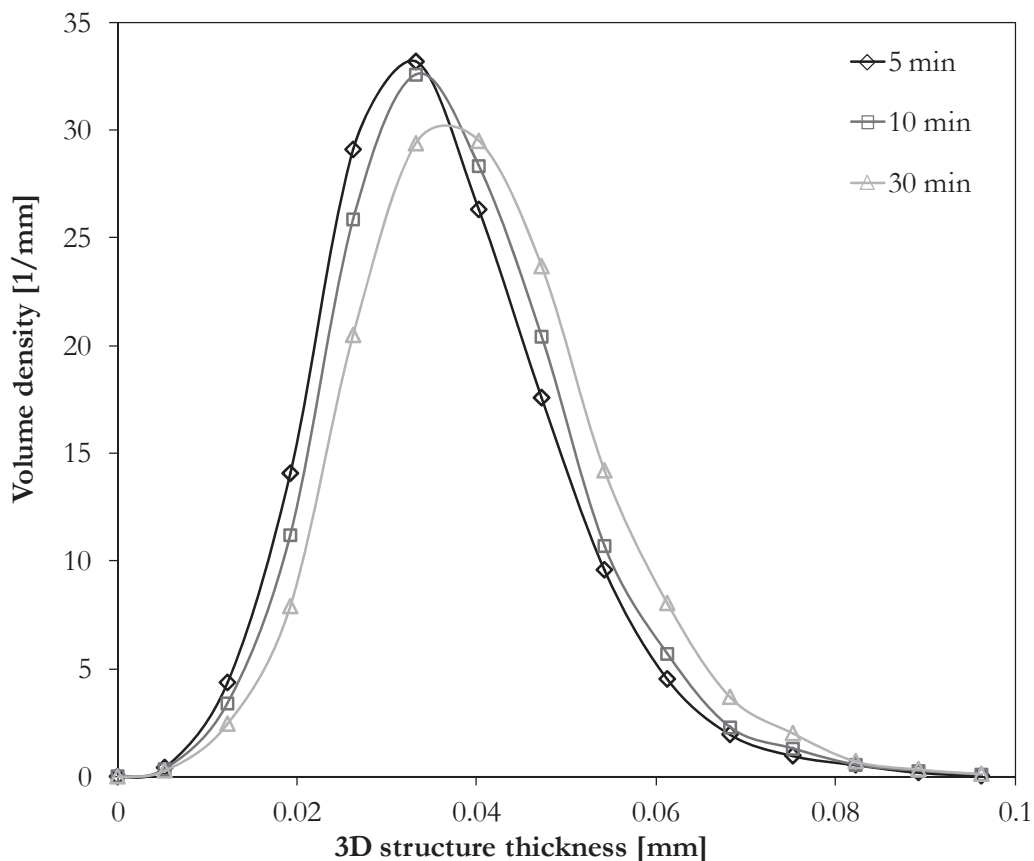


Figure 6-23: Volume-based density distribution of the 3D structure thickness as a function of the injection time.

6.2.2.2 Agglomerate strength

In order to preserve the improved properties of an agglomerated food product until it is used by the consumer, the agglomerates must withstand mechanical stress during filling and transport. The mechanical strength of the agglomerates is therefore an important feature for the quality of the product. In the fluidized bed the agglomerates are subject to disruptive forces related to collisions with other particles and the equipment walls. Consequently, weak or soft agglomerates will be destroyed and the remaining agglomerates become more compact and stiff with time. Since the agglomerate strength is dependent on the stress the particles must resist to during production, the mechanical product properties are determined by the geometry and the flow conditions of the granulator equipment. The influence of the granulator configuration on stiffness and strength of maltodextrin agglomerates is analyzed in this section with the help of compression tests. The applied test conditions are given in section 2.3.2, where the acquisition of the mechanical agglomerate properties from the force displacement curve is shown exemplarily in Fig. 2-9. For the analysis, agglomerates within the size fraction between 1.4 mm and 2.0 mm were

separated from the product batch by sieving. The contact stiffness and the breakage energy are calculated according to Eq. 2-1 and Eq. 2-2, respectively.

Fig. 6-24 a) shows that the average contact stiffness is continuously increasing with time. For the Wurster-coater it doubles from 5 to 25 minutes agglomeration time, while the increase is less pronounced for the spouted bed. The error bars in Fig. 6-24 indicate the 95 % confidence interval (see Appendix C2) of the average value, based on 110-150 loading phases.

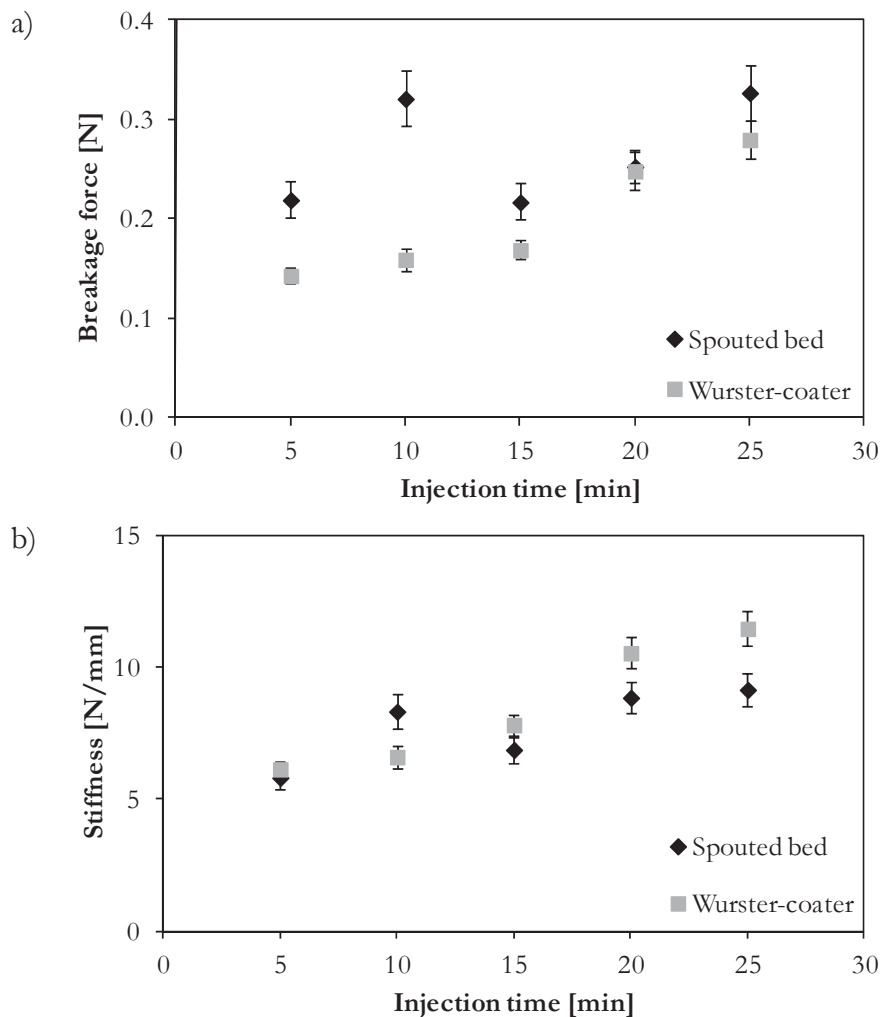


Figure 6-24: a) Contact stiffness and b) breakage force as a function of time for agglomerates produced in the Wurster-coater and in the spouted bed (30°C process temperature, size fraction $1.4 \text{ mm} < d_p < 2.0 \text{ mm}$).

For ideal dense particles a constant stiffness would be obtained, which describes the mechanical behaviour of the material. The measured apparent contact stiffness is dependent on the agglomerate structure, due to possible rearrangements of the particles within the structural network. As the diameter of solid bridge bonds increases with time, the measured contact



stiffness is also increasing. For both equipment geometries the obtained contact stiffness of the maltodextrin agglomerates is in the same range. Looking at the breakage force, a linear increase with time can be observed in Fig. 6-24 b) for the Wurster-coater. The average breakage force doubles from 5 min to 25 min process time. Sinter bridges between two primary particles grow thicker with time and become more stable. Yet, due to the irregular agglomerate structure relatively weak agglomerates are still found after 25 minutes of process time whereas others already exhibit high strength after only 5 minutes. For the spouted bed the observed trend is similar, with an outlier at $t = 10$ minutes.

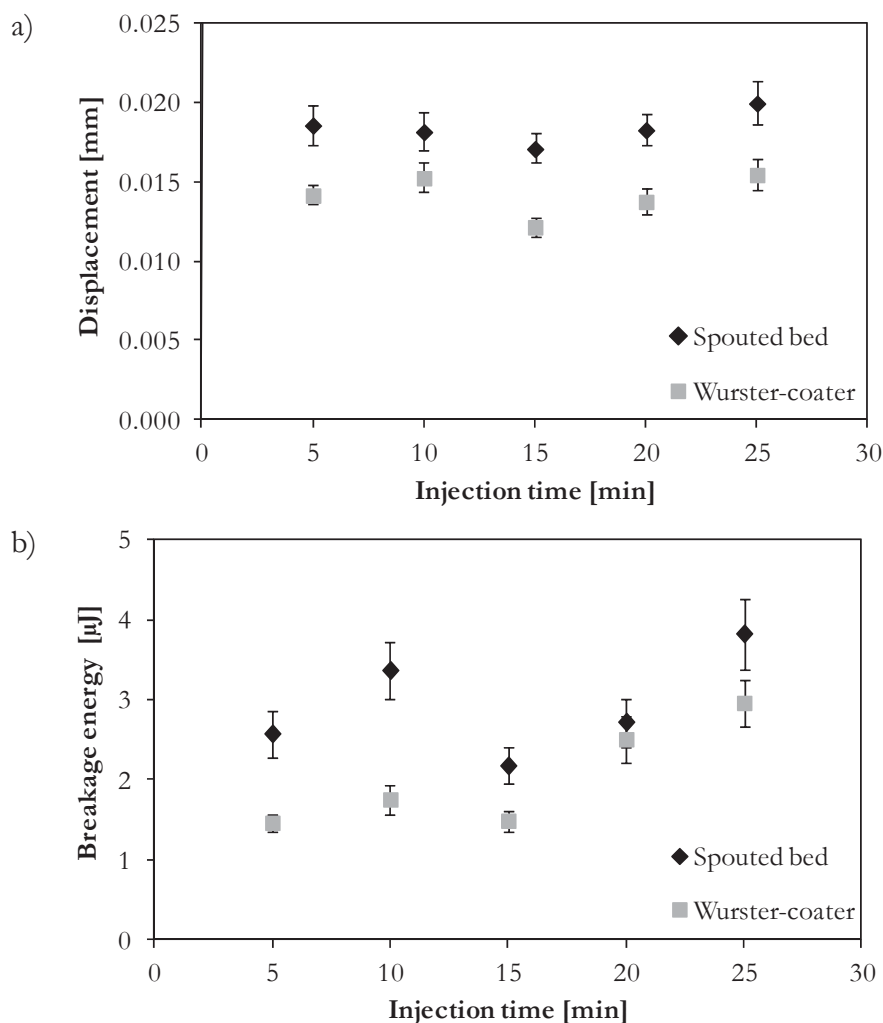


Figure 6-25: a) displacement increment and b) breakage energy as a function of time for agglomerates produced in the Wurster-coater and in the spouted bed (30°C process temperature, size fraction $1.4 \text{ mm} < d_p < 2.0 \text{ mm}$).

The measured agglomerate strength is higher for the spouted bed than for the Wurster-coater for short injection times (see Fig. 6-24 b) and 6.25 b)), which is in agreement with the DPM



simulations, where more frequent and more energetic collisions occurred in the spouted bed. For longer injection times, though, no significantly different strength is measured for agglomerates produced in the Wurster-coater or in the spouted bed. The average deformation of the agglomerates from the beginning of a loading interval to the breakage point (displacement increment) is nearly constant at approximately 1 % of the agglomerate diameter for all tested samples.

Due to differences in the collision intensity and frequency, the highest agglomerate strength is expected for agglomerates produced in the spouted bed and the lowest for those produced in the top-spray granulator based on the simulation results (see Table 6-2 and Fig. 6-10). The experimental findings for maltodextrin agglomerates are in excellent agreement with these predictions. As shown in Table 6-6 the measured breakage force and breakage energy as well as the deformation at the breakage point are higher in the spouted bed than in the other two granulators. Stiffness, breakage force and breakage energy of agglomerates produced in the top-spray granulator are 50 - 90 % lower compared to agglomerates from the other two equipment geometries.

Table 6-6: Average strength of agglomerates produced in different granulator geometries (t = 15 min, T = 70°C, size fraction: 1.4 mm < d_p < 2.0 mm).

Parameter	Unit	Wurster-coater	Spouted bed	Top-spray
Contact stiffness	N/mm	9.26 ± 0.54	8.73 ± 0.53	3.90 ± 0.41
Breakage force	N	0.27 ± 0.02	0.28 ± 0.02	0.07 ± 0.01
Displacement increment	mm	0.017 ± 0.001	0.019 ± 0.001	0.013 ± 0.001
Breakage energy	μJ	3.32 ± 0.29	3.89 ± 0.35	0.36 ± 0.09

These differences can very well be explained by the simulated collision dynamics. In Fig. 6-26 the DPM simulation results for the time-averaged maximum energy dissipation during particle collisions is compared to the experimental findings for the breakage energy of the maltodextrin agglomerates produced in the three different granulator configurations.

Obviously the observed differences of the collision dynamics can well be used as an indicator for the final product properties. The relative strength of agglomerates produced in different granulators is well predicted by the model. Due to different loading rates in simulation and



experiment, the absolute values of the breakage energy found in the compression tests cannot be predicted by the DPM, however.

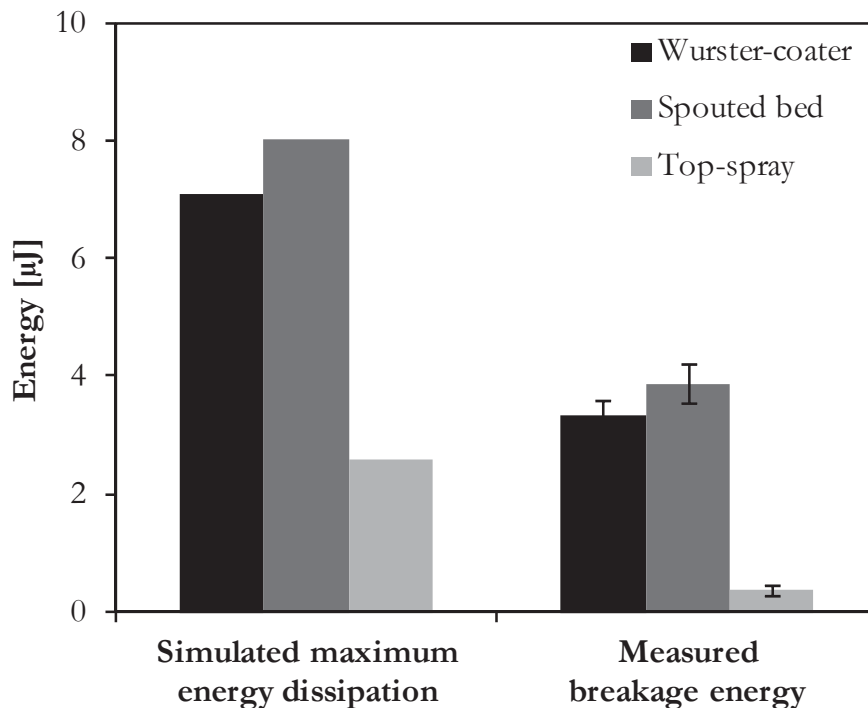


Figure 6-26: Comparison of numerical and experimental results relating the collisional energy dissipation and the agglomerate strength in three different granulator configurations.

In Fig. 6-27 the experimental results for the breakage force of maltodextrin agglomerates produced in the Wurster-coater, the spouted bed and the top-spray granulator are related to the time-averaged maximum contact force observed during particle collisions in the same devices. It can be seen that the collision dynamics clearly determine the product strength and that this influence is correctly described by the DPM. The relative performance of the three compared granulator configurations is well predicted by the model. Absolute values differ again, due to unequal loading rates in simulation and experiment.

Fig. 6-28 finally shows that the measured allowable deformation up to the breakage point is in excellent agreement with the time-averaged maximum of the particle deformation in the DPM simulations. This result is a good proof for the calibration of the contact model based on measured material parameters, as presented in chapter 3.

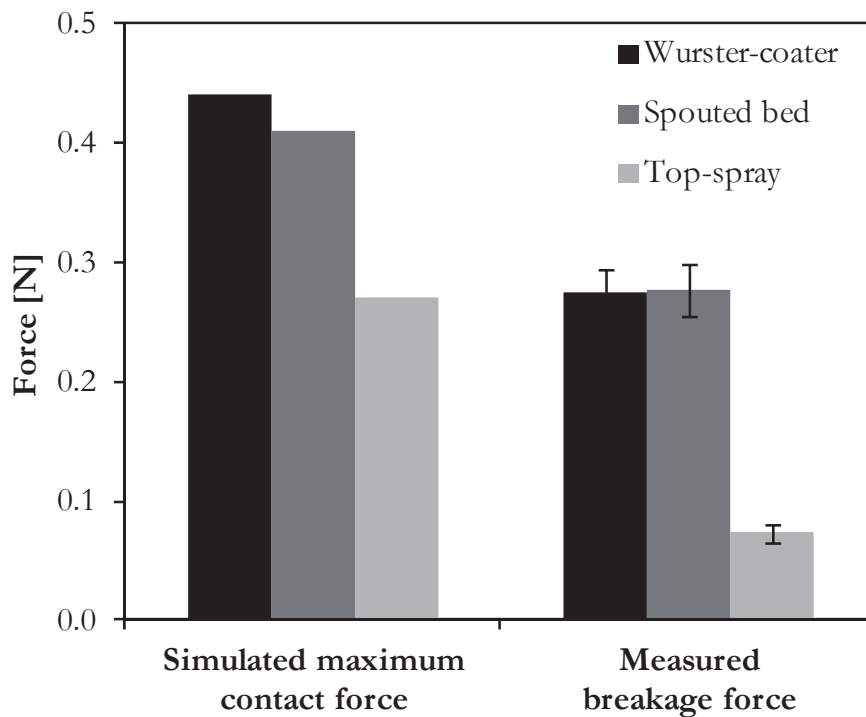


Figure 6-27: Comparison of numerical and experimental results relating the contact force during collisions and the agglomerate strength in three different granulator configurations.

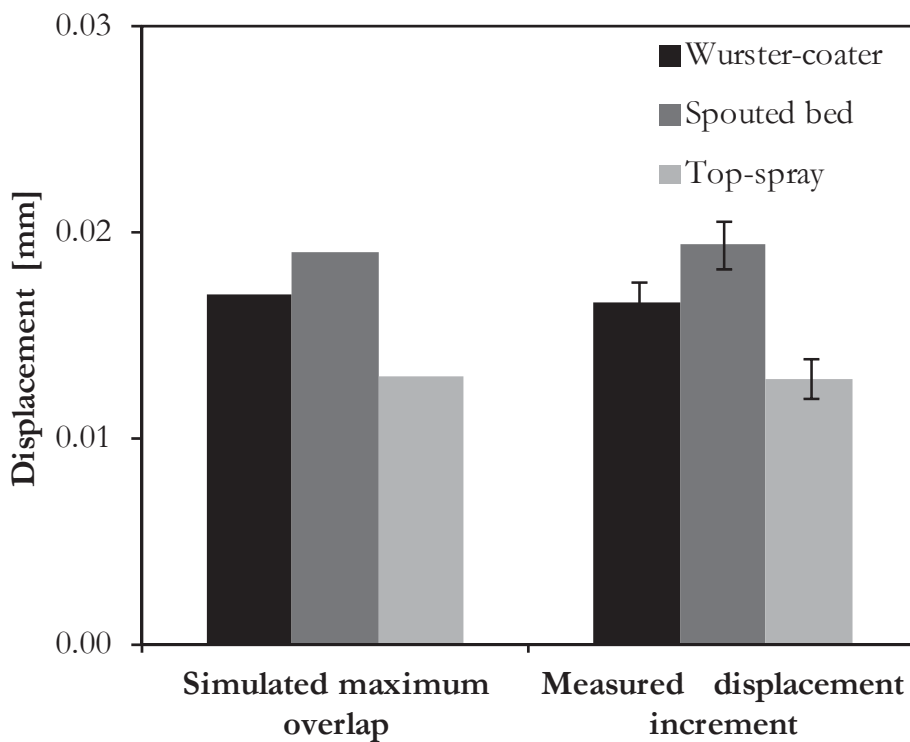


Figure 6-28: Comparison of numerical and experimental results relating the deformation during collisions and the agglomerate strength in three different granulator configurations.



6.3 Conclusion

In a combined computational and experimental study the influence of the geometry of the equipment of a fluidized bed granulator on the particle and collision dynamics and therefore on growth rate, structure and strength of the product particles was investigated. A top-spray granulator, a Wurster-coater and a prismatic spouted bed were compared at identical process conditions. The numerical analysis consisted of DPM simulations to study particle motion and collision dynamics as well as the collision frequency. Experimentally, all granulator configurations were used for the agglomeration of amorphous maltodextrin by adding pure water as binding agent.

Based on the simulation results the Wurster-coater is characterized by a homogeneous moisture distribution and by a medium wetting intensity, which is expected to cause an intermediate growth rate. The experimental results showed that for the given conditions the growth rate is very high especially during the first minutes of liquid injection. The top-spray granulator is characterized by a low adhesion rate and a very low wetting intensity. The overall growth rate should therefore be low, which was approved by the experimental results. Due to the low collision intensity the strength of agglomerates produced in the top-spray granulator is inferior. The spouted bed has the most intensive gas-liquid-solid contact and should therefore provide a high agglomeration rate, which was confirmed experimentally. The mechanical stress related to collisions and therefore the breakage rate is high compared to the other granulators, which leads to the formation of compact and dense agglomerate structures. The best equipment to produce uniform, large and stable agglomerates is the Wurster-coater, based on the presented numerical and experimental results. It should also provide the best redispersibility of the product.

The results presented in this chapter illustrate the outstanding capabilities of a DPM to understand the influence of the equipment geometry on particle-scale interactions in a fluidized bed. Simulation results of the collision dynamics were successfully related to the experimentally obtained size, structure and strength of the agglomerates. Based on this experimental verification, the model can be used to optimize the process conditions and the geometry of a fluidized bed granulator with respect to the desired product properties.



7 Conclusions

This thesis describes the influence of material and process parameters on the agglomeration behaviour of amorphous food powders in fluidized beds. The complex process dynamics are analyzed both experimentally, regarding the agglomeration of maltodextrin DE 21, and numerically with the help of DPM simulations.

It was found by previous research that the kinetics of fluidized bed agglomeration processes are governed on the micro scale by the interactions between individual particles. A strong focus is therefore put on the analysis of the particle and collision dynamics inside the fluidized bed in this work. Non-intrusive experimental techniques for the tracking of the particle motion in non-transparent, three-dimensional fluidized bed granulators are available, but the experimental effort is huge and the accuracy of the results has been limited until now. Therefore numerical simulations offer a promising alternative approach for the description of the process dynamics. The Discrete Element Method (DEM) is particular useful in this context, as it describes the motion of each individual particle as well as the particle-particle interactions on a physical basis. Coupled with a CFD simulation, the gas and particle dynamics in a fluidized bed can be resolved on a high level of detail. Computational and experimental results are combined in this work to analyze in detail the particle dynamics and their impact on the structuration of agglomerates in a fluidized bed.

Batch agglomeration experiments were performed in a wide range of operating conditions to investigate the influence of all relevant process variables on growth rate, structure and strength of the product particles. It was found that the geometry of the equipment plays a dominant role for the particle dynamics and has therefore a strong influence on the properties of the final product. The results of the experimental investigations lead to the following main statements:

1. The agglomeration of amorphous water-soluble food powders is activated by a local exceeding of the glass transition temperature, whereupon the kinetic energy of particle collisions is dissipated in a viscous liquid film.



2. Homogeneous growth of the agglomerates is achieved by uniform particle wetting, limiting the exceeding of the glass transition temperature to a small area near the spray nozzle and keeping the residence time distribution of the particles inside the spray zone as narrow as possible.
3. An internal circulation of the particles inside the granulator improves the homogeneity of particle wetting and allows the application of more intensive process conditions. The liquid throughput can be increased and the required particle growth is achieved within shorter injection times.
4. Process intensification for the agglomeration of amorphous food powders in a fluidized bed has to balance on a thin line between fast growth and a collapse of the bed. An increase of the process temperature or of the fluidization air flow rate always drives the process towards a more stable regime.

The dynamics of particle collisions are currently not accessible with experimental techniques. Therefore, the capabilities of the computational model are indispensable for an investigation of the structuration of agglomerates in a fluidized bed. Numerical simulations of the collision dynamics combined with an experimental analysis of the mechanical properties of maltodextrin agglomerates produced under different process conditions and in different configurations of the granulation equipment have been presented in this work. The findings can be summarized by the following main statements:

5. Structure and strength of agglomerates produced in a fluidized bed are determined by the particle and collision dynamics. The mechanical properties of the final product can be controlled systematically via the applied operating conditions and via the geometry of the equipment.
6. A validated contact model and reliable experimental data for the elastic modulus and for the restitution coefficient are required in order to assure quantitative significance of the simulation results regarding the collision dynamics.
7. The Discrete Particle Model is able to predict the intensity and homogeneity of particle wetting and therefore the growth rate and the width of the size distribution of the product based on the residence time distribution of the particles inside the spray zone.
8. The Discrete Particle Model is able to predict the structuration of the product particles based on the simulated distribution of the relative collision velocity, the collision frequency and the energy dissipation upon particle impacts.



Simulation results for the time-averaged maxima of the contact force are in good agreement with experimental results for the breakage force of the agglomerates. The allowable deformation up to the breakage point can be well be predicted by the time-averaged maximum overlap of the particles in the simulation. Furthermore the measured breakage energy confirms the model predictions based on simulation results of the time-averaged maximum energy loss that occurs during particle collisions.

9. Based on model predictions and experimental results the Wurster-coater is characterized as the optimal equipment for the agglomeration of amorphous food powders. It provides fast growth, stable agglomerates with open pores and superior process stability at intensive wetting conditions.

In this thesis existing granulator geometries were compared in terms of the particle and collision dynamics and their influence on the size and structure of the product. An experimental verification of the model predictions was accomplished for the agglomeration of amorphous maltodextrin. Based on these results, it seems promising to use the DPM for further investigations with the aim to optimize the geometry of the granulator equipment. A promising approach would be to optimize the position of the spray nozzle inside the granulator in order to improve the homogeneity of particle wetting.



Appendix

A Fundamentals in particle technology

Size distributions are used to characterize a particle collective in terms of the grain sizes occurring within the batch and to indicate the corresponding fractions. The particle size x is defined as a length scale, most commonly as the equivalent diameter of a sphere. On the ordinate of the coordinate system the proportion of the corresponding size fraction in the collective is plotted. Two different representations of the size distribution are used:

A1 Cumulative size distribution

The cumulative size distribution $Q(x_i)$ gives for each particle diameter x_i of the collective the fraction of particles, which have a diameter equal to or smaller than x_i .

$$Q_r(x_i) = \frac{\text{fraction}(x_{\min} \dots x_i)}{\text{all fractions}(x_{\min} \dots x_{\max})}. \quad (\text{A-1})$$

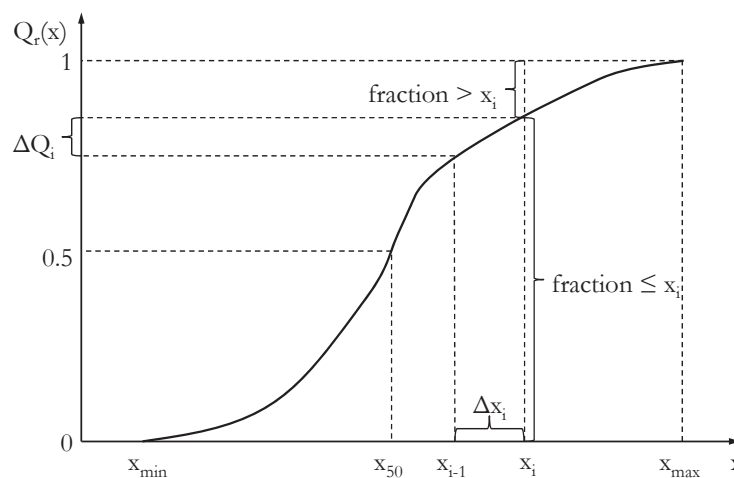


Figure A-1: Continuous representation of the cumulative particle size distribution $Q(x)$.



An illustration of a characteristic cumulative particle size distribution $Q_r(x)$ is given in Fig. A-1. The index r indicates the dimension which is used in the derivation of the equivalent particle diameter. The distribution can be based on the particle number ($r = 0$), a characteristic length ($r = 1$), a characteristic area ($r = 2$) or the particle mass/volume ($r = 3$).

A2 Size density distribution

The derivative of the cumulative size distribution with respect to the particle diameter x is defined as size density distribution $q(x)$. It describes the fraction within a size interval divided by the width of the interval i :

$$q_r(x_i) = \frac{\Delta Q_i}{\Delta x_i} = \frac{\text{fraction}(x_{\min} \dots x_i)}{\text{all fractions} \cdot \text{width of interval } i} \quad (\text{A-2})$$

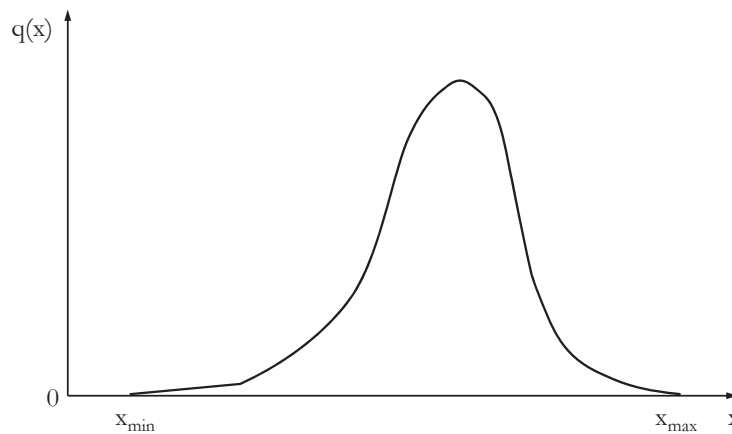


Figure A-2: Continuous representation of the size density distribution $q(x)$.

An illustration of a characteristic size density distribution $q_r(x)$ is given in Fig. A-2.

A3 Sauter mean diameter

The Sauter diameter $d_{3,2}$ is an average particle size which is characteristic for the whole particle collective. If the particle collective of interest was replaced by a monodisperse collective of spheres in such way, that both the total particle volume and the total surface area of the particle collectives were equal, then the diameter of the spheres is called Sauter diameter. It can be calculated from the size distribution according to Eq. A-3:



$$d_{3,2} = \frac{\sum_{i=x_{\min}}^{x_{\max}} \bar{x}_i^3 \cdot q_0 \cdot x_i \cdot \Delta x_i}{\sum_{i=x_{\min}}^{x_{\max}} \bar{x}_i^2 \cdot q_0(x_i) \cdot \Delta x_i} \quad (\text{A-3})$$

A4 Droplet deposition on a single particle

The droplet deposition model proposed by Löffler (1988) used two parameters a and b, which are given in Table A-1 as a function of the Reynolds number.

Table A-1: Parameters for droplet deposition model (Li et al., 2011).

Parameter	Range				
Re	< 1	1 - 30	30 - 50	50 - 90	> 90
a	0.65	1.24	1.03	1.84	2
b	3.7	1.95	2.07	0.506	0.25

B Specifications of used equipment

B1 Components of the fluidized bed agglomeration plant

Air ventilator:

Elektror Hochdruckventilator HRD 60 FU – 105/4,0

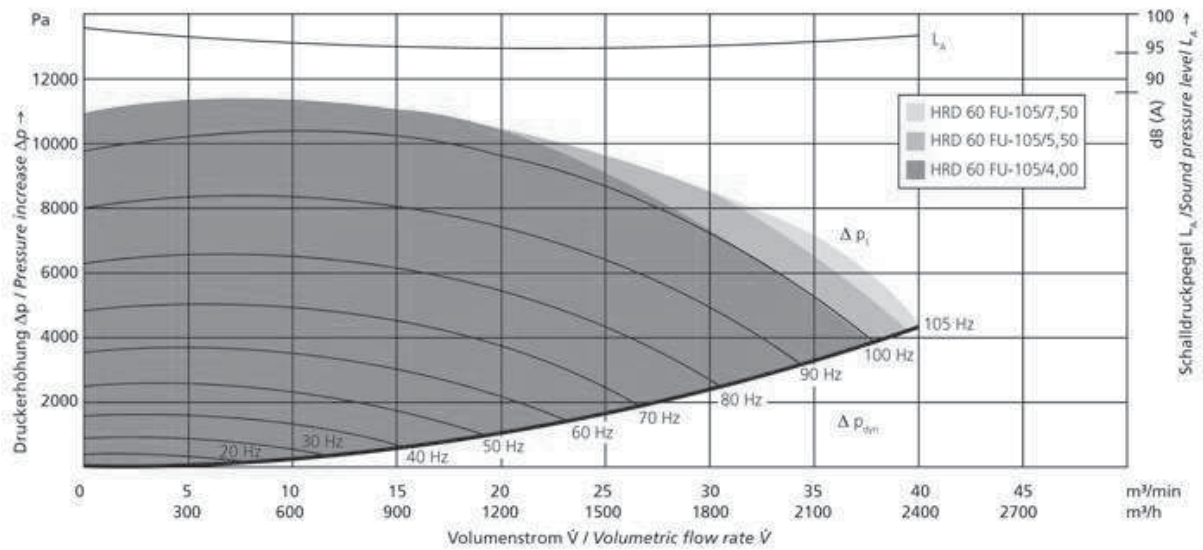


Figure A-3: Characteristic of the used air ventilator.

Air heater

Leister Lufterhitzer Typ 40 000, 3x 400 V, 11.2 kW electrical power

Electric frequency converter

Omron JX – A 4055 – EF, 400 V, 5.5 kW

Air filter

Mahle Entsabungselement (conical shape)

Type 852 903 TI 07/1 – 0.5 + DRG V4A FRV

Air flow meter

Fluidization air: Vane anemometer Schiltknecht MiniAir64 Mini,

Measurement range: 0.5 - 40 m/s



The SPS process control system uses the air flow meter to manipulate the gas flow rate via the electric frequency converter. If a required minimum flow rate is achieved, the air heater is released.

Atomizer air, classification air: ABB Rotameter 3k240000011410, 3k240000011411

Measurement range: 0 – 5,6 m³/h, 0 – 4.0 m³/h at p = 1 bar.

Temperature sensor

Rössel Messtechnik Mantel-Widerstandsthermometer (PT 100)

Ø 3 mm, four conductor circuit

Pressure sensor

SensorTechnics pressure transmitter KTE 6 P01 G O 4 V

Pressure range: 0 – 1 bar

Output signal: 4 ... 20 mA

Humidity sensor

Driesen + Kern DKRF400, Sensirion SHT75DK

Measurement principle: capacitive sensor

Measurement range: 0 ... 100 % RH, -40°C ... 80°C.

Accuracy: ± 0.3 °C, ± 1.8 % RH within region 20 % RH < φ < 80 %.

Peristaltic pump

Medorex TBE / 200 84 – 1 – 8 – 6.4 x 1.6

6 rolls, water flow rate: 42.0 – 840 ml/min

Balance

Kern 572 – 45 precision balance

Measurement range: 0 – 12100 g, accuracy: ± 0.05 g



B2 Particle size analysis

Sympatec Helos 12 LA Laser diffraction spectrometer

Measurement range: 0.5 – 175 μm (f=100 mm),

0.5 – 875 μm (f=500 mm)

0.5 - 1750 μm (f=1000 mm)

C Statistical evaluation of experimental results

C1 Standard deviation

The standard deviation s_N of a sample describes the variation of the individual values relative to the mean value \bar{x} . It is defined as the square root of the variance:

$$s_N = \sqrt{\frac{1}{N-1} \sum_{i=1}^N (x_i - \bar{x})^2} . \quad (\text{A-4})$$

C2 Confidence interval

The confidence interval around the mean value of a sample describes the range of values, within which the true average value \bar{x} of the entire population is situated with a defined probability (i.e. 95 %). It is a function of the variance of the sample and the number of sample values N which are taken into account. If the 95 % confidence intervals of two samples do not overlap, then the two mean values are called significantly different. Based on the student t-distribution function, the confidence interval is defined according to Eq. A-5:

$$\left[\bar{x} - t_{\left(1-\frac{\alpha}{2}; N-1\right)} \frac{s_N}{\sqrt{N}} ; \bar{x} + t_{\left(1-\frac{\alpha}{2}; N-1\right)} \frac{s_N}{\sqrt{N}} \right] , \quad (\text{A-5})$$

$t_{\left(1-\frac{\alpha}{2}; N-1\right)}$ indicates the $(1-\alpha/2)$ -quantile of the t-distribution with $(N-1)$ degrees of freedom.



D Three-dimensional structure thickness

With the introduction of 3D microscopic measuring techniques such as X-ray tomography it is possible to obtain a complete depiction of complex spatial structures. As a consequence, new 3D methods have been developed for the estimation of morphometric parameters such as volume, surface area and connectivity by direct processing of 3D images. Hildebrand & Rüeggsegger (1997) proposed a general thickness definition for arbitrary structures allowing the calculation of the mean structure thickness and the thickness distribution independently of an assumed structure model.

For $\Omega \in \mathbb{R}^3$ being the set of all points included in the investigated spatial structure and p being an arbitrary point in this structure, the volume-based local thickness $\tau(p)$ is defined as the largest diameter of a sphere, which contains the point p and is completely inside the structure.

$$\tau(p) = 2 \max(\forall r \mid p \in sph(x, r) \in \Omega, x \in \Omega). \quad (A-6)$$

Where $sph(x, r)$ is the set of points inside a sphere with center x and radius r .

The volume-based thickness distribution $Q_3(\tau)$ is obtained by integrating over the entire structure Ω . Cumulative and density distributions of the 3D structure thickness can be written according to Eq. A-1 and Eq. A-2.



References

- Adams, M.J; Perchard, V. The cohesive forces between particles with interstitial liquid. *Int. Chem. Eng. Symposium Series* **1985** (91) 147–160.
- Adams, M.J; Edmondson, B. Forces between particles in continuous and discrete liquid media. In *Tribology in particulate technology*. Briscoe, B., Adams, M., Eds. Taylor & Francis: 1987.
- Altzibar, H.; Lopez, G.; Aguado R.; Alvarez, S.; San Jose, M. J.; Olazar, M. Hydrodynamics of Conical Spouted Beds Using Different Types of Internal Devices. *Chemical Engineering and Technology* **2009**, 32 (3) 463–469.
- Anderson, T. B.; Jackson, R. Fluid Mechanical Description of Fluidized Beds. Equations of Motion. *Industrial & Engineering Chemistry Fundamentals* **1967**, 6 (4) 527–539.
- Anh Ho, C.; Sommerfeld, M. Modelling of micro-particle agglomeration in turbulent flows. *Chemical Engineering Science* **2002**, 57 (15) 3073–3084.
- Antonyuk, S. Deformations- und Bruchverhalten von kugelförmigen Granulaten bei Druck- und Stoßbeanspruchung; Docupoint: Magdeburg, **2006**.
- Antonyuk, S.; Heinrich, S.; Deen, N. G.; Kuipers, J.A.M. Influence of liquid layers on energy absorption during particle impact. *Particuology* **2009**, 7 (4) 245–259.
- Antonyuk, S.; Heinrich, S.; Tomas, J.; Deen, N. G.; Buijtenen, M.S.; Kuipers, J.A.M. Energy absorption during compression and impact of dry elastic-plastic spherical granules. *Granular Matter* **2010**, 12 (1) 15–47.
- Antonyuk, S.; Palis, S.; Heinrich, S. Breakage behaviour of agglomerates and crystals by static loading and impact. *Powder Technology* **2011**, 206 (1-2) 88–98.
- Aoki, K.; Akiyama, T. Simulation studies of pressure and density wave propagations in vertically vibrated beds of granules. *Physical Review E* **1995**, 52 (3) 3288–3291.
- Barnocky, G.; Davis, R.H. Elastohydrodynamic collision and rebound of spheres: Experimental verification. *Physics of Fluids* **1988**, 31 (6) 1324.
- Bird, R.B; Steward, W.E; Lightfoot, E.N. *Transport phenomena*; Wiley: New York, **1960**.
- Blake, K.R.; Spragle G.R. Unstructured 3D Delaunay mesh generation applied to planes, trains and automobiles, *ALAA 31th Aerospace Sciences Meeting & Exhibit*, Paper 93-0673, Reno, **1993**.



- Blei, S. On the interaction of non-uniform particles during the spray drying process: Experiments and modelling with the Euler-Lagrange approach; Shaker: Aachen, **2005**.
- Borini, G.; Andrade, T.; Freitas, L. Hot melt granulation of coarse pharmaceutical powders in a spouted bed. *Powder Technology* **2009**, *189* (3) 520–527.
- Bouffard, J.; Kaster, M.; Dumont, H. Influence of Process Variable and Physicochemical Properties on the Granulation Mechanism of Mannitol in a Fluid Bed Top Spray Granulator. *Drug Development and Industrial Pharmacy* **2005**, *31* (9) 923–933.
- Bourrier, F.; Nicot, F.; Darve, F. Physical processes within a 2D granular layer during an impact. *Granular Matter* **2008**, *10* (6) 415–437.
- Braumann, A.; Goodson, M.; Kraft, M.; Mort, P. Modelling and validation of granulation with heterogeneous binder dispersion and chemical reaction. *Chemical Engineering Science* **2007**, *62* (17) 4717–4728.
- Buffière, P.; Moletta R. Collision frequency and collisional particle pressure in three-phase fluidized beds. *Chemical Engineering Science* **2000**, 555555–5563.
- Cameron, A. Basis lubrication theory, 3rd ed.; Ellis Horwood Ltd: Chichester, **1981**.
- Cameron, I.; Wang, F.; Immanuel, C.D.; Stepanek, F. Process systems modelling and applications in granulation: A review. *Chemical Engineering Science* **2005**, *60* (14) 3723–3750.
- Campbell, C.S.; Brennen, C.E. Computer simulation of granular shear flows. *Journal of Fluid Mechanics* **1985**, 151167–188.
- Chua, K.W.; Makkawi, Y.T.; Hewakandamby, B.N.; Hounslow, M.J. Time scale analysis for fluidized bed melt granulation-II: Binder spreading rate. *Chemical Engineering Science* **2011a**, *66* (3) 327–335.
- Chua, K.W.; Makkawi, Y.T.; Hounslow, M.J. Time scale analysis for fluidized bed melt granulation I: Granule–granule and granule–droplet collision rates. *Chemical Engineering Science* **2011b**, *66* (3) 318–326.
- Chua, K.W.; Makkawi, Y.T.; Hounslow, M.J. Time scale analysis for fluidized bed melt granulation III: Binder solidification rate. *Chemical Engineering Science* **2011c**, *66* (3) 336–341.
- Cundall, P.A; Strack, O.D.L. A discrete numerical model for granular assemblies. *Géotechnique* **1979**, *29* (1) 47–65.
- Czok, G.; Ye, M.; Kuipers, J.A.M.; Werther, J. Modeling of Chemical Vapor Deposition in a Fluidized Bed Reactor Based on Discrete Particle Simulation. *International Journal of Chemical Reactor Engineering* **2005**, 3A57.
- Darabi, P.; Pougatch, K.; Salcudean, M.; Grecov, D. A novel coalescence model for binary collision of identical wet particles. *Chemical Engineering Science* **2009**, *64* (8) 1868–1876.



- Deen, N. G. Detailed computational and experimental fluid dynamics of fluidized beds. *Applied Mathematical Modelling* **2006**, *30* 1459–1471.
- Deen, N. G.; van Sint Annaland, M.; van der Hoef, M. A.; Kuipers, J.A.M. Review of discrete particle modeling of fluidized beds. *Chemical Engineering Science* **2007**, *62* (1-2) 28–44.
- Deen, N. G.; van Sint Annaland, M.; Kuipers, J.A.M. Direct numerical simulation of complex multi-fluid flows using a combined front tracking and immersed boundary method. *Chemical Engineering Science* **2009**, *64* (9) 2186–2201.
- Deen, N. G.; Godlieb, W.; Gortler, S.; Kuipers, J.A.M. Numerical Analysis of Solids Mixing in Pressurized Fluidized Beds. *Industrial & Engineering Chemistry Research* **2010**, *49* (11) 5246–5253.
- Denesuk, M. Dynamics of Incomplete Wetting on Porous Materials. *Journal of Colloid and Interface Science* **1994**, *168* (1) 142–151.
- Dhanalakshmi, K.; Ghosal, S.; Bhattacharya, S. Agglomeration of Food Powder and Applications. *Critical Reviews in Food Science and Nutrition* **2011**, *51* (5) 432–441.
- Dixit, R.; Puthli, S. Fluidization technologies: Aerodynamic principles and process engineering. *Journal of Pharmaceutical Sciences* **2009**, *98* (11) 3933–3960.
- Duangkhamchan, W., Ronsse, F., Depypere, F., Dewettinck, K., Pieters, J.G. CFD study of droplet atomisation using a binary nozzle in fluidised bed coating. *Chemical Engineering Science* **2012**, *68* (1) 555–566.
- Dubrovsky, V.; Podvysotsky, A.; Shraiber, A. Particle interaction in three-phase polydisperse flows. *International Journal of Multiphase Flow* **1992**, *18* (3) 337–352.
- Ennis, B.J.; Tardos, G.; Pfeffer, R. A microlevel-based characterization of granulation phenomena. *Powder Technology* **1991**, *65* 257–272.
- Epstein, N., Grace, J. R., Eds.: Spouted and spout-fluid beds: Fundamentals and applications; Cambridge University Press: Cambridge, **2011**.
- Ergun, S. Fluid flow through packed columns. *Chemical Engineering Progress* **1952**, *48* (2) 89–94.
- Feng, Y. Q.; Xu, B. H.; Zhang, S. J.; Yu, A. B.; Zulli, P. Discrete particle simulation of gas fluidization of particle mixtures. *AIChE Journal* **2004**, *50* (8) 1713–1728.
- Ferry, J.D. Viscoelastic properties of polymers, 3rd ed.; Wiley: New York, **1980**.
- Freireich, B.; Litster, J.D.; Wassgren, C. Using the discrete element method to predict collision-scale behavior: A sensitivity analysis. *Chemical Engineering Science* **2009**, *64* (15) 3407–3416.
- Fries, L.; Antonyuk, S.; Heinrich, S.; Palzer, S. DEM–CFD modeling of a fluidized bed spray granulator. *Chemical Engineering Science* **2011a**, *66* (11) 2340–2355.



- Fries, L.; Dosta, M.; Antonyuk, S.; Heinrich, S.; Palzer, S. Moisture Distribution in Fluidized Beds with Liquid Injection. *Chemical Engineering & Technology* **2011b**, *34* (7) 1076–1084.
- Gantt, J.; Cameron, I.; Litster J.D.; Gatzke, E. Determination of coalescence kernels for high-shear granulation using DEM simulations. *Powder Technology* **2006**, *170* (2) 53–63.
- Gantt, J.; Gatzke, E. High-shear granulation modeling using a discrete element simulation approach. *Powder Technology* **2005**, *156* (2-3) 195–212.
- Geldart, D. The size and frequency of bubbles in two- and three-dimensional gas-fluidised beds. *Powder Technology* **1970** (4) 41–55.
- Gidaspow, D. Multiphase flow and fluidization, 1st ed.; Academic Press: London, **1994**.
- Glatt GmbH: <http://www.glatt.com/cm/de/anlagenbau/agglomeration-granulation/kontinuierliche-wirbelschicht-brund-strahlschicht.html>
- Gnielinski, V. Wärme- und Stoffübertragung in Festbetten. *Chemie Ingenieur Technik* **1980**, *52* (3) 228–236.
- Goldman, A.J; Cox, R.G; Brenner, H. Slow viscous motion of a sphere parallel to a plane wall—I Motion through a quiescent fluid. *Chemical Engineering Science* **1967**, *22* (4) 637–651.
- Goldschmidt, M. Hydrodynamic Modelling of Fluidised Bed Spray Granulation; Twente University Press: Enschede, **2001**.
- Goldschmidt, M. Discrete element modelling of fluidised bed spray granulation. *Powder Technology* **2003**, *138* (1) 39–45.
- Goodwin, J.W. Colloids and interfaces with surfactants and polymers, 2nd ed.; Wiley: Chichester, U.K, **2009**.
- Gordon, M.; Taylor, J.S. Ideal copolymers and the second-order transitions of synthetic rubbers. i. non-crystalline copolymers. *Journal of Applied Chemistry* **1952**, *2* (9) 493–500.
- Gryczka, O.; Heinrich, S.; Miteva, V.; Deen, N.G.; Kuipers, J.A.M.; Jacob, M.; Mörl, L. Characterization of the pneumatic behavior of a novel spouted bed apparatus with two adjustable gas inlets. *Chemical Engineering Science* **2008**, *63* (3) 791–814.
- Gryczka, O.; Heinrich, S.; Deen, N.G.; van Sint Annaland, M.; Kuipers, J.A.M.; Jacob, M.; Mörl, L. Characterization and CFD-modeling of the hydrodynamics of a prismatic spouted bed apparatus. *Chemical Engineering Science* **2009**, *64* (14) 3352–3375.
- Haider, C. Mechanical and rheological material properties governing particle contact mechanisms in agglomeration processes, Diplomarbeit, TU München, **2010**.
- Hampel, R. Beitrag zur Analyse von kinetischen Einflüssen auf die Wirbelschicht-Sprühagglomeration; Deutsche Nationalbibliothek: Magdeburg, **2010**.



- Hapgood, K. Drop Penetration into Porous Powder Beds. *Journal of Colloid and Interface Science* **2002**, *253* (2) 353–366.
- Hapgood, K.; Iveson, S.M.; Litster J.D.; Liu, L.X. Granulation Rate Processes. In Handbook of powder technology, Volume 11: Granulation. Eds: Salman, A.D., Hounslow, M.J., Seville, J.P.K.; Elsevier: Amsterdam, **2007**.
- Hede, P.D. Fluid bed coating and agglomeration: Scale-up and process optimisation; Novozymes Bioprocess Academy: Copenhagen, **2008**.
- Hede, P.D.; Bach, P.; Jensen, A.D. Batch top-spray fluid bed coating: Scale-up insight using dynamic heat- and mass-transfer modelling. *Chemical Engineering Science* **2009**, *64* (6) 1293–1317.
- Heinrich, S.; Peglow, M.; Ihlow, M.; Mörl, L. Particle population modeling in fluidized bed-spray granulation—analysis of the steady state and unsteady behavior. *Powder Technology* **2003**, *130* (1-3) 154–161.
- Heinrich, S. Modellierung des Wärme- und Stoffübergangs sowie der Partikelpopulationen bei der Wirbelschicht-Sprühgranulation; VDI-Verl.: Düsseldorf, **2001**.
- Hemati, M.; Cherif, R.; Saleh, K.; Pont, V. Fluidized bed coating and granulation: influence of process-related variables and physicochemical properties on the growth kinetics. *Powder Technology* **2003**, *130* (1-3) 18–34.
- Hertz, H. Über die Berührung fester elastischer Körper. *Journal für die reine und angewandte Mathematik* **1881**, 92156–171.
- Hildebrand, T.; Rüggesegger, P. A new method for the model-independent assessment of thickness in three-dimensional images. *Journal of Microscopy* **1997**, *185* (1) 67–75.
- Hill, R.J.; Koch, D.L.; Ladd, A.J.C. Moderate-Reynolds-number flows in ordered and random arrays of spheres. *Journal of Fluid Mechanics* **2001**, *448*.
- Hoomans, B.P.B.; Kuipers, J.A.M.; Briels, W.J.; van Swaij, W.P.M. Discrete particle simulation of bubble and slug formation in a two-dimensional gas-fluidised bed: A hard-sphere approach. *Chemical Engineering Science* **1996**, *51* (1) 99–118.
- Hoomans, B.P.B.; Kuipers, J.A.M.; Mohd Salleh, M.A.; Stein, M.; Seville, J. P. K. Experimental validation of granular dynamics simulations of gas-fluidised beds with homogenous in-flow conditions using Positron Emission Particle Tracking. *Powder Technology* **2001** (116) 166–177.
- Hounslow, M. J.; Ryall, R. L.; Marshall, V. R. A discretized population balance for nucleation, growth, and aggregation. *AIChE Journal* **1988**, *34* (11) 1821–1832.
- Hunt, C. D'Ancona; Hanson, D. N.; Wilke, C. R. Capacity factors in the performance of perforated-plate columns. *AIChE Journal* **1955**, *1* (4) 441–451.
- Iveson, S.M.; Litster J.D.; Hapgood K.; Ennis B.J. Nucleation, growth and breakage phenomena in agitated wet Nucleation, growth and breakage phenomena in agitated wet granulation processes: a review. *Powder Technology* **2001**, 1173–39.



Jacob, M. ProCell technology: Modelling and application. *Powder Technology* **2009**, *189* (2) 332–342.

Jacob, M. Experimentelle Untersuchungen sowie Beiträge zur Modellierung von Prozessen in Wirbelschichttrinnen am Beispiel der Sprühgranulation; Otto von Guericke Universität: Magdeburg, **2010**.

Jacob, M.; Rümpler, K.; Waskow, M.; Glatt Ingenieurtechnik GmbH, 99427 Weimar, DE. Verfahren zur Herstellung von Instantprodukten in einer Wirbelschicht; DE102004024680A1, May 19, **2004**.

Jäger, K.-F.; Bauer, K.H. Auswirkungen der Gutbewegung im Rotor-Wirbelschicht-Granulator auf die Aufbauagglomeration. *Pharmazeutische Industrie* **1982**, 44193–197.

Jenike, A.W. Storage and flow of solids. Bulletin of the Utah Engineering Experiment Station; University of Utah: Salt Lake City, **1964**, Vol. 123.

Jinapong, N.; Suphantharika, M.; Jamnong, P. Production of instant soymilk powders by ultrafiltration, spray drying and fluidized bed agglomeration. *Journal of Food Engineering* **2008**, *84* (2) 194–205.

Johnson, K. L.; Kendall, K.; Roberts, A. D. Surface Energy and the Contact of Elastic Solids. *Proceedings of the Royal Society A: Mathematical, Physical and Engineering Sciences* **1971**, *324* (1558) 301–313.

Jono, K. A review of particulate design for pharmaceutical powders and their production by spouted bed coating. *Powder Technology* **2000**, *113* (3) 269–277.

Kafui, D.K.; Thornton, C.; Adams, M.J. Discrete particle-continuum fluid modeling of gas-solid fluidized beds. *Chemical Engineering Science* **2002**, *57*, 2395–2410.

Kafui, D.K.; Thornton, C. Fully-3D DEM simulation of fluidised bed spray granulation using an exploratory surface energy-based spray zone concept. *Powder Technology* **2008**, *184* (2) 177–188.

Karlsson, S.; Rasmuson, A.; van Wachem, B.G.M.; Niklasson Björn, I. CFD modeling of the Wurster bed coater. *AIChE Journal* **2009**, *55* (10) 2578–2590.

Ketterhagen, W.R. Modeling the motion and orientation of various pharmaceutical tablet shapes in a film coating pan using DEM. *International Journal of Pharmaceutics* **2011** (409) 137–149.

Kfuri, C. R.; Freitas, L. A. P. A Comparative Study of Spouted and Spout-Fluid Beds for Tablet Coating. *Drying Technology* **2005**, *23* (12) 2369–2387.

Knight, P.C. Structuring agglomerated products for improved performance. *Powder Technology* **2001**, *119* (1) 14–25.

Kobayashi, N.; Yamazaki, R.; Mori, S. A study on the behavior of bubbles and solids in bubbling fluidized beds. *Powder Technology* **2000** (113) 327–344.

- Kristensen, J.; Schæfer, T.; Kleinebudde, P. Direct Pelletization in a Rotary Processor Controlled by Torque Measurements. I. Influence of Process Variables. *Pharmaceutical Development and Technology* **2000**, *5* (2) 247–256.
- Krugger-Emden, H.; Simsek, E.; Rickelt, S.; Wirtz, S.; Scherer, V. Review and extension of normal force models for the Discrete Element Method. *Powder Technology* **2007**, *171* (3) 157–173.
- Kumar, J.; Peglow, M.; Warnecke, G.; Heinrich, S.; Mörl, L. Improved accuracy and convergence of discretized population balance for aggregation: The cell average technique. *Chemical Engineering Science* **2006**, *61* (10) 3327–3342.
- Laverman, J.A.; Roghair, I.; van Sint Annaland, M.; Kuipers, J.A.M. Investigation into the hydrodynamics of gas–solid fluidized beds using particle image velocimetry coupled with digital image analysis. *The Canadian Journal of Chemical Engineering* **2008**, *86* (3) 523–535.
- Li, J.; Kuipers, J.A.M. Effect of pressure on gas–solid flow behavior in dense gas–fluidized beds: a discrete particle simulation study. *Powder Technology* **2002** (127) 173–184.
- Li, Y.; Xu, Y.; Thornton, C. A comparison of discrete element simulations and experiments for ‘sandpiles’ composed of spherical particles. *Powder Technology* **2005**, *160* (3) 219–228.
- Li, Z.; Kind, M.; Gruenewald, G. Modeling the Growth Kinetics of Fluidized-Bed Spray Granulation. *Chemical Engineering & Technology* **2011**, *34* (7) 1067–1075.
- Lian, G.; Thornton, C.; Adams, M.J. Discrete particle simulation of agglomerate impact coalescence. *Chemical Engineering Science* **1998**, *53* (19) 3381–3391.
- Lian, G.; Xu, Y.; Huang, W.; Adams, M.J. On the squeeze flow of a power-law fluid between rigid spheres. *Journal of Non-Newtonian Fluid Mechanics* **2001**, *100* (1-3) 151–164.
- Link, J. M.; Cuypers, L.; Deen, N. G.; Kuipers, J.A.M. Flow regimes in a spout–fluid bed: A combined experimental and simulation study. *Chemical Engineering Science* **2005**, *60* (13) 3425–3442.
- Link, J. M. Development and validation of a discrete particle model of a spout–fluid bed granulator; Twente University Press: Enschede, **2006**.
- Link, J. M.; Godlieb, W.; Deen, N. G.; Kuipers, J.A.M. Discrete element study of granulation in a spout–fluidized bed. *Chemical Engineering Science* **2007**, *62* (1-2) 195–207.
- Link, J. M.; Deen, N. G.; Kuipers, J.A.M.; Fan, X.; Ingram, A.; Parker, D. J.; Wood, J.; Seville, J. P. K. PEPT and discrete particle simulation study of spout–fluid bed regimes. *AIChE Journal* **2008**, *54* (5) 1189–1202.
- Link, J. M.; Godlieb, W.; Tripp, P.; Deen, N. G.; Heinrich, S.; Kuipers, J.A.M.; Schönherr, M.; Peglow, Mirko. Comparison of fibre optical measurements and discrete element simulations for the study of granulation in a spout fluidized bed. *Powder Technology* **2009**, *189* (2) 202–217.
- Link, K.C; Schlünder, E.-U. Fluidized bed spray granulation. *Chemical Engineering and Processing: Process Intensification* **1997**, *36* (6) 443–457.



- Litster J.D. Scaleup of wet granulation processes: science not art. *Powder Technology* **2003**, *130* (1-3) 35–40.
- Litster J.D.; Smit, J.D; Hounslow, M. J. Adjustable discretized population balance for growth and aggregation. *AIChE Journal* **1995**, *41* (3) 591–603.
- Litster, J.D; Sarwono, R. Fluidized drum granulation: studies of agglomerate formation. *Powder Technology* **1996**, *88* (2) 165–172.
- Liu, L.X; Litster J.D.; Iveson, S.M; Ennis B.J. Coalescence of deformable granules in wet granulation processes. *AIChE Journal* **2000**, *45* (3) 529–539.
- Liu, L.X; Litster, J.D. Population balance modelling of granulation with a physically based coalescence kernel. *Chemical Engineering Science* **2002**, *57* (15) 2183–2191.
- Löffler, Friedrich. Staubabscheiden; Thieme: Stuttgart, **1988**.
- Loret, C.; Meunier, V.; Frith, J.; Fryer, P.J. Rheological characterisation of the gelation behaviour of maltodextrin aqueous solutions. *Carbohydrate Polymers* **2004**, *57* (2) 153–163.
- Louge, M.; Adams, M.J. Anomalous behavior of normal kinematic restitution in the oblique impacts of a hard sphere on an elastoplastic plate. *Physical Review E* **2002**, *65* (2).
- Macosko, Christopher W. Rheology: Principles, measurements, and applications. Advances in interfacial engineering series; VCH: New York, **1994**.
- Makkawi, Y.T; Wright, P.C. Fluidization regimes in a conventional fluidized bed characterized by means of electrical capacitance tomography. *Chemical Engineering Science* **2002**, *57* (13) 2411–2437.
- Mangwandi, C.; Cheong, Y.; Adams, M.J; Hounslow, M. J.; Salman, A. D. The coefficient of restitution of different representative types of granules. *Chemical Engineering Science* **2007**, *62* (1-2) 437–450.
- Mann, U. Analysis of spouted-bed coating and granulation. 1. Batch operation. *Industrial & Engineering Chemistry Process Design and Development* **1983**, *22* (2) 288–292.
- Martin, C. Unloading of powder compacts and their resulting tensile strength. *Acta Materialia* **2003**, *51* (15) 4589–4602.
- Martin, H. Wärme- und Stoffübertragung in der Wirbelschicht. *Chemie Ingenieur Technik* **1980**, *52* (3) 199–209.
- Matthewson, M. J. Adhesion of spheres by thin liquid films. *Philosophical magazine. A, Physics of condensed matter, defects and mechanical properties* **1988**, *57* (2) 207–216.
- McAllister, R.A; McGinnis, P.H; Plank, C.A. Perforated-plate performance. *Chemical Engineering Science* **1958**, *9* (1) 25–35.
- Mettler Toledo: Understanding and Controlling Fluid Bed Granulation for Improved Process Performance, Trial report, June 8-9 **2011**, Hamburg.



Mindlin, R.D. Compliance of elastic bodies in contact. *Journal of applied mechanics-Transactions of the ASME* **1949**, *16* (3) 259–268.

Mishra, B. A review of computer simulation of tumbling mills by the discrete element method: Part I—contact mechanics. *International Journal of Mineral Processing* **2003**, *71* (1-4) 73–93.

Mohs, G.; Gryczka, O.; Heinrich, S.; Mörl, L. Magnetic monitoring of a single particle in a prismatic spouted bed. *Chemical Engineering Science* **2009**, *64* (23) 4811–4825.

Mörl, L.; Krüger, G.; Heinrich, S.; Ihlow, M.; Jordanova, E.; Glatt Ingenieurtechnik GmbH, 99424 Weimar. Steuerbare Gasanströmeinrichtung für Strahlschichtapparate; DE 10004939, Feb 05, **2000**.

Müller, C.R; Holland, D.J; Sederman, A.J; Scott, S.A; Dennis, J.S; Gladden, L.F. Granular temperature: Comparison of Magnetic Resonance measurements with Discrete Element Model simulations. *Powder Technology* **2008**, *184* (2) 241–253.

Nestec: Experimental analysis at the Nestlé Research Center Lausanne in the framework of another project, **2011**.

Palzer, S. Anreichern und Benetzen von pulverförmigen Lebensmitteln mit Flüssigkeiten in diskontinuierlichen Mischaggregaten: Benetzungsvorgänge und verfahrenstechnische Einflussparameter; Technische Universität München: München, **2000**.

Palzer, S.; Sommer, K.; Hiebl, C. Penetration of Porous Systems by Nonwetting Liquids. *Chemical Engineering and Technology* **2003**, *26* (9) 962–966.

Palzer, S. The effect of glass transition on the desired and undesired agglomeration of amorphous food powders. *Chemical Engineering Science* **2005**, *60* (14) 3959–3968.

Palzer, S. Influence of material properties on the agglomeration of water-soluble amorphous particles. *Powder Technology* **2009**, *189* (2) 318–326.

Patil, D.; van Sint Annaland, M.; Kuipers, J.A.M. Critical comparison of hydrodynamic models for gas-solid fluidized beds-Part I: Bubbling gas-solid fluidized beds operated with a jet. *Chemical Engineering Science* **2005**, *60* (1) 57–72.

Peglow, M.; Kumar, J.; Hampel, R.; Tsotsas, E.; Heinrich, S. Towards a Complete Population Balance Model for Fluidized-Bed Spray Agglomeration. *Drying Technology* **2007**, *25* (7-8) 1321–1329.

Peirano, E.; Delloume, V.; Leckner, B. Two- or three-dimensional simulations of turbulent gas-solid flows applied to fluidization. *Chemical Engineering Science* **2001**, *56* 4787–4799.

Pitois, O.; Moucheront, P.; Chateau, X. Rupture energy of a pendular liquid bridge. *The European Physical Journal B* **2001**, *23* 79–86.

Popov, Valentin L. Kontaktmechanik und Reibung: Von der Nanotribologie bis zur Erdbebendynamik, 2nd ed.; Springer: Berlin, **2010**.



- Potyondy, D.O; Cundall, P.A. A bonded-particle model for rock. *International Journal of Rock Mechanics and Mining Sciences* **2004**, *41* (8) 1329–1364.
- Radeke, C.A.; Glasser, B.J; Khinast, J.G. Large-scale powder mixer simulations using massively parallel GPU architectures. *Chemical Engineering Science* **2010**, *65* (24) 6435–6442.
- Radl, S.; Kalvoda, E.; Glasser, B.J; Khinast, J.G. Mixing characteristics of wet granular matter in a bladed mixer. *Powder Technology* **2010**, *200* (3) 171–189.
- Rajniak, P.; Stepanek, F.; Dhanasekharan, K.; Fan, R.; Mancinelli, C.; Chern, R. A combined experimental and computational study of wet granulation in a Wurster fluid bed granulator. *Powder Technology* **2009**, *189* (2) 190–201.
- Reynolds, G.K; Fu, J.S; Cheong, Y.S; Hounslow, M.J; Salman, A.D. Breakage in granulation: A review. *Chemical Engineering Science* **2005**, *60* (14) 3969–3992.
- Reynolds, O. On the Theory of Lubrication and Its Application to Mr. Beauchamp Tower's Experiments, Including an Experimental Determination of the Viscosity of Olive Oil. *Philosophical Transactions of the Royal Society of London* **1886** (177) 157–234.
- Ronsse, F.; Pieters, J.G; Dewettinck, K. Modelling side-effect spray drying in top-spray fluidised bed coating processes. *Journal of Food Engineering* **2008**, *86* (4) 529–541.
- Rovero, G.; Brereton, C. M. H.; Epstein, N.; Grace, J. R.; Casalegno, L.; Piccinini, N. Gas flow distribution in conical-base spouted beds. *The Canadian Journal of Chemical Engineering* **1983**, *61* (3) 289–296.
- Salman, A. D.; Reynolds, G.K; Tan, H.; Gabbot, I.; Hounslow, M. J. Breakage in granulation. In *Handbook of powder technology, Volume 11: Granulation*. Salman, A. D., Hounslow, M. J., Seville, J. P. K., Eds. Handbook of powder technology 11; Elsevier: Amsterdam, **2007**.
- Sarkar, S.; van der Hoef, M. A.; Kuipers, J.A.M. Fluid–particle interaction from lattice Boltzmann simulations for flow through polydisperse random arrays of spheres. *Chemical Engineering Science* **2009**, *64* (11) 2683–2691.
- Schaafsma, S.; Vonk, P.; Segers, P.; Kossen, N. Description of agglomerate growth. *Powder Technology* **1998**, *97* (3) 183–190.
- Schulze, D. *Pulver und Schüttgüter: Fließeigenschaften und Handhabung*, 2nd ed.; Springer: Berlin ;, Heidelberg, **2009**.
- Seville, J. Interparticle forces in fluidisation: a review. *Powder Technology* **2000**, *113* (3) 261–268.
- Sommerfeld, M. Experimental analysis and modelling of particle-wall collisions. *International Journal of Multiphase Flow* **1999**, *25* (6-7) 1457–1489.
- Sperling, L. H. *Introduction to physical polymer science*; Wiley: New York, **1986**.
- Stiess, M. *Mechanische Verfahrenstechnik 1*; Springer: Berlin, **1992**.



- Szulc, K.; Lenart, A. Effect of Agglomeration on Flowability of Baby Food Powders. *Journal of Food Science* **2010**, *75* (5) E276.
- Takeuchi, S.; Wang, S.; Rhodes, M. Discrete element simulation of a flat-bottomed spouted bed in the 3-D cylindrical coordinate system. *Chemical Engineering Science* **2004**, *59* (17) 3495–3504.
- Takeuchi, S.; Wang, S.; Rhodes, M. Discrete element method simulation of three-dimensional conical-base spouted beds. *Powder Technology* **2008**, *184* (2) 141–150.
- Talu, I.; Tardos, G.; Khan, M.I. Computer simulation of wet granulation. *Powder Technology* **2000**, (110), 59–75.
- Tan, H.; Goldschmidt, M.; Boerefijn, R.; Hounslow, M. J.; Salman, A. D.; Kuipers, J.A.M. Building population balance model for fluidized bed melt granulation: lessons from kinetic theory of granular flow. *Powder Technology* **2004**, *142* (2-3) 103–109.
- Tan, H.; Salman, A. D.; Hounslow, M. J. Kinetics of fluidised bed melt granulation I: The effect of process variables. *Chemical Engineering Science* **2006**, *61* (5) 1585–1601.
- Tang, E.S.K; Wang, L.; Liew, C.V; Chan, L.W; Heng, P.W.S. Drying efficiency and particle movement in coating—Impact on particle agglomeration and yield. *International Journal of Pharmaceutics* **2008**, *350* (1-2) 172–180.
- Tardos, G.; Irfan Khan, M.; Mort, P. Critical parameters and limiting conditions in binder granulation of fine powders. *Powder Technology* **1997** (94) 245–258.
- Teipel, U.; Mikonsaari, I. Determining Contact Angles of Powders by Liquid Penetration. *Particle & Particle Systems Characterization* **2004**, *21* (4) 255–260.
- Terrazas-Velarde, K. Monte Carlo simulation of fluidized bed spray agglomeration; Sierke: Göttingen, **2010**.
- Terrazas-Velarde, K.; Peglow, M.; Tsotsas, E. Stochastic simulation of agglomerate formation in fluidized bed spray drying: A micro-scale approach. *Chemical Engineering Science* **2009**, *64* (11) 2631–2643.
- Teunou, E.; Poncelet, D. Batch and continuous fluid bed coating - review and state of the art. *Journal of Food Engineering* **2002**, *53* (4) 325–340.
- Thornton, C.; Ning, Z.M. A theoretical model for the stick/bounce behaviour of adhesive, elastic-plastic spheres. *Powder Technology* **1998**, *99* (2) 154–162.
- Tomas, J. Fundamentals of cohesive powder consolidation and flow. *Granular Matter* **2004**, *6* (2-3) 75–86.
- Tsuji, T.; Yabumoto, K.; Tanaka, T. Spontaneous structures in three-dimensional bubbling gas-fluidized bed by parallel DEM-CFD coupling simulation. *Powder Technology* **2008** (184) 132–140.



- Tsuji, Y.; Tanaka, Toshitsugu; Ishida, T. Lagrangian numerical simulation of plug flow of cohesionless particles in a horizontal pipe. *Powder Technology* **1992**, (71) 239–250.
- Tsuji, Y.; Kawaguchi T.; Tanaka, Toshitsugu. Discrete particle simulation of 2-dimensional fluidized bed. *Powder Technology* **1993**, 77 (1) 79–87.
- Turchiuli, C.; Eloualia, Z.; El Mansouri, N.; Dumoulin, E. Fluidised bed agglomeration: Agglomerates shape and end-use properties. *Powder Technology* **2005**, 157 (1-3) 168–175.
- Turton, R. Challenges in the modeling and prediction of coating of pharmaceutical dosage forms. *Powder Technology* **2008**, 181 (2) 186–194.
- Uhlemann, H.; Mörl, L. *Wirbelschicht - Sprühgranulation*; Springer: Berlin, **2000**.
- Uhlemann, J.; Reiß, I. Product Design and Process Engineering using the Example of Flavors. *Chemical Engineering & Technology* **2010**, 33 (2) 199–212.
- van Buijtenen, M. S. *Multiphase flow in spout fluidized bed granulators*; Technische Universiteit Eindhoven: Eindhoven, **2011**.
- van Buijtenen, M. S.; Deen, N. G.; Heinrich, S.; Antonyuk, S.; Kuipers, J.A.M. A discrete element study of wet particle-particle interaction during granulation in a spout fluidized bed. *The Canadian Journal of Chemical Engineering* **2009**, 87 (2) 308–317.
- van den Akker, H.E.A. Toward A Truly Multiscale Computational Strategy For Simulating Turbulent Two-Phase Flow Processes. *Industrial & Engineering Chemistry Research* **2010**, 49 (21) 10780–10797.
- van der Hoef, M.A; van Sint Annaland, M.; Kuipers, J.A.M. Computational fluid dynamics for dense gas–solid fluidized beds: a multi-scale modeling strategy. *Chemical Engineering Science* **2004**, 59 (22-23) 5157–5165.
- van der Hoef, M. A.; Beetstra, R.; Kuipers, J.A.M. Lattice-Boltzmann simulations of low-Reynolds-number flow past mono- and bidisperse arrays of spheres: results for the permeability and drag force. *Journal of Fluid Mechanics* **2005**, 528 233–254.
- van Wachem, B.G.M; Schouten, J.C; Krishna, R.; den Bleek, C.M. Eulerian simulations of bubbling behaviour in gas-solid fluidised beds. *Computers & Chemical Engineering* **1998**, 22 (1) 299–306.
- van Wachem, B.G.M; Schouten, J.C Krishna R.; den Bleek, C.M. Comparative analysis of CFD models of dense gas-solid systems. *AIChE Journal* **2001**, 47 (5) 1035–1051.
- Villabrigos, J.; Guardiola, J. New methodology for scaling hydrodynamic data from a 2D-fluidized bed. *Chemical Engineering Science* **2005**, 60 (18) 5151–5163.
- Waldie, B. Growth mechanism and the dependence of granule size on drop size in fluidized-bed granulation. *Chemical Engineering Science* **1991**, 46 (11) 2781–2785.



Walton, O.R; Braun, R.L. Viscosity, granular temperature and stress calculations for shearing assemblies of inelastic, frictional disks. *Journal of Rheology* **1986**, *30* (5) 949–980.

Washino, K.; Tan, H.S; Salman, A.D; Hounslow, M.J. Direct numerical simulation of solid–liquid–gas three-phase flow: Fluid–solid interaction. *Powder Technology* **2011**, *206* (1-2) 161–169.

Wen, C. Y.; Yu, Y. H. A generalized method for predicting the minimum fluidization velocity. *AIChE Journal* **1966a**, *12* (3) 610–612.

Wen, Y.C; Yu, Y.H. Mechanics of fluidization. *Chemical Engineering Progress Symposium Series* **1966b**, 62100–111.

Werner, S.R.L; Jones, J.R.; Paterson, A.H.J; Archer, R.H.; Pearce, D.L. Air-suspension coating in the food industry: Part II — micro-level process approach. *Powder Technology* **2007a**, *171* (1) 34–45.

Werner, S.R.L; Jones, J.R.; Paterson, A.H.J; Archer, R.H.; Pearce, D.L. Air-suspension particle coating in the food industry: Part I — state of the art. *Powder Technology* **2007b**, *171* (1) 25–33.

Werther, J.; Heinrich, S.; Dosta, M.; Hartge, E.-U. The ultimate goal of modeling - Simulation of system and plant performance. *Particology* **2011**, *9* (4) 320–329.

Wurster, D.E.; Wisconsin Alumni Research Foundation. Method of applying coatings to edible tablets or the like; 2648609, Jan 21, **1949**.

Xie, N.; Battaglia, F.; Pannala, S. Effects of using two- versus three-dimensional computational modeling of fluidized beds - Part I, hydrodynamics. *Powder Technology* **2008**, *182* (1) 1–13.

Xu, B. H.; Yu, A. B. Numerical simulation of the gas-solid flow in a fluidized bed by combining discrete particle method with computational fluid dynamics. *Chemical Engineering Science* **1997**, *92* (16) 2785–2809.

Yang, S.T.; van Savage, G.; Weiss, J.; Ghebre-Sellassie, I. The effect of spray mode and chamber geometry of fluid-bed coating equipment and other parameters on an aqueous-based ethylcellulose coating. *International Journal of Pharmaceutics* **1992**, *86* (2-3) 247–257.

Young, T. An essay on the cohesion of fluids. *Philosophical Transactions of the Royal Society London* **1805**, *95*, 65-87.

Zhu, H. P.; Yu, A. B. Steady-state granular flow in a three-dimensional cylindrical hopper with flat bottom: microscopic analysis. *Journal of Physics D: Applied Physics* **2004**, *37* (10) 1497–1508.

Zhu, H.P; Zhou, Z. Y.; Yang, R.Y; Yu, A. B. Discrete particle simulation of particulate systems: A review of major applications and findings. *Chemical Engineering Science* **2008**, 635728–5770.

Zhu, R.R; Zhu, W. B.; Xing, L.C; Sun, Q.Q. DEM simulation on particle mixing in dry and wet particles spouted bed. *Powder Technology* **2011**, 21073–81.



List of publications

Peer-reviewed journal publications

- [1] **Fries, L.**, Antonyuk, S., Heinrich, S., Palzer, S.:
DEM-CFD modelling of a fluidized bed spray granulator,
Chemical Engineering. Science 66 (2011), 1340-2355.
- [2] **Fries, L.**, Dosta, M., Antonyuk, S., Heinrich, S., Palzer, S.:
Moisture distribution in fluidized beds with liquid injection,
Chemical Engineering. & Technology 34, 7, (2011), 1076–1084.
- [3] **Fries, L.**, Antonyuk, S., Heinrich, S., Dopfer, D., Palzer, S.:
Collision dynamics in fluidized bed granulators – A DEM-CFD study
Chemical Engineering. Science 67 (2012), in press.
- [4] Dopfer, D., Palzer, S., **Fries, L.**, Antonyuk, S., Heinrich, S., Haider, C., Salman, A.G.:
Adhesion mechanisms between water-soluble particles.
Powder Technology (2012), in press.

Conference proceedings

- [5] **Fries, L.**, Antonyuk, S., Heinrich, S., Palzer, S.:
DEM-CFD Modelling of a fluidized bed spray granulator.
In: Proceedings of Fluidization XIII (Eds: S.D. Kim, Y. Kang, J.K. Lee, Y.C. Seo), Eng. Conf. Int. 2010.



- [6] **Fries, L.**, Antonyuk, S., Heinrich, S., Palzer, S., Jacob, M.:
Coupled DEM/CFD simulation of a Wurster-granulator,
In: Proceedings of the 7th International Conference on Multiphase Flow (ICMF),
Paper No. 625, 2010.
- [7] Palzer, S. Heinrich, S., **Fries, L.**, Antonyuk, S.:
Adhesion forces between water-soluble particles: - material properties, theory of adhesion and modelling of agglomeration processes -
In: Proceedings of World Congress on Particle technology (WCPT6),
Paper No. 306, 2010
- [8] Antonyuk, S., **Fries, L.**, Heinrich, S., Palzer, S.:
Impact behaviour of water-soluble amorphous food agglomerates: agglomeration and breakage behaviour
In: Proceedings of World Congress on Particle technology (WCPT6),
Paper No. 309, 2010.
- [9] Antonyuk, S., **Fries, L.**, Heinrich, S., Palzer, S.:
Influence of moisture content on the flow behaviour of amorphous food agglomerates and the collapse of the fluidized bed
In: Proceedings of World Congress on Particle technology (WCPT6),
Paper No. 310, 2010.
- [10] **Fries, L.**, Antonyuk, S., Heinrich, S., Palzer, S.:
Coupled DEM-CFD simulation of a Wurster granulator
In: Proceedings of World Congress on Particle technology (WCPT6),
Paper No. 325, 2010.
- [11] **Fries, L.**, Dosta, M., Antonyuk, S., Heinrich, S., Palzer, S.:
Moisture distribution in fluidized beds with liquid injection
In: Proceedings of 17th International Drying Symposium (IDS2010), Eds: E. Tsotsas, T. Metzger, M. Peglow, Paper No. B52, 2010.



- [12] Dosta, M., Antonyuk, S., **Fries, L.**, Heinrich, S.:
Discrete element modelling of the fluidized bed granulation process by coupling of different simulation systems
In: Proceedings of 17th International Drying Symposium (IDS2010), Eds: E. Tsotsas, T. Metzger, M. Peglow, 2010.
- [13] **Fries, L.**, Antonyuk, S., Heinrich, S., Palzer, S.:
DEM-CFD modelling of a bubbling fluidized bed and a Wurster-coater
In: Proceedings of 10th International Conference on Circulating Fluidized Beds and Fluidization Technology (CFB10), Ed: T.M.. Knowlton, 505-512, 2011.
- [14] **Fries, L.**, Salikov, V., Antonyuk, S., Heinrich, S., Dopfer, D., Palzer, S.:
Agglomeration of amorphous food powders in a fluidised bed: Comparison of different granulator configurations
In: Proceedings of 5th International Granulation Workshop, Eds: M. Hounslow, A. Salman, paper No. 101, 2011.
- [15] Dosta, M., **Fries, L.**, Antonyuk, S., Heinrich, S., Palzer, S.:
Multiscale Simulation of fluidised bed spray agglomeration
In: Proceedings of 5th International Granulation Workshop, Eds: M. Hounslow, A. Salman, paper No. 103, 2011.
- [16] Dopfer, D., Heinrich, S., **Fries, L.**, Antonyuk, S., Haider, C., Salman, A.D., Palzer, S.:
Adhesion mechanisms between water-soluble particles
In: Proceedings of 5th International Granulation Workshop, Eds: M. Hounslow, A. Salman, paper No. 58, 2011.



Curriculum vitae

Personal information:

Name: Lennart Fries
Born: 09.12.1981 in Hamburg, Germany

Education:

1988 – 1992 Elementary school in Geesthacht, Germany
1992 – 2001 Otto-Hahn-Gymnasium Geesthacht
06.2001 Abitur

Civil Service

09.2001 – 06.2002 Stiftung Hamburgisches Krankenhaus Edmunsthal-Siemerswalde

Academic history

10.2002 – 06.2008 Study of Process Engineering at Hamburg University of Technology.
09.2005 – 07.2006 Ecole Nationale Supérieure des Ingénieurs en Arts Chimiques et Technologiques, Toulouse, France.
06.2008 Degree: Diplom-Ingenieur, Hamburg University of Technology.
08.2008 – 12.2011 PhD student at the Institute of Solids Process Engineering and Particle Technology at Hamburg University of Technology.
Supervisor: Prof. Dr.-Ing. Stefan Heinrich

Internships

08.2002 – 09.2002 BUCO Wärmeaustauscher GmbH, Geesthacht, Germany.
05.2007 – 09.2007 PTC Trainee at Nestlé Product Technology Center Orbe, Switzerland.

Professional Experience

Since 01.2012 Associate Specialist, Nestlé Research Center Lausanne, Switzerland.





